UNIMORE
UNIVERSITÀ DEGLI STUDI DI MODENA E REGGIO EMILIA

UNIVERSITÀ DEGLI STUDI DI MODENA E REGGIO EMILIA

Dottorato di ricerca in
"Information and communication technologies (ICT)"

Ciclo XXXVIII

Optoelectronic methods and instrumentation for biomedical smart sensors

Candidato: Ghassem Baridi
Relatore (Tutor): Prof. Luigi Rovati
Correlatore (Co-Tutor): Prof Francesco Rossella

Coordinatore del Corso di Dottorato: Prof. Rovati Luigi

Abstract:

Graphene-based technologies have emerged as a promising platform for next-generation biosensors due to graphene's exceptional electrical, plasmonic, and nonlinear optical properties, along with its scalability and cost-effective fabrication. This thesis presents a comprehensive investigation of graphene-based biosensing devices operating across electrical, plasmonic, and nonlinear terahertz regimes, with particular emphasis on electrostatic effects, quantum capacitance, and the tunability of graphene's electronic properties to enhance sensing performance.

The electrical biosensing part focuses on graphene ion-sensitive field-effect transistors (ISFETs) operating in electrolyte environments, where sensing is governed by the formation of an electric double layer at the graphene-electrolyte interface. A comparative study of the Gouy-Chapman and Stern models is carried out using sodium ions as a case study. The impact of graphene quantum capacitance is explicitly incorporated, demonstrating a pronounced enhancement in device sensitivity and providing deeper insight into the electrostatic mechanisms governing graphene-based ISFET operation.

Building on this framework, the ISFET model is extended to the detection of β_2-microglobulin (β_2M), a clinically relevant protein biomarker. Molecular dynamics simulations reveal that, in addition to small ions, large biomolecules significantly influence the electric double layer near the graphene surface. β_2M adsorption, driven by its size, orientation, and heterogeneous surface charge distribution, induces distinct changes in the local electrostatic potential and graphene Fermi energy, leading to a stable and detectable electrical response. These results highlight the importance of biomolecule-specific electrostatic interactions in graphene biosensors.

Experimental validation is provided through the fabrication and characterization of graphene field-effect transistors using both mechanically exfoliated and chemical vapor deposition (CVD) graphene. Protein sensing experiments with albumin demonstrate distinct and irreversible electrical signatures under liquid-droplet and dried-droplet conditions, revealing the role of adsorption dynamics. Additionally, CVD-grown GFETs are systematically evaluated as pH sensors under varying pH levels and phosphate-buffered saline concentrations. The experimental results show clear shifts in resistance and charge neutrality point, in good agreement with the adopted ISFET theoretical model.

The plasmonic biosensing part investigates electrolyte-gated graphene surface plasmon resonance (SPR) sensors. By incorporating graphene quantum capacitance into the theoretical framework,

improved performance prediction is achieved. Computational results demonstrate enhanced accuracy and a measurable increase in the quality factor for β_2M detection, underscoring the critical role of quantum-electrostatic effects in graphene-based plasmonic sensor design.

Finally, the thesis explores graphene's strong nonlinear optical response in the terahertz regime for biosensing applications. An ultrathin graphene-based plasmonic metasurface is proposed to enhance third-harmonic generation (THG). The sensitivity of THG to variations in graphene Fermi energy is exploited for biosensing, with systematic tuning of structural and material parameters. Simulated absorption, reflection, and THG intensity responses confirm the feasibility of detecting β_2M through nonlinear terahertz spectroscopy.

Overall, this thesis provides a unified and multi-physics study of graphene-based biosensors, demonstrating how electrostatic modeling, quantum capacitance, and nonlinear optical effects can be synergistically leveraged to achieve high sensitivity and accurate biomolecule detection, paving the way for advanced graphene-enabled biosensing platforms.

Keywords:

Graphene biosensors; Graphene field-effect transistors; Quantum capacitance; Electric double layer; Plasmonic biosensing; Terahertz nonlinear optics; Third-harmonic generation; β_2-microglobulin detection

Sommario:

Le tecnologie basate sul grafene sono emerse come una piattaforma promettente per biosensori di nuova generazione, grazie alle eccezionali proprietà elettriche, plasmoniche e ottiche non lineari del grafene, nonché alla sua scalabilità e ai processi di fabbricazione a basso costo. Questa tesi presenta uno studio completo di dispositivi di biosensing basati sul grafene operanti nei regimi elettrico, plasmonico e terahertz non lineare, con particolare attenzione agli effetti elettrostatici, alla capacità quantistica e alla possibilità di modulare le proprietà elettroniche del grafene per migliorare le prestazioni di rilevamento.

La parte dedicata al biosensing elettrico si concentra sui transistor a effetto di campo sensibili agli ioni basati sul grafene (ISFET) operanti in ambienti elettrolitici, nei quali il meccanismo di rilevamento è governato dalla formazione di un doppio strato elettrico all'interfaccia grafene–elettrolita. Viene condotto uno studio comparativo dei modelli di Gouy–Chapman e di Stern utilizzando gli ioni sodio come caso di studio. L'effetto della capacità quantistica del grafene è esplicitamente incluso, mostrando un significativo incremento della sensibilità del dispositivo e fornendo una comprensione più approfondita dei meccanismi elettrostatici che regolano il funzionamento degli ISFET basati sul grafene.

Sulla base di questo quadro teorico, il modello ISFET viene esteso alla rilevazione della β_2-microglobulina (β_2M), un biomarcatore proteico di rilevanza clinica. Le simulazioni di dinamica molecolare rivelano che, oltre agli ioni di piccole dimensioni, anche le biomolecole di grandi dimensioni influenzano in modo significativo il doppio strato elettrico in prossimità della superficie del grafene. L'adsorbimento della β_2M, determinato dalle sue dimensioni, dall'orientazione e dalla distribuzione eterogenea della carica superficiale, induce variazioni distinte del potenziale elettrostatico locale e dell'energia di Fermi del grafene, dando luogo a una risposta elettrica stabile e rilevabile. Questi risultati evidenziano l'importanza delle interazioni elettrostatiche specifiche delle biomolecole nei biosensori basati sul grafene.

La validazione sperimentale è fornita attraverso la fabbricazione e la caratterizzazione di transistor a effetto di campo in grafene realizzati sia mediante esfoliazione meccanica sia tramite deposizione chimica da vapore (CVD). Gli esperimenti di rilevamento proteico con albumina mostrano firme elettriche distinte e irreversibili in condizioni di goccia liquida e di goccia essiccata, mettendo in evidenza il ruolo delle dinamiche di adsorbimento. Inoltre, i GFET cresciuti mediante CVD vengono sistematicamente valutati come sensori di pH a diversi valori di pH e concentrazioni di soluzione

salina tamponata con fosfati. I risultati sperimentali mostrano chiari spostamenti della resistenza e del punto di neutralità di carica, in buon accordo con il modello teorico ISFET adottato.

La parte dedicata al biosensing plasmonico analizza sensori a risonanza plasmonica di superficie (SPR) in grafene con gate elettrolitico. L'inclusione della capacità quantistica del grafene nel quadro teorico consente una previsione più accurata delle prestazioni del dispositivo. I risultati computazionali dimostrano un miglioramento dell'accuratezza e un aumento misurabile del fattore di qualità nella rilevazione della β_2M, sottolineando il ruolo cruciale degli effetti quantistico-elettrostatici nella progettazione di sensori plasmonici basati sul grafene.

Infine, la tesi esplora la forte risposta ottica non lineare del grafene nel regime terahertz per applicazioni di biosensing. Viene proposta una metasuperficie plasmonica ultrafine basata sul grafene per potenziare la generazione della terza armonica (THG). La sensibilità della THG alle variazioni dell'energia di Fermi del grafene viene sfruttata per il biosensing, mediante una modulazione sistematica dei parametri strutturali e dei materiali. Le simulazioni delle risposte di assorbimento, riflessione e intensità della THG confermano la fattibilità della rilevazione della β_2M tramite spettroscopia terahertz non lineare.

Nel complesso, questa tesi fornisce uno studio unificato e multifisico dei biosensori basati sul grafene, dimostrando come la modellizzazione elettrostatica, la capacità quantistica e gli effetti ottici non lineari possano essere sfruttati in modo sinergico per ottenere un'elevata sensibilità e una rilevazione accurata delle biomolecole, aprendo la strada a piattaforme avanzate di biosensing abilitate dal grafene.

Parole chiave:

Biosensori in grafene; Transistor a effetto di campo in grafene; Capacità quantistica; Doppio strato elettrico; Biosensing plasmonico; Ottica non lineare terahertz; Generazione della terza armonica; Rilevazione della β_2-microglobulina

Table of Contents

List of figures:

Chapter one

Biosensors: Classification, Mechanisms, and the Significance of Graphene in Electrical and Optical Detection

1.1- Introduction to Sensors and Biosensors:

Sensors are instruments that detect physical, chemical, or biological changes and convert these changes into measurable signals [1]. They are widely applied across various fields such as medical diagnostics, food safety, industrial process control, and environmental monitoring [2]. Over the past five decades, progress in biosensor technology have grown sharply, motivated by progress in nanotechnology, biotechnology, electronics, and silicon-based technologies [3]. Lately, the combination of artificial intelligence (AI) and big data analytics has led to the emergence of smart biosensors as a significant field of study [4]. Generally, a biosensor is formed of four key components: (1) a sensing element or receptor that selectively interacts with the target analyte; (2) an interface that supports and sustain optimal states for sensor function; (3) a transducer that converts the biological or chemical interaction into an electrical signal; and (4) electronic systems that handle signal amplification, processing, and data interpretation[5,6].

Biosensors are commonly categorized using three different criteria. First, based on the type of biological identification element, they can be classified into biocatalytic biosensors (such as those using enzymes), immunosensors (which rely on antibodies), and nucleic acid-based biosensors (like DNA sensors). Next, classification can be made according to the transduction method, which includes electrochemical, optical, piezoelectric, and thermal (or calorimetric) biosensors. Third, biosensors can also be sorted by purpose-examples include clinical and medical biosensors, environmental monitoring devices, and wearable technologies. Additionally, from a commercial standpoint, they are often distinguished by their form factor, performed under lab conditions-based systems or portable devices. Despite their type or application, all biosensors require a stable and efficient interface to ensure accurate and reliable sensing performance [7].

1.2- Types of Biosensors:

Biosensors are generally classified by two factors: the sensing element and the transduction mode. Sensing elements include enzymes (used in enzyme-based biosensors), antibodies (used in immunosensors), nucleic acids (used in DNA biosensors), biological tissues, organelles, and even whole cells, which are utilized in whole-cell biosensors to detect specific biological activity. The transduction mode, in contrast, is defined by the type of physicochemical change that results from the interaction between the analyte and the sensing element. According to the transducer type, biosensors can be classified as electrochemical (including amperometric, potentiometric, and conductometric),

optical (such as absorbance, fluorescence, and chemiluminescence-based), piezoelectric (involving acoustic or ultrasonic signals), and calorimetric, which measures changes in heat [8].

1.2.1- Amperometric Biosensor:

An amperometric biosensor is a type of electrochemical sensor that measures the electric current resulting from the oxidation or reduction of an electroactive species. This current is directly equivalent to the concentration of the target analyte in the sample. These biosensors function by applying a constant voltage between two electrodes, which causes electrochemical reactions to occur at the electrode surface. The consequent current is then measured and used to calculate the analyte. Amperometric biosensors are known for their high sensitivity and are particularly effective for detecting electroactive compounds naturally present in biological or environmental samples. A typical example is the glucose biosensor used in diabetes monitoring. In this application, glucose in the blood reacts with the enzyme glucose oxidase, producing hydrogen peroxide. The hydrogen peroxide is then oxidized at the electrode surface, generating a current that equivalent to the glucose concentration in the sample [9].

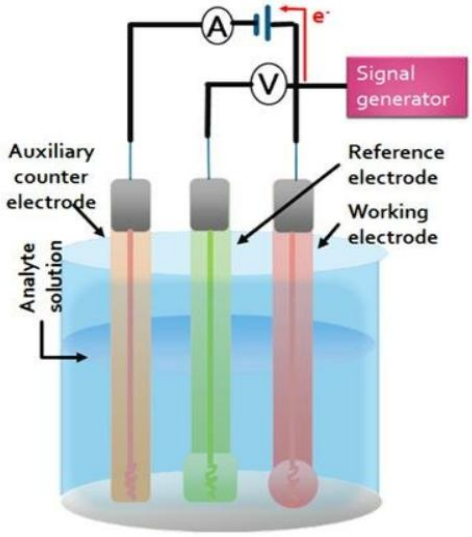

Figure 1-1. Schematic representation of an Amperometric biosensor showing the three-electrode configuration, consisting of a working electrode modified with a biorecognition element, a reference electrode for stable potential control, and a counter electrode to complete the electrochemical circuit. The figure illustrates the generation of an Amperometric signal resulting from the redox reaction between the target analyte and the immobilized biomolecule. The schematic is taken from reference [9].

.

1.2.2- Potentiometric biosensor:

In this method, scientific information is acquired by changing the biorecognition event into an electrical potential signal, which arises from oxidation or reduction reactions triggered by biochemical interactions. A selectively permeable ion-conductive membrane is commonly applied to detect this potential signal, generated when the analyte interacts with the sensor surface. A high-impedance voltmeter is then used to measure the electrical potential difference, or electromotive force (EMF), between two electrodes. One electrode, known as the indicator or ion-selective electrode (ISE), presents a change in potential based on the activity or concentration of the analyte in the solution. The other electrode acts as a reference and provides a stable and constant potential, unaffected by the analyte concentration, to finalize the electrochemical cell [10].

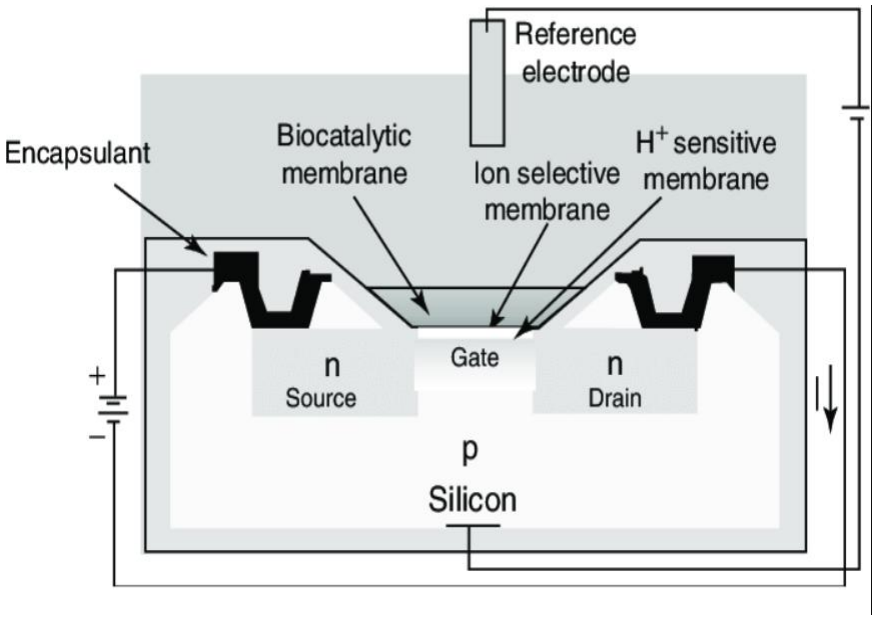

Figure 1-2. Schematic of a potentiometric FET-based biosensor showing the p-type silicon substrate with n-type source and drain, a gate region covered by ion-selective and H^+-sensitive membranes, and a reference electrode. Changes in ion concentration at the gate modulate the surface potential, enabling potentiometric sensing. The schematic is taken from reference [10].

1.2.3- Optical Biosensor:

This type of biosensor operates based on fundamentals such as optical diffraction or electrochemiluminescence. In one common design, a silicon wafer is functionalized with proteins through covalent bonding. The wafer is then exposed to ultraviolet (UV) light through a photomask, which deactivates the antibodies in the exposed regions. When the treated wafer chips are developed with an analyte, antigen-antibody interactions occur in the active regions, leading to the formation of

a diffraction grating. This grating generates a diffraction signal when illuminated by a light source. Optical biosensors typically consist of a light source, various optical components to shape and direct the light beam, a modulating mechanism, a sensing surface, and a photodetector. These devices detect changes based on fluorescence or absorbance, which result from catalytic reactions or molecular interactions between the sensor and the analyte [11,12].

1.2.4- Conductometric Biosensor:

Conductometric biosensors work by measuring the electrical conductance or resistance of a solution, which changes in response to a biorecognition event. These biosensors utilize the relationship between ionic concentration and electrical conductivity. When a biochemical reaction occurs-such as an enzyme-substrate interaction-it often leads to a change in the concentration of ionic species in the solution. This alteration directly affects the conductivity or current flow within the system. A usual conductometric biosensor consists of two metal electrodes, commonly made of platinum or silver, spaced at a fixed distance. An alternating current (AC) voltage is applied across the electrodes to maintain a consistent current flow. During the biorecognition process, the composition and concentration of ions in the solution are modified, which in turn changes the electrical conductance between the electrodes. This alteration is detected using an Ohmmeter or a multimeter, allowing for the evaluation of the analyte. Because these biosensors are sensitive to even small changes in ionic strength, they are ideal for detecting enzymatic reactions or other processes that generate and consume charged species. Moreover, conductometric biosensors are relatively simple in design and low cost, making them attractive for use in environmental monitoring, clinical diagnostics, and industrial applications [13].

1.2.5- Calorimetric Biosensor:

Various enzyme-catalysed reactions are exothermic, meaning they release heat as a byproduct. This release of thermal energy can be used as the basis for measuring reaction rates and, consequently, the concentration of the target analyte. Biosensors that utilize this principle are known as calorimetric or thermal biosensors. In these systems, temperature changes resulting from the biochemical reaction are detected using highly sensitive devices such as thermistors, which measure minute variations in temperature. Typically, the analyte solution is passed through a small reaction chamber that contains immobilized enzymes or other catalytic substances. Thermistors are placed at the input and output of the reaction chamber to measure the temperature of the solution before and after it interacts with the immobilized components. The difference in temperature reflects the heat generated by the biochemical reaction, which correlates with the analyte concentration. This type of biosensor is

particularly proper for detecting analytes that are part of multi-step enzymatic mechanism. Under this circumstance, using two or more enzymes in order within the biosensor can enhance the overall heat output, increasing the sensitivity of detection. As another option, multifunctional enzymes capable of catalysing multiple steps in a reaction pathway may be used. A well-known example of this technology is the use of glucose oxidase in glucose biosensors. As glucose is oxidized, heat is released and measured, allowing for the quantification of glucose levels in clinical or food samples [14].

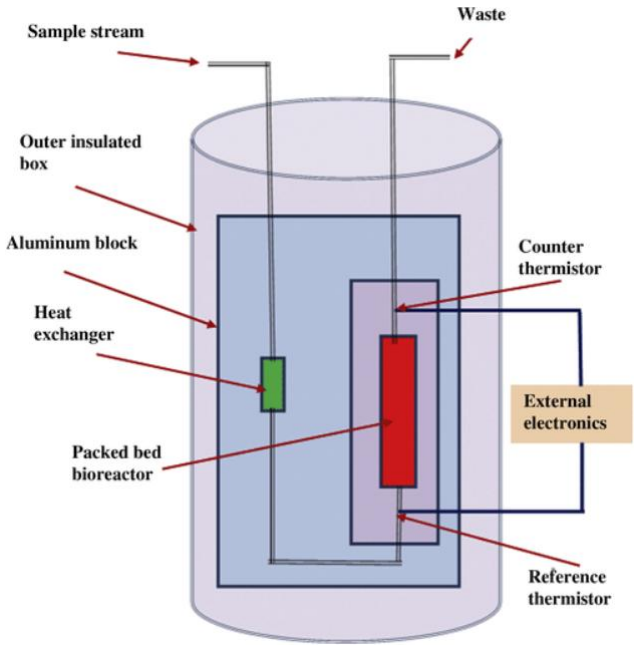

Figure 1-3. Schematic diagram of a calorimetric biosensor showing a packed-bed bioreactor integrated with a heat exchanger inside an insulated aluminum block. The sensor employs reference and counter thermistors to measure temperature changes generated by the biochemical reaction as the sample flows through the system, enabling calorimetric detection. The schematic is taken from reference [14].

1.2.6- Piezoelectric biosensor:

Piezoelectricity relates to the direct interaction between mechanical stress and electrical charge in non-conductive crystalline materials. Basically, piezoelectric biosensors operate on the theory that certain materials-such as quartz-can resonate at a natural frequency when subjected to an alternating electrical signal. This natural resonance changes when there is an alteration in mass on the surface of the piezoelectric material, which is the basis for detection. A typical piezoelectric biosensor consists of two main components: a transducer made of piezoelectric material and a biorecognition element that is fixed on the surface of the transducer. When an alternating current is applied, the piezoelectric crystal oscillates at a specific frequency. This frequency is highly sensitive to any mass changes on the sensor surface. When the target analyte binds to the biorecognition layer, it alters the mass on the

surface, leading to a measurable shift in resonance frequency. This frequency shift is directly related to the amount of analyte present, allowing for numerical analysis.

There are two main types of piezoelectric sensors used in biosensing: bulk wave (BW) devices, such as quartz crystal microbalances (QCM), and surface acoustic wave (SAW) devices. Both related on the piezoelectric effect, but they in contrast in how the acoustic wave spread through or across the material. Quartz is the widely used piezoelectric material due to its affordability, availability in single crystal form, and durability under thermal, chemical, and mechanical stress. However, other materials like lithium niobate and lithium tantalate have also been explored due to their desirable piezoelectric properties. These sensors are specifically advantageous for real-time, unlabelled detection of biomolecules and are used in applications ranging from medical diagnostics to environmental monitoring [15].

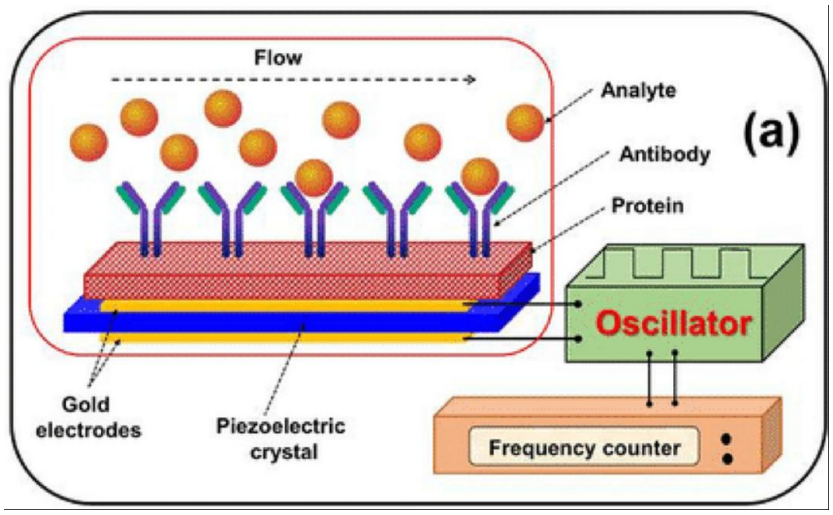

Figure 1-4. Schematic representation of a piezoelectric (mass-sensitive) biosensor based on a quartz crystal microbalance (QCM). Antibodies immobilized on gold electrodes capture target analytes from the flowing sample, causing a mass change on the piezoelectric crystal. This mass variation leads to a shift in oscillation frequency, which is measured by the oscillator and frequency counter for biosensing. The schematic is taken from reference [15].

1.2.7- DNA Biosensor:

DNA-based biosensors, often referred to as bio detectors**,** are dominant tools designed for the detection and analysis of specific DNA sequences. Their mean goal is to determine and measure the interactions between supplementary DNA strands or between antigens and antibodies at the molecular level. These interactions allow for the correct detection and characterization of single DNA molecules or antigenic targets, which is vital in many biological and medical applications. The framework of using nucleic acids for diagnostic purposes dates to the discovery of the DNA double helix in 1953

and has since advanced significantly. A basic principle behind DNA biosensors is the highly particular hybridization between two complementary single-stranded DNA (ssDNA) molecules to form a stable double-stranded DNA (dsDNA) structure. This specific binding event is investigated in nucleic acid-based biosensors, where ssDNA functions as the biorecognition element to capture its complementary strand. These biosensors have advanced significantly beyond traditional detection techniques by enabling rapid, sensitive, and specific detection of genetic material without the need for large scale sample processing. The hybridization event activates a measurable signal-such as optical, electrochemical, or piezoelectric-which relates with the presence or amount of the target DNA. DNA biosensors showing strong promise in clinical diagnostics, particularly for the early detection of genetic disorders, infectious diseases, and cancer. Their ability to detect pathogens and genetic mutations with high precision makes them valuable tools in individualized medicine and biomedical research [16].

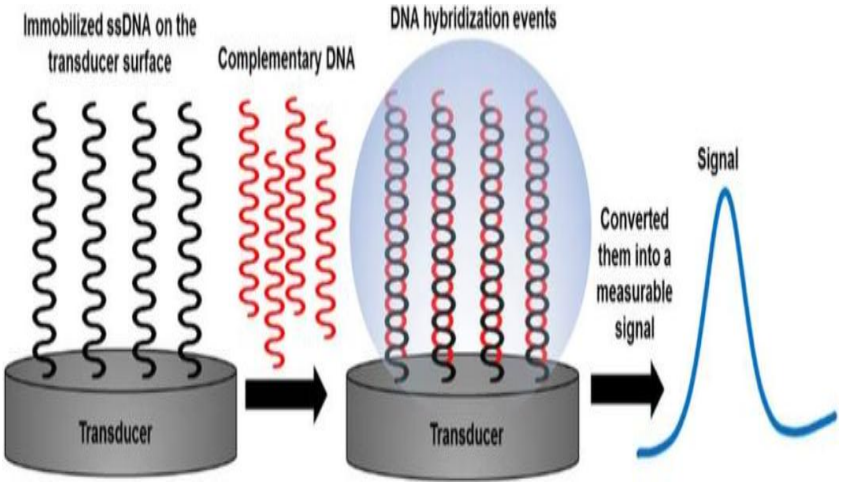

Figure 1-5. Schematic illustration of the DNA biosensor showing probe immobilization, target hybridization, and signal transduction mechanism. The schematic is taken from reference [16].

1.2.8- Surface Plasmon Biosensor:

Surface plasmon resonance (SPR) biosensors employ surface plasmon waves-specialized electromagnetic waves that propagate along a metal/dielectric interface-to detect interactions between a target analyte and a biorecognition element immobilized on the sensor surface. When the sensor is exposed to these binding events, it causes a change in the refractive index at the sensor interface, which can be monitored in real time. The SPR transducer is functionalized with biomolecules such as proteins, antibodies, antigens, nucleic acids, or small molecules that particularly bind to the analyte of interest. When the target analyte interacts with these immobilized recognition elements, it alters the local refractive index at the surface. This shift is detected by measuring changes in the angle or

intensity of reflected light using a spectrophotometer or other optical detection systems. This label-free and highly sensitive technique allows for the real-time observation of molecular interactions without the need for additional markers or labels. Due to its versatility, SPR biosensors have been successfully merged with various biorecognition components, enabling their use in fields such as clinical diagnostics, environmental monitoring, and drug discovery [17].

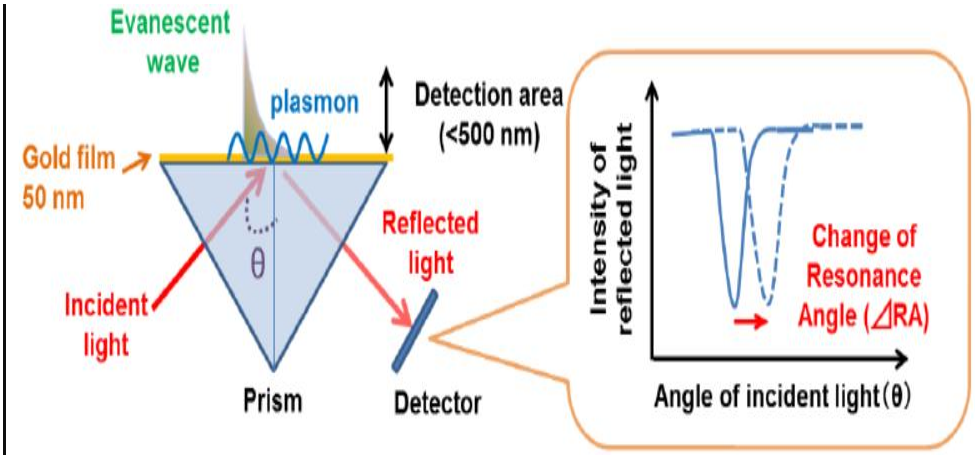

Figure 1-6. Schematic graph illustrating the principle of surface plasmon resonance (SPR) sensing based on refractive index changes at the metal–dielectric interface. The schematic is taken from reference [17].

1.2.9- Chemiluminescence based biosensor:

Chemiluminescence refers to the process in which light is produced because of a chemical reaction. To be more specific, during a chemical reaction, molecules or atoms are excited to a higher energy state and then return to their ground state, releasing energy in the form of light. This emission of light, also known as luminescence, occurs without the need for external light sources, distinguishing chemiluminescence from fluorescence or phosphorescence. This property makes chemiluminescence particularly useful for detecting specific biochemical reactions. In chemiluminescence-based biosensors, the interaction between the target analyte and an immobilized biomolecule is coupled with a chemiluminescent reagent or species. The biochemical reaction triggers the emission of light, which acts as an indicator of the analyte's existence and concentration. The emitted light is typically measured by sensitive detectors such as photomultiplier tubes (PMTs), which can detect even very low levels of light, enabling highly sensitive and precise biosensing. Due to their sensitivity and specificity, chemiluminescence biosensors are widely used in clinical diagnostics, environmental monitoring, and biochemical research [18].

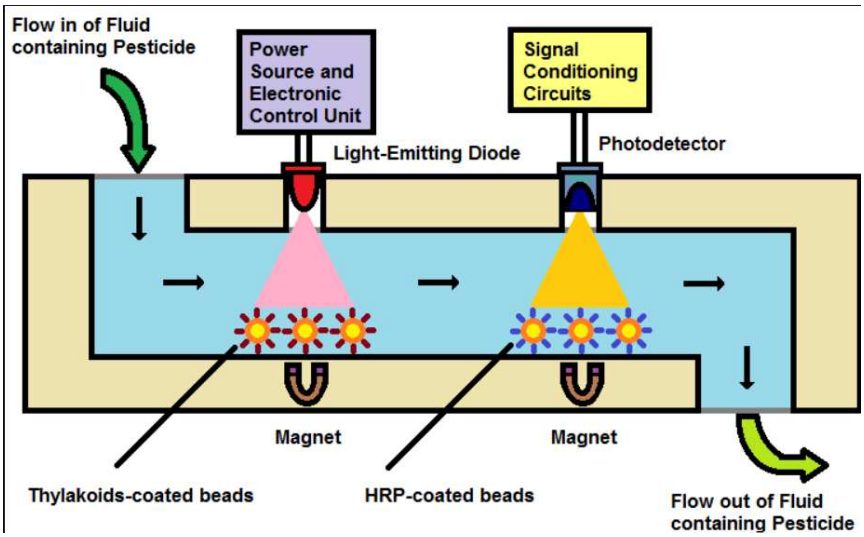

Figure 1-7. Schematic illustration of a chemiluminescence-based biosensor showing target recognition, enzyme-catalyzed luminescent reaction, and signal detection. The schematic is taken from reference [18].

1.2.10- Fluorescence based Biosensor:

Luminescence occurs when molecules or atoms transition from an excited energy state back to their ground state, releasing energy in the form of light. Different types of luminescence are distinguished by the source of energy that excites the particles. For example, photoluminescence (including fluorescence and phosphorescence) is initiated by electromagnetic radiation; pyro luminescence results from heat; triboluminescence arises from mechanical friction; cathodoluminescence is caused by electron impact; and Crystall luminescence occurs during crystallization. Fluorescence specifically requires an external light source, typically ultraviolet or short-wavelength light, to excite the molecules. These molecules then emit light at a longer wavelength as they return to their ground state. Fluorescence-based biosensors commonly use fluorochrome labels that emit light during the biorecognition process. Since many natural recognition elements and analytes lack inherent fluorescent properties, these biosensors depend on attaching fluorescent probes to the recognition molecules. This enables the optical detection of binding events by altering molecular interactions into detectable light signals [19].

- FRET (Förster Resonance Energy Transfer),
- FLIM (Fluorescence Lifetime Imaging),
- FCS (Fluorescence Correlation Spectroscopy),
- FI (changes in Fluorescence Intensity).

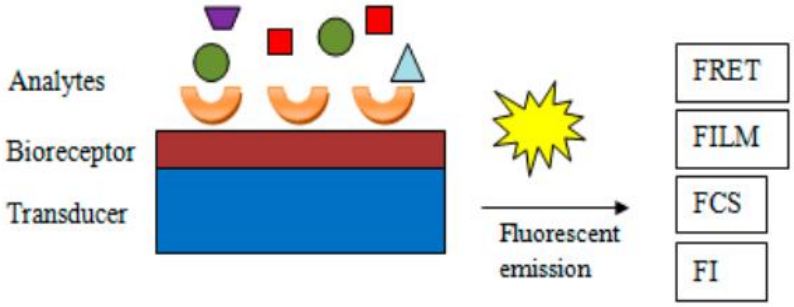

Figure 1-8. Diagram of a fluorescence-based biosensor depicting target binding, fluorophore activation, and resulting fluorescence signal for detection. The schematic is taken from reference [19].

1.2.11- Cell based Biosensor:

Cell-based biosensors are a kind of biosensor that employ living cells as the biorecognition element. These sensors leverage the natural ability of living cells to detect alters in both intracellular and extracellular environments, including variations in physiological conditions. The interaction between the cells and external stimuli generates a measurable response, which forms the basis of detection. Microorganisms such as bacteria and fungi can be used in these biosensors to identify specific molecules or evaluate the overall condition of the surrounding environment. Furthermore, cellular proteins can act as bioreceptors to recognize analytes. Unlike other biosensors that depend on isolated biological molecules or synthetic materials, cell-based biosensors use intact, living cells, making them unique. The sensitivity and performance of these biosensors are largely influenced by the cells' natural ability to survive and function over extended periods, which rely on carefully controlled physical and chemical conditions. However, a significant limitation of cell-based biosensors is maintaining cell viability and stability, which can be affected by various environmental factors [20].

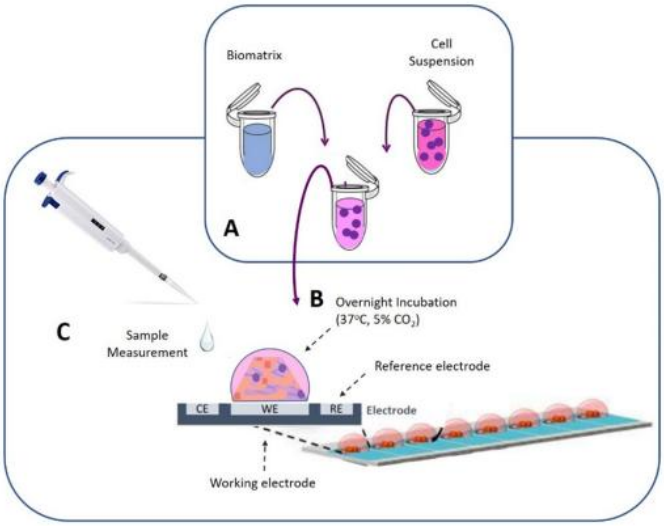

Figure 1-9. Diagram of a cell-based biosensor depicting target analyte interaction with living cells, cellular signal generation, and readout detection. The schematic is taken from reference [20].

1.3- Application of Biosensor:

Recently, biosensors have become increasingly vital across diverse sectors, such as healthcare, food safety, water quality monitoring, and environmental protection [21], [22], [23],[24]. These innovative devices are used to detect a wide range of analytes with high specificity and sensitivity. Since their initial development, biosensors have continuously advanced, integrating cutting-edge technologies to enhance their performance. Progress in materials science, nanotechnology, and biotechnology have played a vital role in increasing their speed, accuracy, and reliability. As a result, research and development in the field of biosensors have grown significantly, driving to the creation of more adaptable and efficient systems that meet the growing demand for rapid and precise analytical tools [25].

1.3.1- Medical applications:

In the modern medical scope, there is a growing demand for low cost, practical, and safe diagnostic tools that support personalized healthcare, enable early disease detection, and increase treatment strategies. Appearing biosensor technologies are addressing these needs by offering innovative solutions that help reduce the overall costs related with early diagnosis, medical procedures, and patient hospitalization. Due to their ease of fabrication, affordability, and swift response capabilities, biosensors are becoming strong substitutes for traditional diagnostic devices.

Among diverse types, laboratory-based biosensors have a critical role in clinical diagnostics. These devices analyse biological samples such as blood, urine, or tumour tissues to detect cancer biomarkers, enzymes, proteins, small molecules, and even live cancer cells. Their sensitivity and

specificity make them valuable tools in diagnosing diseases at an early stage, which is vital for effective treatment and improved patient outcomes [26]. The relevance of biosensors in detecting infectious diseases has grown substantially, particularly during and after the COVID-19 pandemic. The critical need for rapid, precise, and accessible testing methods emphasized the importance of biosensor-based diagnostics in managing public health dilemmas. As a result, research and development in this field have speeded up, further expanding the potential applications of biosensors in modern medicine [27].

1.3.2- Food and water safety:

Biosensors have emerged as valuable tools in the field of public health due to their ability to provide real-time results, cost-effectiveness, and flexibility in monitoring the safety of water and food supplies. These devices enable fast, accurate, and user-friendly detection methods, which are essential for effective environmental surveillance and quality control. In the context of water quality assessment, biosensors offer a practical alternative to conventional laboratory testing by allowing on-site analysis with minimal equipment and technical expertise. By combining various biorecognition elements biosensors can detect a wide range of chemical and biological contaminants. This includes measuring biochemical oxygen demand (BOD), identifying the presence of heavy metals, detecting organic toxins, and identifying specific environmental pollutants. These analytes can be measured either qualitatively or quantitatively through different transduction mechanisms, including electrical, optical, thermometric, or mass-based signals. The adaptability and sensitivity of biosensors make them a powerful solution for continuous monitoring and rapid response in maintaining the safety and sustainability of water resources [28], [29].

1.3.3- Environmental applications:

The widespread release of environmental contaminants such as pesticides, toxic metals, pharmaceutical residues, and other xenobiotic compounds has become a significant global matter. Timely and accurate detection of these pollutants is essential for mitigating their negative effect on ecosystems and human health. Electrochemical nucleic acid-based biosensors have illustrated high sensitivity and selectivity in detecting environmental toxins, heavy metals, and antibiotics across various ecological samples [30].

Pesticide-contaminated water sources, especially groundwater, represent a major source of pollution. The capability to detect pesticides using small-volume samples is necessary for effective environmental monitoring and remediation. Between environmental contaminants, toxic heavy

metals such as mercury (Hg^{2+}), lead (Pb^{2+}), cadmium (Cd), and chromium (Cr) are of specific issue arising from their persistence and toxicity. Biosensor technologies offer a potential solution for detecting these metals, with both electrochemical and optical methods being explored. One modern technique gaining traction is Surface-Enhanced Raman Scattering (SERS)-based biosensing. SERS is a powerful plasmonic analytical method that enhances the Raman scattering signals of molecules adsorbed onto nanostructured metallic surfaces, enabling the detection of trace-level analytes with exceptional sensitivity and specificity. The application of SERS in environmental monitoring provides a fast, selective, and highly sensitive means of identifying even minute quantities of pollutants, making it a beneficial tool in the attempt to protect environmental and public health [31].

1.4- Future perspectives:

latest advancements in technology have considerably affected the growth of biosensor research, steering it toward combining with modern innovations. One noteworthy trend is the miniaturization of biosensors, enabling their incorporation into microchip platforms and the development of condensed, high-performance devices capable of detecting analytes at highly low concentrations with enhanced speed and sensitivity.

Furthermore, to miniaturized systems, the development of cost-effective and eco-friendly biosensors-such as those based on recyclable paper substrates-has extended the availability and application range of these devices. These paper-based sensors are particularly appealing because of their affordability, simplicity, and suitability for point-of-care testing.

Portable biosensors are another milestone, providing real-time, on-site monitoring of variety physiological parameters without the need for time-consuming laboratory procedures. These devices can continuously track vital signs, biochemical levels, or disease markers, facilitating personalized healthcare and timely interventions.

Furthermore, the integration of biosensors with smart technologies-such as smartphones, wireless communication systems, and the Internet of Things (IoT)- is paving the way for a new production of intelligent, wearable, and user-friendly diagnostic tools. As interest in this field grows, continuous research continues to push the boundaries of what biosensors can achieve, with new technological developments emerging to fulfil the requirments of modern healthcare, environmental monitoring, and beyond.

1.5- Impact of nanomaterial on biosensing

Nanomaterials have emerged as useful tools in the field of biological sensing because of their unique physicochemical characteristics and nanoscale dimensions. Their uniquely tiny size and the ability to functionalize their surfaces enable highly specific interactions with objective biomolecules, which is necessary for sensitive and selective detection [32]. In the last few decades, researchers have developed a large scope of nanostructured materials-each possessing special optical, electrical, magnetic, electrochemical, and thermal properties-that have been successfully applied to sensing molecular biomarkers with significant accuracy and sensitivity.

The basic rule behind nanomaterial-based biosensing include the transformation of molecular recognition events-such as the binding of a biomarker to a specific probe-into measurable physical signals. These signals can then be enhanced and accurately measured using advanced analytical techniques. This method allows for the real-time monitoring of biomolecular interactions and provides a strong platform for early disease diagnosis and prognosis [33].

Nanomaterials have found wide range application in vitro diagnostics, where they are applied to detect disease-related biomarkers exist in biological fluids such as blood, saliva, and urine. These markers often act as indicators of different health conditions, such as cancer, neurodegenerative disorders, and infectious diseases. Moreover, in under laboratory condition sensing, nanomaterials are also applied in living system imaging applications. When conjugated with imaging agents and introduced into the body, nanomaterials can act as contrast enhancers for imaging modalities like magnetic resonance imaging (MRI), computed tomography (CT), and positron emission tomography (PET). This permit for the non-invasive visualization of the spatial and temporal dispersion of disease-related biomarkers within living organisms [34].

One key benefit of emerging nanomaterials into biosensor designs rely on their capability to amplified signal transduction. Different forms of nanomaterials-like carbon-based structures (including graphene and carbon nanotubes), metallic nanoparticles (such as gold and silver), nanowires, nanofibers, and quantum dots-have been used to enhance the sensitivity and functionality of biosensors. By adjusting the surface of electrodes with these nanomaterials, researchers have notably increase sensor performance, including higher current response, enhanced stability, and quicker reaction kinetics.

The favourable characters of nanomaterials, such as their high surface-to-volume ratio, remarkable electrical conductivity, chemical stability, and biocompatibility, make them perfect candidates for

detecting applications. Their nanoscale dimensions provide a high density of reactive sites for biomolecular attachment; on the other hand, their electronic properties simplify effective signal transmission. Furthermore, their amplified electrocatalytic activity and mechanical strength, additionally contribute to their effectiveness in sensor progress [35].

Generally, nanomaterials are described as substances that have at least one dimension measuring less than 100 nano meters. At this scale, materials often show novel properties not seen in their bulk counterparts, like quantum effects, increased surface reactivity, and specific mechanical behavior. These properties open new gates for the development of next-generation biosensors that are more sensitive, specific, and reliable [36].

In conclusion, the emerging of nanomaterials into biosensing platforms depict a considerable progress in biomedical diagnostics and imaging. Their multifunctional properties and the ability to tailor their interactions at the molecular level make them extremely valuable for the early recognition and monitoring of diseases, ultimately paving the way for more personalized and effective healthcare solutions.

1.6- Classification of Nanomaterials

Nanomaterials can be categorised as per the size and dimensions. There are four kinds of nanomaterials like zero-dimension, one dimension, two dimensions, and three dimensions.

A) Zero-dimensional: In zero-dimensional (0D) nanomaterials, all three dimensions of materials occur in nanoscale, e.g., nano particles such as gold, palladium, platinum, silver, or quantum dots. Nano particles can be spherical in size with a diameter of 1-50 nm.

b) One-dimensional: These nanomaterials having one dimension are in the scope of 1-100 nm and the other two dimensions can be in macroscale. Nanowires, nanofibers, nanorods, and nanotubes are examples of one-dimensional (1D) nanomaterials. Some metals (Au, Ag, Si, etc.), metal oxides (ZnO, TiO_2, CeO_2, etc.), quantum dots, and others can provide 1D nanostructures.

c) Two-dimensional: In this category of nanomaterials, two dimensions are in nanoscale, and one dimension is in macroscale. Nano thin-films, thin-film multilayers, nanosheets, or nano walls are two-dimensional (2D) nanomaterials. The domain of 2D nanomaterials can be several square micrometres keeping thickness always in the nanoscale range.

D) Three-dimensional: In three-dimensional (3D) nanomaterials, there are no dimensions in nanoscale, and all dimensions are in macroscale. Bulk materials are 3D nanomaterials that are formed of distinct blocks which may be in nanometre scale (1-100 nm) or more [37].

1.7- Application of carbon nanomaterials in biosensing:

The last two decades have been critical in the understanding of nanotechnologies for the synthesis of nanomaterials and their basic characteristic. Carbon nano materials, such as carbon nano tube (CNTs), Graphene, reduced Graphene, carbon nanowires, graphene nanoribbon, and graphene quantum dots (GQDs), have caught the eye due to their exceptional physical, chemical, and electrical properties for tiny biosensors. Their geometry results in a large surface-to-volume ratio, ensuring the exposure of most of the surface atoms, which can then bind a significant number of sensing elements. furthermore, the excellent surface-to-volume ratio and the sp^2 hybridization structure confirm the surface modification by the sensing elements and the transformation of the sensing signals. For example, CNTs graphene are often utilized as electrical channels in transistor-type sensors or as the sensitive elements in chemiresistor-type sensors, meanwhile particular sensing probes are inserted on their surface for sensitive and selective detections. Moreover, carbon nanomaterials fill a nonnegligible position in the biosensing field. Additionally, by applying suitable fabrication techniques, such as photolithography, microprinting, and electro spinning, carbon nanomaterials can be easily organized and combined with advanced microelectronics to generate devices on a large scale [38].

1.8- Functionalization mechanisms of Carbon Nanomaterials:

The sensing-element immobilization approach with carbon nanomaterials is vital and has two types: covalent and noncovalent. Covalent functionalization combines the sensing elements with carbon nanomaterials using covalent bonds. One method is to build active sites, such as with carbonyl groups and hydroxyl groups on carbon based nano substances, since they can be further modified using variety chemicals based on the condensation reaction, electrophilic/nucleophilic substitution, and additional reactions. Thus, different chemical or biological groups, such as antibodies, can be presented for particular detection. In contrast, this strategy depended on the chemical reactions between sensing probes and nanomaterials, which may need complicated reaction circumstances and cause alters in the transducers' features.

consequently, the noncovalent functionalization strategy was suggested to decrease the side effects on transducers. The noncovalent interaction is primarily based on four strong interactions, namely, hydrogen bonds, van der Waals interactions, electrostatic interactions, and $\pi - \pi$ stacking. sp^2 hybridization presences in most carbon nanomaterials and functionalizing their surface with some aromatic groups is common [39].

Compared to other carbon material materials, graphene shows major responses to weak surface charge perturbations induced by Dirac points, enabling highly sensitive detection of target molecules. From this viewpoint, Graphene Field Effect Transistor (GFET)-based sensor technology presents specific potential in getting highly sensitive detection of biomarkers [40].

1.9-Structure and working principle of GFET Biosensor:

The fundamental structure of the Graphene Field Effect Transistor (GFET) is analogous to that of traditional Field Effect Transistor (FET). It includes a source (S), a drain (D), a gate (G), a graphene channel, a dielectric layer, and a substrate. The source and drain are connected through the graphene channel, meanwhile the gate is isolated from the graphene by the dielectric layer**.**

The back-gate set up is normally beneficial when the sensor acts in air or other gaseous environments. Back-gated GFETs use a graphene channel to connect the source and drain, with a gate placed at the bottom to provide gate voltage. In a back-gate configuration, the gate capacitance is controlled by that of the insulating layer separating graphene from the planar gate electrode, typically an oxide with a thickness t varying from ∼10 nm to a few micrometre. Impacting the gate voltage enables control over the Fermi level of charge carriers in the graphene channel. This drive to a seamless shift of carrier type from holes to electrons. This shift causes the widely recognized phenomenon known as “bipolar behaviour”.

In the transition region between electron and hole states, the current is minimized, and this point is also known as the charge neutrality point (CNP). Alters in the electric field can be induced either by modifying the back-gate voltage or by physical or chemical adsorption of target molecules. Hence, when the back-gate voltage remains constant, alteration in current between the source and drain electrodes can be contributed to molecules adhering to the graphene surface [41].

In biosensing applications, GFETs typically act in electrolyte solutions, needing a liquid-gate setup. Liquid-gate GFETs apply gate voltage to the electrolyte solution by utilize a reference electrode positioned on top of the device. When GFET is used as a biosensor, analytes could change one or diverse parameters of the graphene channel under the electric field, which in turn produces alteration in the current or potential signal. Distinctly, biorecognition elements are immobilized on the channel via Varity linkers. These elements will concentrate the targets at the solution/graphene interface.

Follow adsorption of positively(negatively) charged analytes onto the graphene surface, build-up of electrons (holes) at the graphene surface because of the electrostatic gate modulation process drive to

a negative(positive)shift in the transfer curve, due to the N(P) doping impact. Oppositely, in the charge transfer mechanism, induction charges move directly from the charged analyte to the graphene surface. Thus, upon adsorption of positively charged analytes, VCNP shifts toward positive potential, revealing p-type doping effect, and in reverse [42].

1.10- The electronic properties of graphene

The most explored component of graphene physics concerns its electronic properties, which are unique and different from those of any other known material because of multiple notable characteristics. Initially, due to the band structure of graphene, electrons traveling through the honeycomb lattice completely lose their effective mass, leading to relativistic quasi-particles that are well described by a Dirac-like equation. This makes graphene a suitable table-top platform for probing quantum electrodynamics (QED) phenomena. Secondly, electron waves in graphene propagate within a one-atom thick layer, which makes them accessible to different scanning probes, as well as sensitive to the vicinity of other materials such as superconductors and ferromagnets. Finally, graphene has an exceptional electronic quality, as its charge carriers can travel for sub-micrometer distances without scattering even at room temperature. Owing to the massless carriers and of the reduced scattering, quantum effects in graphene are strong and can survive even at room temperature [49].

1.11- Graphene band structure:

The specific electronic features of graphene become from its band structure. Due to graphene 2D conjugated honeycomb-shaped lattice, each carbon atom has four valence electrons: three of them occupy the planar SP^2 hybrid orbital to form covalent in-plane bonds, while the rest electron occupies a P_z orbital (the z-axis being perpendicular to the graphene plane). Overlap between the P_z orbitals result in free electrons which can contribute to the electrical conductivity. The honeycomb lattice of graphene (see Figure 1-10) includes two interpenetrating triangular sublattices: the sites of one sublattice (yellow) are at the centers of triangles defined by the other (blue). The graphene lattice thus has two carbon atoms (denoted by A and B) per unit cell and is fixed under 120° rotations around any lattice site [50].

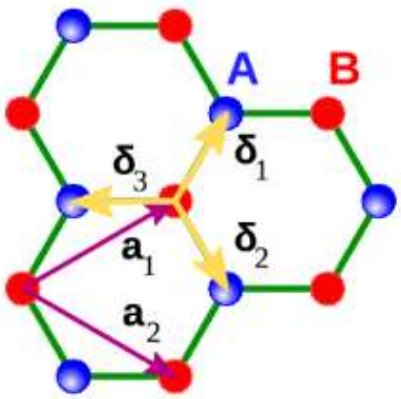

Figure 1-10. Schematic representation of the hexagonal lattice structure of graphene, illustrating its decomposition into two interpenetrating triangular sublattices, labeled A and B. This bipartite arrangement is fundamental to understanding graphene's distinctive electronic behavior, including the emergence of Dirac cones, high charge carrier mobility, and its unusual band structure.

$$a_1 = a(\frac{\sqrt{3}}{2}, \frac{1}{2}) \qquad a_2 = a(\frac{\sqrt{3}}{2}, -\frac{1}{2}) \qquad (1\text{-}1)$$

Where a 142 $\dot{A}$ is the side of the hexagons. This structure results in a hexagonal first Brillouin zone in the reciprocal space (see Figure 1-11) [50]:

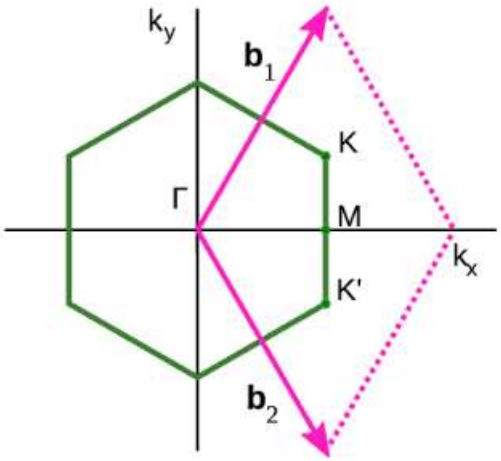

Figure 1-11. Portion of graphene's reciprocal lattice highlighting the first Brillouin zone, the fundamental region in momentum space that contains all unique wavevectors and key symmetry points relevant for band structure analysis.

with basis vectors:

$$b_1 = \frac{2\pi}{3a}(1, \sqrt{3}) \qquad b_1 = \frac{2\pi}{3a}(1, -\sqrt{3}) \qquad (1\text{-}2)$$

The band structure of graphene can be computed from the following tight-binding Hamiltonian, which consider that electron scan hops to both nearest and next-to-nearest-neighbor atoms [50]:

$$H = -t\sum_{\langle i,j\rangle\sigma}(a^{\dagger}_{\sigma,i}b_{\sigma,j} + b^{\dagger}_{\sigma,j}a_{\sigma,i} - \acute{t}\sum_{\langle\langle i,j\rangle\rangle\sigma}(a^{\dagger}_{\sigma,i}a_{\sigma,j} + a^{\dagger}_{\sigma,j}a_{\sigma,i} + b^{\dagger}_{\sigma,i}a_{\sigma,j} + b^{\dagger}_{\sigma,j}a_{\sigma,i}) \qquad (1\text{-}3)$$

where the plus sign is used to the conduction band (anti-bonding solution) and the minus sign to the valence band (bonding solution), meanwhile $f(k)$ is a periodic function given by [50]:

$$f(k) = 2\cos\left(\sqrt{3}k_y a\right) + 4\cos\left(\frac{\sqrt{3}}{2}k_y a\right)\cos\left(\frac{3}{2}k_x a\right) \qquad (1\text{-}4)$$

The resulting valence and conduction bands touch at six points that coincide with the corners of the first hexagonal Brillouin zone (see Figure 1-12):

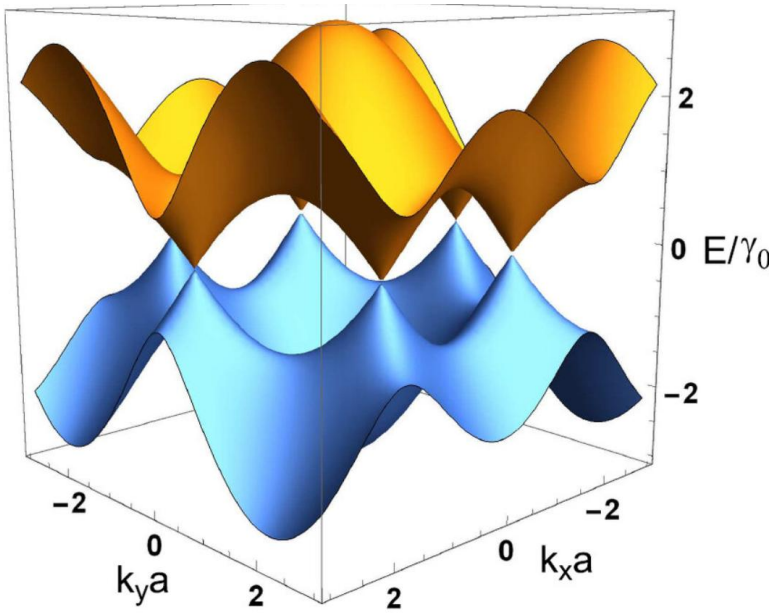

Figure 1-12. Electronic dispersion in the graphene honeycomb lattice. Left: full energy spectrum. Right: zoomed-in view of the energy bands near one of the Dirac points, highlighting the linear dispersion characteristic of massless Dirac fermions. The schematic is taken from reference [50].

Because there are two valence electrons per unit cell, the Fermi surface decreases to just the se six points, which are referred to as K or Dirac points. Considering that the electronic properties of a conductor are defined by the charge carriers near Fermi energy, the shape and position of the bands near the K points are of cardinal importance to understand electronic transport in graphene. The two K points at the corners of the graphene Brillouin zone (indicated as K and $K^{'}$) have the following coordinates in the momentum space:

$$K = \left(\frac{2\pi}{3a}, \frac{2\pi}{3\sqrt{3}a}\right) \qquad K^{'} = \left(\frac{2\pi}{3a}, -\frac{2\pi}{3\sqrt{3}a}\right) \qquad (1\text{-}5)$$

The dispersion around the Dirac points can be computed by extending the full band structure applying $K = K + q \; and \; |q| \ll |K|$ (q being the momentum measured relatively to the Dirac points):

$$E_{\pm}(q) \approx \pm v_F|q| + O\left[\left(\frac{q}{k}\right)^2\right] \qquad (1\text{-}6)$$

where $v_f = \frac{3ta}{2} = 1 * 10^6 \frac{m}{s}$ is the Fermi velocity [50].

1.12-Transport properties of Graphene:

As a result of its peculiar electronic features, graphene exhibits a pronounced ambipolar electric field effect (see Figure 1-13) [51]:

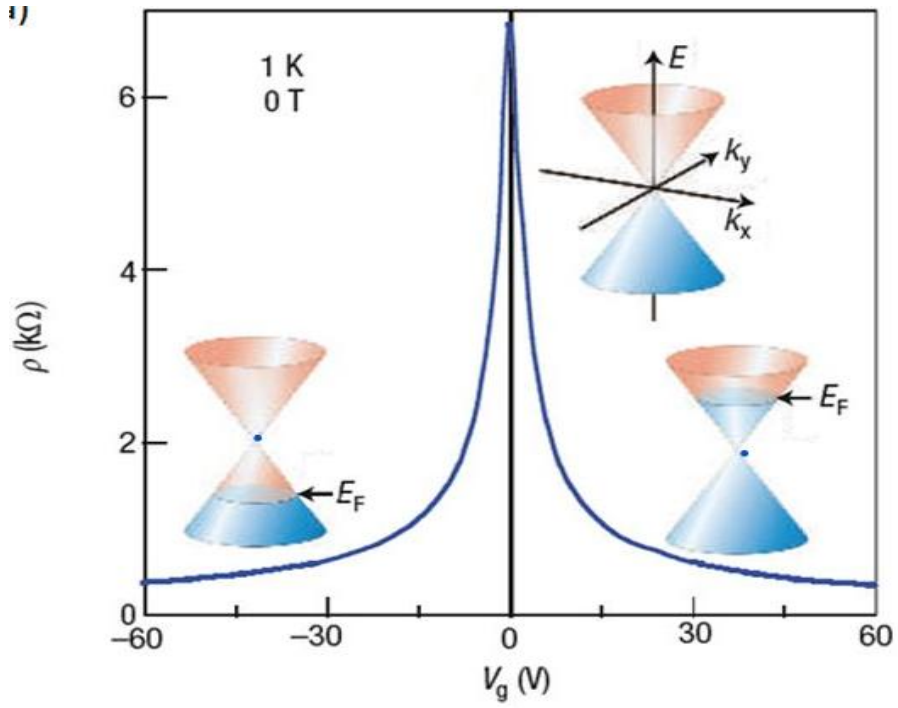

Figure 1-13. Linear dispersion relation of graphene shown as a contour plot of the band structure near the Dirac points, illustrating the cone-like energy spectrum characteristic of massless Dirac fermions. The schematic is taken from reference [51].

Under applied voltage, the charge carriers can be continuously tuned between electrons and holes with concentrations n as high as $10^{13} cm^{-2}$ and mobilities that can attain $2.5 * 10^5 cm^2 V^{-1} s^{-1}$ even under ambient conditions . (for the highest-quality graphene samples), where they are limited by impurity and phonon scattering. Such high values of (that have been shown to increase by one order of magnitude at $4K$[86]) translate into ballistic transport on the sub-μm scale. Without external voltage the level of fermi energy of graphene positioned in Dirac point that means conductivity of that material is a low meanwhile applying positive back gate voltage changed that position toward up so, result of that enhance of density of carrier, here this duty carried by electron so our graphene will be n-doped(electron-doped) in contrast if we apply negative back gate voltage the level of fermi energy reduced from Dirac point so in this condition also carrier density it will be enhanced but our carrier it will be hole, so our graphene in this mode named as p-doped(hole-doped).

1.13- Performance assessment:

The experiments and theory considered in the scope of this research in purpose developing GFET for the detection or measuring of molecules relevant in biology. In this section, we discuss the criteria used to assess the performance of GFETs as biosensors. In this context, performance include two aspects: quality and reliability. Quality criteria are established by the performance of the sensor itself with respect to several detection metrics. In the following, we investigate five of these metrics: spatial range of detection, sensitivity to target concentration, selectivity, response time and recovery time.

1.13.1- Spatial range of detection:

For electrolyte-gated GFETs, it is important to consider charge screening by mobile ions in the medium. Based on the Debye–Hückel model, charged molecules in solution are screened by mobile counter-ions such that their electric potential is dampen exponentially with distance, with s a diminish constant λ_D called the Debye length. This constant represents the screening length and is given by:

$$\lambda_D = \sqrt{\frac{\epsilon K_B T}{2 N_A e^2 I}} \qquad (1\text{-}7)$$

where ε is the permittivity of the medium, K_B the Boltzmann constant, T the temperature, N_A the Avogadro's number, e the electron charge and I the ionic strength of the solution. ionic strength is given by $I = \sum \rho_i z_i$ where ρ_i and z_i are respectively the density and valence of ion species i. The Debye length represents the distance at which charges are screened; thus, charges located farther than the Debye length are usually considered out of range for electrostatic detection by a FET sensor [52].

1.13.2- Sensitivity:

Sensitivity is an important performance metric for measurement applications, specifically when it's required to recognising analyte concentration with great accuracy. Sensitivity can be determined from the calibration curve of the sensor, i.e. the evolution of a chosen electrical metric (ex. CNP voltage, current) as role of analyte concentration. For that aim we describe Sensitivity (S) as the shift in the Dirac point position of the graphene channel in response to a change in ion concentration. Mathematically, it is represented as [52]:

$$S = \frac{\nabla V_{Dirac}}{\nabla C} \qquad (1\text{-}8)$$

1.13.3- Selectivity:

Selectivity is the feature of a biosensor to distinguish the target analyte from other molecules and produce a signal output versus the target analyte only. Specificity and selectivity are two important parameters often used utilize alternately in biosensor literature. Specificity is the ideal circumstance, where the biosensors using aptamers, antibody, or biotin-avidin such as conjugation pairs. Selectivity is the property to detect a closely related group of molecules recognize only a single target analyte even in a complex solution. Specificity can be obtained by utilizing aptamers, antibody, or biotin-avidin such as conjugation pairs. Selectivity is the property to detect a vicinity related group of molecules.

1.13.4-Response time:

The time required for a biosensor to produce a signal against an analyte concentration, or the time taken by sensor to capture a detectable number of analyte molecules on its surface. Microfluidics, analyte capture by beads distributed in solution, nano/micromotors are some of the approaches used to decrease the response time of a biosensor.

1.13.5- Recovery time:

The time required by a biosensor to be ready for the second sensing cycle after completing the first one is called recovery time. An ideal biosensor has a wide LDR, low LOD, high sensitivity, high selectivity, fast response time and low recovery time.

1.14- Thesis outline:

The primary objective of this research is the design, simulation, and fabrication of optoelectronic sensors for smart and sensitive detection applications. This thesis is organized into several chapters, each addressing a specific aspect of sensor modelling, design, simulation, and experimental validation.

Chapter 2 focuses on the fundamental role of simulation in the development of advanced sensing technologies. In this chapter, the importance of numerical modelling in predicting sensor behaviour,

optimizing device performance, and reducing experimental cost is discussed. A comprehensive theoretical model of the Graphene Field-Effect Transistor (GFET) is presented, which serves as the foundational framework for the electrical aspect of this research. This model is used to analyse the electrical characteristics of graphene-based sensors and can be extended and adapted to other metal-based field-effect transistor (FET) structures. The developed model provides the basis for computing the electrical response of sensors throughout the thesis.

In Chapter 3, the theoretical framework established in Chapter 2 is applied to the simulation of an Ion-Sensitive Graphene Field-Effect Transistor (ISGFET) for the detection of sodium ions (Na^+). The core concept of this chapter is based on the influence of the Electrical Double Layer (EDL) at the graphene-electrolyte interface. The impact of different EDL models on sensor sensitivity and electrical response is systematically analysed, demonstrating the capability of graphene-based ISGFETs for ion detection.

Chapter 4 extends the ISGFET concept to biosensing applications, specifically for the detection of β_2-microglobulin, a clinically relevant protein biomarker. This chapter begins with an investigation of the physical, chemical, and electrical properties of β_2-microglobulin. Subsequently, the interaction mechanisms between this protein and the graphene surface are examined, using information and insights provided by Professor Brancolini. Based on these interactions, the ISGFET structure is adapted and optimized for selective and sensitive detection of β_2-microglobulin.

Chapter 5 presents experimental studies related to the fabrication, characterization, and electrical measurement of graphene field-effect transistors. The GFET devices were fabricated using mechanical exfoliation techniques in collaboration with the University of Salamanca. In addition, this chapter includes both theoretical and experimental investigations of a graphene-based pH sensor fabricated by Graphenea using chemical vapor deposition (CVD) technology, highlighting the consistency and reliability of graphene sensors produced through different fabrication approaches.

Beyond electrical sensing, this thesis also explores optical sensing techniques. In Chapter 6, simulation-based design of an optical sensor is presented. Specifically, a perfect absorber based on surface plasmon resonance is designed and analysed. The optical response, absorption efficiency, and resonance behaviour of the structure are investigated with the aim of achieving high sensitivity for sensing applications.

Finally, to further enhance the sensitivity of the optical sensor, nonlinear optical effects in graphene are explored. The simulation of third-harmonic generation (THG) in graphene is presented and

utilized as a novel detection mechanism for β_2-microglobulin. This approach demonstrates the potential of combining plasmonic structures with nonlinear graphene optics to achieve highly sensitive and multifunctional biosensors.

Reference:

[1]-Song, Min, et al. "Materials and methods of biosensor interfaces with stability." *Frontiers in Materials* 7 (2021): 583739.

[2]- Elli, Giulia, et al. "Field-effect transistor-based biosensors for environmental and agricultural monitoring." *Sensors* 22.11 (2022): 4178.

[3]- Pourmadadi, Mehrab, et al. "Properties and applications of graphene and its derivatives in biosensors for cancer detection: a comprehensive review." *Biosensors* 12.5 (2022): 269.

[5]- Pumera, Martin. "Graphene in biosensing." *Materials today* 14.7-8 (2011): 308-315.

[6]- Song, Min, et al. "Materials and methods of biosensor interfaces with stability." *Frontiers in Materials* 7 (2021): 583739.

[7]- Turner, Anthony, Isao Karube, and George S. Wilson. *Biosensors: fundamentals and applications*. Oxford university press, 1987.

[8]- Ronkainen, Niina J., H. Brian Halsall, and William R. Heineman. "Electrochemical biosensors." *Chemical Society Reviews* 39.5 (2010): 1747-1763.

[9]- Wang, Joseph. "Amperometric biosensors for clinical and therapeutic drug monitoring: a review." *Journal of pharmaceutical and biomedical analysis* 19.1-2 (1999): 47-53.

[10]- Ding, Jiawang, and Wei Qin. "Recent advances in potentiometric biosensors." *TrAC Trends in Analytical Chemistry* 124 (2020): 115803.

[11]- Lei, Zong-Lin, and Bo Guo. "2D material-based optical biosensor: status and prospect." *Advanced Science* 9.4 (2022): 2102924.

[12]- Chen, Chen, and Junsheng Wang. "Optical biosensors: An exhaustive and comprehensive review." *Analyst* 145.5 (2020): 1605-1628.

[13]- Jaffrezic-Renault, Nicole, and Sergei V. Dzyadevych. "Conductometric microbiosensors for environmental monitoring." *Sensors* 8.4 (2008): 2569-2588.

[14]- Abdelhamid, Hani Nasser. "Calorimetric biosensors." *Fundamentals of Biosensors in Healthcare*. Academic Press, 2025. 359-372.

[15]- Pohanka, Miroslav. "The piezoelectric biosensors: Principles and applications, a review." *International Journal of Electrochemical Science* 12.1 (2017): 496-506.

[16]- Ronkainen, Niina J., H. Brian Halsall, and William R. Heineman. "Electrochemical biosensors." *Chemical Society Reviews* 39.5 (2010): 1747-1763.

[17]- Homola, Jiří. "Present and future of surface plasmon resonance biosensors." *Analytical and bioanalytical chemistry* 377.3 (2003): 528-539.

[18]- Das, Ankita, et al. "Chemiluminescence-based biosensor: From principle to its applications." *Fundamentals of Biosensors in Healthcare*. Academic Press, 2025. 315-336

[19]- Strianese, Maria, et al. "Fluorescence-based biosensors." *Spectroscopic methods of analysis: methods and* -. Totowa, NJ: Humana Press, 2012. 193-216

[20]- Liu, Qingjun, et al. "Cell-based biosensors and their application in biomedicine." *Chemical reviews* 114.12 (2014): 6423-6461.

[21]- Mohankumar, P., et al. "Recent developments in biosensors for healthcare and biomedical applications: A review." *Measurement* 167 (2021): 108293.

[22]- Yasmin, Jannat, Mohammed Raju Ahmed, and Byoung-Kwan Cho. "Biosensors and their applications in food safety: a review." *Journal of Biosystems Engineering* 41.3 (2016): 240-254.
[23]- Woldu, Aster. "Biosensors and its applications in Water Quality Monitoring." *International Journal of Scientific and Engineering Research* 13.5 (2022): 12-29.
[24]- Marco, María-Pilar, and Damia Barcelo. "Environmental applications of analytical biosensors." *Measurement Science and Technology* 7.11 (1996): 1547.-
[25]- Malik, Sumit, et al. "Nanomaterials-based biosensor and their applications: A review." *Heliyon* 9.9 (2023).
[26]- Haleem, Abid, et al. "Biosensors applications in medical field: A brief review." *Sensors International* 2 (2021): 100100.
[27]- Bahl, Shashi, et al. "Biosensors applications in fighting COVID-19 pandemic." *Apollo Medicine* 17.3 (2020): 221-223.
[28]- Lozano, Marleny García, et al. "Biosensors for food quality and safety monitoring: fundamentals and applications." *Enzymes in food biotechnology*. Academic Press, 2019. 691-709.
[29]- Qi, Xiang, et al. "An electroactive biofilm-based biosensor for water safety: Pollutants detection and early-warning." *Biosensors and Bioelectronics* 173 (2021): 112822.
[30]- Huang, Chi-Wei, et al. "A review of biosensor for environmental monitoring: principle, application, and corresponding achievement of sustainable development goals." *Bioengineered* 14.1 (2023): 58-80.
[31]- Ren, Wen, Chengzhou Zhu, and Erkang Wang. "Enhanced sensitivity of a direct SERS technique for Hg2+ detection based on the investigation of the interaction between silver nanoparticles and mercury ions." *Nanoscale* 4.19 (2012): 5902-5909.
[32]- Song, Min, et al. "Materials and methods of biosensor interfaces with stability." *Frontiers in Materials* 7 (2021): 583739.
[33]- Hou, Sichao, Aiying Zhang, and Ming Su. "Nanomaterials for biosensing applications." *Nanomaterials* 6.4 (2016): 58.
[34]- Lai, Huiying, et al. "Classification and applications of nanomaterials in vitro diagnosis." *Heliyon* 10.11 (2024)
[35]- Holzinger, Michael, Alan Le Goff, and Serge Cosnier. "Nanomaterials for biosensing applications: a review." *Frontiers in chemistry* 2 (2014): 63.
[36]- Pirzada, Muqsit, and Zeynep Altintas. "Nanomaterials for healthcare biosensing applications." *Sensors* 19.23 (2019): 5311.
[37]- Sannino, Diana. "Types and classification of nanomaterials." *Nanotechnology: trends and future applications*. Singapore: Springer Singapore, 2021. 15-38.
[38]- Pourmadadi, Mehrab, et al. "Properties and applications of graphene and its derivatives in biosensors for cancer detection: a comprehensive review." *Biosensors* 12.5 (2022): 269.
[39]- Kour, Ravinder, et al. "Recent advances in carbon nanomaterials as electrochemical biosensors." *Journal of The Electrochemical Society* 167.3 (2020): 037555
[40]- Andronescu, Corina, and Wolfgang Schuhmann. "Graphene-based field effect transistors as biosensors." *Current Opinion in Electrochemistry* 3.1 (2017): 11-17.
[41]- Elli, Giulia, et al. "Field-effect transistor-based biosensors for environmental and agricultural monitoring." *Sensors* 22.11 (2022): 4178.
[43]- Singh, Paramjot, Parsoua Abedini Sohi, and Mojtaba Kahrizi. "Finite element modelling of bandgap engineered graphene FET with the application in sensing methanethiol biomarker." *Sensors* 21.2 (2021): 580.

[44]- Koppens, F. H. L., et al. "Photodetectors based on graphene, other two-dimensional materials and hybrid systems." *Nature nanotechnology* 9.10 (2014): 780-793.
[45]- Junaid, Muhammad, et al. "A review on graphene-based light emitting functional devices." *Molecules* 25.18 (2020): 4217.
[46]- Chen, Weiwei, et al. "Electro-optical logic gates based on graphene–silicon waveguides." *Optics Communications* 372 (2016): 85-90.
[47]- Das, Santanu, et al. "Graphene synthesis and application for solar cells." *Journal of Materials Research* 29.3 (2014): 299-319.
[48]- Peña-Bahamonde, Janire, et al. "Recent advances in graphene-based biosensor technology with applications in life sciences." *Journal of nanobiotechnology* 16.1 (2018): 75.
[49]- Molitor, Françoise, et al. "Electronic properties of graphene nanostructures." *Journal of Physics: Condensed Matter* 23.24 (2011): 243201.
[50]- Castro Neto, Antonio H., et al. "The electronic properties of graphene." *Reviews of modern physics* 81.1 (2009): 109-162.
[51]- Peres, Nuno MR. "Colloquium: The transport properties of graphene: An introduction." *Reviews of modern physics* 82.3 (2010): 2673-2700.
[52]- Béraud, Anouk, et al. “Graphene field-effect transistors as bioanalytical sensors: Design, operation and performance.” *Analyst* 146.2 (2021): 403-428.

Chapter two

Simulation of Graphene-Based Field Effect Transistors (GFETs) Using COMSOL: Modelling, Setup, and Analysis

2.1- The importance of simulation in knowledge acquisition:

Simulation has appeared as an important approach in increasing obtaining information over variety fields like medicine, engineering, aviation, military training, and education. It provides a dynamic, interactive learning environment that mimics real-world situation, allowing individuals to apply theoretical aspect, advanced critical thinking, and improve skills without countering real-world results. As learning increasingly shifts toward experiential and education-centered models, the role of simulation in simplifying prefund understanding and knowledge retention has become more visible [1].

One of the most critical contributions of simulation is its ability to bridge the gap between theoretical learning and practical application. In customary learning models, students often struggle to translate abstract knowledge into real-world skills. Simulation deal with this by creating authentic contexts where learners can apply concepts in a controlled setting. According to Gaba (2004), simulations enable learners to experiment, make mistakes, and receive immediate feedback, which support higher-level learning [2].

For example, in medical education, simulation allows students to practice surgeries or emergency procedures with patient simulators or in virtual environments before performing them on real patients. This not only builds proficiency but also enhances confidence and reduces the risk of errors in real-life situations. A study by Issenberg et al. (2005) showed that high-fidelity medical simulations are effective in teaching clinical skills and improving patient safety performances [3].

Simulations also foster the development of cognitive and metacognitive skills. They encourage learners to analyse situations, make decisions, and reflect on results. In problem-based learning (PBL), simulation allows learners to involve with complex problems, evaluate hypotheses, and review strategies based on results. This iterative process is crucial for developing higher-order thinking skills and field-specific expertise [4].

For instance, flight simulators used in pilot training enable trainees to face various weather conditions, technical failures, and urgent cases, forcing them to think critically and act decisively. Such experience under realistic but risk-free conditions ensures that learners develop the ability to manage complex and stressful circumstance. Another important advantage of simulation is its ability to enhance long-term knowledge retention and transfer. Learning by doing has been shown to be more effective than passive forms of learning. Dale's Cone of Experience proposed that people remember 90% of what they do compared to only 10% of what they read [1]. Simulation, as a form of active

learning, enhances participation and permit researcher to process and store information in proper ways.

In addition, simulations can be repeated, refined, and customized based on the researchers needs, which supports personalized learning. In complex domains like cybersecurity or engineering, simulations give a hand to the students to understand system behaviour and troubleshoot problems, boosting their readiness for real-world challenges.

Simulations often engage teamwork and role-playing, enhancing collaboration and communication. These social aspects of learning are crucial in professional domains where coordination and cooperation are vital. For example, interprofessional simulations in healthcare help train doctors, nurses, and paramedics to work together efficiently during urgent care scenarios. In addition, simulations can be interdisciplinary, integrating knowledge from multiple domains. In business schools, for example, management simulations incorporate economics, psychology, data analytics, and decision sciences, offering students a holistic learning experience that reflects real-world complexity [5].

In general, simulation has an important role in knowledge acquisition by creating realistic, experiential, and contextualized learning experiences. It connects theory and practice, improve critical thinking, enhances retention, and promotes collaborative learning. As technology progress to engage, simulation will likely become even more central in educational and professional development approaches. Investing in high-quality simulation tools and integrating them thoughtfully into curricula can considerably increase learning results through various fields.

2.2- Importance of simulation in biosensing:

biosensors are extensively used in medical diagnostics, environmental monitoring, food safety, and bioprocessing. The design and optimization of biosensors include complex interactions between biological, chemical, and physical processes. To speed up development and enhance performance, simulation techniques have become critical approach in the domain of biosensing. Simulation permits researchers to model the behaviour of biosensors under different physical and chemical circumstance, decreasing the require for expensive and time-consuming experimental interactions. applying computational approaches such as finite element analysis (FEA) and computational fluid dynamics (CFD), researchers can make more efficient sensor structure, electrode placement, and microfluidic channel design before fabricating test models.

For instance, in electrochemical biosensors, simulations able to model mass transport, reaction kinetics, and electric field distribution, helping to enhance the sensor's sensitivity and response time. This process enables rapid prototyping and considerably speeds up the development cycle [6].

At the molecular level, molecular dynamics (MD) and Monte Carlo simulations are used to study the interactions between biomolecules and sensor surfaces. These techniques present realization into binding affinity, conformational changes, and surface functionalization, which are crucial for increasing selectivity and specificity. Simulations can, for example, help in designing aptamer- or antibody-based biosensors by forecasting how the recognition element behaves based on target binding, or how surface chemistry impacts the immobilization of biomolecules [7].

various modern biosensors integrate microfluidic systems for sample handling and processing. Simulating fluid dynamics is vital to understanding how analytes move and interact within microchannels. CFD helps in designing flow paths that amplify analyte-sensor contact, decrease dead zones, and enhance mixing, which finally improve detection performance. Simulations also help in cooperating elements like valves, mixers, and detectors, creating lab-on-a-chip systems for point-of-care monitoring [8].

Another important field is the forecast of biosensor performance under different environmental and operational circumstances. Simulations permit for stress testing against changes in temperature, pH, flow rate, and interference from non-target molecules. Long-term stability, degradation of biological elements, and fouling can also be modelled, supporting the development of robust sensors for real-world applications [9].

2.3- Why COMSOL:

As technology progress, recognising new research ideas for potential use is becoming more and more time-consuming and costly. With this advances, computer-based simulations are obtaining more acceptance within the scientific society. Simulations can save both time and considerably decrease the cost of research and development. On the other hand, their major benefit depended on the confidence they provide to researcher before starting to a project.in addition, computer-based simulations need less assumptions compared to conventional hand computational, driving to more valid results.

COMSOL Multiphysics is a powerful simulation platform based on the finite element method (FEM), utilized wildly through the physical sciences and engineering disciplines. It permits researchers to

model and solve complex, coupled systems of partial differential equations (PDEs) that describe a wide range of physical phenomena. With its modular architecture, COMSOL supports a different of fields -such as electromagnetics, heat transfer, structural mechanics, fluid dynamics, acoustics, and chemical transport -making it a flexible approach for theoretical studies, device design, and real-world engineering applications.

COMSOL also components modern solvers that permit for in-prefund computations, and it provides numerous high-resolution meshing choices to improve the validity of complex simulations. In addition, the software includes a comprehensive mathematics and differential equation package, permitting researcher to manually input equations and parameters for conventional simulations.

COMSOL plays a crucial role in progressing research and innovation in physics through supporting:

A) Multiphysics Coupling: Physical systems rarely exist in isolation. COMSOL permits simultaneous simulation of several interacting physical processes (e.g., thermoelectric, magnetohydrodynamics, piezoelectricity), which is crucial for accurate modelling of real-world systems.

B) Custom Equation Implementation: Users can add their own PDEs and physical laws using the PDE and Equation-Based Modelling interfaces, giving users the flexibility to simulate novel physical phenomena that are not covered by built-in modules.

C) Parameter Studies and Optimization: COMSOL allows users to systematically differ parameters, run parametric sweeps, and perform optimization tasks to find ideal system designs or operating conditions.

D) High-Fidelity Visualization: It provides comprehensive post-processing tools for mapping fields, gradients, fluxes, and more in 1D, 2D, and 3D, supporting prefund understanding of complex behaviour.

COMSOL is utilized through virtually all sub-domain of physics, such as:

E) Electromagnetics: Simulating electromagnetic fields in waveguides, antennas, metamaterials, and photonic devices.

F) Quantum and Semiconductor Physics: Modelling drift-diffusion, carrier recombination, tunnelling, and electrostatics in nanostructured materials.

G) Thermodynamics and Heat Transfer: Studying conduction, convection, radiation, and phase change in complex environments.

H) Acoustics and Vibration: Analysing acoustic wave propagation, resonances, and noise control in devices ranging from MEMS to loudspeakers.

I) Fluid Dynamics: Modelling laminar, turbulent, multiphase, or non-Newtonian flow, including interactions with solids and heat.

On the other hand, COMSOL decrease the demand for costly and time-consuming prototyping, permitting users and researchers to simulate, prove, and boost designs virtually before experimental implementation. In both field of academic and industrial, this drives to quicker innovation cycles, lower costs, and profonde insights into physical systems. It also acts as a useful teaching and learning approach in university courses on physics, engineering, and applied mathematics.

COMSOL's Multiphysics capabilities are uniquely suitable for biosensor modelling because of:

A) Multidomain Modelling: Biosensors often include simultaneous fluid flow, molecular transport, surface reactions, and electric/optical signal generation. COMSOL permits these processes to be simulated together in a single, combined model.

B) Chemical Kinetics and Mass Transport: The software can correctly model diffusion, convection, and adsorption/desorption of biomolecules using the Transport of Diluted Species and Surface Reactions interfaces.

C) Microfluidics and Lab-on-a-Chip: For biosensors combined with microfluidic systems, COMSOL allows accurate modelling of flow dynamics, shear stress, and analyte distribution.

D) Electrochemical and Optical Detection: With modules for electrostatics, current distribution, and wave optics, COMSOL is used to simulate sensing mechanisms likes impedance spectroscopy, voltammetry, surface plasmon resonance (SPR), and fluorescence.

In the meantime, COMSOL Multiphysics is a revolutionary approach in both general physics and the specific field of biosensor design. Its ability to simulate complex, coupled physical phenomena enables researchers to develop prefund insights, decrease experimental overhead, and build more efficient and effective devices. Whether modelling quantum mechanics, electromagnetic fields, or

biological sensing interfaces, COMSOL continues to be a vital portion of advanced scientific investigation and innovation.

In this case, the Semiconductor module is being utilized because of the widely research COMSOL has carried on theory, meshes, and complex solvers. This module combined the drift-diffusion equations, enhanced electrostatics modelling capabilities, and an electrical circuit interface to solve for numerous transistor parameters, embodying the concept of "Multiphysics." For ease of geometry creation, models can be builded in AutoCAD (Computer-Aided Design) and imported directly into COMSOL. On the other hand, as much as possible, a simpler structure is preferred to decrease computational challenges. When using the Semiconductor module, researcher will recognize that a variety of parameters are calculated, such as electron concentration, hole concentration, electric potential, current concentration, terminal current, and space charge density, among others. COMSOL can compute a wide list of important parameters in zero, one, two, and three dimensions, making it perfect for this kind of analysis.

To sum up, Simulation has a crucial impact in the progress of biosensing technology. From design and optimization to understanding molecular interactions and system-level integration, simulations minimize development time, less costs, and enhance sensor validity and accuracy. As computational power continues to grow and modelling techniques become more sophisticated, the impact of simulation in biosensing is expected to increase, leading innovation in diagnostics, environmental monitoring, and personalized medicine.

2.4- COMSOL setup:

In COMSOL, the first step is to generate a structure that precisely demonstrated the system the research aims to simulate. The design of the structure has a vital role in building a mesh that confirms more correct results. Under these circumstances, a simplified model of a transistor was constructed to simulate the Graphene Field Effect Transistor (GFET), (see Figure 2-1).

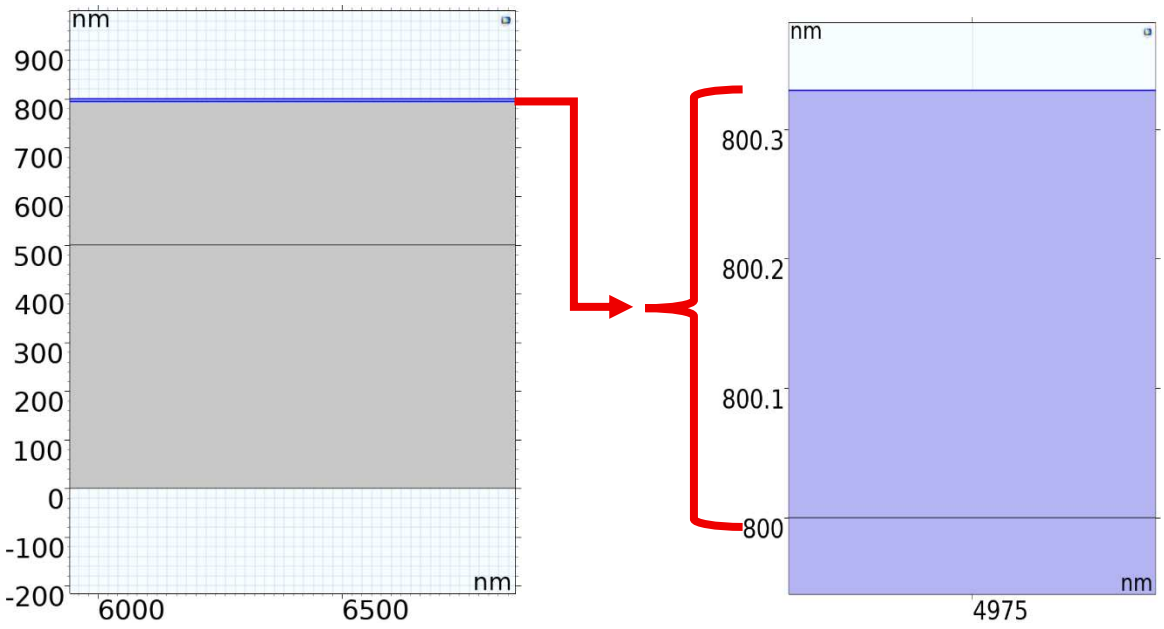

Figure 2-1. Structure of the Graphene Field-Effect Transistor (GFET) employed in the simulations (left), with a zoomed-in view highlighting the graphene channel layer and surrounding device interfaces (right). The enlarged view emphasizes the atomically thin graphene sheet that forms the conductive channel between the source and drain electrodes, illustrating its placement within the gate dielectric stack used in the device model.

2.4.1- COMSOL mesh:

COMSOL includes variety meshing choices, such as triangular, quadrilateral (quad), and mapped meshes. For 2-dimensional analyses, COMSOL suggested utilizing a triangular mesh, as it generally provides swifter convergence and more precise results. The mesh is a sensitive parameter in COMSOL, and unsuitable use can drive to considerable inaccuracies. In the transistor design, using a coarse mesh is undesirable because the mesh points may be too large, causing the individual triangles to become visible in surface plots.

For more reliable results, a uniform thick mesh is recommended, as it improves the precision of the simulation. On the other hand, this comes at the cost of enhanced calculation time because of the higher number of mesh points. The main disadvantage of using a denser mesh is the require for computational resources, specifically when dealing with very fine meshes. In extreme cases, where the mesh size is remarkably small, simulation times can extend up to 24 hours.

The biggest obstacle in simulating the characteristics of a transistor is figuring out a suitable mesh size. For the most correct results, each mesh triangle would require to be the same size as an electron. However, the computational time for such a small mesh point is incalculable, making it impractical to determine how long COMSOL would take to produce a result. To decrease computational time, an approach is too different the mesh size across different portions of the transistor, where a dense mesh may not be as important in specific areas. For example, a dense mesh can be applied in the graphene

layer, while a coarser mesh in other components can still provide equivalent or even better accuracy, all while reducing computation time. The substrate is another area where a thick mesh is less important, permitting for a lower dense mesh to save on resources. Finding an optimal mesh size is an iterative process, where simulations are run until there is no considerable alter in the results (see figure 2-2).

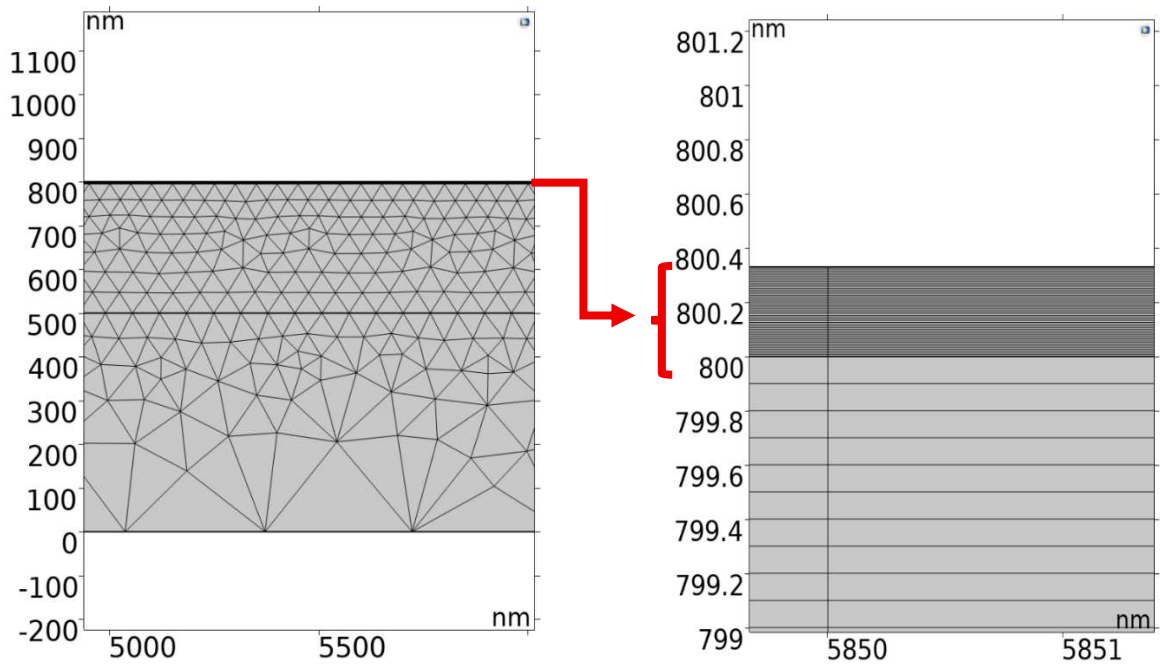

Figure 2 2. Meshing features employed in the simulations, with different level of refinement. (left) overall view of the computational mesh for the graphene field-effect transistor; (right) zoomed-in view highlighting the finer mesh applied in the graphene layer and the adjacent region to improve numerical accuracy.

2.5- Theory of GFET

For visualize charge distribution and voltage on the surface of graphene which induced by gate voltage we solve below equation in semiconductor model by COMSOL Multiphysics [1]:

$$\nabla^2\varphi = \frac{-\rho(r)}{\varepsilon_0\varepsilon_r} \qquad (2\text{-}1)$$

The dielectric constant or relative permittivity, ε_r, is defined as the ratio of the permittivity in the dielectric,ε, to the permittivity in vacuumε_0.

$$\varepsilon_r = \frac{\varepsilon}{\varepsilon_0} \qquad (2\text{-}2)$$

Sheet carrier concentrations (electrons or holes) in the source and drain regions can be approximated by [1]:

$$n \cong \sqrt{n_0^2 + \left(\frac{c_{back}\left(V_{backgate} - V^0_{dirac\ point}\right)}{e}\right)^2} \qquad (2\text{-}3)$$

The back-gate capacitance (c_{back}) which computed by equation (2-4) [2]:

$$C_{back} = \frac{\varepsilon_r \varepsilon_0}{t_{ox}} \quad (2\text{-}4)$$

The plot below shows the quantity used to compute the current in the graphene channel. [3].

expersion	value	Discription
n_0	1.75e11[$\frac{1}{cm^2}$]	Intrinsic charge carrier density of graphene
$V_{backgate}$	40-60[V]	Back gate voltage
$V^0_{dirac\ point}$	50.3[V]	Gate voltage at the charge neutrality
t_{ox}	300[nm]	Thickness of SiO_2
c_{back}	1.24e-4[$\frac{F}{m^2}$]	Back-gate capacitance
e	1.6e-19[C]	Electron charge

Table 2-1. Constant parameters employed in the computation of GFET resistance.

With this consideration, the current in the channel is expressed by below equation [4]:

$$I_d = \frac{W}{L} e * \mu * V_{DS} * n \quad (2\text{-}5)$$

Here, W and L represent the width and length of the graphene channel, respectively, e denotes the elementary charge, μ is the carrier mobility. The source-drain voltage V_{SD} is set to 1 mV in the calculations, if not specified differently.

2.6- Result of computation GFET by COMSOL

Using this simplified model, the electron, hole concentration and potential distribution over transistor can be observed to determine if COMSOL is performing the accurate simulations. In this analysis,

the potential that's applied to the source and drain are kept constant at 1mV for consistency and a sweep is performed at the back gate.

In Figure 2-3, this plot displays the electric potential across the structure with equal potential of 10 V applied at the back gate. Observe the potential is greater at the gate due to the doping profile and the electron affinity of the gate in comparison to that of the graphene layer. This is caused by the different electron affinity which for silicon is 4.05 V and for graphene is 4.55 V.

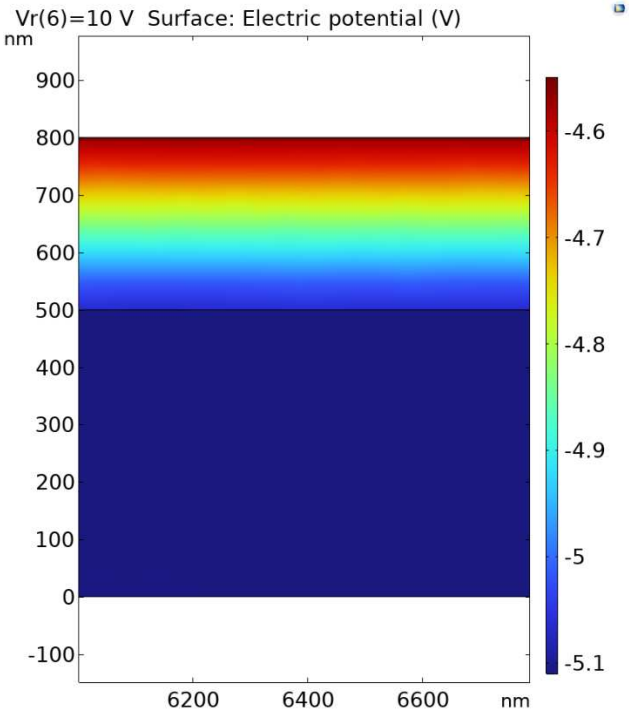

Figure 2 -3. Electric potential distribution in the Graphene Field-Effect Transistor (GFET) under an applied back-gate bias of 10 V, illustrating the electrostatic potential profile across the device and the modulation of the graphene channel induced by the back-gate field.

Figure 2-4(a-b) shows the behaviour of electron concentration in the structure under the same conditions as described earlier. As expected, the electron concentration is less dense near the middle of the graphene layer around the Dirac point. However, when a voltage is applied far from the Dirac point, the electron concentration increases and becomes denser at the centre of the graphene layer.

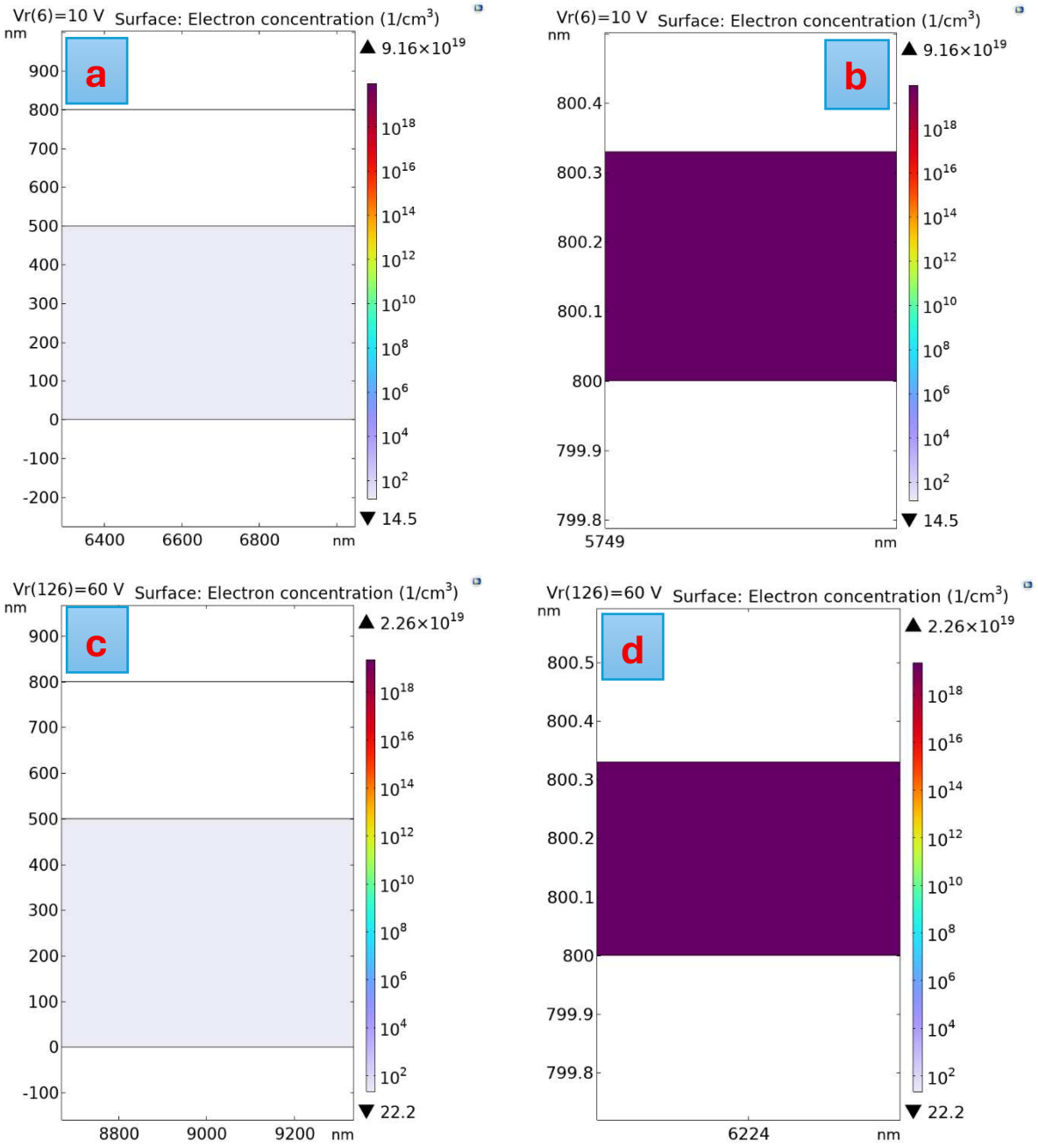

Figure 2-4 (a–d). Electron concentration distribution in the GFET channel under different back-gate voltages. (a) Electron concentration at a back-gate voltage of 10 V. (b) Zoomed-in view highlighting the electron concentration in the graphene layer for 10 V. (c) Electron concentration at a back-gate voltage of 60 V. (d) Zoomed-in view showing the electron concentration in the graphene channel at 60 V.

Electrons according to the basic theory are attracted to a higher potential, and holes are attracted to lower potential. This is displayed in the next analysis that is performed with a 10 V and 60 V potentials applied to the back gate. See Figure 2-5(a-b). These figures depict a smaller hole concentration and a greater electron concentration inside the graphene layer. There should be no electron or hole concentration inside of the oxide layer because it is an insulator which means it has no carrier mobility.

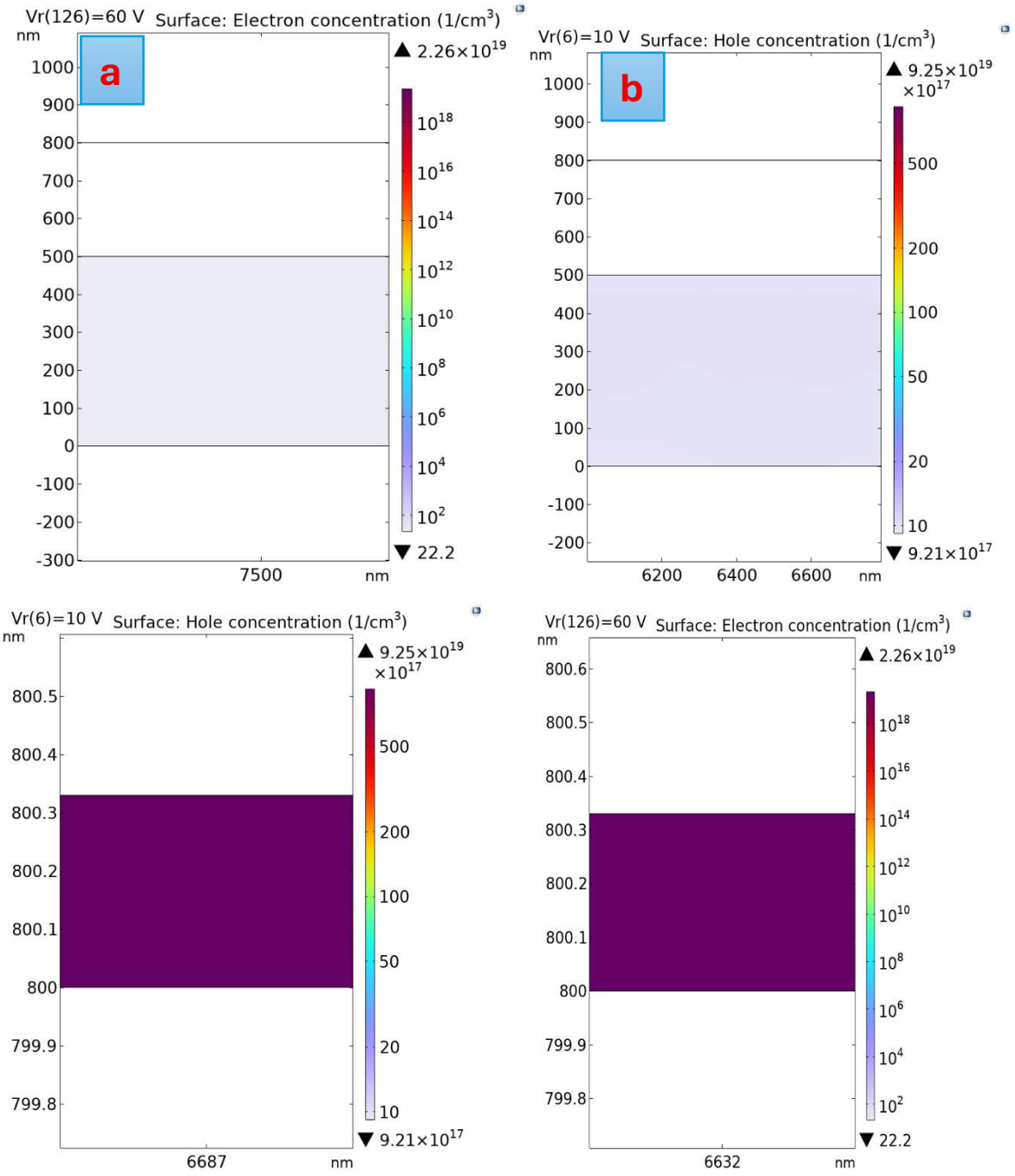

Figure 2-5 (a–d). Hole concentration distribution in the GFET channel under different back-gate voltages. (a) Hole concentration at a back-gate voltage of 10 V. (b) Zoomed-in view highlighting the hole concentration in the graphene layer for 10 V. (c) Hole concentration at a back-gate voltage of 60 V. (d) Zoomed-in view showing the hole concentration in the graphene channel at 60 V.

Finally, to test the performance of our model for the GFET, we computed its resistance at different widths and lengths. The results of the computation showed that the transistor's behavior corresponded well with low resistance, which is described by Equation (2-6)

$$R = \rho \frac{L}{A} \qquad (2\text{-}6)$$

Graph 2-6(a-b) describe this performance:

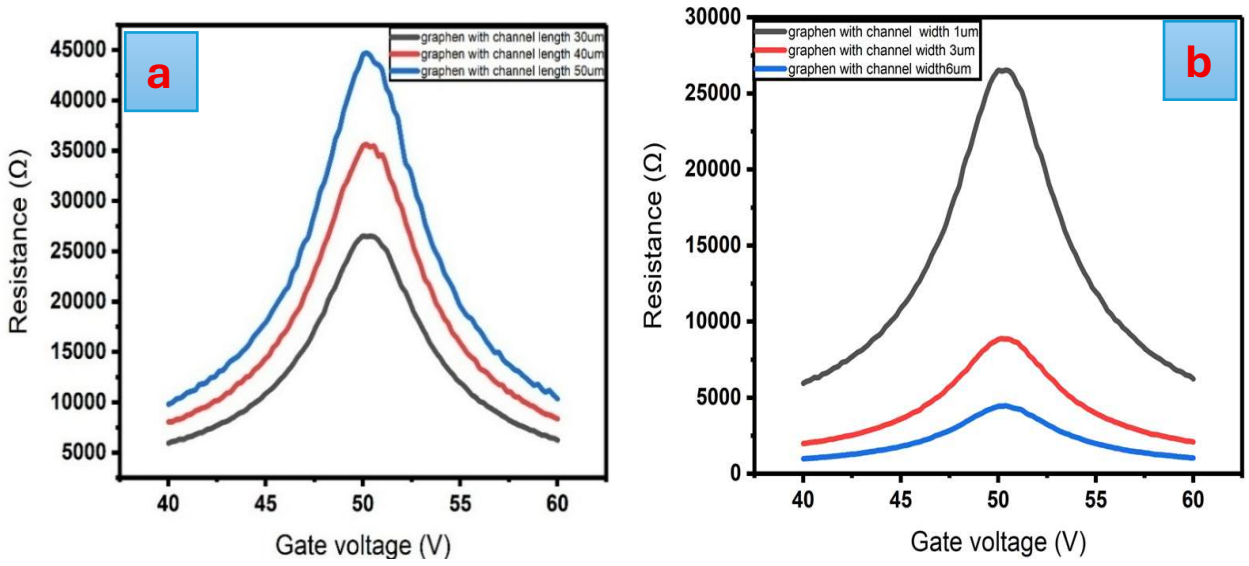

Figure 2-6 (a-b). show the resistance of the graphene channel versus back gate voltage for different lengths and widths, respectively.

For computations with different channel lengths, a width of 1 µm is used, while for different channel widths, the length is kept at 30 µm.

References:

[1]- Dale, Edgar. "Audiovisual methods in teaching." (1969).

[2]- Gaba, David M. "The future vision of simulation in health care." *BMJ quality & safety* 1 (2004).

[3]- Barry Issenberg, S., et al. "Features and uses of high-fidelity medical simulations that lead to effective learning: a BEME systematic review." *Medical teacher* 27.1 (2005): 10-28.

[4]- Kolb, David A. *Experiential learning: Experience as the source of learning and development*. FT press, 2014.

[5]- Salas, Eduardo, et al. "Using simulation-based training to improve patient safety: what does it take?." *The Joint Commission Journal on Quality and Patient Safety* 31.7 (2005): 363-371

[6]- Rebelo, Patrícia Catarina Santos. *Computer-aided design of molecular imprinted electrochemical sensors for analysis of pharmaceuticals in waters*. Diss. Universidad do Porto (Portugal), 2022.

[7]- Sampath, Janani, Sarah Alamdari, and Jim Pfaendtner. "Closing the gap between modeling and experiments in the self-assembly of biomolecules at interfaces and in solution." *Chemistry of Materials* 32.19 (2020): 8043-8059.

[8]- Ferreira, Mariana, et al. "Advances in microfluidic systems and numerical modeling in biomedical applications: a review." *Micromachines* 15.7 (2024): 873.

[9]- Jin, Xin. *A multi-scale and multi-physics framework for integrated electronics operating in harsh environment: a sensor-to-system perspective*. Diss. Purdue University, 2020.

Chapter three

Graphene-based chemical field effect transistors: impact of electric double layer models and quantum capacitance on Na^+ detection capabilities

3.1- Electrical Detection Mechanisms in Graphene Field-Effect Biosensors:

Ultrasensitive biosensors are opening new opportunities for “personalized medicine” tailored to the specific biochemistry and diagnostic of individual patients. While versatile detection strategies exist, the main requirement for a biosensor is that the detection is sensitive (identification of clinically relevant concentrations of biomarkers in biological samples) and selective (availability of a suitable biological recognition element). Since the experimental preparation and observation of the electric field effect in graphene by the Manchester group in 2004, biochemical sensing using graphene electronic devices has been actively pursued [1].

The sensing principal roots on a change of the electrical conductance of the graphene channel upon adsorption of a molecule on the sensor surface. The uniqueness of graphene among other solid-state materials is that all carbon atoms are located on the surface, making the graphene surface potentially highly sensitive to any changes of its surrounding environment. Along with the excellent electrical properties of graphene, extraordinary high Graphene nanoelectronics provide a versatile platform for a wide spectrum of biochemical sensing applications [2].

Detection can be realized through various mechanisms, including charge transfer, charge scattering, capacitive effect and field effect. The field effect (i.e., the modulation of the electrical conductivity of a material upon the application of an external electric field, for example, induced by a charged bio molecule) has been widely regarded as the most reliable sensing mechanism. This effect has been harvested to design the first graphene field-effect transistor (GFET), which has inspired considerable experimental and theoretical work relating to the application of GFETs for high performance label-free chemical and biological sensors [3]. The G-FET architecture used in the present work is depicted in Figure 1. In the left panel, the three-dimensional rendering of the GFET is reported, showing the graphene channel (grey-colored) between source and drain electrodes (yellow colored), the dielectric film (red), the bulk substrate (black) and the droplet of Na^+ ions-rich electrolyte (purple). The right panel reports the cross-sectional view of the device, indicating the dimensions of each device component (graphene channel, source/drain electrodes, overall substrate, electrolyte droplet).

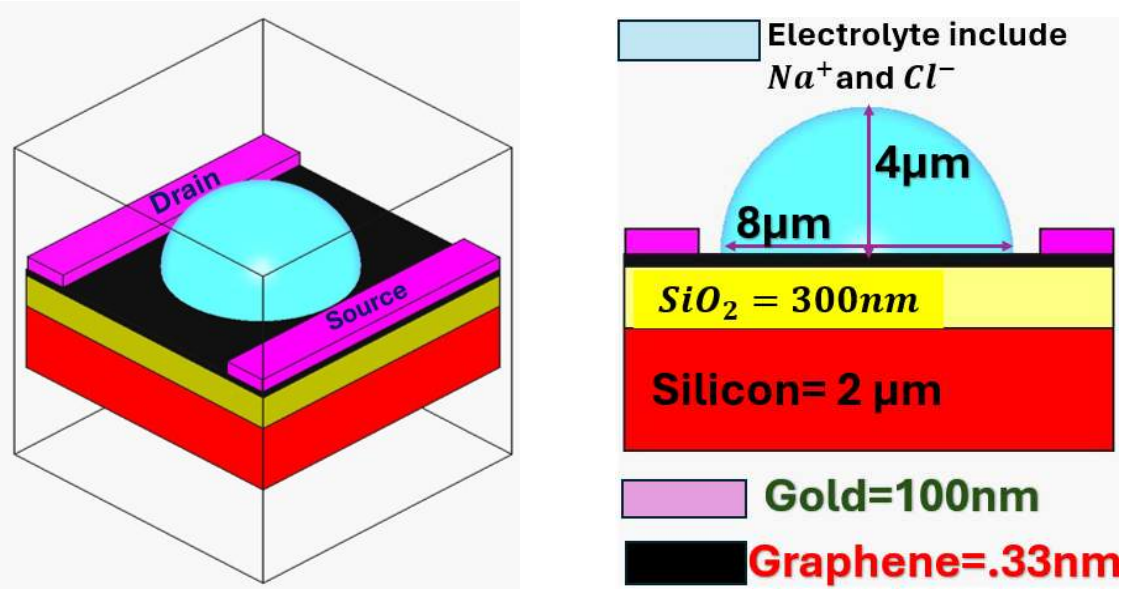

Figure 3-1. (left) Schematic diagram of a graphene field-effect transistor (GFET) gated by an electrolyte. (right) cross sectional view of the device. Red, yellow, black, light-blue and violet color is used for the silicon substrate, the silicon oxide dielectric, the graphene layer, the electrolyte with Na+ and Cl- ions and the metallic electrodes, respectively.

A change in the electric field can either be achieved using the back-gate voltage or be induced by physisorption or chemisorption of the target molecules. When the back gate is held at a fixed voltage the change in current between the drain and source thus can be ascribed to molecules adsorbed on the graphene surface. When the physiological molecule reaches graphene surface, the electrical double layer of the electrolyte (EDL) appears. The EDL is a virtual capacitor formed by the separated charges located at the solid side and the solution side of the interface [4].

3.2- Models and Mechanisms of the Electric Double Layer:

To understand the operation of graphene electrolyte-gated field-effect transistors (EGFETs), it's essential to first explore the concept of the Electric Double Layer (EDL). The electric double layer (EDL) is the most important part of any electrochemical system because it is the region in space where the electrochemical reaction takes place. It was always understood that the composition and conformation of this interfacial region are important to the electrochemical reaction. The composition, thickness, conformation, and other parameters are already expected to be dependent on the electrode material, the electrolyte chemistry, and the interaction between these two phases. Near the electrode surface, ions in the electrolyte are influenced by the unscreened excess charge on the electrode, resulting in attraction and repulsion. At the interface, where the electrode meets the solution, an EDL forms, adding complexity to the development of the interfacial potential difference. Therefore, understanding the EDL is crucial for electrochemical research. The concepts used to understand the structure of an EDL were developed over 100 years ago. Over time, multiple

theoretical frameworks have been introduced to describe this phenomenon. Among the most recognized are the Helmholtz model, the Gouy-Chapman model, and the Gouy-Chapman-Stern model.

3.2.1- Helmholtz model for EDL:

The earliest and most straightforward of these, the Helmholtz model, was introduced in 1879. This model describes the potential distribution within the Helmholtz layer using the one-dimensional Poisson equation, which links electric potential to the spatial distribution of charge [5,6,7,8]:

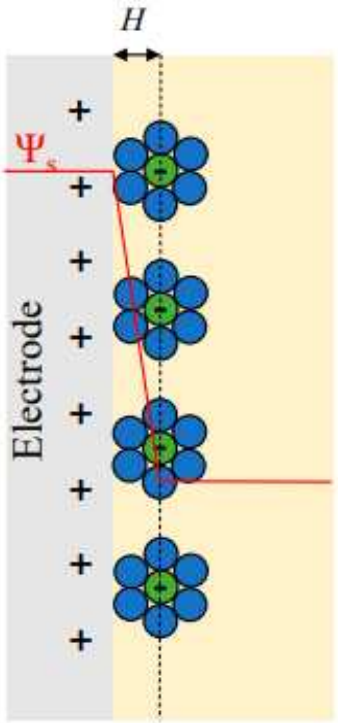

Figure 3-2. Schematic illustration of the Helmholtz layer, showing the compact layer of ions adsorbed at the charged surface, forming part of the electrical double layer at the electrode–electrolyte interface. The schematic is taken from reference [7].

The electrode holds a charge density (σ_M) arising from either an excess ($-\sigma_M$) or deficiency ($+\sigma_M$) of electrons at the electrode surface. The charge on the electrode is balanced by redistribution of the ions in the solution by an equal but oppositely charged number of ions. The result is two layers of opposite charge separated by some distance $l = \frac{d}{2}$ limited to the radius d/2 of the attracted ions and a single layer of solvation around each ion (see figure 3-2).[9]

The potential in the Helmholtz layer is described by the Poisson's equation in 1D, which relates the potential with the charge distribution:

$$\frac{d^2\varphi}{dx^2} = -\frac{\rho(x)}{\varepsilon_r \varepsilon_0} \quad (3\text{-}1)$$

Where φ is the electric potential, ρ is the charge density, x is the distance from the electrode, ε_0 is the permittivity of vacuum, ε_r is the relative permittivity of the medium.

The approach treats the ions as point charges, and this allows us to rewrite equation (3-1) between the two layers to [9]:

$$\frac{d^2\varphi}{dx^2} = 0 \quad (3\text{-}2)$$

To quantitatively understand the Helmholtz capacitance, we follow the traditional model regarding Helmholtz layer as a parallel-plate capacitor, and its capacitance is written as [10]

$$C_H = \frac{\varepsilon_r \varepsilon_0}{l} \quad (3\text{-}3)$$

According to the traditional Helmholtz model, l is defined as the distance from the nuclei of surface counter ions to surface charges [10].

Where l is the thickness of the double layer. For $\varepsilon_0 = 8.85 * 10^{-12}\,\frac{F}{m}$, $\varepsilon_r = 78.5$ and $l = .3nm$, we get $C_H = 231.41\,\frac{\mu F}{cm^2}$.

The model does not account for the dependence of the measured capacity on potential or electrolyte concentration. Another drawback is the neglect of interactions that occur away from OHP, also The Helmholtz model did not consider the thermic motion of the ions in the solution, such as that considered for the ion–ion interaction in the Debye–Hückel model [5].

3.2.2- Gouy-Chapman Model:

Gouy and Chapman were the first to consider the thermal motion of ions near a charged surface. They envisioned a diffuse double layer (DDL) composed of counterions (ions with opposite charge to the surface) that are attracted to the surface, and co-ions, which are repelled. These ions are embedded in a dielectric continuum described by the Poisson-Boltzmann (PB) differential equation [11].

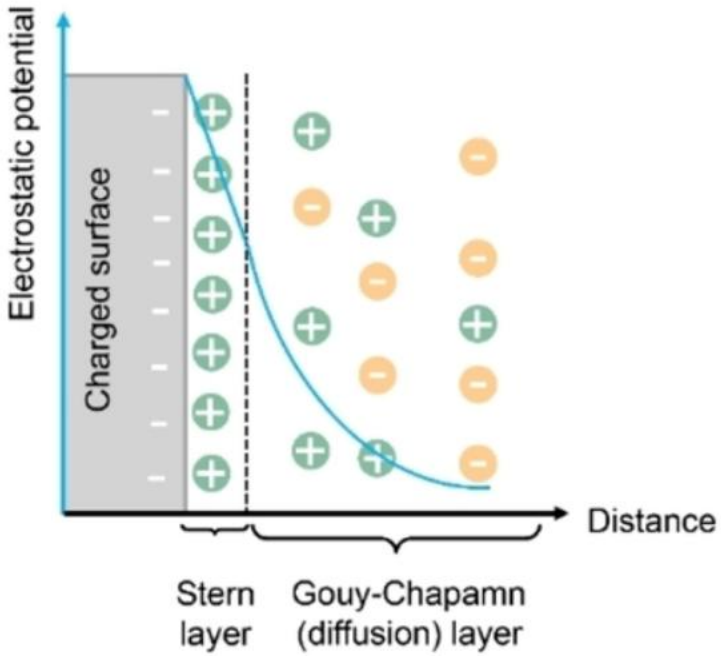

Figure 3-3. Schematic illustration of the Gouy–Chapman model showing the diffuse electrical double layer near a charged surface, where mobile ions redistribute and the electric potential gradually decays with distance into the electrolyte. The schematic is taken from reference [11].

The distribution of ions is described by the Boltzmann distribution [11]:

$$n_i = n_{\pm}^{\infty} \exp\left(\frac{-Z_{\pm} e\varphi}{K_B T}\right) \tag{3-4}$$

where $n_+$is related to the cation population, n_- to the anion, $n_{\pm}^{\infty}$ to the bulk ion population, and $Z_{\pm}$ to the ion charge number e is the unit charge, K_B Boltzmann constant, T absolute temperature.

The total charge density per unit volume for all ionic species is the sum over all ions [11]:

$$\rho(x) = \sum_i n_{\pm} Z_{\pm} e = \sum_i e Z_{\pm} n_{\pm}^{\infty} \exp\left(\frac{-Z_{\pm} e\varphi}{KT}\right) \tag{3-5}$$

Combining Eq. (1) and Eq. (3-5) leads to the Poisson-Boltzmann equation [11]:

$$\frac{d^2\varphi}{dx^2} = -\frac{e}{\varepsilon_r \varepsilon_0} \sum_i Z_{\pm} n_{\pm}^{\infty} \exp\left(\frac{-Z_{\pm} e\varphi}{K_B T}\right) \tag{3-6}$$

The thermal motion is the reason for the ions' kinetic energy, and if this quantity is higher than the expected for the electric potential energy, or in mathematical terms ,if $K_B T >> |ze\varphi|$,then the exponent term in Equation (3-6)can be expended in a polynomial form and trunked in the second term, linearizing the equation:

$$\frac{d^2\varphi}{dx^2} = -\sum \frac{Z_{\pm} n_{\pm}^{\infty} e}{\varepsilon_r \varepsilon_0} + \frac{e}{\varepsilon_r \varepsilon_0} \sum_i Z_{\pm} n_{\pm}^{\infty} \left(\frac{-Z_{\pm} e\varphi}{K_B T}\right) \tag{3-7}$$

The first term at the right side of Equation (3-7) is related to the total charge of the electrolyte bulk, which is known to be zero since electroneutrality is observed. In this way, it is possible to reduce Equations (3-7) to the below equation:

$$\frac{d^2\varphi}{dx^2} = \frac{e^2\varphi}{\varepsilon_r\varepsilon_0 K_B T}\sum_i Z_{\pm}^{\infty} n_{\pm}^{\infty} \quad (3\text{-}8)$$

A solution for the differential equation (3-8) is:

$$\varphi = \varphi_0 \exp\left(\frac{xe^2}{\varepsilon_r\varepsilon_0 K_B T}\sum Z_{\pm}^2 n_{\pm}^{\infty}\right. \quad (3\text{-}9)$$

The phrase $I = \mu = 1/2\sum n_i^0 Z^2$ which defined by Lewis and Randall to reflect the effect of charges and interionic interactions on electrolyte activities, and hence on ionic activity coefficients called bulk ionic strength [12].

The Debye length, λ_D, is defined as the thickness of the ionic cloud around the center ion, in the Debye–Hückel theory. The total charge of this cloud has the same modulus as the central ion charge, but the signal is the opposite, which guarantees electroneutrality. This quantity is presented in Equation (3-10).

$$\lambda_D = \sqrt{\frac{\varepsilon_r\varepsilon_0 T K_B}{e^2\sum Z_{\pm}^2 n_{\pm}^{\infty}}} \quad (3\text{-}10)$$

If it is substituted in (3-9), Equation (3-10) is obtained:

$$\varphi(x) = \varphi_0(x)\exp\left(\frac{-x}{\lambda_D}\right) \quad (3\text{-}11)$$

For a symmetrical (Z_Z) electrolyte, Eq. (3-11) has the form [13]:

$$\frac{\partial\varphi}{\partial x} = \left(\frac{8K_B T n_{\pm}^{\infty}}{\varepsilon_r\varepsilon_0}\right)^{\frac{1}{2}} \sinh\left(\frac{Z_{\pm}e\varphi}{2K_B T}\right) \quad (3\text{-}12)$$

The charge density of the diffuse layer is used as [14]:

$$\sigma_M = \varepsilon_r\varepsilon_0\left(\frac{d\varphi}{dx}\right)_x = (8KTn_{\pm}^{\infty}\varepsilon_r\varepsilon_0)^{\frac{1}{2}}\sinh\left(\frac{Z_{\pm}e\varphi}{2KT}\right) \quad (3\text{-}13)$$

By differentiating, the differential capacitance is obtained as [13]:

$$C_{GC} = \frac{d\varphi_M}{d\varphi} = \left(\frac{2e^2 n_{\pm}^{\infty}\varepsilon_r\varepsilon_0 Z^2}{KT}\right)^{\frac{1}{2}}\cosh\left(\frac{2e\varphi}{2KT}\right) \quad (3\text{-}14)$$

By replacing equation number (3-11) in equation number (3-14) the capacitance in Gouy-Chapman it will be in below form.

$$C_{Gc} = \frac{\varepsilon_r \varepsilon_0}{\lambda_D} \cosh\left(\frac{2e\varphi}{2KT}\right) \quad (3\text{-}15)$$

3.2.3- Stern model:

In 1924, Stern advanced the double-layer theory by proposing a more realistic approach to describing the physical situation at the interface. He combined the two earlier models, adapting Helmholtz's compact ion layer and incorporating the diffuse layer of Gouy-Chapman extending into the bulk solution. Stern also accounted for the finite size of ions, which meant that the closest approach of the outer Helmholtz plane (OHP) to the electrode would depend on the ionic radius [8]. The outer edge of the Stern layer is called the outer Helmholtz plane (OHP); the potential is denoted φ_{OHP}[14].

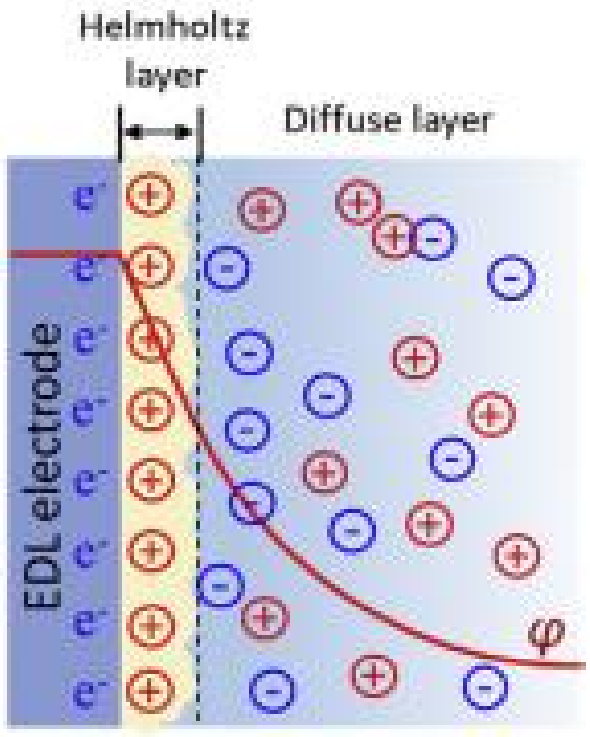

Figure 3-4. Schematic illustration of the Stern model of the electrical double layer (EDL), showing the compact Helmholtz layer near the charged surface and the adjacent diffuse layer where ion concentration gradually decreases into the electrolyte. The schematic is taken from reference [14].

In mathematical terms the differential capacitance of the double layer $C_{EDL}$is equivalent to two capacitors in series or:

$$\frac{1}{C_{EDL}} = \frac{1}{C_H} + \frac{1}{C_{Gc}} \quad (3\text{-}16)$$

where C_H is the capacitance of the charges held inside the OHP and C_{Gc} is the capacitance of the diffuse layer [15].

3.3- Graphene Charge Distribution and Back-Gate Modulation Modelling:

As already discussed in chapter two to visualize the charge distribution and voltage on the surface of graphene induced by the gate voltage as already discussed in chapter two, we solve the following equation using the semiconductor model in COMSOL Multiphysics [16]:

$$\nabla^2\varphi = \frac{-\rho(r)}{\varepsilon_0\varepsilon_r} \tag{3-17}$$

The dielectric constant or relative permittivity, ε_r, is defined as the ratio of the permittivity in the dielectric,ε, to the permittivity in vacuumε_0 [17].

$$\varepsilon_r = \frac{\varepsilon}{\varepsilon_0} \tag{3-18}$$

Sheet carrier concentrations (electrons or holes) in the source and drain regions can be approximated by [17]:

$$n \cong \sqrt{n_0^2 + \left(\frac{C_{back}\left(V_{backgate} - V^0_{dirac\ point}\right)}{e}\right)^2} \tag{3-19}$$

The back-gate capacitance (C_{back}) which computed by below equation [18,19]:

$$C_{back} = \frac{\varepsilon_r\varepsilon_0}{t_{ox}} \tag{3-20}$$

t_{ox} is the thickness of graphene which equal .33nm.

The source-current modulation is expressed as a function of the change in the carrier density (n) in the graphene channel, which is proportional to the number of targets attached on the graphene surface [20,21]:

$$I_d = \frac{W}{L} e * \mu * V_{DS} * n \tag{3-21}$$

Here, W and L represent the width and length of the graphene channel, respectively. The symbol **e** denotes the elementary charge, μ is the carrier mobility, and the source-drain voltage V_{SD} is set to 1 mV.

3.4- Influence of Top and Back Gates on Graphene Charge Distribution:

When both the top gate and back gate are applied with an electrolyte gate as a top gate, each of them independently connected to the same graphene channel. As a result, the capacitances are in parallel, and the total capacitance is calculated using the following equation [16]:

$$C_{total} = C_{back-gate} + C_{top-gate} \quad (3\text{-}22)$$

Under these conditions, the carrier concentrations are influenced by both the top and back gate effects. Therefore, equation (3-19) is modified to the following equation [16]:

$$n \cong \sqrt{n_0^2 + \left(\frac{c_{back}\left(V_{backgate} - V^0_{dirac\ point\ back}\right)}{e}\right) + \left(\frac{c_{top}\left(V_{topgate} - V^0_{dirac\ point\ top}\right)}{e}\right)^2} \quad (3\text{-}23)$$

where c_{top} is the effective top-gate capacitance per unit area and $V^0_{dirac\ point\ top}$ is potential of Dirac point of Graphene due to existence of top gate.

Equation (25) is modified to the following form when one gate is variable, and the other is fixed. In our computation, we applied different back gate voltages while the electrolyte gate, with a specific concentration, is kept at a fixed value [15,16]:

$$n(V_{back-gate}) \cong \sqrt{n_0^2 + \left(\frac{c_{back}\left(V_{backgate} - V(x) - V_0\right)}{e}\right)^2} \quad (3\text{-}24)$$

$V(x)$ is the potential along the channel, V_0 represents the potential at the Dirac point which computed by below equation [15,16]:

$$V_0 = V^0_{back-gate} + \frac{C_{top}}{C_{back}}\left(V^0_{top-gate} - V_{top-gate}\right) \quad (3\text{-}25)$$

3.5- Modelling Electrostatics and Ion Migration in the Electric Double Layer:

After computing the designed structure, various plots and graphs were generated to compare key parameters and evaluate the impact of applying different electric double layer (EDL) models. To achieve this, we first simulated the migration of cations and anions within the EDL. For the electric

field and mass transport analysis, an electrostatic problem governed by the Poisson equation, $\nabla(\varepsilon\varepsilon_0\nabla\varphi) = 0$, was solved in the compact layer. In the diffuse layer, a coupled Nernst–Planck and electrostatic model was employed to capture the transport phenomena more accurately [21,22]

$$\frac{\partial c_i}{\partial t} = \nabla(D_i\nabla c_i + z_i F D_i c_i \nabla\frac{\varphi}{RT}) \qquad (3\text{-}26)$$

and $\nabla(\varepsilon\varepsilon_0\nabla\varphi) = \rho$, where $\rho = \sum z_i c_i$, is solved in the electrolytic domain outside of the compact layer. HereD_i , z_i, andc_i are respectively the diffusivity, the charge valence and the concentration of the ionic species i, t is time, F is the Faraday constant, R is the gas constant, T is the absolute temperature, φ is potential, ε is the dielectric constant, ε_0 is the vacuum permittivity, and ρ is charge density.

3.6- Results and discussion:

Figure 3-5(a-d) illustrates the migration of cations and anions, as well as the distribution of electric potential and electric field within the electric double layer (EDL) [21,22].

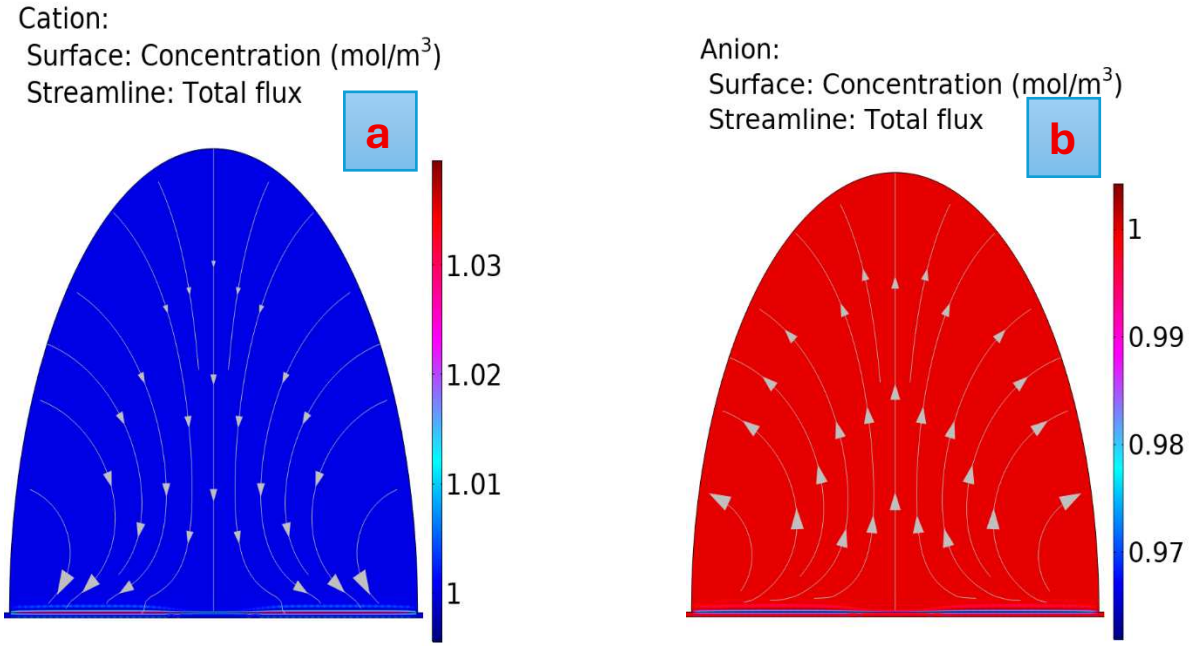

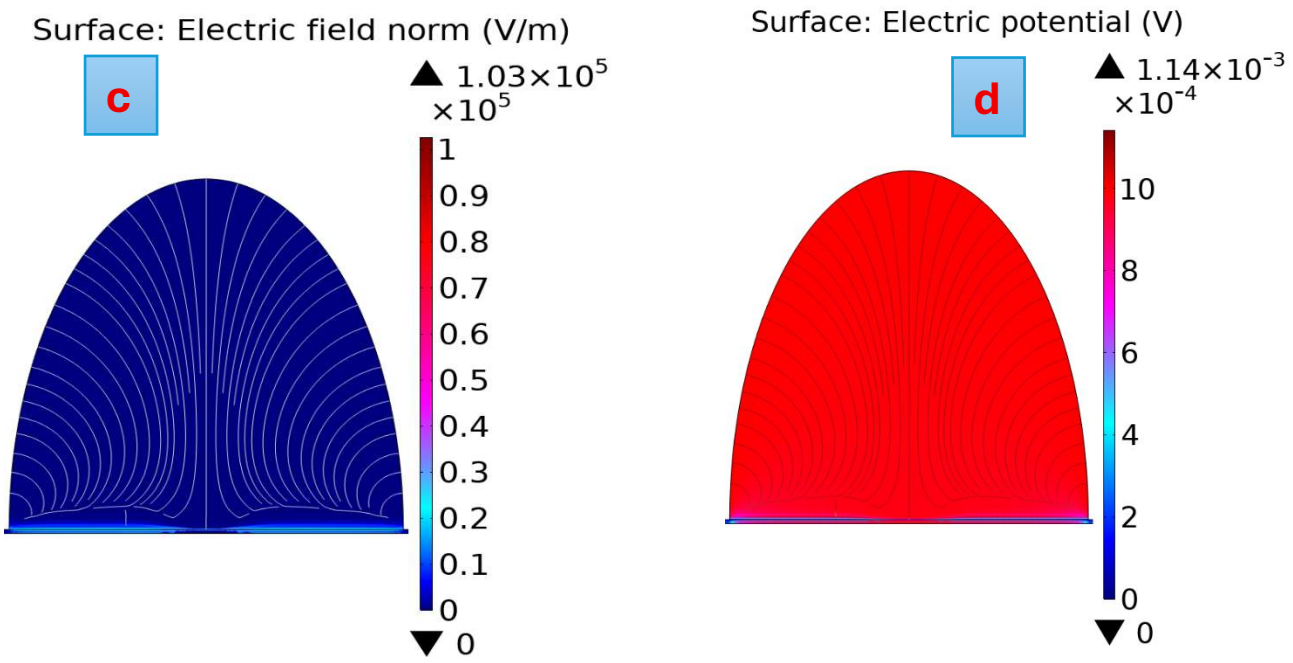

Figure 3-5. Panels a–d show the migration of cations (a) and anions (b), as well as the electric potential (c) and electric field (d) in the electrolyte, including the region near the electric double layer (EDL). The simulation uses the Stern model of EDL.

Because the electrode is polarized negatively against bulk solutions, it is negatively charged and attracts cation while repelling anion. The direction of the cation and anion confirm that the cation in the electrolyte is accumulated at the surface, while the anion is depleted.

Next step is a calculation of the potential within the layer at different Na^+ concentrations and varying distances from the electrolyte-graphene interface. Given the critical role of the potential along the electrolyte in the overall computational framework, the parameter was initially evaluated across two concentrations while varying distances from the interface between electrode and electrolyte. Figures 3-6 present the results of these computations, which are consistent with the behaviour described by Equation (11).

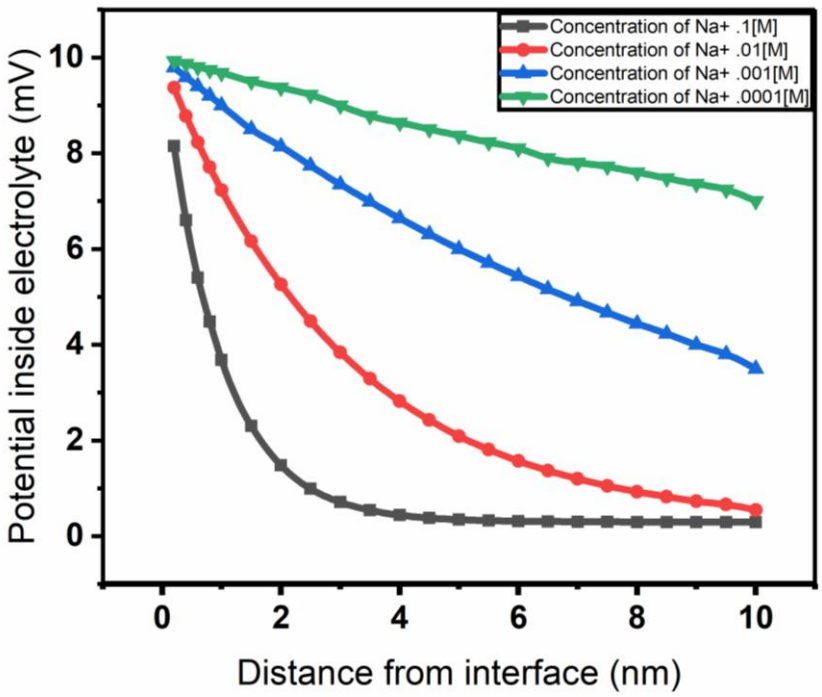

Figure 3-6. Electricla potential inside the electrolyte as a function of the distance from the electrolyte-graphene interface, for different concentations of Na+ (The computation uses the Stern model of the electric double layer (EDL).

The charge density of graphene and the resistance of the graphene channel under varying Na^+ concentrations were analysed. The analysis initially employed the Gouy-Chapman model and was subsequently refined using the more accurate Stern model for enhanced precision. Gouy-Chapman model is effective for analysing the influence of ion concentration on the charge density of graphene. Specifically, increasing the concentration of Na^+ ions near the graphene surface results in a shift of the Dirac point toward the negative (left) side. This shift arises because the presence of positively charged Na^+ ions induce electron accumulation in the graphene as a compensatory mechanism to maintain charge neutrality. Given that the graphene channel in our setup exhibits p-type behaviours (i.e., a positive Dirac point), this electron accumulation drives the system toward n-type characteristics. As indicated in Equation (23), the current between the drain and source is linearly related to the charge concentration in the graphene channel. this interaction can influence the current that f lows between drain and source electrodes. The current variation, resulting from this interaction, can be used to detect the analyte's presence and measure its concentration. Consequently, the

resistance of the channel is altered due to this shift in carrier concentration. Figures 3-7(a-b) illustrate the charge density and resistivity of the graphene channel under varying concentrations of Na^+ ions.

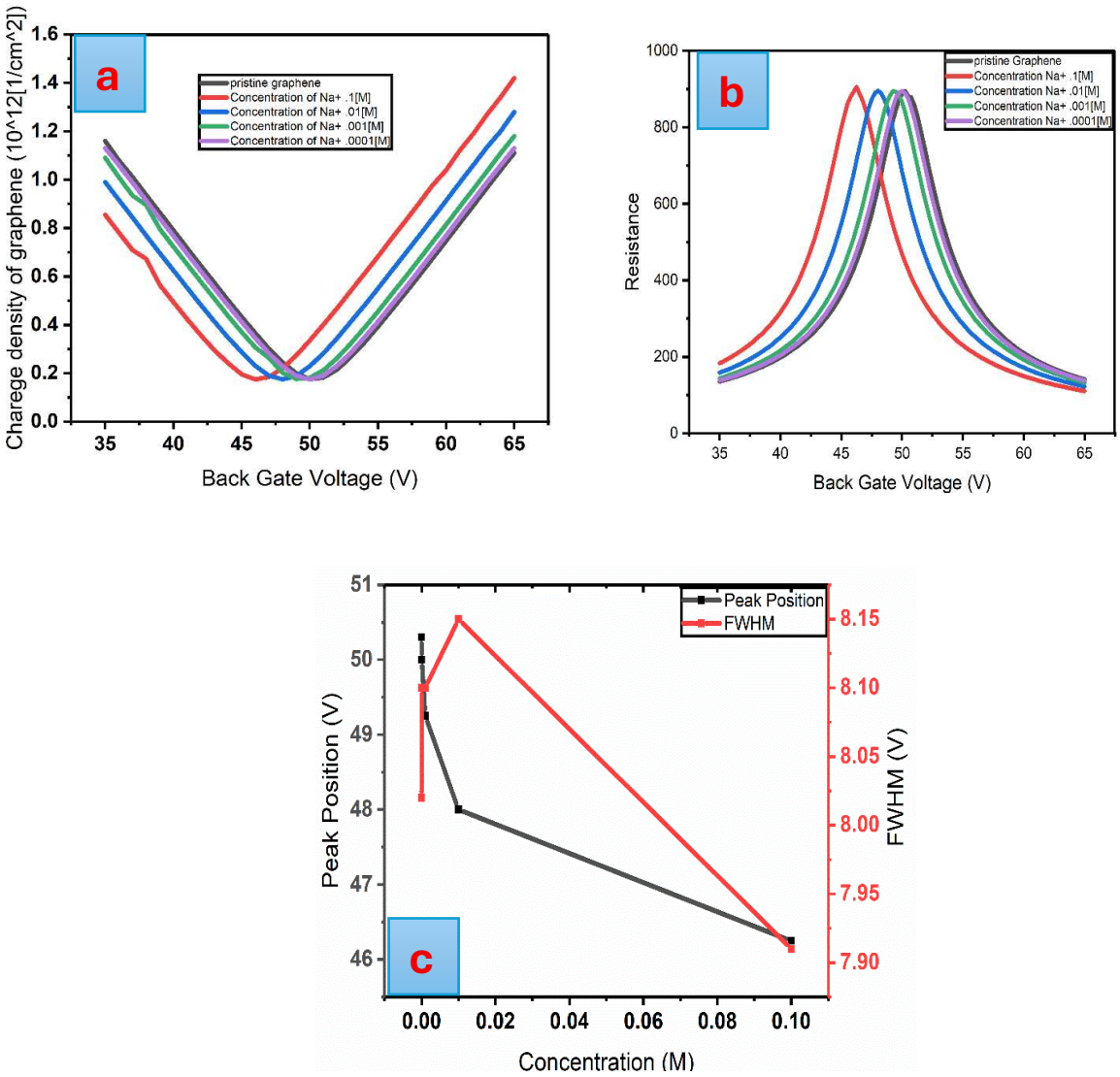

Figure 3-7. a) Charge concentration and b) resistance of graphene channel as function of back gate voltage calculatred according to the Gouy-chapman model of EDL; (c) Position of the resistance peak and its full width at half maximum (FWHM) as functions of the concentration.

On the other hand, the Stern model is employed to compute the aforementioned parameters of graphene, as previously discussed. This model accounts for both the capacitance of the diffusion layer—which is primarily influenced by ion concentration—and the Helmholtz layer, which depends on the ionic radius. Incorporating these factors enhances the precision of the calculations and increases the selectivity of the sensor. Figures 3-8(a-b) present the previously computed parameters; by contrast, the Stern model is utilized here to provide a more comprehensive and accurate analysis.

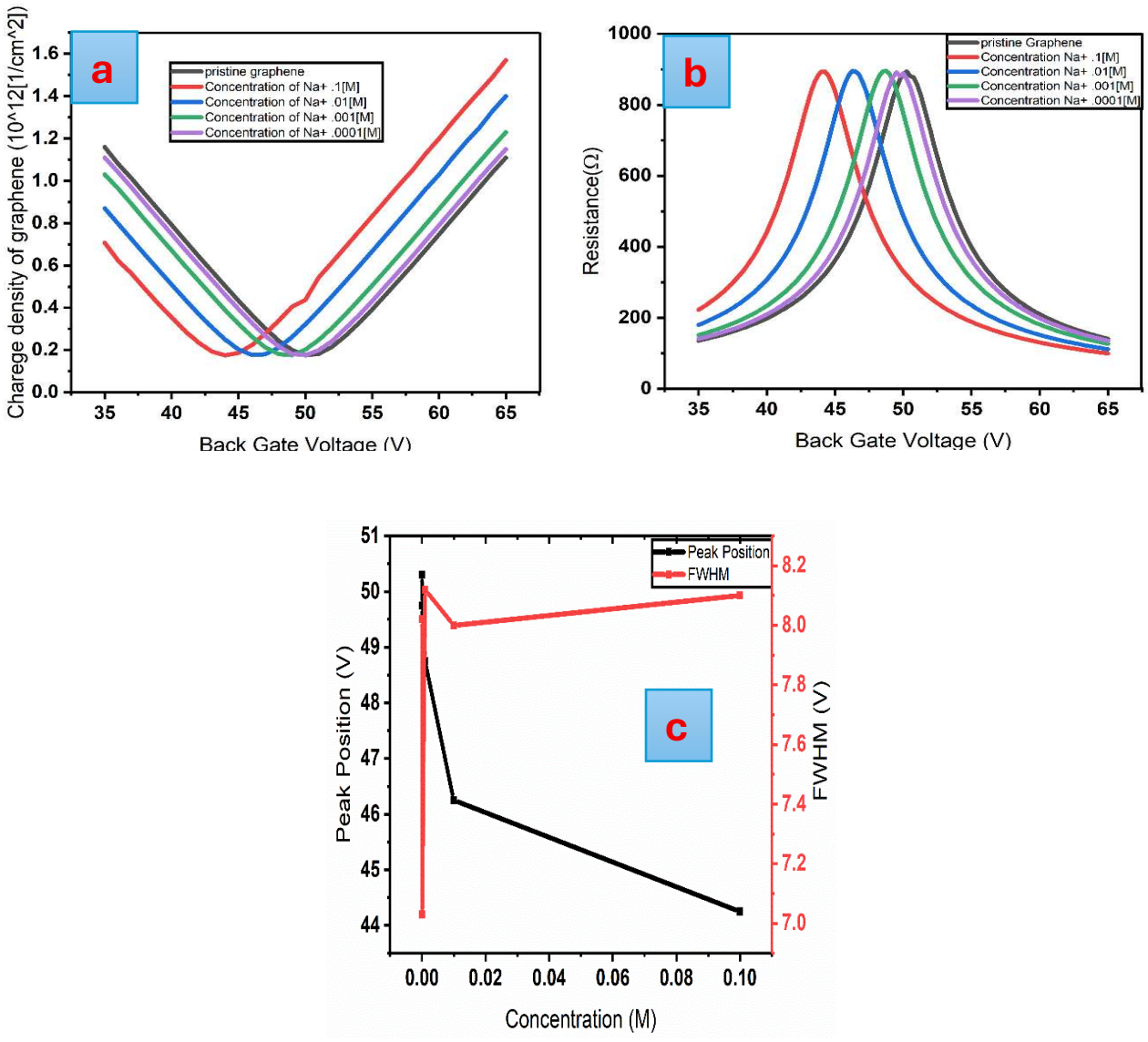

Figure 3-8. a) Charge concentration and b) resistance of graphene channel as function gate voltage calculated according to the Stern model of EDL; (c) Position of the resistance peak and its full width at half maximum (FWHM) as functions of the concentration.

3.6.1- Quantum Capacitance of 2D Graphene: Theory and Electrolyte Effects:

The electron transport properties of graphene devices are critical to many applications, but our understanding of these properties is still incomplete, despite rapid advances in recent years. One unsolved puzzle is the minimum in the conductivity at the Dirac point, which has stimulated many recent theoretical and experimental efforts. It has been proposed that this minimum is due to charged impurities that induce puddles of electrons and holes in the graphene. To fully understand the transport properties, it is important to investigate the scattering of the carriers by the impurities, and the density of carriers at and near the Dirac point (which is related to the quantum capacitance).

Electron transport in graphene has been studied using the field-effect transistor (FET) configuration, in which a graphene sample is placed on an oxidized silicon substrate and connected to source and drain electrodes, and the current through the graphene controlled with a back gate. The capacitance in these devices is dominated by the capacitance of the oxide layer, which makes it difficult to determine the quantum capacitance [23].

However, to decrease the operation voltage, it is expected that the oxide layers in future devices will be much thinner and have higher values of dielectric constant k, which means that the quantum capacitance will eventually be the dominant source of capacitance. To establish a theoretical prediction of quantum capacitance for ideal graphene, we use free-electron gas model taking the form of to compute quantum capacitance of graphene based on two-dimensional. The dispersion of mobile electrons in graphene in the first Brillouin zone (BZ) is given by [24]:

$$E(K) = S\hbar|K| \tag{3-27}$$

where $S = 1$ is the conduction band CB and $S = -1$ is the valence band VB, ħ is the reduced Planck's constant and $K = K_x^2 + K_y^2$ 2 is the wave vector of carriers in the 2D x−y plane of the graphene sheet.

The point k=0, referred to as the "Dirac point," is a convenient choice for the reference of energy; thus, $E(K) = 0\ eV$. Each k point is twofold spin degenerate $g_s = 2$, and there are two valleys in the first BZ the K and K valleys, $g_v = 2$.

In an undoped layer of graphene in thermal equilibrium, there are mobile electrons in the CB and holes in the VB, like the intrinsic carriers in a pure bulk semiconductor. To find the 2D sheet density of such intrinsic carriers in graphene, the linear density of states DOS [25],

$$\rho_{gr}(E) = \frac{g_s g_v}{2p(\hbar v_f)^2}|E| \tag{3-28}$$

is used to write the 2D electron gas sheet density in graphene as [25]:

$$n = \int_0^\infty dE \rho_{gr}(E)\, f(E) \tag{3-29}$$

Where $f(E)$ is the Fermi-Dirac distribution function given by [24]:

$$f(E) = (1 + \exp\left[\frac{E-E_F}{K_B T}\right])^{-1} \tag{3-30}$$

Where K_B the Boltzmann constant, T the absolute temperature, and E_F the Fermi level. With the aid of the dimensionless variables $\mu = \frac{E}{K_B T}$ and $\delta = \frac{E_f}{K_B T}$, the electron density may be rewritten as [24]:

$$n = \frac{2}{\pi}\left(\frac{K_B T}{\hbar v_f}\right)^2 \mathfrak{F}_1(+\delta) \tag{3-31}$$

and the hole density is symmetric, given by:

$$p = \frac{2}{\pi}\left(\frac{K_B T}{\hbar v_f}\right)^2 \mathfrak{F}_1(-\delta) \tag{3-32}$$

Were

$$\mathfrak{F}_1(\delta) = \frac{1}{\Gamma(j+1)} \int_0^\infty \frac{duu^j}{(1+e^{u-\delta})} \tag{3-33}$$

is the Fermi-Dirac integral with $j = 1$ and $\Gamma(\ldots)$ is the gamma function.

Under thermal equilibrium and under no external perturbation no applied bias, no optical illumination, the Fermi level is unique, and moreover, it is exactly at the Dirac point $E_f = 0\ eV$. Then, the intrinsic carrier concentration in 2D graphene is given by [24]:

$$n = p = n_i = \frac{\pi}{6}\left(\frac{K_B T}{\hbar v_f}\right)^2 \tag{3-34}$$

which is dependent on only one material parameter—the Fermi velocity. The point to note is that the intrinsic sheet density of electrons/holes does not depend on temperature exponentially; it has a T^2 dependence, due to the absence of a band gap, and the linear energy dispersion.

Writing the total charge in a graphene sheet with a local channel electrostatic potential V_{ch}as $Q = q(p - n)$ where q is the electron charge ,and using the definition of quantum capacitance $C_Q = \frac{\partial Q}{\partial V_{ch}}$ one obtain for 2D graphene[24]:

$$C_Q = \frac{2q^2 K_B T}{\pi(\hbar v_f)^2} Ln\left[2\left(1 + cosh\frac{qV_{ch}}{K_B T}\right)\right] \tag{3-35}$$

$$qV_{ch} = E_f \tag{3-36}$$

where ħ is the Planck constant, e the electron charge, K_B the Boltzmann constant, $v_f = \frac{C}{300}$ the Fermi velocity of the Dirac electron (The symbol *c* represents the speed of light in a vacuum), and $V_{ch} = \frac{E_f}{e}$ is the potential of graphene. When $eV_{ch} \gg K_B T$ equation number (37) reduced to below equation [23]:

$$C_Q = \frac{2e^2}{\hbar v_f \sqrt{\pi}} \sqrt{n} \qquad (3\text{-}37)$$

To gain a clearer understanding of the behaviour of this component, calculations were performed for both pristine graphene and graphene with an electrolyte gate at varying Na^+ concentrations. As expected, the presence of the aforementioned cation influences the Dirac point of graphene. Consequently, the minimum value of the capacitance, as shown in Figure 3-9, shifts toward lower voltages.

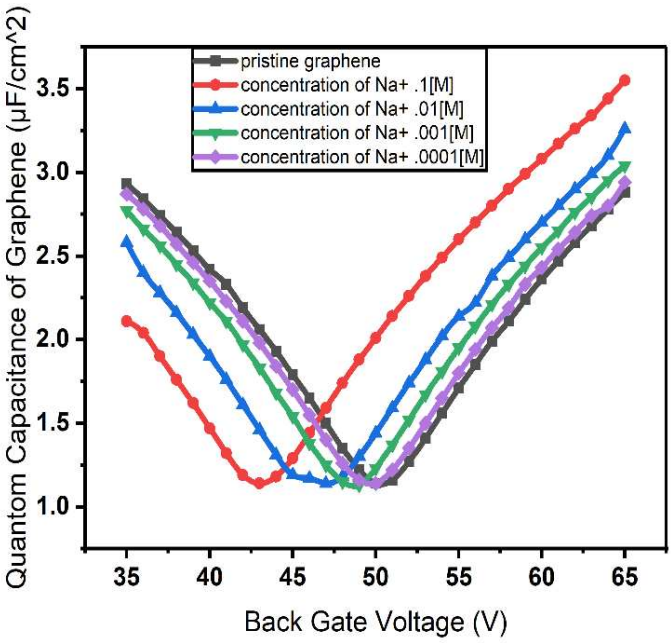

Figure 3-9. Quantum capacitance of graphene for different concentration of Na^+ versus gate voltage.

This capacitance is connected in series with the electric double layer (EDL) capacitance. Therefore, the top gate capacitance can be calculated using the following equation [26]:

$$\frac{1}{C_{top}} = \frac{1}{C_{EDL}} + \frac{1}{C_Q} \qquad (3\text{-}38)$$

Considering quantum capacitance, as illustrated in Figures 3-10(a-b), enhances the sensor's performance, particularly in terms of sensitivity. The Dirac point shift in this case is approximately 7.5 V, compared to 6 V and 4.75 V for the Stern model and the Gouy-Chapman model, respectively.

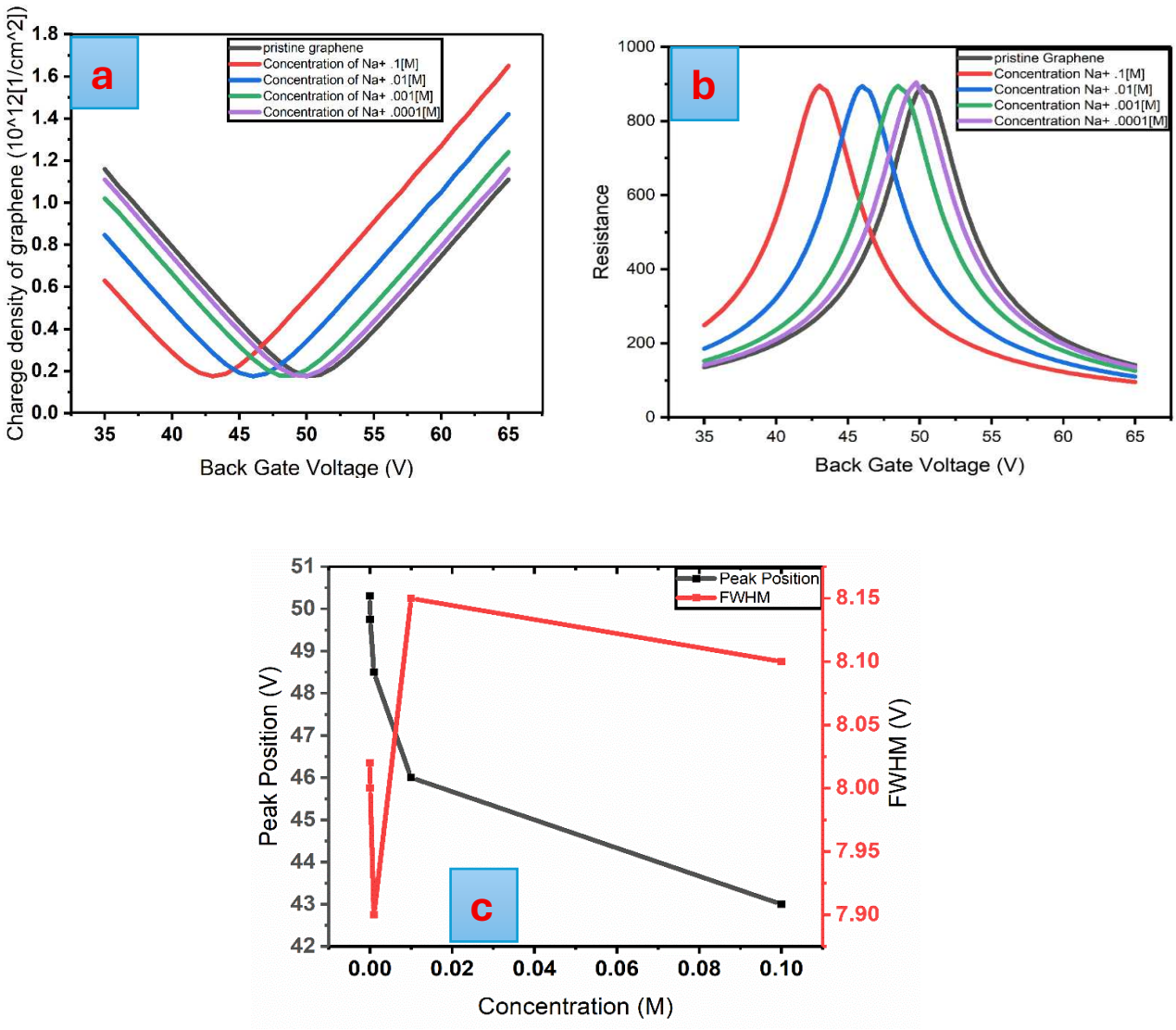

Figure 3-10- a) Charge concentration and 5-b) resistance of graphene channel as function gate voltage, calculated using the Stern model of EDL by considering impact of quantum capacitance of Graphene; (c) Position of the resistance peak and its full width at half maximum (FWHM) as functions of gate voltage.

3.6.2- Evaluation performance of GFET biosensor:

The performance of a biosensor can be evaluated using key parameters such as sensitivity, detection accuracy, and quality factor. For optimal biosensor performance, these parameters should be maximized. In this study, these metrics are derived from the resistance versus gate voltage (transfer) characteristics. Sensitivity (S) is defined as the shift in the Dirac point position of the graphene channel in response to a change in ion concentration. Mathematically, it is expressed as [27]:

$$S = \frac{\nabla V_{Dirac}}{\nabla C} \qquad (3\text{-}39)$$

Another key performance parameter of a biosensor is the Figure of Merit (FOM), which is closely related to the sensitivity (S) and the full width at half maximum (FWHM) of the resistance curve. The FWHM is defined as the voltage range between the points on the resistance curve where the resistance reaches half of its maximum value. It represents the effective bandwidth of the sensor's response. The Figure of Merit is typically expressed as [28]:

$$FOM = \frac{S}{FWHM} \tag{3-40}$$

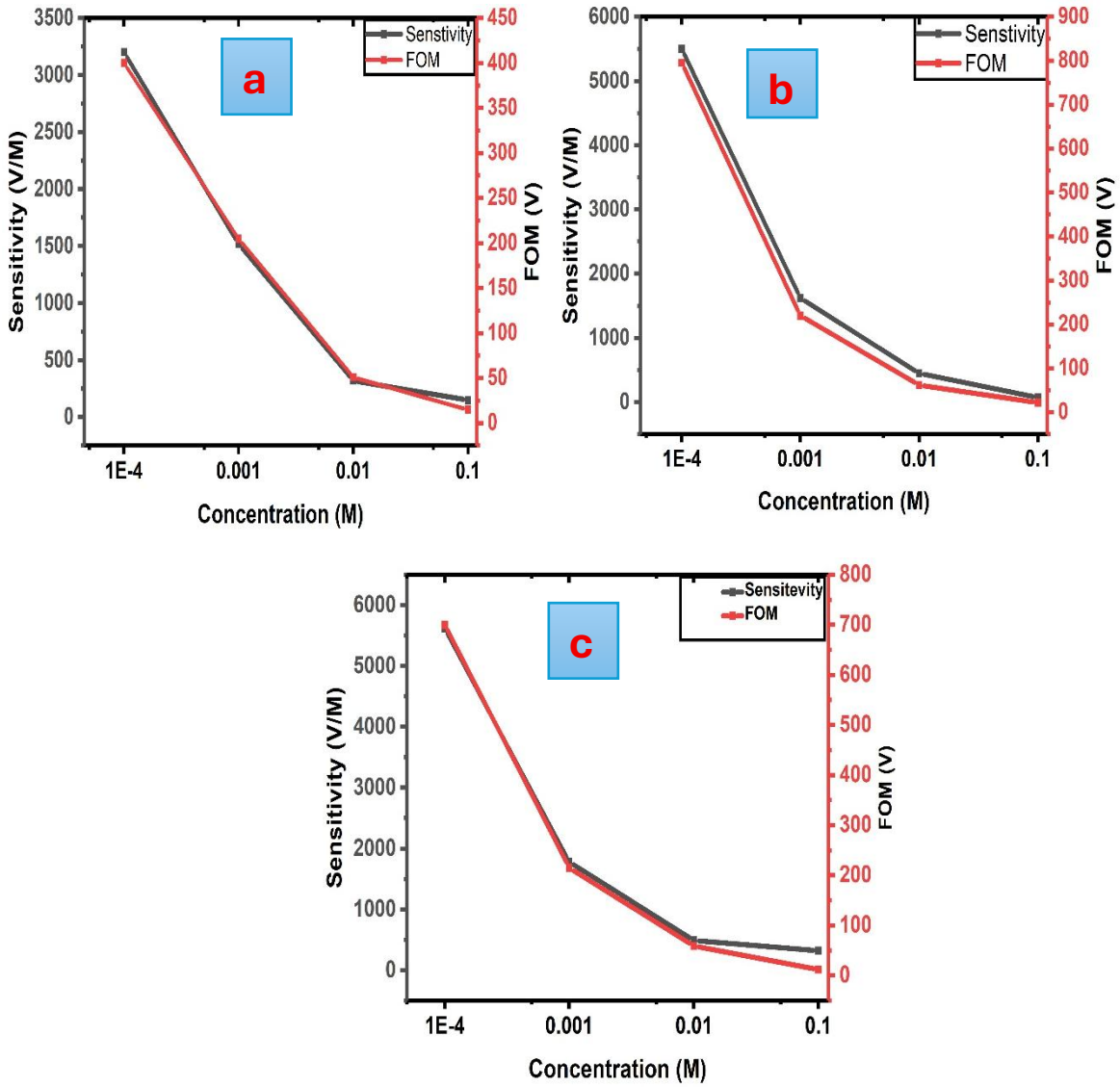

Figure 3-11. Sensor sensitivity and FOM as function of analyte concentration: a) Gouy-Chapman model of EDL b) Stern model of the EDL, and c) Stern model of EDL including the effect of graphene quantum capacitance.

By adopting more reliable models that consider all relevant factors affecting performance—as illustrated in Figure 8a–c-we can achieve improved sensitivity values of 3200 V/m, 5500 V/m, and 5600 V/m for the Gouy-Chapman model, the Stern model for the electric double layer (EDL), and the model incorporating quantum capacitance effects, respectively.

Table 3-1. GFET biosensor parameters computed for the Gouy-Chapman model of electric double layer

concentration	FWHM (V)	Sensitivity V/M)	FOM (V)
.0001 [M]	8.1	3200	400
.001 [M]	8.12	1520	205
.01 [M]	8.15	320	51
.1 [M]	7.9	150	15

Table3- 2. GFET biosensor parameters computed for the Stern model of electric double layer without considering quantum capacitance

concentration	FWHM (V)	Sensitivity (V/M)	FOM (V)
.0001 [M]	7	5500	795
.001 [M]	8.19	1620	220
.01 [M]	8.1	450	62
.1 [M]	8.15	75	22

Table 3-3. GFET biosensor parameters computed for the Stern model of electric double layer incorporating quantum capacitance

concentration	FWHM (V)	Sensitivity (V/M)	FOM (V)
.0001 [M]	7.97	5620	700
.001 [M]	7.9	1780	215
.01 [M]	8.13	490	59
.1 [M]	8.1	320	12

3-7 Conclusion:

In this work, we investigated the correlation between different models of the EDL in electrolytes and the sensitivity of graphene field-effect transistors, demonstrating the potential to tune their electronic properties by varying the concentration of Na^+ ions in the electrolyte gate. Furthermore, we included the quantum capacitance of graphene in a series configuration with the electric double layer, which allowed us to achieve higher sensitivity compared to using only the Gouy-Chapman and Stern models. More specifically, we showed that the resistance and charge carrier density of the graphene channel in Dirac point shifted from higher Dirac point potential to lower, this shift depended on concentration of Na^+ no surface of graphene channel and type of model which applied for EDL, that means increasing concentration of cation mentioned enhance this shit , meanwhile using proper model increase this parameter, proving that it is possible to predict the device behaviour in experiment approach by considering more realistic model for device. More specifically, we demonstrated that the resistance and charge carrier density at the Dirac point of the graphene channel shifted from a higher to a lower Dirac point potential. This shift depended on the concentration of Na^+ ions near the graphene surface and the specific electric double layer (EDL) model applied. An increase in Na^+ concentration enhanced this shift, and the use of more accurate EDL models further amplified the effect. These findings suggest that incorporating realistic models enables more accurate prediction of device behaviour in experimental settings.

Finally, we note that this model can be extended to different types of ions, as each ion possesses a specific ionic radius, which determines the Helmholtz capacitance, and a unique Debye length, which defines the Gouy-Chapman capacitance. Consequently, each ion type induces a distinct shift in the Dirac point of the graphene channel.

References:

[1]- Zhao, Weilong, et al. "Sensitivity-Enhancing Strategies of Graphene Field-Effect Transistor Biosensors for Biomarker Detection." *ACS sensors* 9.6 (2024): 2705-2727.

[2]- He, Qiyuan, et al. "Graphene-based electronic sensors." *Chemical Science* 3.6 (2012): 1764-1772.

[3]- Béraud, Anouk, et al. "Graphene field-effect transistors as bioanalytical sensors: Design, operation and performance." *Analyst* 146.2 (2021): 403-428.

[4]- Fu, Wangyang, et al. "Sensing at the surface of graphene field-effect transistors." *Advanced Materials* 29.6 (2017): 1603610.

[5]- Gongadze, E., Petersen, S., Beck, U., & Van Rienen, U. (2009, October). Classical Models of the Interface between an Electrode and an Electrolyte. In *COMSOL conference* (pp. 14-16).

[6]-Ivanov, Vladimir D. "The Helmholtz model." *Journal of Solid State Electrochemistry* 28.8 (2024): 2487-2493.

[7]- Bard, Allen J., Larry R. Faulkner, and Henry S. White. *Electrochemical methods: fundamentals and applications*. John Wiley & Sons, 2022.

[8]- Elliott, Joshua D., et al. "The electrochemical double layer at the graphene/aqueous electrolyte interface: what we can learn from simulations, experiments, and theory." *Journal of Materials Chemistry C* 10.41 (2022): 15225-15262.

[9]- Li, Xiang-Ying, et al. "Molecular understanding of the Helmholtz capacitance difference between Cu (100) and graphene electrodes." *The Journal of Chemical Physics* 158.8 (2023).

[10]- Grahame, David C. "The electrical double layer and the theory of electrocapillarity." *Chemical reviews* 41.3 (1947): 441-501.

[11]- Kirby, Brian J., and Ernest F. Hasselbrink Jr. "Zeta potential of microfluidic substrates: 1. Theory, experimental techniques, and effects on separations." *Electrophoresis* 25.2 (2004): 187-202.

[12]- Li, Su-zhen, and Ren-kou Xu. "Electrical double layers' interaction between oppositely charged particles as related to surface charge density and ionic strength." *Colloids and Surfaces A: Physicochemical and Engineering Aspects* 326.3 (2008): 157-161.

[13]- Nam, Kwang-Mo, and Byoung-Yong Chang. "Electrochemical impedance method to measure the potential of the outer Helmholtz plane." *Journal of The Electrochemical Society* 161.6 (2014): H379.

[14]-Kesler, Vladimir, Boris Murmann, and H. Tom Soh. "Going beyond the Debye length: overcoming charge screening limitations in next-generation bioelectronic sensors." *Acs Nano* 14.12 (2020): 16194-16201.

[15]- Huang, Jun. "Zooming into the inner helmholtz plane of Pt (111)–aqueous solution interfaces: Chemisorbed water and partially charged ions." *JACS Au* 3.2 (2023): 550-564

[16]- Meric, I., Han, M. Y., Young, A. F., Ozyilmaz, B., Kim, P., & Shepard, K. L. (2008). Current saturation in zero-bandgap, top-gated graphene field-effect transistors. *Nature nanotechnology*, *3*(11), 654-659.

[17]- Wu, Guangfu, Meyya Meyyappan, and King Wai Chiu Lai. "Simulation of graphene field-effect transistor biosensors for bacterial detection." *Sensors* 18.6 (2018): 1715.

[18]- Clericò, Vito. "Fabrication and characterization of quantum materials: graphene heterostructures and topological insulators." (2020)

[19]- Froehlicher, Guillaume, and Stéphane Berciaud. "Raman spectroscopy of electrochemically gated graphene transistors: Geometrical capacitance, electron-phonon, electron-electron, and electron-defect scattering." *Physical Review B* 91.20 (2015): 205413.

[20]- Meric, Inanc, et al. "Current saturation in zero-bandgap, top-gated graphene field-effect transistors." *Nature nanotechnology* 3.11 (2008): 654-659.

[21]- Elliott, Joshua D., et al. "The electrochemical double layer at the graphene/aqueous electrolyte interface: what we can learn from simulations, experiments, and theory." *Journal of Materials Chemistry C* 10.41 (2022): 15225-15262.

[22]- Zhang, Guigen. "Simulating the electrical double layer capacitance." *Excerpt from Proceedings of the COMSOL Conference. Boston*. 2010.

[23]- Xia, Jilin, et al. "Measurement of the quantum capacitance of graphene." *Nature nanotechnology* 4.8 (2009): 505-509.

[24]- Fang, Tian, et al. "Carrier statistics and quantum capacitance of graphene sheets and ribbons." *Applied Physics Letters* 91.9 (2007).

[25]- Thiele, S. A., J. A. Schaefer, and Frank Schwierz. "Modeling of graphene metal-oxide-semiconductor field-effect transistors with gapless large-area graphene channels." *Journal of Applied Physics* 107.9 (2010).

[26]- Ju, Wonbin, and Sungbae Lee. "Al back-gated graphene field-effect transistors for capacitive sensing applications based on quantum capacitance effect." *AIP Advances* 12.9 (2022).

[27]- Béraud, Anouk, et al. "Graphene field-effect transistors as bioanalytical sensors: Design, operation and performance." *Analyst* 146.2 (2021): 403-428.

[28]- Hajian, Hodjat, et al. "High-figure-of-merit biosensing and enhanced excitonic absorption in an MoS2-integrated dielectric metasurface." *Micromachines* 14.2 (2023): 370.

Chapter four:

Detection of β2-Microglobulin Using Graphene Field-Effect Transistors: Structural Insights and Electrical Response

4-1- Introduction:

Over the past few decades, progress in medical diagnostics and therapeutic approaches have considerably extended average human lifespan. In contrast, even with substantial advancement in treating variety diseases, some disorders continue to be strongly associated with aging. The worldwide prevalence of dementia and related neurodegenerative conditions is increasing continuously, and projections indicate that the number of affected individuals could two-fold every two decades, potentially increasing to 115 million by 2050[1].

Alzheimer's disease, Parkinson's disease, Creutzfeldt–Jakob disease, type II diabetes, and dialysis connected to amyloidosis are between the most common and serious disorders that are extensively observed, almost epidemic behave and usually absence curative therapies. These illnesses are related to a phenomenon called protein misfolding, in which proteins adopt incorrect conformations or lose the stable structures required to function correctly. Obtaining deeper knowledge of the molecular mechanisms that lead these structural abnormalities is crucial for designing effective treatments for this group of conditions, broadly classified as protein misfolding disorders [2].

β2-microglobulin (β2-m), a protein of significant biological and clinical relevance, was first recognised in 1964 during studies of urine samples from individuals with Wilson's disease [3]. Considering its molecular structure, β2-m shows the characteristic secondary and tertiary architecture of immunoglobulin-like proteins and normally connected with the heavy chain of main histocompatibility complex class I (MHC-I), which exists on the surface of all nucleated cells. The binding of β2-m to MHC-I is crucial for efficient immune function [4]. Including of 99 amino acids and consisting of a molecular mass of approximately 11.4 kDa, β2-m forms a structure composed of seven antiparallel β-strands organized into a β-sandwich configuration. This structure is stabilized by a disulfide bridge between cysteine residues at positions 25 and 80. Beyond it's a connection with MHC-I, β2-m is also able to interact with additional molecules that play crucial role in mucosal immunity and tumor surveillance.

Disruptions in these molecular interactions are mainly related to kidney-related conditions on the other hand may also have an impact in systemic disorders. In healthy individuals, β2-m is efficiently removed by the kidneys following its release from MHC-I. Meanwhile, patients with reduced renal function, specifically those on long-term hemodialysis, may exhibit a 60-fold enhancement in serum β2-m levels [5]. This high accumulation increases the formation of fibrillar deposits in osteoarticular tissues, leading to dialysis-associated amyloidosis (DRA), a disease defined by joint degeneration and bone fractures [6]. In patient, amyloid deposits in DRA

predominantly includes wild-type β2-m (approximately 70%), with the remaining 30% comprising a truncated form referred to as ΔN6 β2-m [7,8].

The adsorption of proteins onto surfaces is a fundamental phenomenon over various biomedical applications, such as design of implants, tissue engineering, and strategies for immobilizing proteins on solid supports-like lab-on-a-chip devices and diagnostic biosensors [9,10,11]. This function is extremely complicated, needing an in-profound understanding of molecular-level interactions. Parameters in the surrounding environment, such as temperature, pH, and ionic strength, can extremely impact adsorption behave. Proteins themselves may also undergo conformational alters upon interacting with a surface. Moreover, the characteristics of the surface-whether inorganic or chemically modified-are vital, with associated including surface energy, charge, polarity, and topography all affecting the adsorption process.

When a protein approaches a surface, it commonly assumes a specific orientation, which shows which parts of the molecule interact with the surface and which remain exposed to the surrounding solution [11]. This orientation is affected by the biomolecule's size and structural complexity. In environments with extreme molecular density, adsorption becomes more competitive, with both interactions between the protein and the surface and between neighbouring proteins shaping the final configuration.

Amyloid-forming proteins and peptides have been widely studied for their interactions with numerous nanoparticles (NPs) and surfaces [12,13]. Factors include the material type, particle size, and the sequence and properties of the protein or peptide can considerably affect the results, driving to either a considerable boost [15,16] or complete inhibition of fibril formation [17–18]. The pathological aggregation of β2-microglobulin (β2-m) depended on dialysis-related amyloidosis (DRA), a disorder generally recognised in patients receiving long-term hemodialysis. For this circumstance, insoluble fibrils predominantly accumulate in bones, ligaments, and joints. While β2-m acts as an extensively implemented model for amyloid formation, the early stages of its aggregation are still unexplored. Specifically, the process, which β2-m interacts with surfaces and nanoparticles require further investigation. Notably, Linse et al. [19] demonstrated that exposure of β2-m to different NPs can significantly accelerate its fibrillation.

In a similar context of material–protein interactions, graphite-an allotrope of carbon consisting of sp^2-hybridized atoms-presents desirable physicochemical properties for interfacing with biomolecules, in contrast its use is restricted by limited biocompatibility and low water solubility [20]. The extensive conjugation within graphite's two-dimensional graphene layers, which stack to

form its three-dimensional structure, creates a highly reactive surface with unique electronic and structural properties. These characteristics allow graphite to interact with proteins in a way that can alter both the speed of fibril formation and the architecture of the resulting amyloid fibrils.

Raffaini and Ganazzoli investigated the interaction between graphite and different globular proteins-such as albumin [21, 22], fibronectin [23], and lysozyme [24]-each with unique structural characteristics. Applying simulations that employed a Morse potential to model the carbon-protein interactions on graphite, they recognised that these proteins communally show a high tendency to adsorb onto the graphitic surface. This adsorption often drives to partial unfolding or complete adherence of the proteins to the hydrophobic layer.

In this study, COMSOL Multiphysics is employed to model the detection of β2-microglobulin (β2-m) using a graphene-based field-effect transistor (GFET). The focus is on the wild-type conformation of β2-microglobulin, which represents the most prevalent structural form found in nature. The primary objective is to investigate the initial stages of interaction between β2-m and the graphene surface, with particular attention to the conformational changes that occur in the monomeric unit upon adsorption.

Graphene, a single atomic layer of sp^2-hybridized carbon atoms, exhibits unique electronic feature compared to bulk graphite [25]. A graphene field-effect transistor (GFET) can be applied to detect β_2-microglobulin (β_2M) by leveraging the same electrostatic sensing mechanisms used in ion detection (e.g., Na^+), but with specificity toward the protein's unique charge distribution and structure [First paper reference].

Graphene's large surface area, excellent carrier mobility, and high sensitivity to local electrostatic changes make it a highly demanded platform for biosensing applications. As β_2-microglobulin (β_2M) molecules approach the graphene surface, their net charge at physiological pH generates a local electric field. This field alters the carrier density within the graphene channel, producing measurable alters in conductivity or threshold voltage of field-effect modulation. While the mechanism is like ion sensing, it is more complex due to the protein's size, shape, and heterogeneous charge distribution [26].

β_2M is a 12 kDa protein with an approximate diameter of 3–4 nanometres. However, unlike small ions, the protein may interact with the surface through more complex mechanisms, such as partial unfolding or specific binding, which can partially impact the local dielectric environment and capacitance. Molecular dynamics simulations conducted by G. Brancolini et al. exhibit that the

radius of a β₂-microglobulin (β2M) is approximately 14.23 Å in water and 14.13 Å on a graphite surface. Experimentally, the folded monomer of β2M has a radius in the range of 12–15 Å, related on its conformation and the measurement method. At physiological ionic strength (e.g., 50 mM), the protein's net negative charge significantly perturbs the Helmholtz potential near the graphene surface. Under these conditions, wild-type β₂M carries a net charge of -2, which further supports its detectability using graphene field-effect transistor (GFET)-based sensing platforms. [26].

Atomistic molecular dynamics simulations indicate that β₂-microglobulin (β₂M) adopts a horizontal orientation when adsorbed onto the graphene surface. The main interface for this interaction is a patch comprising the C strand (Ile35, Val37, Leu39), the C′ strand (Glu44, Arg45), and the CD loop (Ile46, Lys48). Within this region, Glu44 carries a negative charge, Arg45 and Lys48 are positively charged, and Ile35, Val37, Leu39, and Ile46 are neutral hydrophobic residues [26].

Among the proteins of clinical interest, β₂-microglobulin (β₂M) represents an important biomarker in several pathological conditions. β₂M is a small (≈11.8 kDa) non-glycosylated protein that forms the light chain of major histocompatibility complex class I (MHC-I) molecules present on the surface of nearly all nucleated cells.[27] It is continuously released into the bloodstream during normal cellular turnover and is primarily cleared through glomerular filtration followed by tubular reabsorption in the kidneys.[28] As a consequence, circulating β₂M levels are strongly correlated with renal function. In healthy individuals, serum β₂M concentrations typically range between 1 and 3 mg/L, whereas significantly elevated levels are observed in patients with renal impairment, inflammatory disorders, and hematological diseases.[26] In individuals undergoing long-term hemodialysis, β₂M concentrations may increase dramatically, often reaching 20–60 mg/L or higher, which can lead to protein aggregation and the development of dialysis-related amyloidosis [29]. Moreover, β₂M is widely used as a prognostic biomarker in diseases such as multiple myeloma and lymphoma, where its serum concentration correlates with disease stage and tumor burden.[30] Due to its strong clinical relevance and the need for sensitive and rapid detection methods, β₂M represents a valuable target for biosensing technologies. To date, previous studies have examined the behavior of this amyloidogenic proteins in the presence of different surfaces [31,33].

The combination of electrostatic and hydrophobic interactions facilitates stable and specific adsorption of β₂-microglobulin (β₂M) onto the graphene surface. Upon adsorption, the protein induces a localized change in the graphene's surface potential, producing a measurable and distinctive electrical signal. These alterations in the electrostatic environment can be detected as changes in the graphene field-effect transistor (GFET)'s conductivity or threshold voltage,

highlighting β2M as a promising target for sensitive, label-free detection [26]. **Figure 4-1** shows both 3D and 2D schematics of the GFET setup.

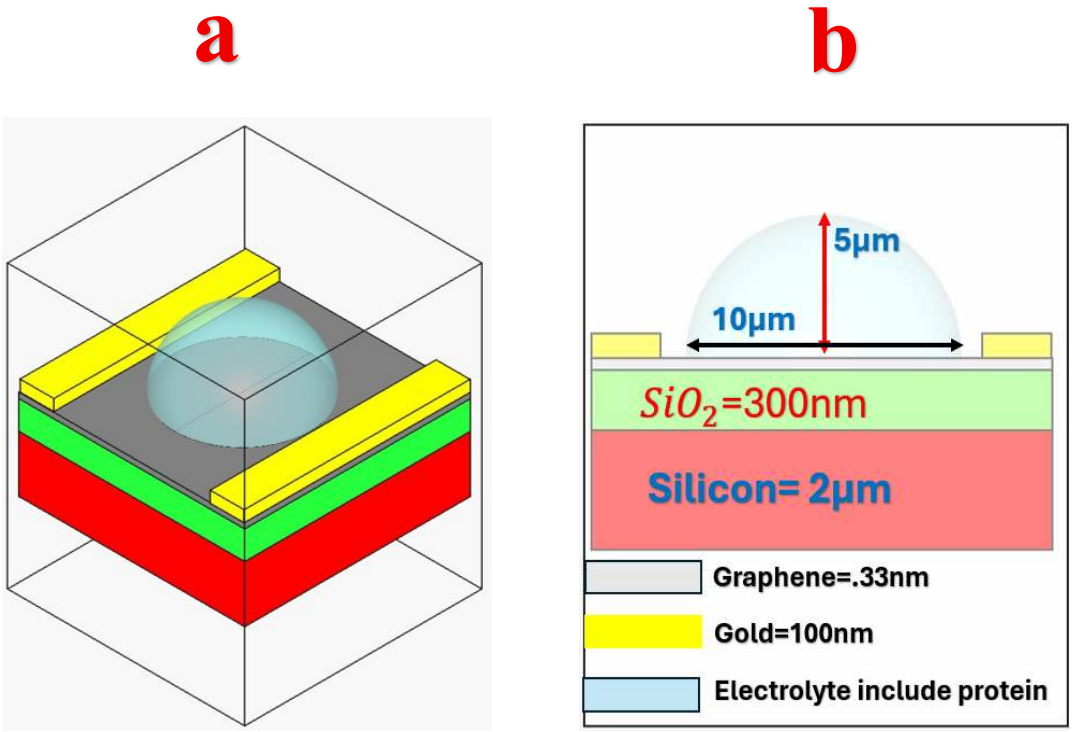

Figure 4-1. a) Schematic diagram of a graphene field-effect transistor (GFET) gated by an electrolyte. (b) cross sectional view of the device

4-2- Theory:

In this chapter, we adapted the theoretical framework previously developed in Chapter Three for Na^+ ion detection to the detection of β2-microglobulin protein using a graphene-based electrolyte-gated field-effect transistor (EGFET). The approach models how protein adsorption at the graphene–electrolyte interface modifies the local electric potential, leading to changes in the charge density of the graphene channel through the formation of an electric double layer (EDL). The EDL is described using the Stern model, which combines a compact Helmholtz layer and a diffuse Gouy–Chapman layer to capture both the immediate and spatially distributed ionic effects. In addition, the unique quantum capacitance of graphene is considered, as it significantly influences the total capacitance in two-dimensional materials and impacts the device's response to target molecules. Numerical simulations account for the combined effects of top-gate and back-gate voltages, the EDL structure, and graphene's quantum capacitance to estimate carrier concentrations and surface potential changes in response to protein adsorption. Finally, key sensor performance metrics, including sensitivity, figure of merit, signal-to-noise ratio, and detection accuracy, are evaluated based on the shifts in the Dirac point induced by the presence of β2-microglobulin, enabling a quantitative assessment of the biosensor's functionality.

4-3- Results and discussion:

As an initial step in our numerical investigation, we examined the electric potential profile across the electrical double layer by considering variety β₂-microglobulin concentrations and varying distance from the graphene-electrolyte interface. Since this potential it has significant role in the overall framework approach and examined how the potential changes with distance from the electrode–electrolyte boundary and different concentrations. The corresponding simulation results, shown in Figure 2, follow the pattern predicted by Equation (1).

$$\varphi(x) = \varphi_0(x)\exp\left(\frac{-x}{\lambda_D}\right) \qquad (4\text{-}1)$$

According to Debye–Hückel theory, the Debye length λ_D, characterizes the typical extent of the ionic atmosphere around a central ion and can be expressed by using the following relation [46]:

$$\lambda_D = \sqrt{\frac{\varepsilon_r \varepsilon_0 T K_B}{e^2 \sum Z_{\pm}^2 c_{\pm}^{\infty}}} \qquad (4\text{-}2)$$

The expression $I = \mu = 1/2 \sum c_i^{\pm} Z^2$ introduced by Lewis and Randall, is used to quantify the impact of charge and interionic interactions on the behave of electrolytes, known as the bulk ionic strength [47,48].

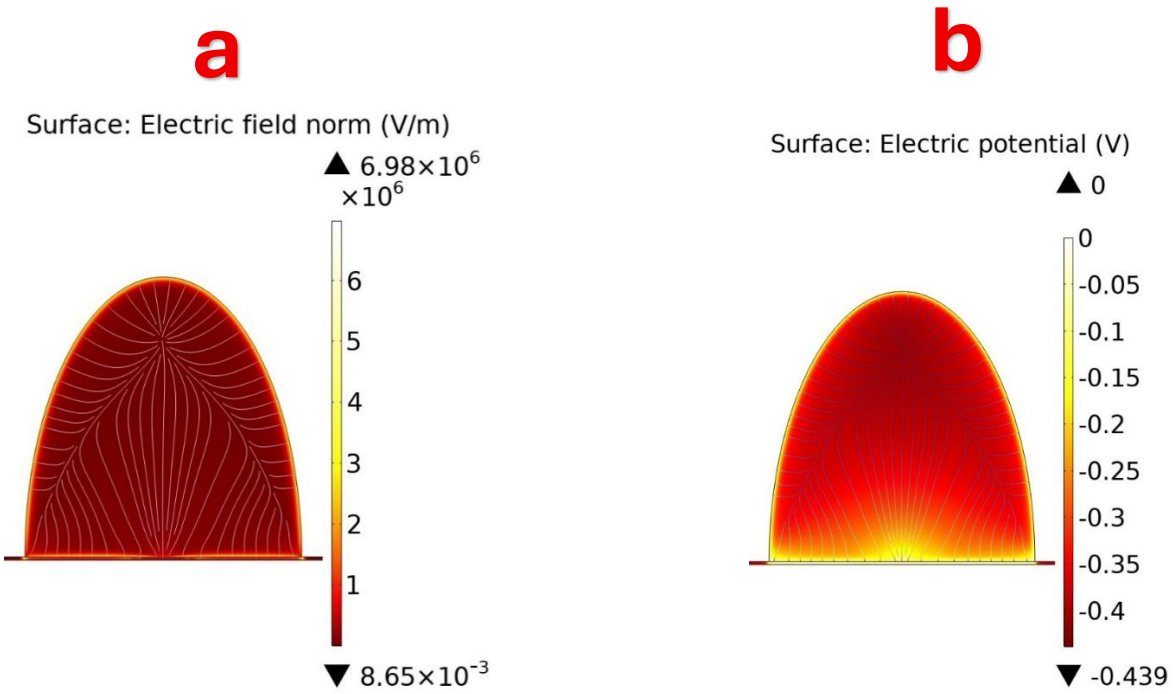

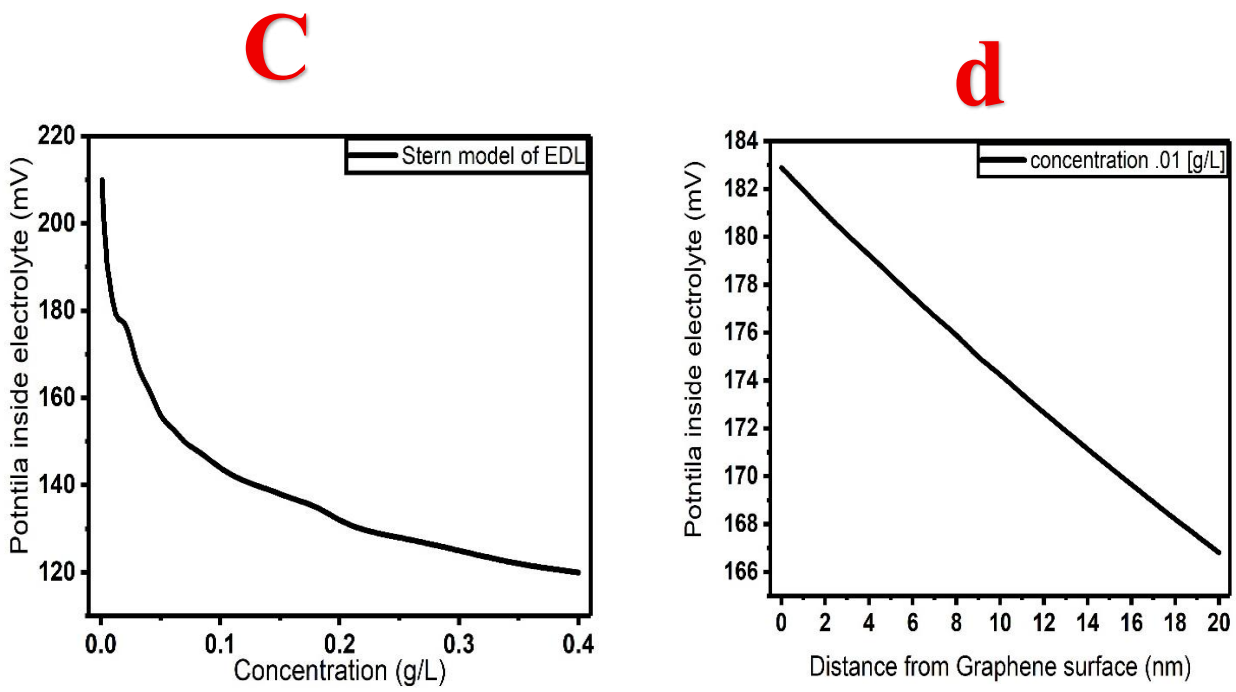

Figure 4- 2. Simulation of (a) electric field and (b) electrical potential at the interface between graphene and an electrolyte containing 0.01 g/L β2-microglobulin. The electrical double layer (EDL) is modeled using the Stern model. Electrolyte potential profiles in the Stern model of the EDL for β2-microglobulin: (c) at different β2-microglobulin concentrations (distance from graphene surface 1nm); and (d) at varying distances from the graphene interface (concentration .01g/L).

Increasing β2-microglobulin concentration reduces the Debye length, which in turn decreases the electrostatic potential, as described by Eq. (1). Additionally, moving farther from the graphene-electrolyte interface leads to a progressive decay of the potential, consistent with the exponential behavior predicted by the same equation. According to this equation, the trends in both graphs 4-2(c) and 4-2(d) are expected to exhibit exponential decay. However, this pattern is not observed at certain distances. This deviation arises from computations performed near the graphene-electrolyte interface, where the potential exhibits a predominantly linear behavior rather than the expected exponential decay.

In the next step, we calculate the current between o of the graphene channel between drain and source for different concentrations of β2-microglobulin adsorbed on its surface. The concentration range was selected from 0.001 g/L to 0.4 g/L, as it is clinically relevant for medical diagnostics. Figures 4-3(a) and 4-3(b) illustrate the variations in current and position of Dirac point and full width half maximum, respectively, as a function of β2-microglobulin concentration.

a b

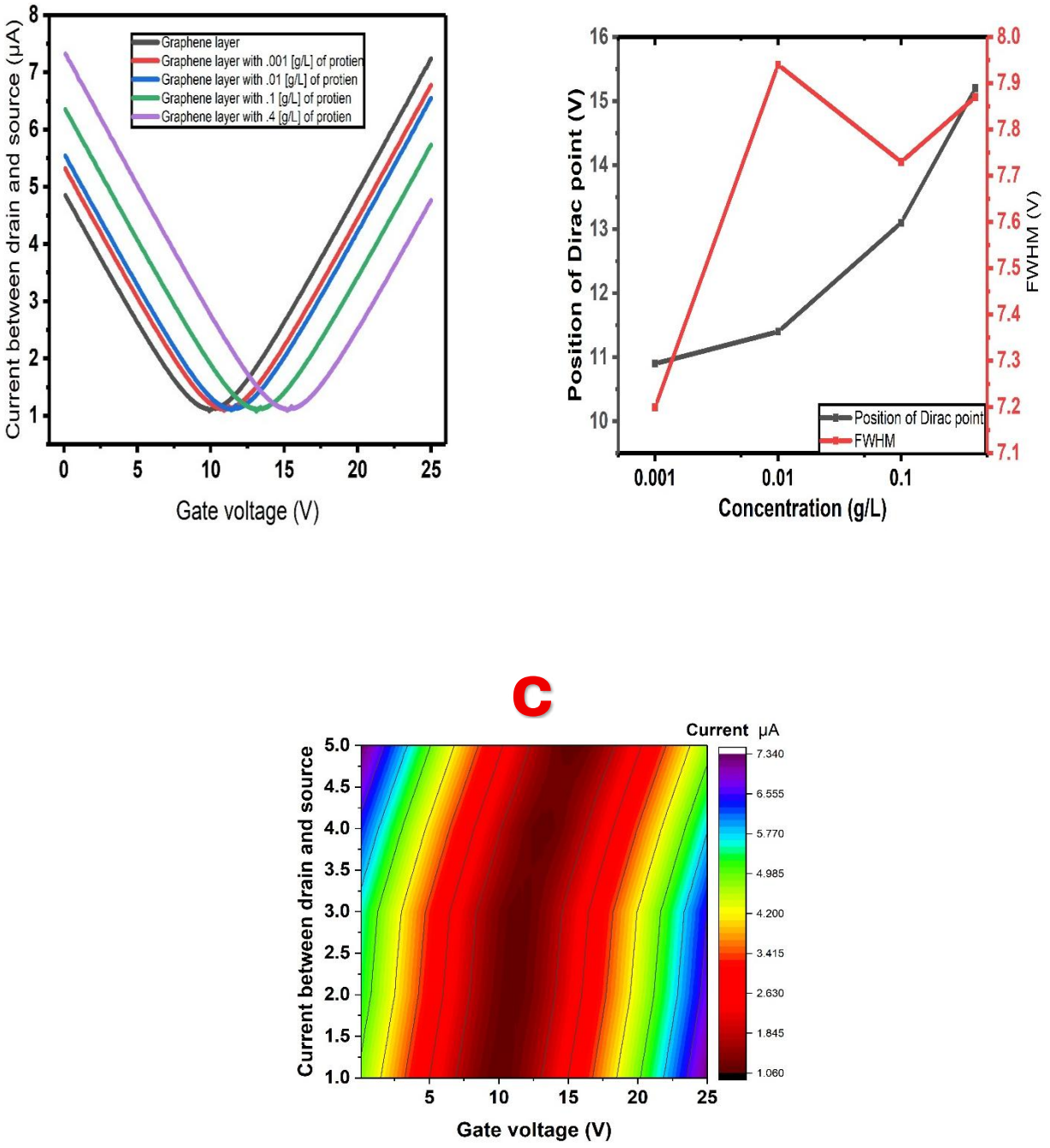

Figure 4-3. (a) Drain–source current of the graphene channel as a function of back-gate voltage, calculated using the Stern model of the electrical double layer (EDL). (b) Dirac point position and its full width at half maximum (FWHM) as functions of concentration. (c) Colour map of the drain–source current as a function of gate voltage

Because β_2-microglobulin (β_2M) carries a net charge of approximately -2 under the experimental pH conditions, its adsorption onto the graphene surface induces an electrostatic gating effect. This negative surface charge density alters the local carrier distribution within the graphene channel, resulting in a shift of the Dirac point toward more positive gate voltages. The observed positive displacement of the Dirac voltage reflects an effective p-doping behavior, as additional gate bias is required to re-establish charge neutrality in the presence of the negatively charged protein layer.

Furthermore, increasing the concentration of β_2-microglobulin enhances surface coverage and amplifies the interfacial charge density. As a consequence, the magnitude of the Dirac point shift increases proportionally with protein concentration, demonstrating a concentration-dependent modulation of graphene's electronic properties. This relationship suggests that the sensor response is governed by electrostatic interactions between the charged biomolecules and the graphene channel, highlighting the sensitivity of graphene-based field-effect devices to variations in biomolecular surface charge density.

In conventional graphene field-effect transistors (GFETs) incorporating relatively thick gate dielectrics, for example 300 nm thermally grown SiO_2, the overall gate capacitance is dominated by the geometrical capacitance of the oxide layer, while the quantum capacitance of graphene can be reasonably neglected in a first-order approximation. In contrast, emerging device configurations employ substantially thinner high-κ dielectric materials, leading to enhanced gate capacitance and lower operating voltages. In such architectures, the quantum capacitance of graphene becomes comparable to the oxide capacitance and therefore significantly influences the electrostatic response of the device.

Accordingly, in our analysis the graphene quantum capacitance is treated as a series capacitance in combination with the electric double-layer capacitance at the electrolyte interface. Based on this model, we calculate the electrostatic potential distribution within the electrolyte for various ionic concentrations and separation distances, as illustrated in Figure 4-4.

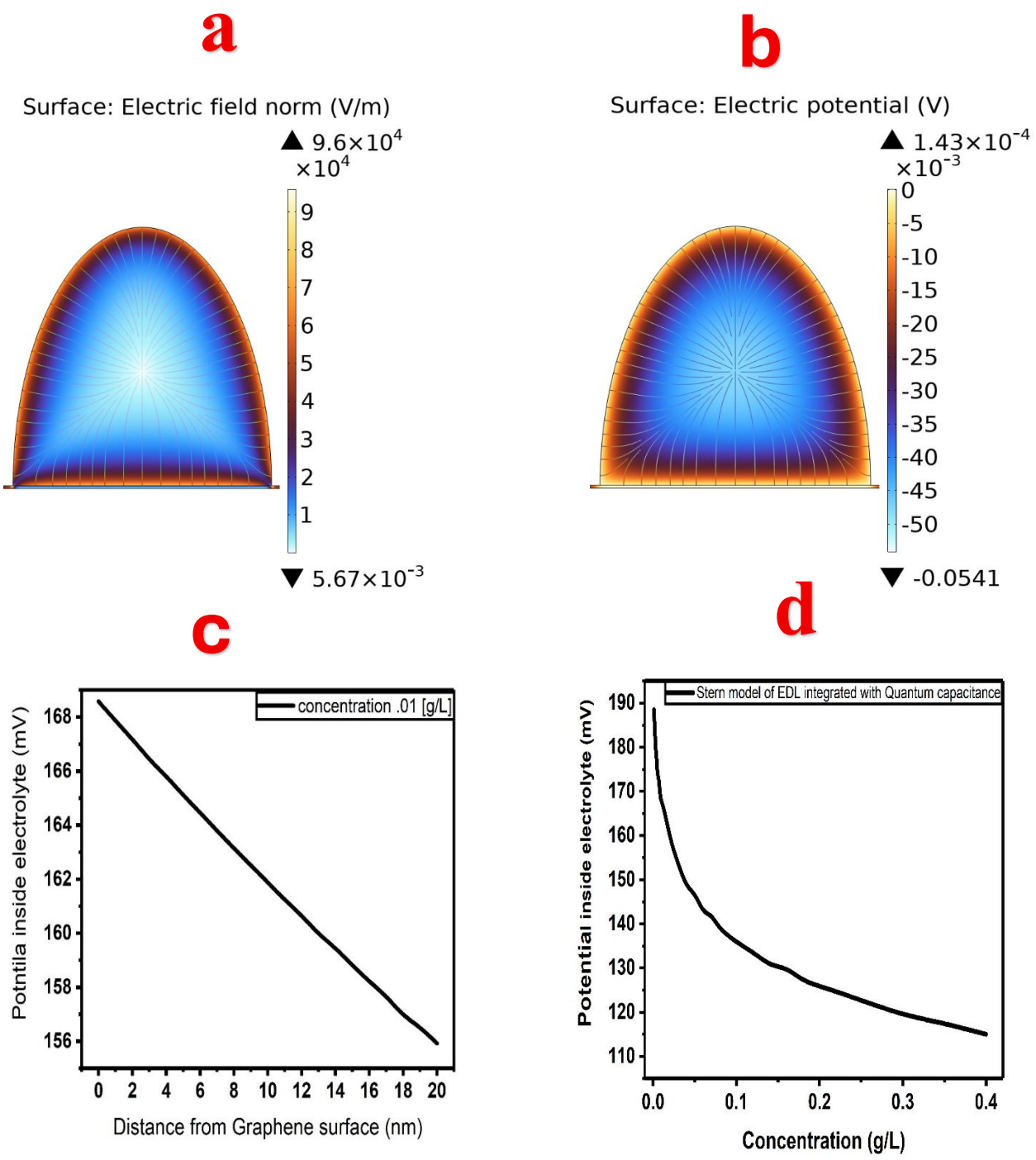

Figure 4-4. Simulated electrostatic characteristics at the graphene/electrolyte interface in the presence of 0.01 g/L β₂-microglobulin. (a) Electric field distribution and (b) electric potential profile calculated using the Stern model of the electrical double layer (EDL), incorporating graphene quantum capacitance in a series configuration. (c) Electrolyte potential profiles at varying β₂-microglobulin concentrations (evaluated at 1 nm from the graphene surface). (d) Electrolyte potential as a function of distance from the graphene interface at a fixed concentration of 0.01 g/L.

The computational results indicate that, upon incorporating quantum capacitance into the model, the electrostatic potential difference between the electrolyte and the graphene surface decreases. However, the Dirac point shift-being directly dependent on both the interfacial potential and the total capacitance-exhibits an overall increase. This behavior arises because the inclusion of quantum

capacitance increases the effective total capacitance of the system. The enhancement in total capacitance has a more significant influence on the Dirac point shift than the reduction in interfacial potential. For example, at a concentration of 0.4 g/L, the Dirac point shift predicted by the Stern model is 5.2 V, whereas inclusion of quantum capacitance increases this value to 5.7 V. These results highlight the critical role of quantum capacitance in accurately describing the electrostatic response of graphene-based systems.

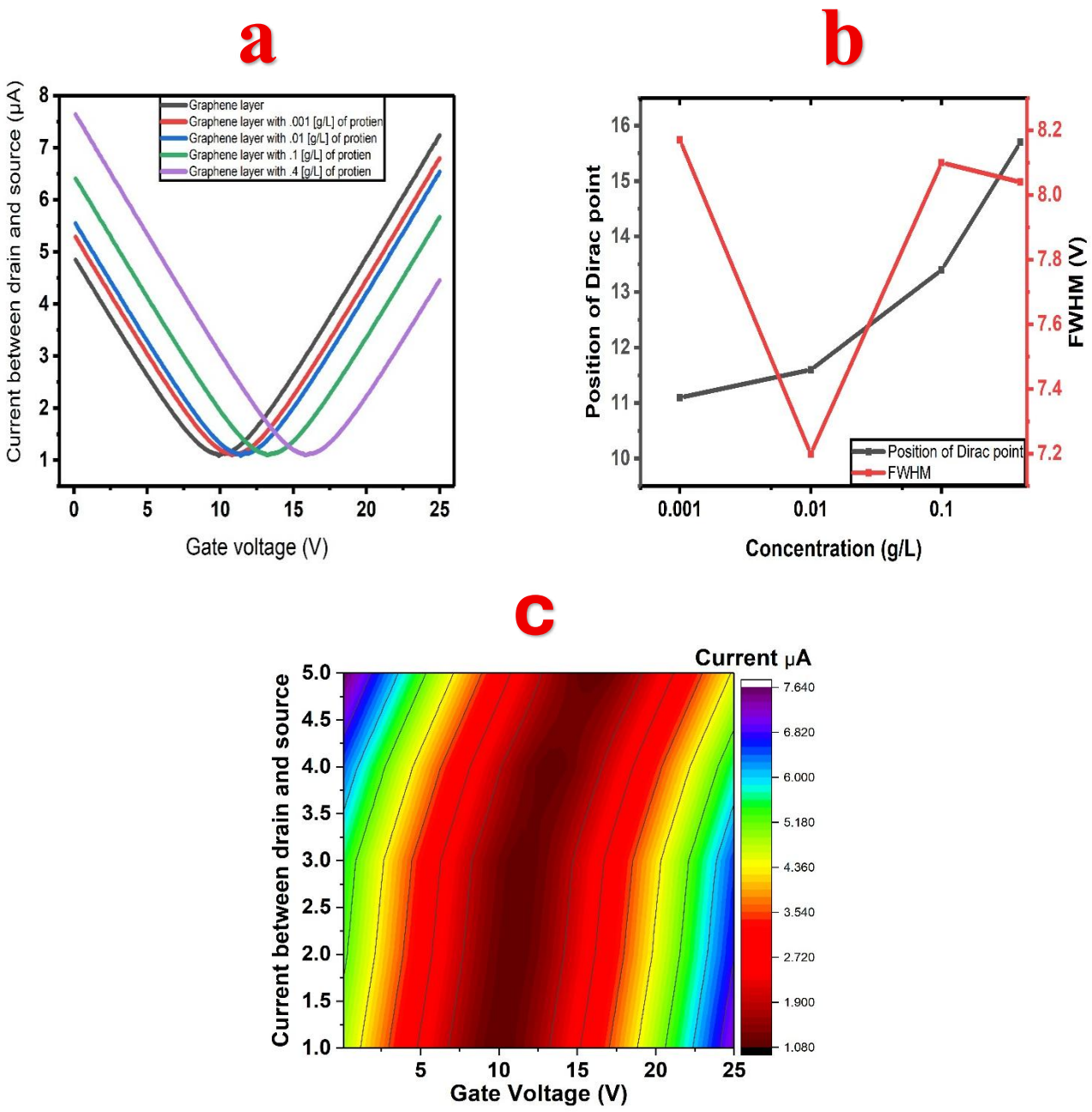

Figure 4-5. (a) Drain–source current of the graphene channel as a function of back-gate voltage, calculated using the Stern model of the electrical double layer (EDL) by considering impact of quantum capacitance. (b) Dirac point

position and its full width at half maximum (FWHM) as functions of concentration. (c) Colour map of the drain–source current as a function of gate voltage

The key performance metrics used to evaluate sensor effectiveness are summarized in Table 1. The results demonstrate that incorporating quantum capacitance into the electrical double layer (EDL) framework of the Stern model significantly enhances sensor sensitivity, which is one of the most critical performance parameters. For example, at a concentration of 0.001 g/L, the sensitivity increases to 200 $V \cdot L \cdot g^{-1}$ when quantum capacitance is taken into account. These findings further emphasize the importance of including quantum capacitance effects for accurate performance assessment of graphene-based sensors.

Sensor parameters performance	C=.4 g/L		C=.001g/L	
	EDL in Stern model	EDL + quantom capacitance	EDL in Stern model	EDL + quantom capacitance
S (V*L/g)	13	14.25	900	1100
FOM (L/g)	1.65	1.77	125	134
SNR	.708	.66	.125	.134
DA (1/V)	.127	.124	.138	.122

Table 4- 1. Key parameters influencing the performance of the graphene field effect transistor (GFET) sensor for different electrical double layer (EDL) models at two concentrations of β_2-microglobulin. The table compares sensor performance metrics including sensitivity (S), figure of merit (FOM), quality, signal-to-noise ratio (SNR), and detection accuracy (DA), highlighting the influence of the EDL model and biomolecule concentration on overall sensor performance.

4-4- Conclusions:

we have demonstrated a graphene-based field-effect transistor (GFET) biosensor for the sensing of β2-microglobulin (β2M) at different concentrations. The target protein was considered as a charged ionic species with a defined effective size and electric charge, enabling a physics-based description of its electrostatic interaction with the graphene surface. Numerical simulations present that

alteration in β2-microglobulin concentration induce a measurable shift in the Dirac point of graphene. Due to the negative charge of the protein, the Dirac voltage shifts toward higher gate voltages, showing effective p-type doping pattern. Meanwhile, increasing the protein concentration results in a progressively larger Dirac point shift, proving the concentration-dependent response of the proposed sensor.

In addition, the impact of graphene quantum capacitance was systematically investigated. The results show that incorporating quantum capacitance-beyond the conventional electrical double-layer (EDL) Stern model-modifies the overall interfacial electrostatics and significantly enhance the sensor's figure of merit (FOM). For instance, at a concentration of 0.001 g/L, the FOM increases from 125 to 134 when quantum capacitance is integrated. This enhancement highlights the vital role of graphene's intrinsic electronic properties in accurately predicting and optimizing biosensor performance.

In summary, the presented GFET-based biosensor architecture demonstrates high potential for physiological and clinical applications, specifically for the sensitive detection of protein biomarkers. By combining electrochemical double-layer modelling with graphene quantum capacitance effects, the proposed

approach provides a more comprehensive framework for designing high-sensitivity, label-free biosensors with tunable electrical response and enhanced detection capability.

References:

[1]- Prince, Martin, Maëlenn Guerchet, and Matthew Prina. "The global impact of dementia 2013-2050." (2013).

[2]- Tartaglia, Gian Gaetano, et al. "Life on the edge: a link between gene expression levels and aggregation rates of human proteins." *Trends in biochemical sciences* 32.5 (2007): 204-206.

[3]- Berggård, I., and A. G. Bearn. "Isolation and properties of a low molecular weight β2-globulin occurring in human biological fluids." *Journal of Biological Chemistry* 243.15 (1968): 4095-4103.

[4]- Cox, Josephine H., et al. "Antigen presentation requires transport of MHC class I molecules from the endoplasmic reticulum." *Science* 247.4943 (1990): 715-718.

[5]- Eichner, Timo, and Sheena E. Radford. "Understanding the complex mechanisms of β2-microglobulin amyloid assembly." *The FEBS journal* 278.20 (2011): 3868-3883.

[6]- Inoue, Sadayuki, et al. "Ultrastructural organization of hemodialysis-associated β2-microglobulin amyloid fibrils." *Kidney international* 52.6 (1997): 1543-1549.

[7]- Stoppini, Monica, and Vittorio Bellotti. "Systemic amyloidosis: lessons from β2-microglobulin." *Journal of biological chemistry* 290.16 (2015): 9951-9958.

[8]- Corazza, Alessandra, et al. "Native-unlike long-lived intermediates along the folding pathway of the amyloidogenic protein β2-microglobulin revealed by real-time two-dimensional NMR." *Journal of Biological Chemistry* 285.8 (2010): 5827-5835.

[9]-Lafleur, Josiane P., et al. "Recent advances in lab-on-a-chip for biosensing applications." *Biosensors and Bioelectronics* 76 (2016): 213-233.

[10]- Bhakta, Samir A., et al. "Protein adsorption onto nanomaterials for the development of biosensors and analytical devices: A review." *Analytica chimica acta* 872 (2015): 7-25.

[11]- Ozboyaci, Musa, et al. "Modeling and simulation of protein–surface interactions: achievements and challenges." *Quarterly reviews of biophysics* 49 (2016): e4.

[12]- Brancolini, Giorgia, et al. "The interaction of peptides and proteins with nanostructures surfaces: a challenge for nanoscience." *Current Opinion in Colloid & Interface Science* 41 (2019): 86-94.

[13]- John, Torsten, et al. "Impact of nanoparticles on amyloid peptide and protein aggregation: a review with a focus on gold nanoparticles." *Nanoscale* 10.45 (2018): 20894-20913.

[14]- Gladytz, Anika, Bernd Abel, and Herre Jelger Risselada. "Gold-induced fibril growth: the mechanism of surface-facilitated amyloid aggregation." *Angewandte Chemie International Edition* 55.37 (2016): 11242-11246.

[15]- Gladytz, Anika, et al. "Structure-making effects of metal nanoparticles in amyloid peptide fibrillation." *Particle & Particle Systems Characterization* 32.5 (2015): 573-582.

[16]- Álvarez, Yanina D., et al. "Influence of gold nanoparticles on the kinetics of α-synuclein aggregation." *Nano letters* 13.12 (2013): 6156-6163.

[17]- Liao, Yi-Hung, et al. "Negatively charged gold nanoparticles inhibit Alzheimer's amyloid-β fibrillization, induce fibril dissociation, and mitigate neurotoxicity." *Small* 8.23 (2012): 3631-3639.

[18]- Wang, Miaoyi, et al. "Differential effects of silver and iron oxide nanoparticles on IAPP amyloid aggregation." *Biomaterials science* 5.3 (2017): 485-493.

[19]- Linse, Sara, et al. "Nucleation of protein fibrillation by nanoparticles." *Proceedings of the National Academy of Sciences* 104.21 (2007): 8691-8696.

[20]-Mücksch, Christian, and Herbert M. Urbassek. "Molecular dynamics simulation of free and forced BSA adsorption on a hydrophobic graphite surface." *Langmuir* 27.21 (2011): 12938-12943.

[21]- Raffaini, Giuseppina, and Fabio Ganazzoli. "Simulation study of the interaction of some albumin subdomains with a flat graphite surface." *Langmuir* 19.8 (2003): 3403-3412.

[22]- Raffaini, Giuseppina, and Fabio Ganazzoli. "Adsorption of charged albumin subdomains on a graphite surface." *Journal of Biomedical Materials Research Part A: An Official Journal of The Society for Biomaterials, The Japanese Society for Biomaterials, and The Australian Society for Biomaterials and the Korean Society for Biomaterials* 76.3 (2006): 638-645.

[23]- Raffaini, Giuseppina, and Fabio Ganazzoli. "Molecular dynamics simulation of the adsorption of a fibronectin module on a graphite surface." *Langmuir* 20.8 (2004): 3371-3378.

[24]- Raffaini, Giuseppina, and Fabio Ganazzoli. "Protein adsorption on a hydrophobic surface: a molecular dynamics study of lysozyme on graphite." *Langmuir* 26.8 (2010): 5679-5689.

[25]- Reddy, Dharmendar, et al. "Graphene field-effect transistors." *Journal of Physics D: Applied Physics* 44.31 (2011): 313001.

[26]- Male, MARIA CELESTE. "Modeling of an amyloidogenic protein in solution and on surfaces." (2019).

[27]- Mage, Michael G., et al. "A recombinant, soluble, single-chain class I major histocompatibility complex molecule with biological activity." *Proceedings of the National Academy of Sciences* 89.22 (1992): 10658-10662.

[28]- Amici, Gianpaolo, et al. "Serum beta-2-microglobulin level and residual renal function in peritoneal dialysis." *Nephron* 65.3 (1993): 469-471.

[29]- Bianchi, Claudio, et al. “Reappraisal of serum β2-microglobulin as marker of GFR.” *Renal failure* 23.3-4 (2001): 419-429.

[30]- Stein, G., et al. "Beta 2-microglobulin serum concentration and associated amyloidosis in dialysis patients." *Nephrology, Dialysis, Transplantation: Official Publication of the European Dialysis and Transplant Association-European Renal Association* 6 (1991): 57-61.

[31]- Rossi, Davide, et al. "Beta-2-microglobulin is an independent predictor of progression in asymptomatic multiple myeloma." *Cancer* 116.9 (2010): 2188-2200.

[32]- Brancolini, Giorgia, et al. "Citrate stabilized gold nanoparticles interfere with amyloid fibril formation: D76N and ΔN6 β2-microglobulin variants." *Nanoscale* 10.10 (2018): 4793-4806.

[33]- Brancolini, Giorgia, et al. "Probing the influence of citrate-capped gold nanoparticles on an amyloidogenic protein." *Acs Nano* 9.3 (2015): 2600-2613.

[34]- Bard, Allen J., Larry R. Faulkner, and Henry S. White. *Electrochemical methods: fundamentals and applications*. John Wiley & Sons, 2022.

[35]- Zhang, Guigen. "Simulating the electrical double layer capacitance." *Excerpt from Proceedings of the COMSOL Conference. Boston*. 2010.

[36]- Wu, Jianzhong. "Understanding the electric double-layer structure, capacitance, and charging dynamics." *Chemical Reviews* 122.12 (2022): 10821-10859.

[37]- Burt, Ryan, Greg Birkett, and X. S. Zhao. "A review of molecular modelling of electric double layer capacitors." *Physical Chemistry Chemical Physics* 16.14 (2014): 6519-6538.

[38]- Doblhoff-Dier, Katharina, and Marc TM Koper. "Electric double layer of Pt (111): Known unknowns and unknown knowns." *Current Opinion in Electrochemistry* 39 (2023): 101258.

[39]- Gongadze, E., Petersen, S., Beck, U., & Van Rienen, U. (2009, October). Classical Models of the Interface between an Electrode and an Electrolyte. In *COMSOL conference* (pp. 14-16).

[40]-Ivanov, Vladimir D. "The Helmholtz model." *Journal of Solid State Electrochemistry* 28.8 (2024): 2487-2493.

[41]- Bard, Allen J., Larry R. Faulkner, and Henry S. White. *Electrochemical methods: fundamentals and applications*. John Wiley & Sons, 2022.

[42]- Elliott, Joshua D., et al. "The electrochemical double layer at the graphene/aqueous electrolyte interface: what we can learn from simulations, experiments, and theory." *Journal of Materials Chemistry C* 10.41 (2022): 15225-15262.

[43]- Huang, Jun. "Zooming into the inner helmholtz plane of Pt (111)–aqueous solution interfaces: Chemisorbed water and partially charged ions." *JACS Au* 3.2 (2023): 550-564.

[44]- Wu, Guangfu, Meyya Meyyappan, and King Wai Chiu Lai. "Simulation of graphene field-effect transistor biosensors for bacterial detection." *Sensors* 18.6 (2018): 1715.

[45]- Clericò, Vito. "Fabrication and characterization of quantum materials: graphene heterostructures and topological
[46]- Huang, Jun. "Zooming into the inner helmholtz plane of Pt (111)–aqueous solution interfaces: Chemisorbed water and partially charged ions." *JACS Au* 3.2 (2023): 550-564.

[47]- Froehlicher, Guillaume, and Stéphane Berciaud. "Raman spectroscopy of electrochemically gated graphene

insulators." (2020)

[48]- Meric, Inanc, et al. "Current saturation in zero-bandgap, top-gated graphene field-effect transistors." *Nature nanotechnology* 3.11 (2008): 654-659.

[49]- Zhan, Cheng, et al. "Quantum effects on the capacitance of graphene-based electrodes." *The Journal of Physical Chemistry C* 119.39 (2015): 22297-22303.

[50]- Xia, Jilin, et al. "Measurement of the quantum capacitance of graphene." *Nature nanotechnology* 4.8 (2009): 505-509.

[51]-Wekalao, Jacob, et al. "Graphene-based THz surface plasmon resonance biosensor for hemoglobin detection applicable in forensic science." *Plasmonics* 19.4 (2024): 2141-215.

[52]- Zhao, Jialin, et al. "Lithium-ion-based solid electrolyte tuning of the carrier density in graphene." *Scientific reports* 6.1 (2016): 34816.

[53]- Solomon, Theodros. "The definition and unit of ionic strength." *Journal of Chemical Education* 78.12 (2001): 1691

[54]- Zhang, Weitao, et al. "Experimental and modeling of conductivity for electrolyte solution systems." *ACS omega* 5.35 (2020): 22465-22474.

[55]- Kesler, Vladimir, Boris Murmann, and H. Tom Soh. "Going beyond the Debye length: overcoming charge screening limitations in next-generation bioelectronic sensors." *Acs Nano* 14.12 (2020): 16194-16201.

Chapter five

Fabrication, Characterization, and Electrical Measurements of Graphene Field-Effect Transistor for Albumin Detection and pH Sensing

5-1 Graphene Synthesis Techniques for Sensing Applications:

Advancing manufacturing techniques is critical for the continued development of graphene-based structures, particularly in sensing applications. Among the various methods available for graphene synthesis, two primary approaches are commonly employed: bottom-up and top-down techniques. The bottom-up method typically involves the growth of graphene by depositing vaporized carbon precursors onto a substrate, enabling layer-by-layer formation. In contrast, the top-down approach relies on breaking down bulk graphite oxide into individual graphene layers through mechanical or chemical exfoliation.

The properties of the resulting graphene-such as purity, layer thickness, and structural integrity-can vary significantly depending on the production technique. Additionally, factors such as cost-effectiveness and scalability are crucial when considering practical and commercial applications. One of the major barriers to widespread adoption of graphene in sensing technologies is the challenge of scaling up production without sacrificing the material's exceptional properties [1].

5.2- Mechanical Exfoliation Process for the Preparation of Graphene:

Mechanical exfoliation is one of the most effective techniques for producing high-quality graphene. This process involves the application of mechanical force to separate individual graphene layers from bulk graphite by overcoming the weak Van der Waals forces binding them together. As a top-down process, mechanical exfoliation typically applies either vertical or lateral stress to layered graphite structures to initiate separation. Two main types of forces are utilized in this method: normal (perpendicular) and shear (lateral) forces. For example, applying normal force using adhesive tape can break the interlayer attraction, while graphite's natural lubricating behavior in the planar direction allows shear forces to further facilitate exfoliation. By carefully adjusting these forces, it becomes possible to peel thin layers from graphite and obtain high-purity graphene with minimal defects [2].

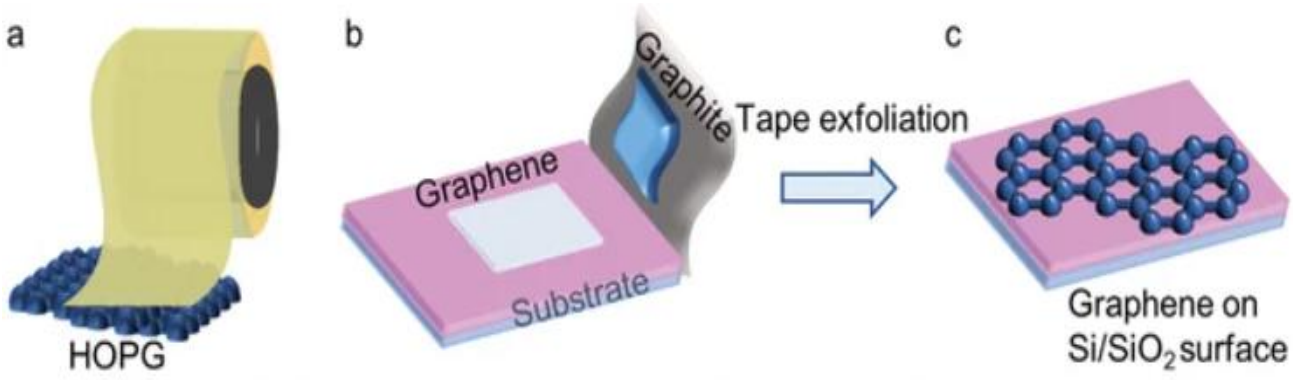

Figure 5-1. Schematic illustration of graphene fabrication through the micromechanical exfoliation (mechanical cleavage) method, where thin graphene layers are obtained by repeatedly peeling graphite using adhesive tape. [2]

Despite the high quality of graphene obtained through mechanical exfoliation, the method suffers from poor scalability, making it less suitable for large-scale production. Nonetheless, it remains a foundational and widely studied technique-particularly for research purposes-due to its ability to yield monolayer or few-layer graphene flakes with excellent structural integrity [2].

A well-known variant of this technique is micromechanical cleavage, first successfully employed in 2004 using highly ordered pyrolytic graphite (HOPG). In this approach, adhesive tape is used to lift layers from the HOPG surface. Repeatedly applying and removing the tape gradually thins the graphite until monolayer or few-layer graphene is achieved. This process relies on repeated stress application, which controls the resulting flake thickness. Graphene produced through this method has been instrumental in revealing many of its fundamental properties due to its exceptional quality and high surface area [3,4].

The fabrication process typically begins with the preparation of a suitable substrate—most commonly a p-doped silicon wafer coated with a 300 nm layer of thermally grown silicon dioxide (SiO_2). The substrate undergoes a thorough cleaning process using acetone and isopropanol, with sonication in each solvent for one minute to enhance cleanliness. Following this, the wafer is dried with nitrogen gas and subjected to oxygen plasma treatment to eliminate residual contaminants and improve surface hydrophilicity. To remove any remaining moisture, the wafer is then baked at 120°C under a nitrogen atmosphere for approximately 20 minutes [3,4].

Graphene flakes are subsequently deposited onto the cleaned Si/SiO_2 substrate using the scotch tape method, a standard micromechanical exfoliation technique. Initially, adhesive tape is pressed onto a graphite crystal to remove its uppermost layers. The remaining graphite film on the tape is then repeatedly cleaved (typically 4–5 times) to reduce its thickness and yield few-layer graphene. The tape is then gently pressed onto the substrate to ensure good contact and transfer of graphene onto the

wafer. Finally, the tape is carefully peeled away, leaving behind randomly distributed graphene flakes of varying sizes and thicknesses [3,4].

Although this method is straightforward and produces graphene with high structural quality and minimal defects, it is not well-suited for large-scale production. The flake sizes typically range from a few micrometers up to several hundred micrometers, making it difficult to obtain large-area, continuous graphene sheets through this technique alone [3,4].

5.3- chemical vapor deposition (CVD) Process for the Preparation of Graphene:

Since its introduction in 2004, graphene has drawn widespread attention due to its extraordinary electrical, mechanical, and thermal properties. Among the many methods developed for synthesizing graphene, chemical vapor deposition (CVD) has gained particular significance since around 2008–2009, when it was first demonstrated as a viable technique for producing high-quality graphene films suitable for various technological applications [5].

CVD-produced graphene exhibits electronic properties that make it highly suitable for integration into a range of advanced systems. For example, few-layer graphene (FLG) grown on nickel (Ni) substrates has shown promise as a flexible and transparent conductive material, particularly for applications in biosensing and flexible electronics. The versatility of this approach lies in the ability to tailor the number of graphene layers by adjusting growth parameters and substrate characteristics [6].

Initial studies have focused on the growth of few-layer graphene on polycrystalline nickel films, as well as on single-crystal Ni (111) surfaces. Each of these substrates offers distinct advantages in terms of growth behaviour and layer uniformity. Following this, research has expanded to the deposition of monolayer graphene on copper (Cu), which has become one of the most widely used approaches for producing large-area, uniform graphene sheets with high crystalline quality [6].

Out of the different strategies available for synthesizing graphene, CVD on transition metal substrates has emerged as the most efficient and scalable method. This technique is not only relatively low-cost but also capable of yielding graphene films over large surface areas, which is essential for industrial and commercial applications.

5.3.1- CVD process:

During the CVD process, a mixture of gaseous precursors-commonly hydrocarbons such as methane-is introduced into a high-temperature reaction chamber. As the gases travel through the heated zone, they undergo thermal decomposition on the surface of the metal substrate. This results in the formation of reactive carbon species, which then diffuse and assemble into graphene layers. The role of the metal substrate in this process is crucial. It serves both as a catalyst that facilitates the breakdown of carbon-containing precursors by lowering the reaction's energy barrier and as a template that influences the growth kinetics and morphology of the resulting graphene. Depending on the specific metal used, the deposition mechanism can vary significantly. For instance, nickel, with its relatively high carbon solubility, supports a dissolution-precipitation mechanism that leads to the formation of few-layer graphene. In contrast, copper, which has low carbon solubility, promotes the growth of monolayer graphene through surface-mediated reactions [7].

The interplay between the substrate type, growth conditions, and precursor chemistry ultimately governs the thickness, quality, and uniformity of the graphene film. Understanding these interactions is key to optimizing the CVD process for targeted applications in electronics, optoelectronics, energy storage, and other fields [7].

5.3.1.1- CVD Growth of Graphene on nickel (Ni):

Typically, the synthesis of graphene on polycrystalline nickel (Ni) films begins with an annealing step in an argon (Ar) and hydrogen (H_2) atmosphere at high temperatures, generally between 900°C and 1000°C. This thermal treatment enhances the grain size of the Ni film, which is crucial for improving the uniformity and crystallinity of the resulting graphene layers. Following annealing, the Ni films are exposed to a gas mixture containing hydrogen (H_2) and methane (CH_4)**.** During this stage, the hydrocarbon molecules decompose upon contact with the hot metal surface, releasing carbon atoms that diffuse into the bulk of the nickel film, forming a Ni–C solid solution [8].

As the system is cooled-typically under an argon atmosphere-the solubility of carbon in nickel significantly decreases. Unlike copper, which has a low carbon solubility, nickel retains a considerable amount of carbon at elevated temperatures. Upon cooling, the supersaturated carbon atoms migrate from the bulk of the Ni film back to the surface, where they precipitate and assemble into graphene layers. This process, governed by carbon segregation and precipitation, is highly dependent on the cooling rate**.** Because carbon solubility in Ni drops rapidly with temperature, controlled cooling is essential to regulate the number of graphene layers formed [8].

Nickel, particularly the Ni (111) crystallographic surface, provides an excellent platform for graphene growth due to its close lattice match with graphene's hexagonal structure. Both materials have nearly identical lattice constants, which minimizes strain and promotes epitaxial alignment during graphene formation [9].

The rate at which the sample is cooled plays a critical role in determining the final structure and thickness of the graphene film. Faster cooling rates tend to trap more carbon within the Ni bulk, leading to thinner or discontinuous graphene, while slower rates may result in excessive carbon precipitation, producing multilayer regions. Intermediate cooling rates have been found to be optimal, facilitating the segregation of a controlled amount of carbon that typically results in few-layer graphene (FLG) with better uniformity [9].

In addition to cooling rate, the microstructural characteristics of the nickel substrate-such as grain boundaries and crystallinity-greatly influence the morphology and uniformity of the graphene layer. Graphene grown on polycrystalline Ni is usually continuous but consists of regions with varying layer numbers. Grain boundaries in Ni, which act as defects, are often the nucleation sites for multilayer graphene, disrupting the uniformity of the film. Therefore, minimizing these boundaries through high-temperature annealing improves the overall quality by increasing the grain size and reducing defect density [10].

This annealing step also serves to remove impurities from the Ni surface, particularly in the presence of hydrogen, which can aid in achieving cleaner interfaces and better crystalline order. Furthermore, other process parameters such as growth duration and hydrocarbon concentration significantly affect the amount of carbon incorporated into the Ni film. These variables, in turn, influence the graphene thickness, as they dictate the total carbon available for segregation and precipitation during the cooling phase [10].

5.3.1.2- CVD Growth of Graphene on Copper (Cu):

In addition to nickel, researchers have investigated a wide range of metal substrates-including copper (Cu), ruthenium (Ru), iridium (Ir), platinum (Pt), cobalt (Co), palladium (Pd), and rhenium (Re)—each offering different levels of carbon solubility and catalytic activity during chemical vapor deposition (CVD). Among these, copper has emerged as a particularly effective substrate, especially for synthesizing monolayer graphene, due to its low carbon solubility and relatively low cost. The pioneering work by Ruoff and co-workers demonstrated the successful growth of uniform single-

layer graphene on polycrystalline Cu foils, sparking considerable interest within the materials science community [11].

In their method, graphene was synthesized on 25-micrometer-thick copper foils using a hot-wall CVD furnace. The process began with the thermal annealing of the copper foil under a hydrogen (H_2) atmosphere at 1000°C. This step is critical for increasing the grain size of the Cu substrate, reducing surface roughness, and eliminating residual surface oxides or contaminants that may hinder graphene nucleation. After annealing, a hydrogen and methane (CH_4) gas mixture was introduced into the reaction chamber. At these elevated temperatures, the methane decomposes on the Cu surface, releasing carbon atoms that rearrange to form a continuous graphene layer [11].

Unlike nickel, copper's extremely low carbon solubility means that carbon atoms do not diffuse into the bulk of the substrate. Instead, the entire growth process occurs on the surface of the copper foil, leading to surface-mediated growth that favors the formation of monolayer graphene. This makes copper particularly suitable for applications where precise control over the number of graphene layers is essential [11].

Once a continuous graphene film is established on the Cu surface, the system is gradually cooled to ambient temperature under an inert or reducing atmosphere. Due to the surface-based nature of growth, the cooling rate does not significantly affect the number of layers, in contrast to growth on nickel [12].

An important advantage of graphene synthesized on copper is its ease of transfer to other substrates. After growth, the underlying copper foil can be etched away using chemical solutions, allowing the graphene film to be transferred onto target substrates such as SiO_2/Si wafers, glass, or flexible polymers for subsequent characterization or device fabrication. This transferability makes Cu-grown graphene highly compatible with a variety of applications in electronics, photonics, and sensing technologies [12].

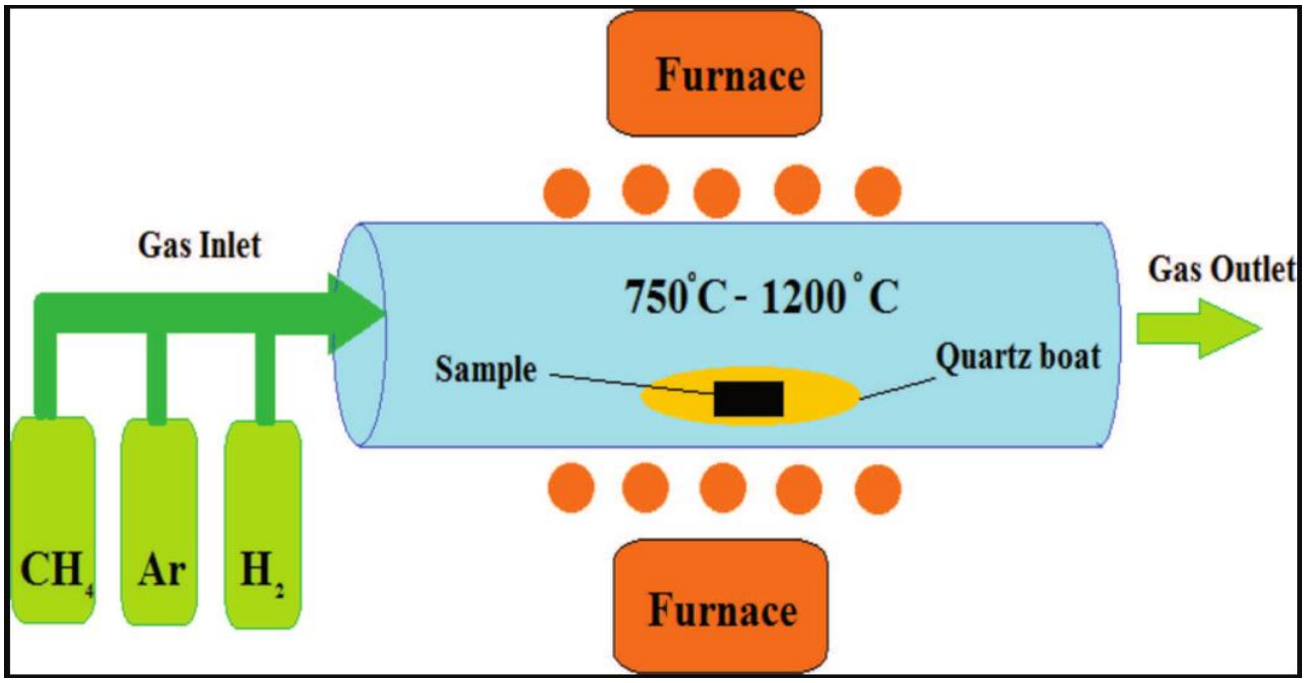

Figure 5-2. Schematic of the chemical vapor deposition (CVD) process used for graphene synthesis on copper (Cu), where hydrocarbon precursors decompose at high temperature and carbon atoms assemble into a graphene layer on the metal catalyst surface. [12].

5.3.2- Graphene Film Transfer Process:

For the integration of graphene into nano electronic devices, it is essential to detach the graphene layer from its catalytic metal substrate-such as copper or nickel-and transfer it onto a target substrate suitable for device fabrication. This transfer process enables the use of graphene on a variety of insulating or flexible surfaces [13].

A typical transfer procedure begins by coating the graphene surface with a protective polymer layer, most commonly polymethyl methacrylate (PMMA). This PMMA layer provides mechanical support to the ultrathin graphene film during the subsequent handling steps. After the coating, the sample is baked at approximately 120°C to evaporate any residual solvent from the PMMA solution and to solidify the polymer layer [13].

Once the PMMA layer is set, the underlying metal substrate-either a copper foil or nickel film-is etched away using a suitable chemical etchant, such as ammonium persulfate for copper or iron chloride solution for nickel. This etching process dissolves the metal substrate, leaving behind the freestanding PMMA/graphene stack, which is then floated on the surface of the etchant solution [13].

The resulting film is carefully rinsed multiple times with deionized (DI) water to remove residual etchant and other contaminants. It is then gently transferred onto the desired substrate, which could

include glass slides, silicon/silicon dioxide (Si/SiO_2) wafers, or flexible polyethylene terephthalate (PET) films, depending on the application [13].

After placement on the target surface, the assembly is typically air-dried or baked to remove any trapped moisture between the graphene and the substrate. Finally, the PMMA support layer is removed by immersing the sample in acetone, which dissolves the polymer without damaging the graphene. This results in a clean graphene film securely adhered to the target substrate, ready for further processing or device fabrication [13].

Using this approach, it is possible to transfer large-area graphene films, including full-wafer-scale sheets, from both nickel and copper substrates. This versatility makes the method widely applicable for both rigid and flexible electronics platforms, offering a scalable route for incorporating high-quality graphene into practical technologies [13].

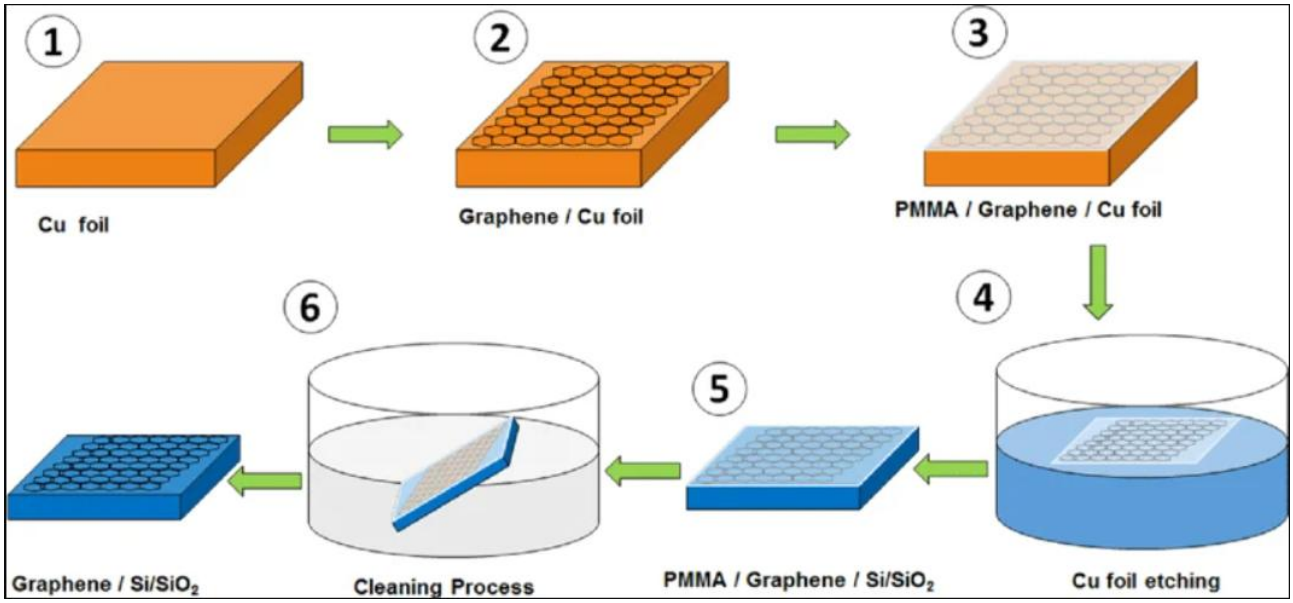

Figure 5-3. Simplified schematic of the wet transfer process for graphene onto substrates, illustrating the steps for transferring both freestanding and flat graphene layers while preserving their structural integrity [13]

5.4- Fabrication and Characterization Techniques:

This section provides a concise overview of the primary fabrication and characterization techniques employed throughout this thesis. The fabrication process primarily relied on electron-beam lithography (EBL), which played a crucial role in defining and patterning the device structures with high precision. Following fabrication, various characterization methods were applied to analyse the material's structural, morphological, and electrical properties. This included Raman spectroscopy, used to investigate molecular vibrations and assess crystal quality; optical imaging, employed to

examine surface morphology and uniformity; and probing station measurements, which enabled accurate evaluation of electrical performance through current–voltage (I–V) characterization and contact behaviour analysis.

5.4.1- Optical microscope:

The Optical Microscope was used for an optical identification of graphene flakes and in general for a qualitatively control of the samples/devices. It has six objectives with different magnification and working distance (5X, 10X, 20X, 50X, 100X). A LED illumination is integrated within the microscope, as well a motorized aperture diaphragm, filters and different contrast modes: Bright Field (BF), Dark Field (DF). It is coupled to a camera and with the Leica LAS software. In this way the optical images can be treated.

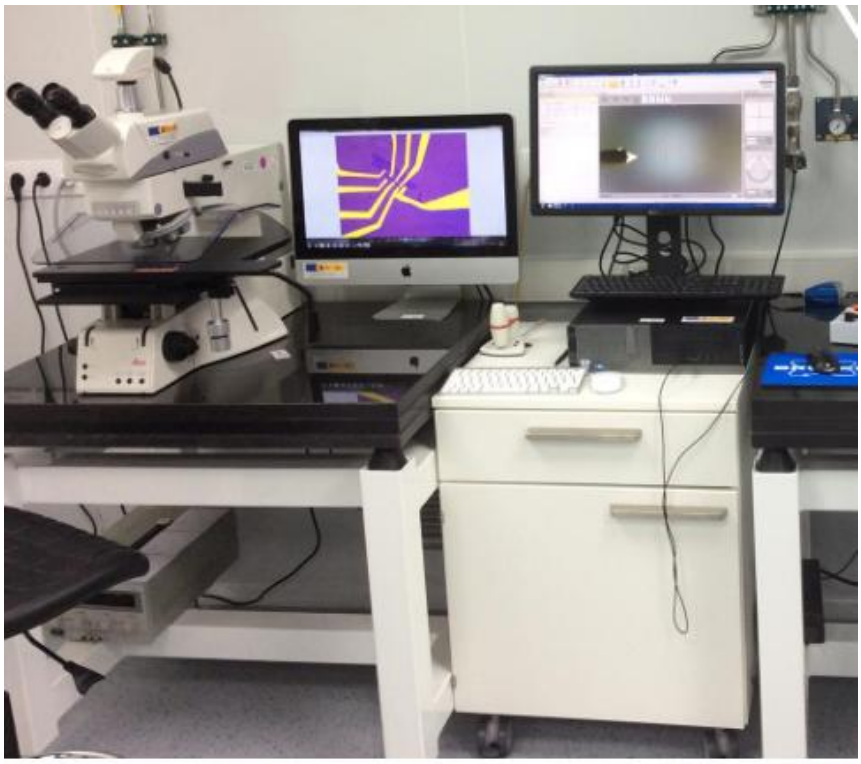

Figure 5-4. Leica DM8000 Optical Microscope- High-resolution optical microscope used for imaging and characterization of materials at the micro- and nanoscale.

5.4.2- Raman spectroscopy:

Raman spectroscopy is a rapid, non-destructive technique used to analyse a material's structural, electronic, and vibrational properties. It relies on the inelastic scattering of monochromatic light-typically from a laser-where most light is scattered without energy change (Rayleigh scattering), but a small portion undergoes an energy shift (Raman effect), first discovered by C.V. Raman and K.S. Krishnan in 1928. When the scattered photon loses energy, it's known as Stokes scattering; if it gains energy, it's Anti-Stokes scattering. These shifts occur due to interactions between the light and molecular vibrations [14].

Since each material has a unique vibrational signature, Raman spectra can be used for identifying and characterizing substances. An important indicator of the crystalline quality of graphene is the intensity ratio between the 2D peak and the G peak in its Raman spectrum. This ratio provides insights into the number of layers and the level of disorder or defects in the graphene structure. For graphene deposited on SiO_2 substrates, the 2D/G ratio typically ranges from around 1, which is characteristic of defective or disordered graphene, to values of 3 or higher, which indicate high-quality, monolayer graphene with minimal defects.

Figure 5-5. Raman spectroscopy used to assess the quality of graphene, providing information on layer number, structural defects, and crystallinity through characteristic vibrational modes.

5.4.3- Fabrication of electrode for electrical measurement:

Based on the spatial mapping data obtained from the Raman measurements, we designed a customized CAD file to define the pattern for electron beam lithography (EBL). The CAD design was carefully aligned to ensure that the critical device structures would be fabricated precisely on the regions of optimal graphene quality. This approach maximizes device performance and reproducibility by leveraging the intrinsic properties of pristine graphene.

The final layout of the CAD file, used during the EBL should be includes alignment markers, contact pads, and the intended nanoscale patterns for device fabrication. The design parameters-such as feature dimensions, spacing, and orientation-were optimized to match both the physical characteristics of the graphene flake and the intended electrical measurement configuration. Figure 5-6 present layout of CAD file which used for fabrication graphene which produced by mechanical exfoliation approach.

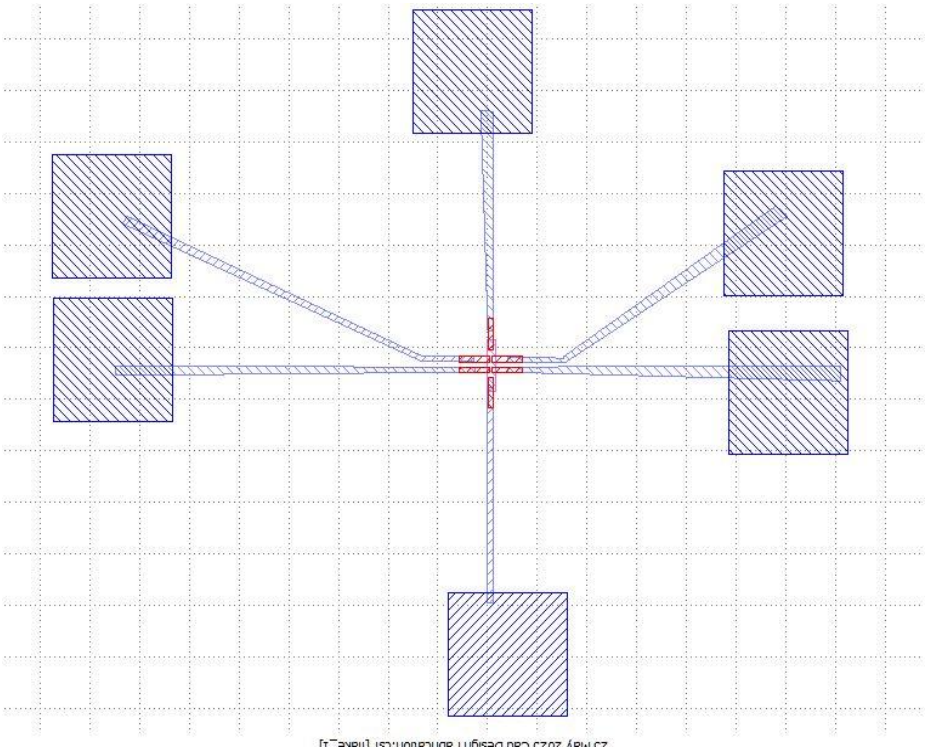

Figure 5-6. Layout of the CAD design used for fabricating graphene devices obtained via mechanical exfoliation, showing the patterning and electrode arrangement for experimental characterization.

5.4.4- Electron-Beam Lithography (EBL):

Electron-beam lithography (EBL) is an advanced nanofabrication method that enables the creation of highly precise and customized patterns at the nanoscale. It is particularly valued for its exceptional spatial resolution, which surpasses the limitations of conventional optical lithography. In this technique, a finely focused beam of electrons is directed onto the surface of a substrate that has been coated with an electron-sensitive polymer layer known as a resist. The electron beam is scanned in a pre-defined pattern that corresponds to the desired geometry of nano electronic or nanophotonic devices. When the resist is exposed to the energetic electrons, localized chemical and structural modifications occur within the polymer, altering its solubility in specific developers. Subsequent development removes either the exposed or unexposed regions-depending on whether a positive or negative resist is used-thus transferring the desired nanoscale pattern onto the resist layer. This

patterned resist can then serve as a mask for subsequent processes such as etching, metal deposition, or lift-off, allowing for precise material structuring at resolutions below 10 nanometers. Owing to its flexibility and high precision, EBL is widely utilized in research and prototype fabrication of graphene-based devices, quantum dots, photonic crystals, and other nanoscale systems.

The resist is typically a two-component polymer system consisting of:

1. A base matrix that is largely insensitive to electron exposure and provides the structural integrity of the resist film.
2. An active component that responds to the electron beam, altering the solubility of the resist in a developer solution.

Depending on the type of resist used, the material can behave either as a positive resist—where electron exposure increases solubility-or as a negative resist-where exposure decreases solubility.

Prior to electron-beam exposure, the resist material is prepared by dissolving a polymer in an appropriate solvent to produce a homogeneous solution. This resist solution is then applied to the surface of the substrate using the spin-coating technique, where the substrate is rapidly rotated to spread the liquid evenly across its surface. The rotation speed, polymer concentration, and solution viscosity are key factors that determine the resulting film thickness, which can be accurately controlled-often with nano meter-level precision. After spin coating, the coated substrate is subjected to a soft-baking process, typically carried out at temperatures between 100°C and 200°C. This heating step removes residual solvent from the resist film and enhances both its adhesion to the substrate and its overall surface uniformity, ensuring the resist is well-prepared for the subsequent patterning stage.

Following electron-beam exposure, the patterned sample is subjected to a development process, during which it is immersed in a developer solution that selectively dissolves specific regions of the resist according to their exposure to the electron beam. For positive-tone resists, the irradiated areas become more soluble and are removed during development, while in negative-tone resists, the unexposed portions are dissolved, leaving behind the cross-linked exposed regions. Once the desired pattern has been revealed, the development reaction is quenched by rinsing the sample-typically with isopropyl alcohol (IPA) or another suitable solvent-to remove any residual developer and prevent overdevelopment. This step ensures that the nanoscale features remain well-defined and free from chemical contamination.

5.4.5- Reactive Ion Etching (RIE):

Reactive Ion Etching (RIE) is a plasma-based dry etching method commonly employed in nanofabrication to achieve precise and directional material removal from wafer surfaces. The process operates under low-pressure conditions, where a reactive plasma is generated using an applied electromagnetic field.

In a standard RIE system, a plasma is produced inside a vacuum chamber by applying a radiofrequency (RF) signal-typically at 13.56 MHz-to a reactive gas mixture. The alternating electric field ionizes the gas molecules, generating a plasma that contains electrons, ions, and neutral radicals. These reactive species interact with the substrate material through a combination of chemical reactions and physical ion bombardment, facilitating controlled etching of the exposed regions.

The substrate is typically placed on the cathode electrode at the base of the chamber, which is capacitively coupled to the RF power source. Because electrons move much faster than ions, a negative self-bias voltage naturally develops on the substrate surface when the plasma is ignited. This bias accelerates positively charged ions toward the surface in a nearly perpendicular trajectory, promoting anisotropic etching-that is, material removal that proceeds mainly in the vertical direction. The synergistic action of ion-driven sputtering and chemical etching from neutral radicals results in high-resolution, uniform, and directional pattern transfer, making RIE an indispensable technique in modern micro- and nanofabrication processes [4].

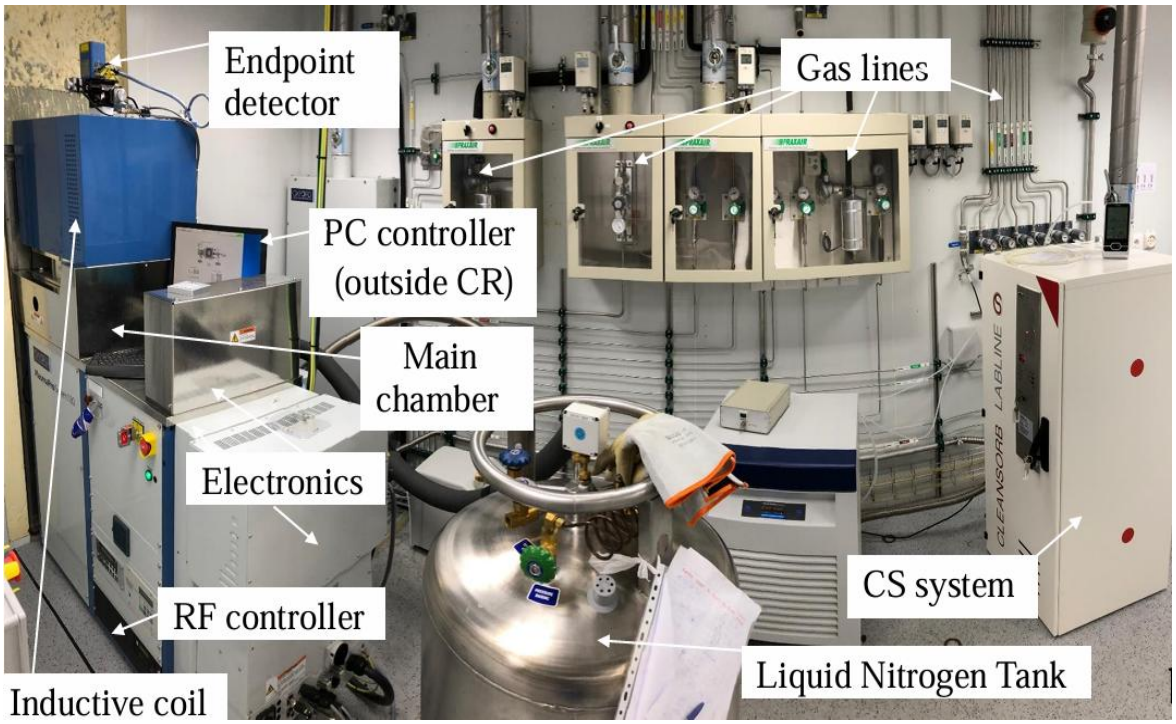

Figure 5-7. Schematic of the etching system employed for patterning graphene produced by mechanical exfoliation, illustrating the setup and tools used to selectively remove graphene regions while preserving the desired device structures.

5.4.6- Atomic Layer Deposition (ADL):

Atomic Layer Deposition (ALD) is an advanced thin-film growth technique widely utilized in nanofabrication to deposit metals, oxides, and other compound materials with atomic-scale precision. This process enables the creation of highly uniform and conformal coatings through a cyclic, self-limiting sequence of surface reactions, making it ideal for applications requiring precise thickness control and excellent film uniformity over complex structures.

In a typical ALD process, the substrate is placed inside a vacuum reactor where the deposition occurs. The process begins with the introduction of the first precursor gas, which chemisorbs onto reactive sites on the substrate surface. Once all available surface sites are saturated, further reaction is naturally inhibited, resulting in the deposition of only a single monolayer of material. The chamber is then purged with an inert gas to remove unreacted precursor molecules and gaseous by-products. Next, a second precursor is introduced, which reacts with the chemisorbed layer formed in the previous step, completing one full ALD cycle. Like the first reaction, this second step is also self-limiting, ensuring consistent layer formation.

By continuously repeating these alternating exposure and purge cycles, thin films can be grown atom-by-atom, offering unparalleled control over film thickness, composition, and uniformity. Owing to

its precision and conformality, ALD is extensively employed in semiconductor device fabrication, surface passivation, and the development of nanoscale coatings for graphene and other two-dimensional materials.

5.4.7- Fabrication of Metallic Contacts:

Once the graphene flakes were identified under optical microscopy and Raman Spectroscopy, metal electrodes were fabricated using a two-stage electron-beam lithography (EBL) procedure in combination with metal deposition. This multi-step approach ensured precise alignment and reliable electrical contact formation on the selected graphene regions.

5.4.7.1-First EBL Step: Marker Fabrication:

To ensure accurate positioning and pattern registration in subsequent lithography stages, alignment markers were initially fabricated. These markers serve as crucial reference points during later processing steps, enabling precise overlay and alignment between multiple electron-beam lithography (EBL) patterns. The fabrication of these markers was carried out using the following procedure:

1. A 300 nm-thick layer of poly (methyl methacrylate) (PMMA) 950K resist was spin-coated onto the wafer at 4000 revolutions per minute (rpm) for 60 seconds.
2. The coated substrate was then soft baked at 115 °C for 15 minutes. This step facilitated the evaporation of residual solvents from the PMMA layer without causing polymer degradation or reaching its glass transition temperature.
3. Marker patterns were exposed using electron-beam lithography with a 30 μm beam aperture and an exposure dose of 240 $\mu C/cm^2$.
4. After exposure, the sample was developed by immersing it in a solution of methyl isobutyl ketone (MIBK) for 2 minutes, selectively dissolving the regions of PMMA exposed to the electron beam.
5. The development process was quenched by rinsing the substrate in isopropyl alcohol (IPA) for 30 seconds to remove any remaining developer and to halt further chemical reactions.

5.4.7.2- Second EBL Step: Fabrication of Metal Electrodes:

A second electron-beam lithography process was carried out to pattern the metallic electrodes on the preselected graphene flakes. Alignment for this step was achieved using the marker array created during the initial lithography stage. The fabrication of the electrical contacts proceeded through the following steps:

1. Electron-beam lithography was carried out on the same PMMA resist layer used earlier for the alignment markers. These pre-defined markers served as reference points for accurately positioning the electrode structures. A beam aperture of 7.5 µm was used to define the fine features near the graphene flake, while a larger aperture and a dose of 120 µC/cm² were used for the more distant features. For the areas directly on top of the flake and the contact pads, an exposure dose of 310 µC/cm² was applied, whereas a slightly lower dose of 290 µC/cm² was used for the interconnecting leads.
2. After exposure, the resist was immersed in a methyl isobutyl ketone (MIBK) solution for 2 minutes, enabling selective dissolution of the exposed areas.
3. The development step was concluded by rinsing the sample in isopropyl alcohol (IPA) for 30 seconds, effectively removing any residual developer.
4. Metal deposition was performed via thermal evaporation. Initially, a 10 nm layer of chromium (Cr) was applied to enhance adhesion to the SiO_2 substrate, followed by a 50 nm layer of gold (Au) to create the conductive electrodes.
5. Finally, the residual PMMA resist was subsequently eliminated using a lift-off procedure in acetone, maintained at 50 °C for around two hours. This process dissolved unwanted metal, resulting in the retention of only the intended electrode patterns on the graphene surface.

The final shape of the fabricated device, as shown in Figure 5-8, was characterized using optical microscopy.

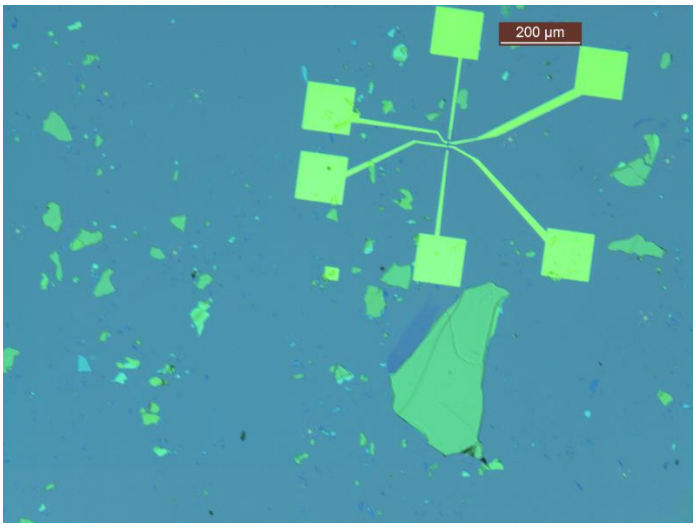

Figure 5-8. Optical microscopy image of the fabricated device, highlighting the final shape and structural features after graphene patterning and device fabrication.

5.5- Probe station:

Electrical measurements of the graphene junctions were performed at room temperature under both ambient and vacuum conditions (pressure ≈10^{-6} mbar) using a Lakeshore TTPX probe station, as shown in Figure 4.4. This versatile setup enables a variety of non-destructive, low-noise electrical characterizations of devices. It includes six micromanipulated stages, each fitted with a probe arm capable of precise three-axis movement, ensuring accurate positioning of tungsten tips on the test samples. The system's top optical access and high-magnification microscope facilitate efficient contacting and characterization of multiple devices, which is especially beneficial for electroburning measurements.

The probe station can function over a broad temperature range, spanning from 4.2 K to 475 K, using a continuous-flow liquid helium system for cooling. A radiation shield is incorporated to minimize thermal losses, while thermal links between the probe tips and the sample stage help reduce unwanted heat transfer to the devices. Nonetheless, even though the system supports variable-temperature operation, all measurements presented in this study were conducted at room temperature.

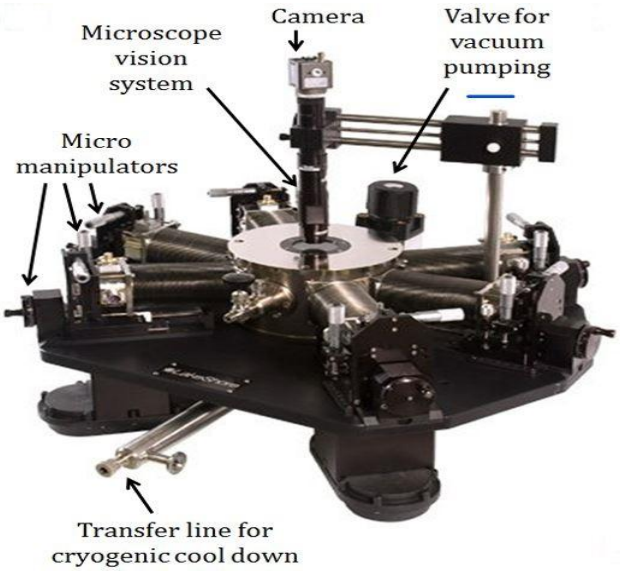

Figure 5-9. Probe station setup used for performing electrical measurements on the fabricated graphene device, showing the arrangement of probes, contacts, and instrumentation for accurate characterization of device performance.

5.6- Electrical Characterization of GFET produced by mechanical exfoliation approch Using Albumin as the Electrolyte Gate:

As discussed in Chapters Three and Four, the electrical properties of graphene exhibit high sensitivity to changes in the surrounding environment. Even small impurities can significantly influence the surface charge concentration of graphene. The presence of an electrolyte containing a specific

concentration of albumin on the top surface of graphene can alter the position of the Dirac point as well as the resistance of the graphene channel. This shift in the Dirac point has a direct correlation with the concentration of the protein, indicating that graphene can serve as an effective transducer for detecting biomolecular interactions.

In this context, the electrolyte with a defined albumin concentration functions as a top gate, thereby modulating the charge carrier density in the graphene layer. As previously discussed, such modulation plays a crucial role in determining the overall electrical response of the graphene-based device. The sensitivity of graphene to its electrochemical environment makes it a promising candidate for biosensing applications, where the detection of biomolecules such as proteins relies on measurable changes in electronic properties.

In this experiment, we investigated the impact of both liquid droplets and dried droplets of albumin-containing electrolyte on the electrical behaviour of the graphene channel. The comparative analysis of these two conditions provides insight into the reversible and irreversible effects of protein adsorption on graphene surfaces. Figures 10(a) and 10(b) illustrate the experimental results, demonstrating the variations in resistance and Dirac point shift under the droplet and dry-droplet conditions, respectively.

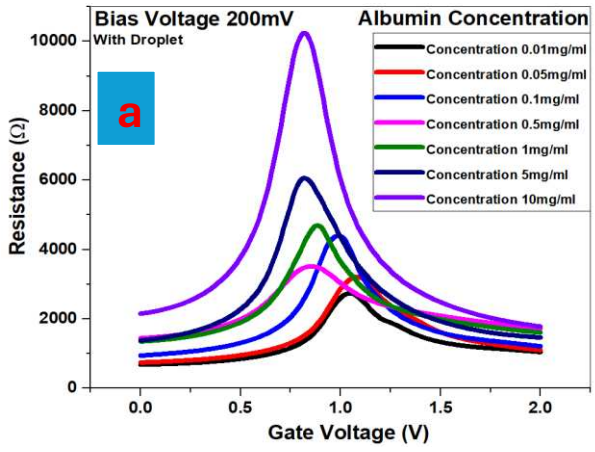

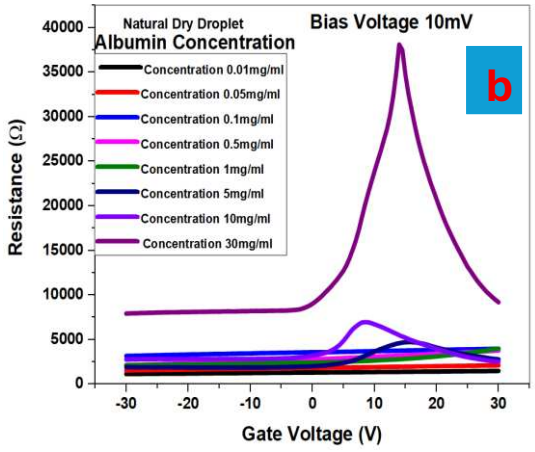

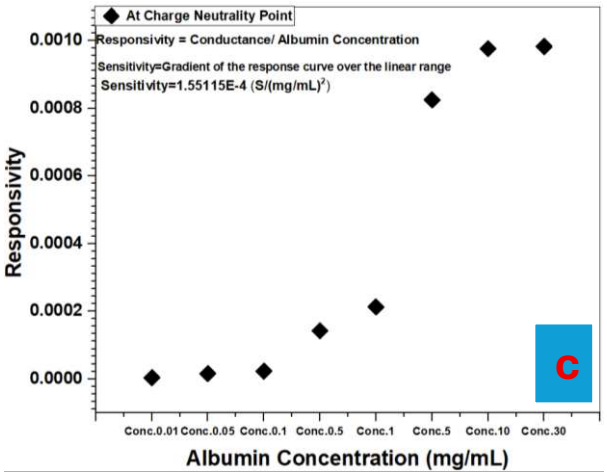

Figure 5-10. Resistance of the graphene channel: (a) in an electrolyte droplet containing different concentrations of albumin, (b) after drying of the droplet, and (c) resistivity of the graphene channel as a function of albumin concentration.

5.7- Electrical Performance of CVD-Grown Graphene FETs Under Electrolytes with Different pH Levels:

The chip produced by Graphenea is specifically designed for high-performance sensing applications and is completely corresponded with measurements conducted in liquid environments. To guaranty durability and decrease undesired electrical impacts, the metal contact pads are passivated, which prevents chemical degradation and significantly reduces leakage currents during operation. At the center of the chip lies a non-encapsulated graphene electrode, providing direct liquid gating without the demand for an external reference electrode such as an Ag/AgCl probe. This combined design not only simplifies experimental setups but also enhance the signal-to-noise ratio and reduce parasitic capacitances, resulting in more accurate and stable measurements.

This model contains 14 graphene-based devices, comprising seven single-channel and seven triple-channel configurations, which together offer 28 individual graphene channels. Such an arrangement provides enhanced flexibility for multi-channel sensing, calibration, and comparative analysis across different sensing conditions or analytes. Each graphene channel on the chip has dimensions of 85 µm × 85 µm. The overall configuration and layout of the chip are illustrated in Figure 5-11.

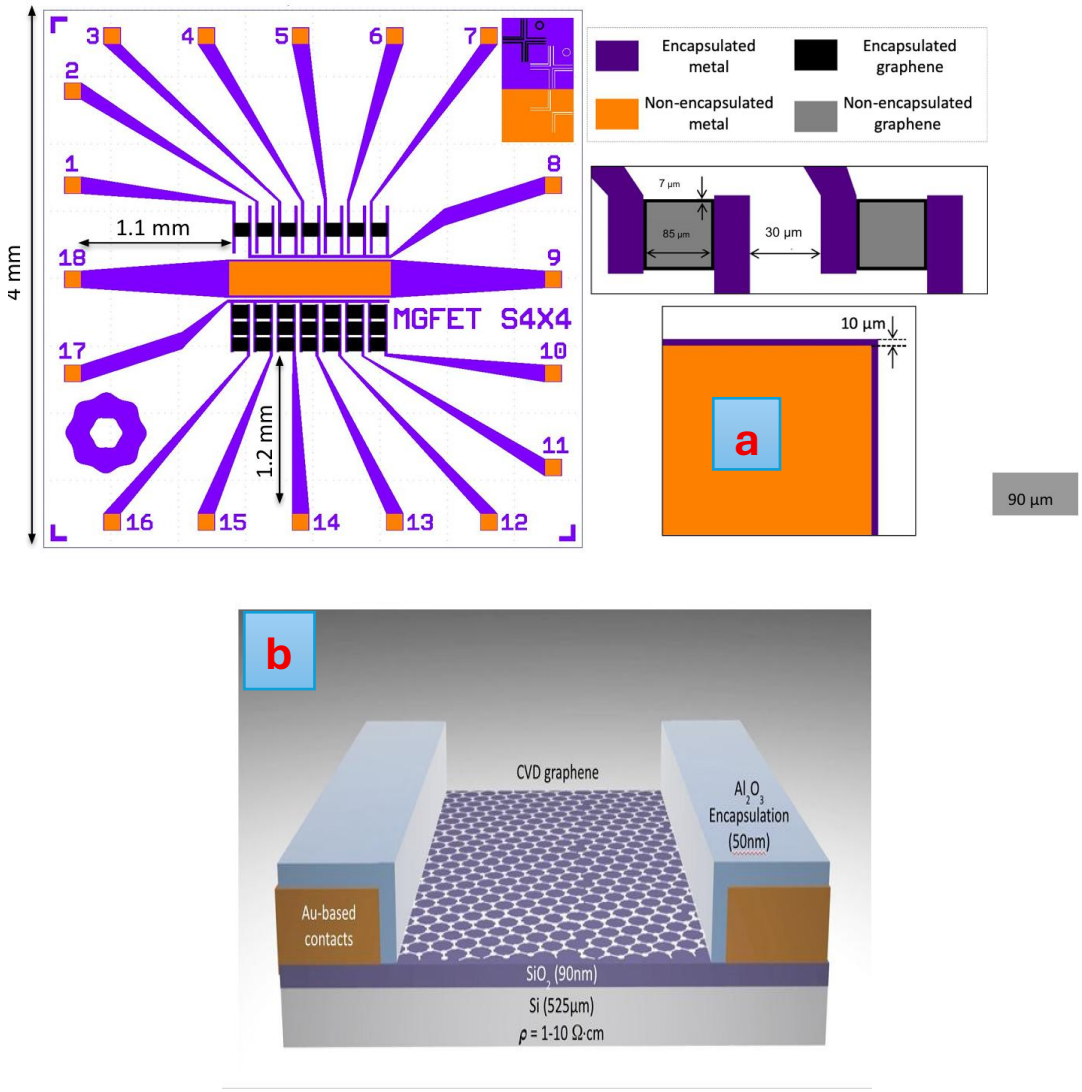

Figure 5-11. (a) Layout of the graphene chip fabricated by Graphenea using the chemical vapor deposition (CVD) method. (b) Cross-sectional schematic of the device structure, illustrating the graphene layer, electrodes, and supporting substrate.

To evaluate the structural and morphological quality of the synthesized graphene, several complementary characterization techniques were employed, including optical microscopy**,** Raman spectroscopy**,** scanning electron microscopy (SEM)**,** and high-resolution transmission electron microscopy (HRTEM).

Optical microscopy was utilized to provide a rapid and non-destructive assessment of the graphene film. It allowed visualization of the surface uniformity, detection of visible defects such as cracks, folds, or multilayer regions, and verification of the overall coverage of graphene on the substrate.

Scanning Electron Microscopy (SEM) analysis was then performed to obtain high-resolution images of the graphene surface morphology. This technique provided detailed insights into the film

continuity, grain boundaries, and the presence of any contaminants or surface irregularities introduced during the chemical vapor deposition (CVD) process.

To further investigate the atomic structure and crystallinity of the graphene layers, High-Resolution Transmission Electron Microscopy (HRTEM) was employed. This technique enabled direct imaging of the hexagonal lattice structure of carbon atoms, confirming the high crystalline quality and the presence (or absence) of lattice defects or dislocations.

Finally, Raman spectroscopy was conducted to assess the structural integrity and the number of graphene layers. The Raman spectrum exhibited characteristic G and 2D bands, and the intensity ratio of the 2D to G peaks was found to be approximately 1.56, which is indicative of monolayer graphene. This result confirms that the graphene synthesized by Graphenea possesses excellent structural uniformity and high electronic quality, suitable for sensing applications

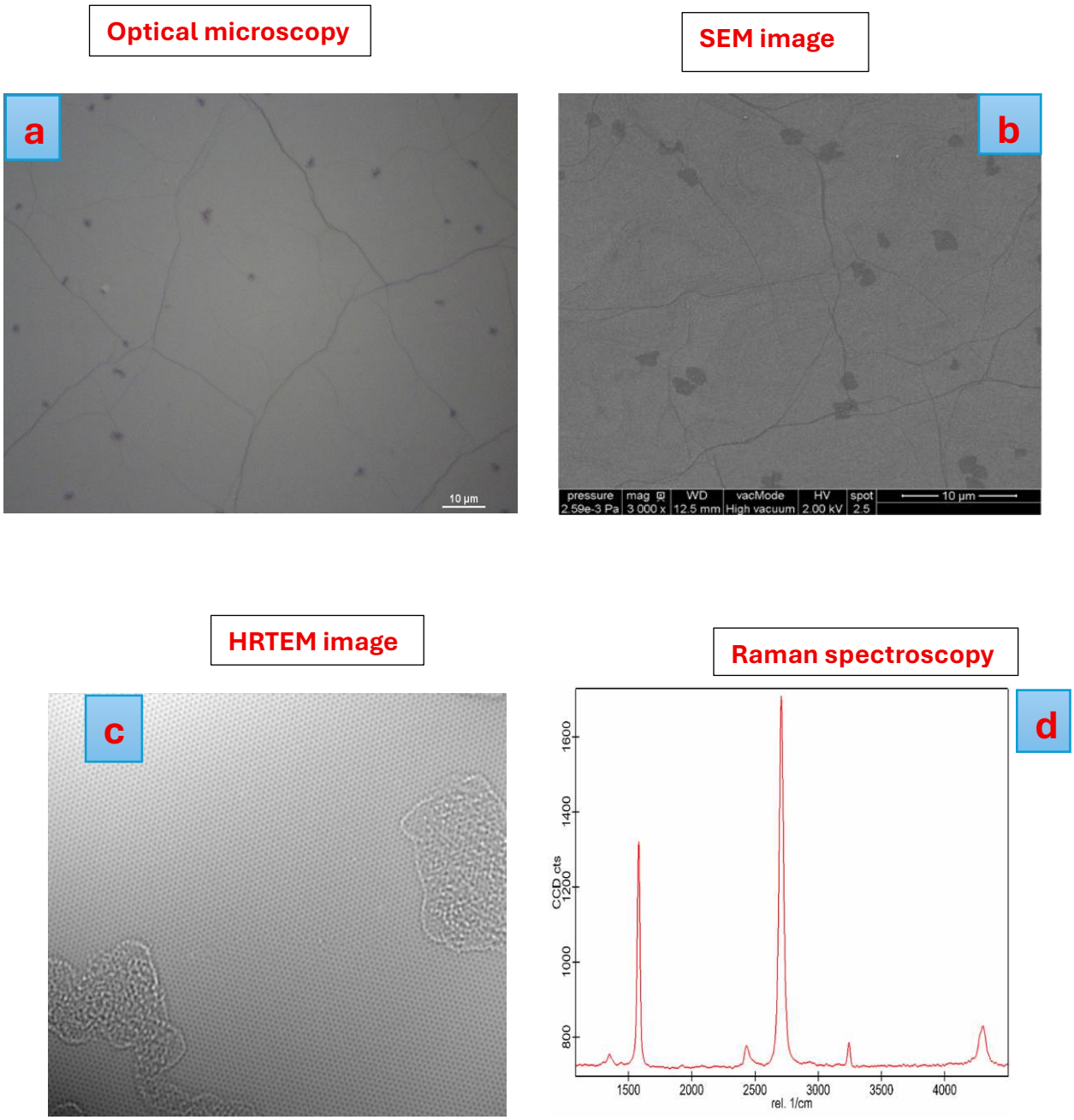

Figure 5-12. Characterization techniques used to analyze the quality and structure of graphene: (a) Optical microscopy image, (b) Scanning Electron Microscopy (SEM) micrograph, (c) High-Resolution Transmission Electron Microscopy (HRTEM) image, and (d) Raman spectroscopy spectrum highlighting structural and defect information.

5.8- Results and discussion:

Finally, the performance of the Graphene Field-Effect Transistor (GFET) fabricated by Graphenia using the Chemical Vapor Deposition (CVD) technique was investigated under different pH conditions in order to evaluate its suitability for pH sensing applications. In this study, the GFET electrical behaviour was analysed using the GFET model discussed in the previous chapter. This model accurately captures the carrier transport characteristics of graphene, particularly the strong correspondence between charge carrier concentration and conductance variations in the vicinity of the Dirac point, where graphene exhibits high sensitivity to surface charge perturbations.

The sensing principle relies on the modulation of the graphene channel conductivity induced by changes in the hydrogen ion concentration at the graphene-electrolyte interface. Variations in pH alter the surface charge density and the electrostatic environment of the graphene layer, resulting in measurable shifts in the Dirac point voltage and corresponding changes in the transfer characteristics of the GFET. Due to the atomically thin structure of graphene and its high carrier mobility, such effects are especially pronounced, making GFETs promising candidates for chemical and biological sensing.

For this purpose, two phosphate-buffered saline (PBS) solutions with different ionic strengths were employed, namely 0.01× PBS and 1× PBS, in order to investigate the influence of electrolyte concentration on the device response. The PBS solution consisted of 137 mM sodium chloride (NaCl), 2.7 mM potassium chloride (KCl), 10 mM disodium hydrogen phosphate (Na_2HPO_4), and 1.8 mM potassium dihydrogen phosphate (KH_2PO_4). The pH of the solutions was adjusted to values of 5, 6, 7, and 8, covering the mildly acidic to mildly alkaline range relevant for many biological and environmental applications.

Electrical measurements were performed for each pH condition, and the resulting transfer characteristics were analysed to observe shifts in the Dirac point and changes in channel conductance. Comparing the responses obtained in 0.01× PBS and 1× PBS allowed for assessment of the role of ionic screening and Debye length on the sensitivity of the GFET. This systematic evaluation provides insight into the operational limits and sensing performance of the CVD-grown GFET, confirming its potential for reliable pH sensing in liquid environments.

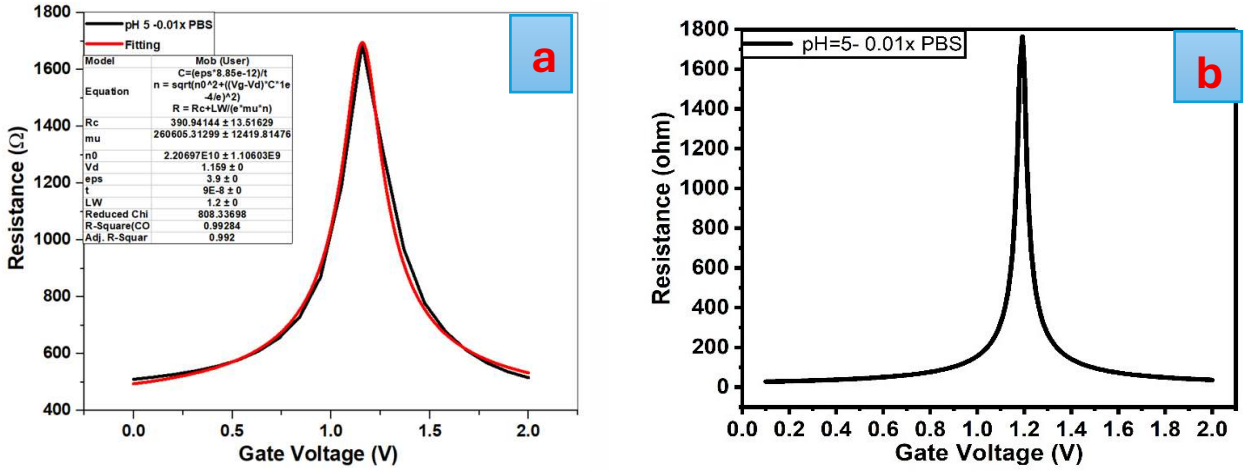

Figure 5-13. Resistance of graphene versus back-gate voltage, pH=5: (a) Experiment result, (b) Simulation results. Concentration is .01x PBS.

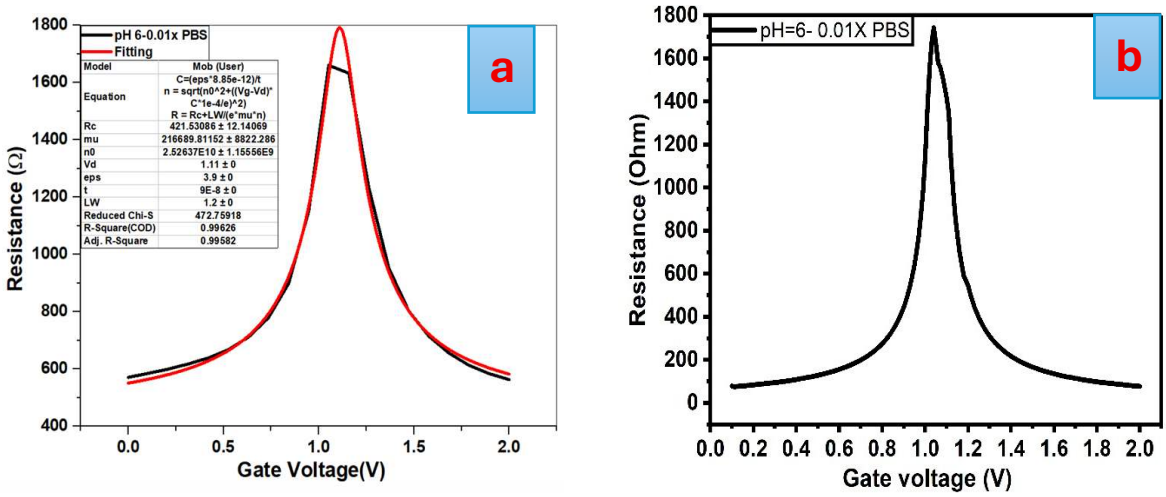

Figure 5-14. Resistance of graphene versus back-gate voltage, pH=6: (a) experiment result, (b) simulation results. Concentration is .01x PBS.

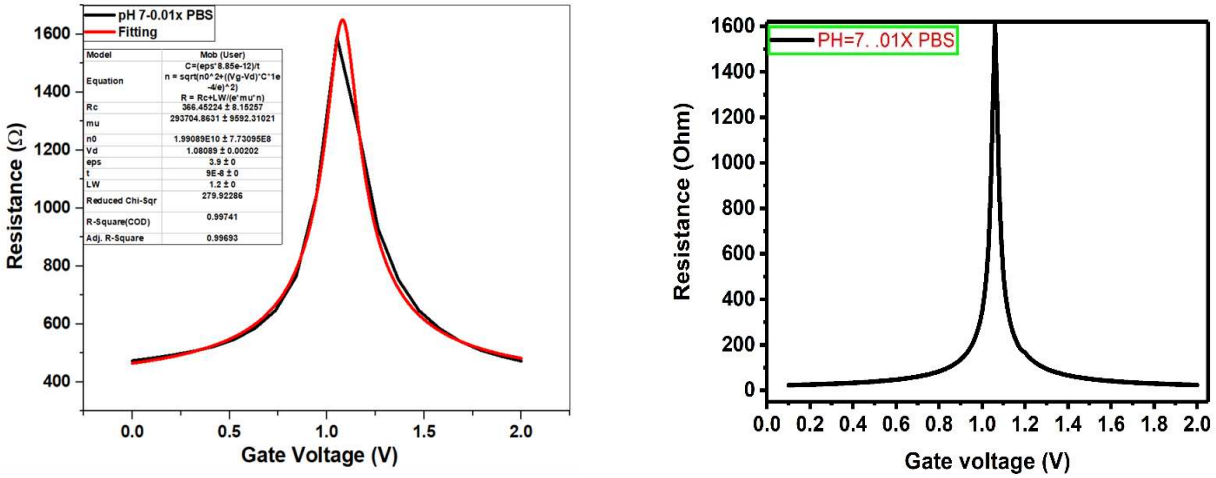

Figure 5-15. Resistance of graphene versus back-gate voltage, pH=7: (a) experiment result, (b) simulation results Concentration is .01x PBS.

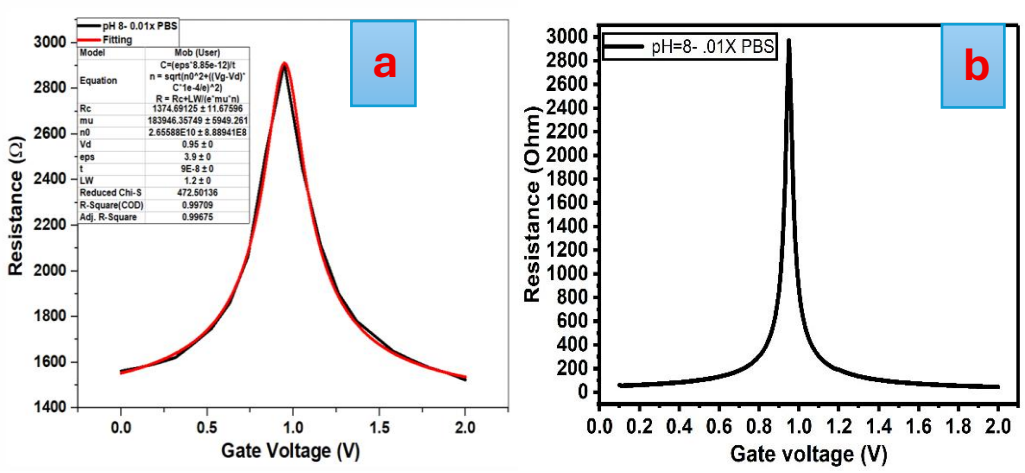

Figure 5-16. Resistance of graphene versus back-gate voltage, pH=8: (a) experiment result, (b) simulation results . Concentration is .01x PBS.

To investigate the key parameters that indicate the performance of the sensor at different pH levels, we analysed the resistance intensity, the charge neutrality points position of graphene, and the full width at half maximum (FWHM). Figure 5-17 shows the results of this experiment.

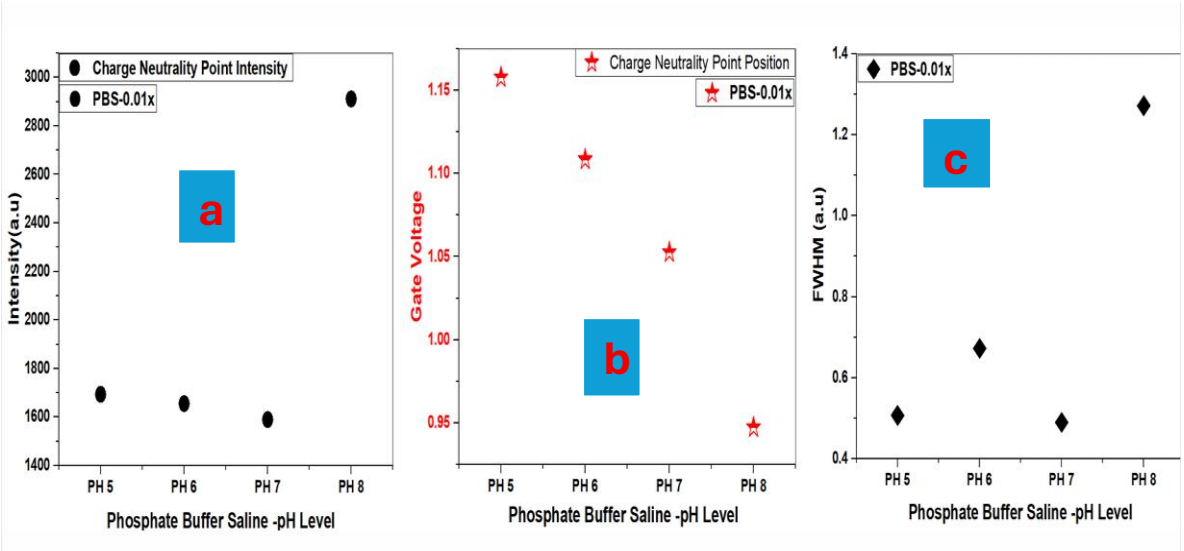

Figure 5-17. Representation of (a) graphene resistance intensity, (b) charge neutrality point position, and (c) full width at half maximum (FWHM). Concentration is .01x PBS.

Finally, we repeated the same experiment, but in this case, we varied the concentration of the phosphate-buffered saline (PBS) solution. In this experiment, the PBS concentration was set to 1x. This allowed us to examine the effect of PBS concentration on the sensor's performance, including its resistance response, charge neutrality point, and overall stability. The results provide insights into how electrolyte concentration influences the behaviour of graphene-based sensors.

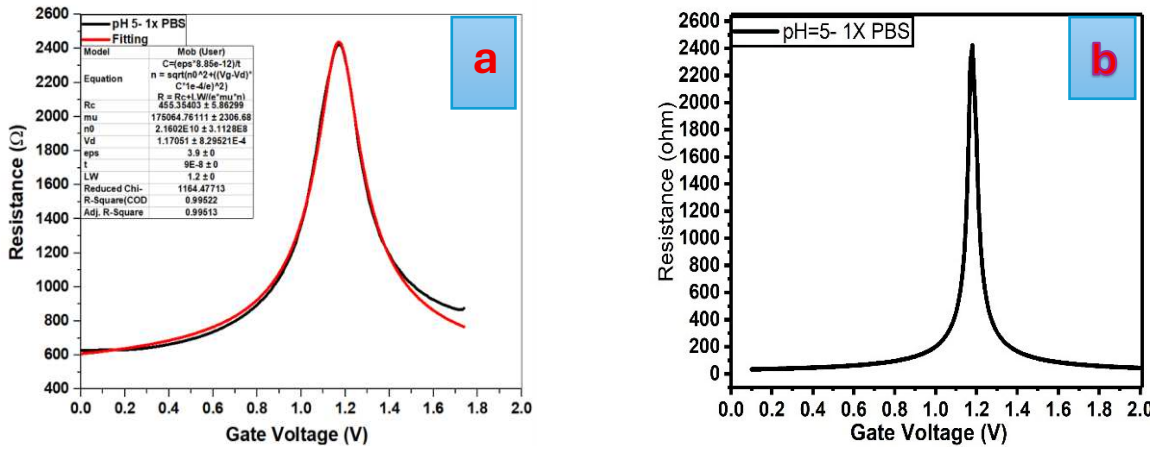

Figure 5-18. Resistance of graphene versus back-gate voltage, pH=5: (a) experiment result, (b) simulation results . Concentration is 1x PBS.

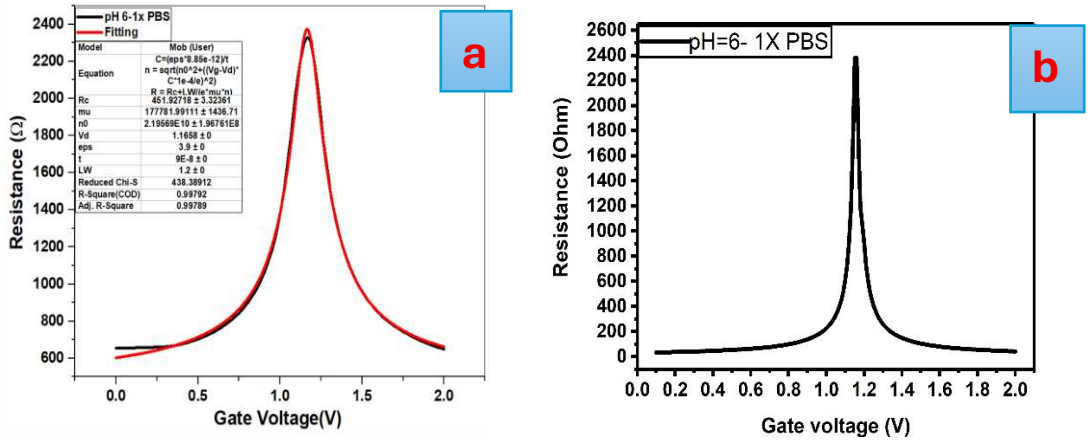

Figure 5-19. Resistance of graphene versus back-gate voltage, pH=6: (a) experiment result, (b) simulation results . Concentration is 1x PBS.

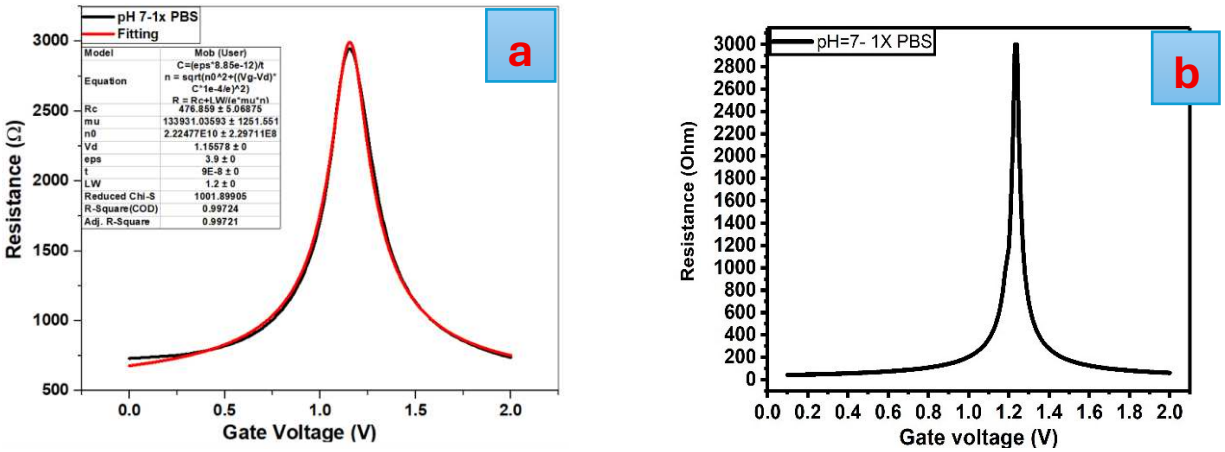

Figure 5-20. Resistance of graphene versus back-gate voltage, pH=7: (a) experiment result, (b) simulation results . Concentration is 1x PBS.

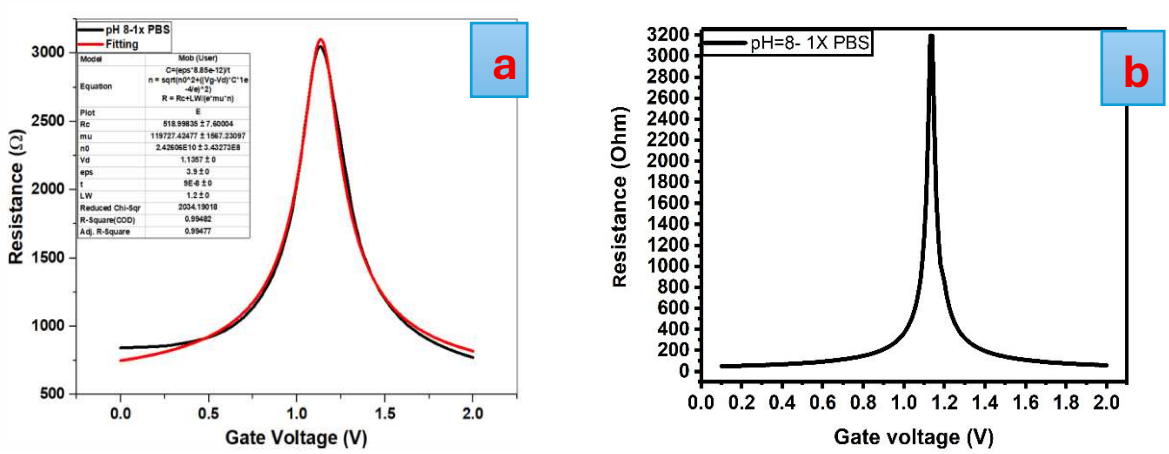

Figure 5-21. Resistance of graphene versus back-gate voltage, pH=8: (a) experiment result, (b) simulation results . Concentration is 1x PBS.

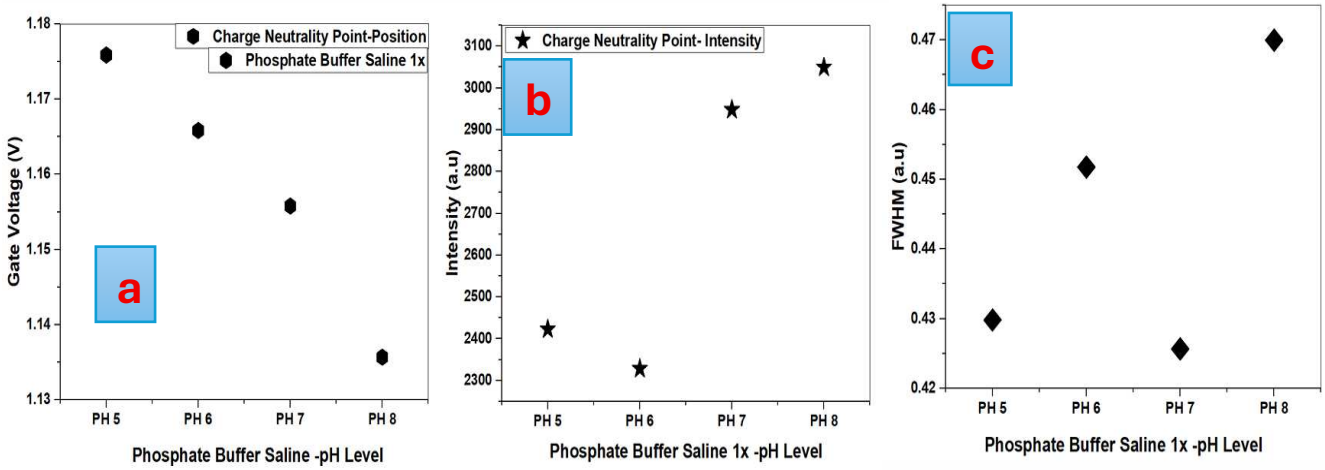

Figure 5-22. Representation of (a) graphene resistance intensity, (b) charge neutrality point position, and (c) full width at half maximum (FWHM). Concentration is 1x PBS.

References:

[1]- Novoselov, Konstantin S., et al. "A roadmap for graphene." *nature* 490.7419 (2012): 192-200.

[2]- Denissova, AI, AV Volokitin, and IE Volokitina. “PROSPECTS OF APPLICATION AND GLOBAL SIGNIFICANCE OF GRAPHENE.” *Progress in Physics of Metals/Uspehi Fiziki Metallov* 23.2 (2022).

[3]- Sumdani, M. G., et al. "Recent advances of the graphite exfoliation processes and structural modification of graphene: a review." *Journal of Nanoparticle Research* 23.11 (2021): 253.

[4]- Lumetti, Stefano. "Single-molecule spin transistors: exploiting the use of graphene-based electrodes for the next generation of molecular spintronic devices." (2018).

[5]- Zhang, Y.I., Luyao Zhang, and Chongwu Zhou. "Review of chemical vapor deposition of graphene and related applications." *Accounts of chemical research* 46.10 (2013): 2329-2339.

[6]- Zhang, Y. I., Luyao Zhang, and Chongwu Zhou. "Review of chemical vapor deposition of graphene and related applications." *Accounts of chemical research* 46.10 (2013): 2329-2339.

[7]- Lin, Li, et al. "Bridging the gap between reality and ideal in chemical vapor deposition growth of graphene." *Chemical reviews* 118.18 (2018): 9281-9343.

[8]- Al-Shurman, K. M., and Hameed Naseem. "CVD Graphene growth mechanism on nickel thin films." *Proceedings of the 2014 COMSOL Conference in Boston*. 2014.

[9]- Chae, Seung Jin, et al. "Synthesis of large-area graphene layers on poly-nickel substrate by chemical vapor deposition: wrinkle formation." *Advanced materials* 21.22 (2009): 2328-2333.

[10]- Kimia, Jadi Melalui Pemendapan Berhaba Wap, et al. "Growth of graphene on nickel using a natural carbon source by thermal chemical vapor deposition." *Sains Malaysiana* 43.8 (2014): 1205-1211.

[11]- Terasawa, Tomo-O., and Koichiro Saiki. "Growth of graphene on Cu by plasma enhanced chemical vapor deposition." *Carbon* 50.3 (2012): 869-874.

[12]- Esmaeilpour, Meysam, et al. "Multiscale Model of CVD Growth of Graphene on Cu (111) Surface." *International Journal of Molecular Sciences* 24.10 (2023): 8563.

[13]- Goniszewski, Stefan, et al. "Self-supporting graphene films and their applications." *IET Circuits, Devices & Systems* 9.6 (2015): 420-427.

[14]- Dietzek, Benjamin, et al. "Introduction to the fundamentals of Raman spectroscopy." *Confocal Raman Microscopy*. Berlin, Heidelberg: Springer Berlin Heidelberg, 2010. 21-42.

Chapter six:

Computational Simulation of Surface Plasmon Resonance Biosensor for β2-Microglobulin based on Electrolyte-Gated Graphene

6-1. Ultrasensitive Optical Biosensing Using Surface Plasmon Resonance:

Ultrasensitive biosensors with emerging micro/nano technologies attract attentions due to potentials of early detection, emergence of precision medicine, genetic diagnosis, and gene sequencing. A biosensor, defined by International Union of Pure and Applied Chemistry (IUPAC), is a device that uses specific biochemical reactions mediated by isolated enzymes, immune systems, tissues, or whole cells to detect chemical compounds by electrical, thermal or optical signals. In other words, a biosensor is an analytical tool to monitor dynamics and interactions of biological activities, e.g. DNA hybridization and cell activities [1,2].

In recent years, optical biosensors utilizing surface plasmon resonance (SPR) have gained significant attention due to their high sensitivity and versatility. One of the key advantages of SPR technology is its ability to perform real-time, label-free detection of biomolecular interactions with high efficiency [3]. This makes it an invaluable tool across various scientific and industrial domains. SPR-based biosensors are increasingly being applied in fields such as agriculture and food safety, where they contribute to the detection of contaminants and the monitoring of food quality [4,5]. In the medical sector, they play a crucial role in diagnostics by enabling the identification of disease biomarkers [6,7]. Additionally, SPR has proven useful in environmental monitoring by detecting pollutants and harmful substances, as well as in industrial processes for quality control and safety assurance [8,9].

The primary function of SPR biosensors is the detection and analysis of a wide range of biomolecules, including lipids [10], peptides [11], receptors [12], nucleic acids [13], proteins [14], and antibodies [15]. This broad detection capability has made SPR a valuable technique in both research and applied sciences. Moreover, beyond biosensing applications, SPR is also widely used for the characterization of thin films and material surfaces, providing insights into film thickness, refractive index, and molecular adsorption behaviour. These features highlight the versatility and growing importance of SPR in modern analytical science [16,17].

The first commercially available surface plasmon resonance (SPR) instrument was introduced in 1990 by Biacore AB, a Swedish company. Since then, numerous manufacturers have developed and released various SPR systems to meet growing demand across different research and industrial sectors. Typically, an SPR instrument consists of three main integrated components: (i) an optical system featuring a high-refractive-index prism, (ii) a sensor chip coated with a thin metallic layer optimized for plasmon excitation, and (iii) a microfluidic flow channel that delivers the analyte or sample to the sensor surface for analysis. Surface plasmons are basically the charge density oscillations that propagate along the metal–dielectric interface with electric field decaying exponentially in both the medium. [18]

6.2-Optical properties of Graphene:

Among the variety of nanostructured materials, graphene has recently emerged as a unique option for enhancing the sensitivity of various types of biosensors due to its exceptional optical and electrical properties. Graphene, discovered recently, is a single layer of graphite and one atom thick two-dimensional plane of sp^2 bonded carbon atoms arranged in honeycomb lattice [19]. The properties include zero band gap, high electron mobility, the same mobility for charge carriers (i.e. electrons and holes) and 2D structure. Due to these properties and relatively low cost, graphene may be used in fabrication of excellent sensors [20].

For pristine graphene (Fermi level E_f is equal to the energy at Dirac point), there is only one kind of electron–hole excitation (interband transition) at low electron hopping energy because of the empty π band (conduction band) and the completely filled π^* band (valence band). While for n/p-doped graphene, E_f will be away from the Dirac point, which may cause the other kind of electron–hole excitation: intraband transition [21]. In graphene, interband transitions occur when electrons are excited from the valence band to the conduction band, crossing the Dirac point. These transitions become prominent in undoped or lightly doped graphene at higher photon energies-typically in the infrared to visible range-when the photon energy exceeds twice the Fermi energy [22,23]. In contrast, intraband transitions involve electronic excitations within the same energy band, either the conduction or valence band. In graphene, intraband transitions are primarily associated with low-energy (terahertz to far-infrared) absorption and are more significant in doped graphene where free carriers are present Taking the n-doped case as an example, as shown in Fig. 6-1, E_f is higher than the Dirac point, where π band is completely filled and electrons can also be found in the π^* band. The electrons both at the bottom of the conduction band and at the top of the valence band can be excited after absorbing a certain amount of energy and momentum [22,23]. Figure 1 illustrate this type of transition in n-doped graphene.

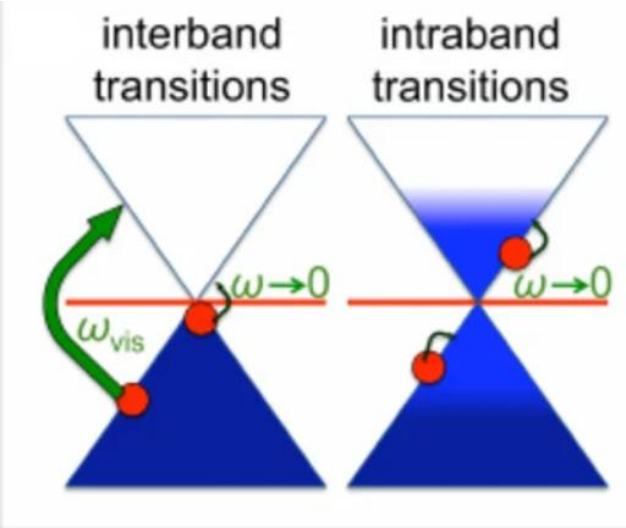

Figure 6-1. Interband and intraband transitions in n-doped graphene, illustrating electronic excitations between valence and conduction bands as well as within the conduction band, governed by the position of the Fermi level and relevant for optical and transport properties. The schematic is taken from reference [23].

Among graphene's many exceptional optical properties, its ability to support surface plasmons has opened a new and rapidly growing field of research known as graphene plasmonic. Unlike conventional plasmonic materials such as gold and silver, which exhibit strong plasmonic activity in the visible spectrum, graphene supports plasmonic resonances predominantly in the terahertz (THz) to mid-infrared (mid-IR) range. This spectral region is particularly important because it overlaps 50with the vibrational modes of many molecules and biological signatures, making graphene plasmonic highly relevant for sensing and spectroscopy applications.

Graphene plasmons can be efficiently excited under specific conditions, such as through nanostructuring (e.g., into ribbons or disks) or by coupling with near-field probes. Once excited, these plasmons demonstrate deep subwavelength confinement, meaning they can trap and guide electromagnetic energy in regions much smaller than the wavelength of incident light. The resulting field enhancement is significantly stronger than that achieved with noble metals, making graphene an excellent platform for strong light–matter interaction—a critical requirement in applications like biosensing**,** infrared photodetection**,** and nonlinear optics [24].

A key advantage of graphene plasmons lies in their electrical tunability. The plasmon resonance frequency in graphene can be dynamically adjusted by modulating the carrier concentration, either through electrostatic gating or chemical doping. This tunability enables the design of reconfigurable and broadband photonic devices, in contrast to traditional metal-based plasmonics, which have fixed optical properties [25].

Moreover, in the THz to mid-IR range, graphene exhibits lower propagation losses compared to its metallic counterparts. This is primarily due to the lower scattering rates of Dirac fermions in high-quality graphene, which result in longer plasmon lifetimes and improved efficiency [26]. Performance can be further enhanced by encapsulating graphene with hexagonal boron nitride (hBN), black phosphorene, or other high-quality dielectrics, which reduce impurity scattering and increase the plasmon propagation length and quality factor [27].

These unique characteristics have enabled the development of advanced plasmonic devices, including highly sensitive biosensors, terahertz modulators, photodetectors, and metamaterials. Additionally, graphene's atomic thinness and mechanical flexibility make it well-suited for integration into flexible and wearable optoelectronic systems [28].

In conclusion, graphene plasmonics offers a powerful, tunable, and compact platform for manipulating light at the nanoscale, particularly in the mid-IR and THz domains. With its unparalleled combination of high field confinement, low losses, and tunability, graphene is poised to become a cornerstone material in the development of next-generation photonic and optoelectronic technologies.

6.3- Plasmonic theory:

The theory of plasmonic has evolved from classical electromagnetism and quantum mechanics, primarily concerning the interaction of light with free electrons in a metal. Following J. J. Thomson's discovery of the electron, Paul Drude introduced a model in 1909 to explain how metals conduct electricity and heat. Drawing inspiration from the kinetic theory of gases, Drude's approach treated the conduction electrons in metals as a type of free electron gas. In this model, these loosely bound electrons move freely through a background of fixed, widely spaced positive ions—composed of atomic nuclei and tightly bound inner electrons—responding to applied electromagnetic fields [29].

In this model, the only interaction considered is the instantaneous collision between electrons and stationary ions. These collisions occur randomly with a probability defined by the inverse of a characteristic time, τ^{-1} , where τ is referred to as the relaxation time—a parameter introduced to describe the average time between collisions. As a result, the classical motion of an electron within a metal under the influence of an external electric field can be described accordingly $E = E_0 e^{-i\omega t}$, becomes [30]:

$$\frac{dp(t)}{d(t)} = -\frac{p(t)}{\tau} + eE(t) \qquad (6\text{-}1)$$

Where $e > 0$ is the elementary charge. To find a steady-state solution that mirrors the harmonic time variation of the applied field, we apply a Fourier transform to equation (6-1), which results in [31]:

$$-i\omega P(\omega) = -\frac{P(\omega)}{\tau} - eE(\omega) \tag{6-2}$$

Whose solution is:

$$P(\omega) = \frac{eE(\omega)}{i\omega - \tau^{-1}} \tag{6-3}$$

Moreover, notice that the current density due to n_e electrons per unit volume, travelling with net velocity v, is $J = en_e v$. Hence, one can write [32]:

$$J(\omega) = \frac{en_e P(\omega)}{m_e} = -\frac{e^2 n_e}{m_e}\frac{1}{\tau - i\omega}E(\omega) \tag{6-4}$$

Where m_e is the mass of the electron. By comparing the result (6-4) with the relation $J = \sigma E$, an expression for the optical conductivity can be determined [32]:

$$\sigma(\omega) = \frac{\frac{e^2 n_e}{m_e}}{\tau^{-1} - i\omega} \tag{6-5}$$

It will be useful for what follows to note that the conductivity and the dielectric function are linked through the following relationship [33]**:**

$$\varepsilon(\omega) = 1 + i\frac{\sigma(\omega)}{\varepsilon_0 \omega} \tag{6-6}$$

Allowing us to write:

$$\varepsilon(\omega) = 1 - \frac{\omega_p^2}{\omega^2 + i\tau^{-1}\omega} \tag{6-7}$$

Where $\omega_p^2 = \frac{e^2 n_e}{m_e \varepsilon_0}$ denotes the plasma frequency of the free electron gas [31].

We now use the previously introduced formalism to explore how an interface between two materials with distinct optical characteristics can give rise to surface-bound modes with spatial confinement smaller than the wavelength of light. These particular solutions to Maxwell's equations are known as surface plasmon-polaritons (SPP). To start, we examine the most basic configuration that supports SPPs: a flat interface separating a dielectric and a metal. For simplicity, we assume that both materials are isotropic and extend infinitely in their respective regions, with the dielectric occupying the region $z < 0$, as illustrated in Fig. 6-2 [6].

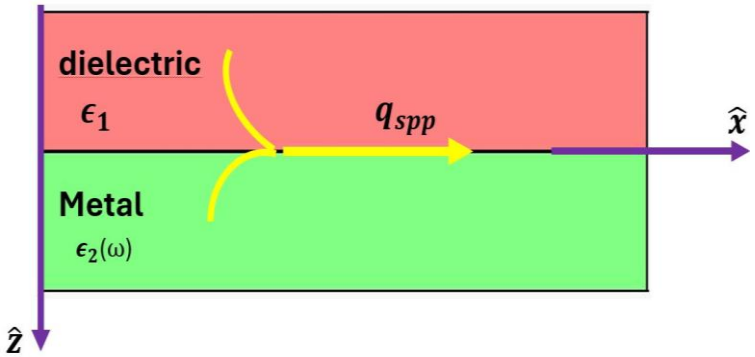

Figure 6-2. Schematic illustration of a surface plasmon–polariton propagating along the interface between a metal and a dielectric, showing the coupled oscillations of electromagnetic waves and surface charge density confined near the boundary

The dielectric medium is characterized by a positive real dielectric constant, ϵ_1, whereas the electromagnetic properties of the metal will be taken into account by a complex, frequency-dependent, dielectric function, $\epsilon_2(\omega)$, of the form (equation 6-7) [34]:

$$\epsilon_2(\omega) = 1 - \frac{\omega_p^2}{\omega^2 + i\tau^{-1}\omega} \tag{6-8}$$

As shown in what follows, in the spectral region where $Re\{\epsilon_2(\omega)\} < 0$, the dielectric-metal interface supports longitudinal waves that are tightly confined to the interface between the two media (see, for instance, Fig. 6-2). These surface waves are Surface Plasmon-Polaritons (SPP) modes. By considering Transverse Magnetic (TM) the solution can be as follow [31]:

$$E_j(r,t) = (E_{j,x}\hat{x} + E_{j,z}\hat{z})e^{-k_j|z|}e^{i(qx-\omega t)} \tag{6-9}$$

$$B_j(r,t) = E_{j,y}\hat{y}e^{-k_j|z|}e^{i(qx-\omega t)} \tag{6-10}$$

where the index j = 1,2 identifies the medium as in Fig.6-2. Inserting equations (6-9) and (6-10) into Maxwell's equations (while assuming that the materials are non-magnetic, μj = μ0) [31]:

$$\nabla \times E_j = -\frac{\partial B_j}{\partial t} \tag{6-11}$$

$$\nabla \times B_j = -\frac{\epsilon_j}{C^2}\frac{\partial E_j}{\partial t} \tag{6-12}$$

Yields:

$$B_{j,y} = -\frac{\omega\epsilon_j}{C^2 q}E_{j,z} \tag{6-13}$$

$$B_{j,y} = -isgn(z)\frac{\omega\epsilon_j}{C^2 k_j}E_{j,x} \tag{6-14}$$

$$E_{j,x} = -isgn(z)\frac{k_j}{q}E_{j,z} \tag{6-15}$$

$$k_j = \sqrt{q^2 - \frac{\epsilon_j \omega^2}{c^2}} \qquad (6\text{-}16)$$

Maxwell's equations require the continuity of the tangential components (relative to the interface) of the electric and magnetic fields across the interface (at z = 0) [31],

$$E_{1,x} = E_{2,x} \qquad (6\text{-}17)$$

$$B_{1,y} = B_{2,y} \qquad (6\text{-}18)$$

Making use of equation 6-(14) to eliminate the magnetic field amplitudes in the boundary conditions (6-17) and (6-18), we arrive at the following pair of equations [31]:

$$E_{1,x} = E_{2,x} \qquad (6\text{-}19)$$

$$\frac{\epsilon_1}{k_1} E_{1,x} = -\frac{\epsilon_2}{k_2} E_{2,x} \qquad (6\text{-}20)$$

The linear system composed by equations (6-19) and (6-20) has a non-trivial solution if

$$\frac{\epsilon_1}{k_1(q,\omega)} + \frac{\epsilon_2}{k_2(q,\omega)} = 0 \qquad (6\text{-}21)$$

Note that in equation (6-21) we emphasize the fact that $k_{1,2}$ depends on the frequency as well as on the wavevector in accordance with equation (6-16). Moreover, in order to have an electromagnetic wave confined to the interface which follow equation (6-21), if $\epsilon_1 > 0$, then we must have $Re\{\epsilon_2(\omega)\} < 0$. This means that SPP can only exist at interfaces between materials whose (real parts of the) dielectric permittivities have opposite signs, such as an interface between an insulator and a metal [31].

We can write a more explicit relation for the SPP wavevector, q_{SPP}, as a function of the frequency, by substituting equation (6-16) into equation (6-21), obtaining [31]:

$$q_{SPP} = \frac{\omega}{c} \sqrt{\frac{\epsilon_1 \epsilon_2(\omega)}{\epsilon_1 + \epsilon_2(\omega)}} \qquad (6\text{-}22)$$

6.4- Plasmonic in monolayer of Graphene:

We begin our study of surface plasmon in graphene by considering a system consisting in a single graphene sheet cladded between two semi-infinite dielectric media, characterized by the real dielectric constants (relative permittivity) ϵ1 and ϵ2, referring respectively to the top and bottom dielectrics, as depicted in Fig.6-3.

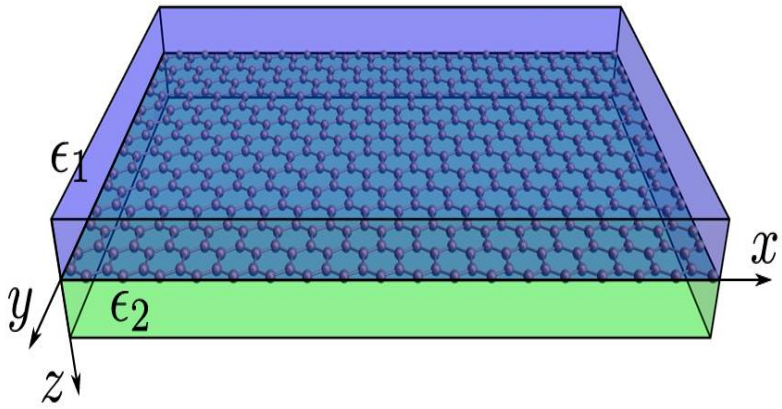

Figure 6-3. Illustration of a single graphene sheet sandwiched between two semi-infinite insulators with dielectric constants ϵ1 and ϵ2. Medium 1 occupies the z <0 half-space and the z > 0 half-space is occupied by medium 2. The graphene sheet is located at the z = 0 plane.

Let us assume a solution of Maxwell's equations, in the form of a p-polarized electromagnetic wave (TM wave). As already discussed, we use the ansatz [31,35,36]

$$E_j = (E_{j,x}\hat{x} + E_{j,z}\hat{z})e^{-k_j|z|}e^{iqx} \quad (6\text{-}23)$$

$$B_j = E_{j,y}\hat{y}e^{-k_j|z|}e^{iqx} \quad (6\text{-}24)$$

where j = 1,2 refers to the dielectric media with relative permittivity ϵ1, ϵ2. Equations (6-23) and (6-24) describe an electromagnetic surface wave which is confined to the neighbourhood of the graphene sheet and propagates along the $\hat{x}$-direction. Using eqation (6-23) and (6-24) into Maxwell's equations (6-11) and (6-12) for dielectric media [31,35,36]:

$$-sgn(z)k_jE_{j,x} - iqE_{j,z} = i\omega B_{j,y} \quad (6\text{-}25)$$

$$sgn(z)k_jB_{j,x} = -\frac{i\omega\epsilon_j}{C^2}E_{j,x} \quad (6\text{-}26)$$

$$iqB_{j,y} = -\frac{i\omega\epsilon_j}{C^2}E_{j,z} \quad (6\text{-}27)$$

which can be rewritten with respect to the magnetic field amplitudes, while also obtaining an expression for $k_j(q,\omega)$:

$$E_{j,x} = isgn(z)\frac{C^2k_j}{\omega\epsilon_j}B_{j,y} \quad (6\text{-}28)$$

$$E_{j,z} = -\frac{C^2q}{\omega\epsilon_j}B_{j,y} \quad (6\text{-}29)$$

$$k^2 = q^2 - \frac{\omega^2\epsilon_j}{C^2} \quad (6\text{-}30)$$

The boundary conditions linking the electromagnetic fields at z = 0 read:

$$E_{1,x}(x,z) = E_{2,x}(x,z) \quad (6\text{-}31)$$

$$B_{1,y}(x,z) - B_{2,y}(x,z) = \mu_0 j_x(x) = \mu_0 \sigma_{xx} E_{2,x}(x,z) \quad (6\text{-}32)$$

which assures the continuity of the tangential component of the electric field and the discontinuity of the tangential component of the magnetic field across the interface. Additionally, we further assume that graphene is a truly two-dimensional material, whose entire electromagnetic properties are accounted in its frequency dependent conductivity, σ(ω). Letting $\sigma(\omega) \equiv \sigma_{xx} = \sigma_{yy}$, meaning that graphene's conductivity is isotropic (which is true for unstrained graphene) and substituting the fields into the boundary conditions (6-31) and (6-32), we arrive to:

$$\frac{\epsilon_1}{k_1(q,\omega)} + \frac{\epsilon_2}{k_2(q,\omega)} + \boldsymbol{i}\frac{\boldsymbol{\sigma(\omega)}}{\boldsymbol{\varepsilon_0 \omega}} = 0 \quad (6\text{-}33)$$

which describes the dispersion relation, ω(q), of graphene TM surface plasmon. Meanwhile, the simple geometry of the system, the dispersion relation (6-33) does not have an analytical solution and must be solved by numerical means. In addition, it is clear that Eq. (6-33) only has real solutions when the imaginary part of the conductivity is positive, and its real part vanishes [31,35,36].

6.5- Theory of perfect absorber metamaterial:

Although graphene is optically transparent, it exhibits a remarkably high absorption of approximately 2.3% per monolayer in the optical spectrum, with even greater absorption observed in the terahertz (THz) range. When structured appropriately, graphene films can achieve absorption levels approaching 100%. This enhanced absorption arises from modifications in the surface conductivity due to both a reduction in the effective conductive area and the excitation of plasmonic resonances. Higher absorption can also be attained by stacking multiple conductive graphene layers, separated by dielectric spacers. A basic yet effective configuration involves placing a structured graphene metamaterial layer above a metallic mirror (ground plane), which creates a resonant cavity that enhances light–matter interaction [37].

In most cases, the modelling of graphene metamaterial-based devices relies heavily on numerical simulations and optimization techniques, often involving the analysis of multiple interdependent variables. While effective, this approach can significantly complicate and slow down the design process. To address these challenges, Andrei Andryieuski et al. proposed a simple yet powerful analytical method for describing graphene metamaterials and designing tunable perfect absorbers. Their approach is based on a transmission line analogy, in which the graphene metamaterial is

represented through an effective surface conductivity. Specifically, a thin conductive layer characterized by a complex surface conductivity (2D) surface or point load.

$$\sigma_s = \sigma_s' + i\sigma_s'' \qquad (6\text{-}34)$$

The analysis employs Transition Boundary Conditions (TBCs) to placed at the planar interface between two dielectric media with refractive indices n_1 and n_1 (as illustrated in Fig. 4), is modeled as a junction between two transmission lines. When the thickness of the conductive layer is much smaller than the operating wavelength-a condition that holds true for graphene over an ultrabroad spectral range, from radio frequencies to the deep ultraviolet-the layer's thickness can be neglected. As a result, it may be treated as an idealized two-dimensional rigorously account for the interaction of electromagnetic fields with this 2D conductive surface, enabling accurate and physically intuitive modelling [38].

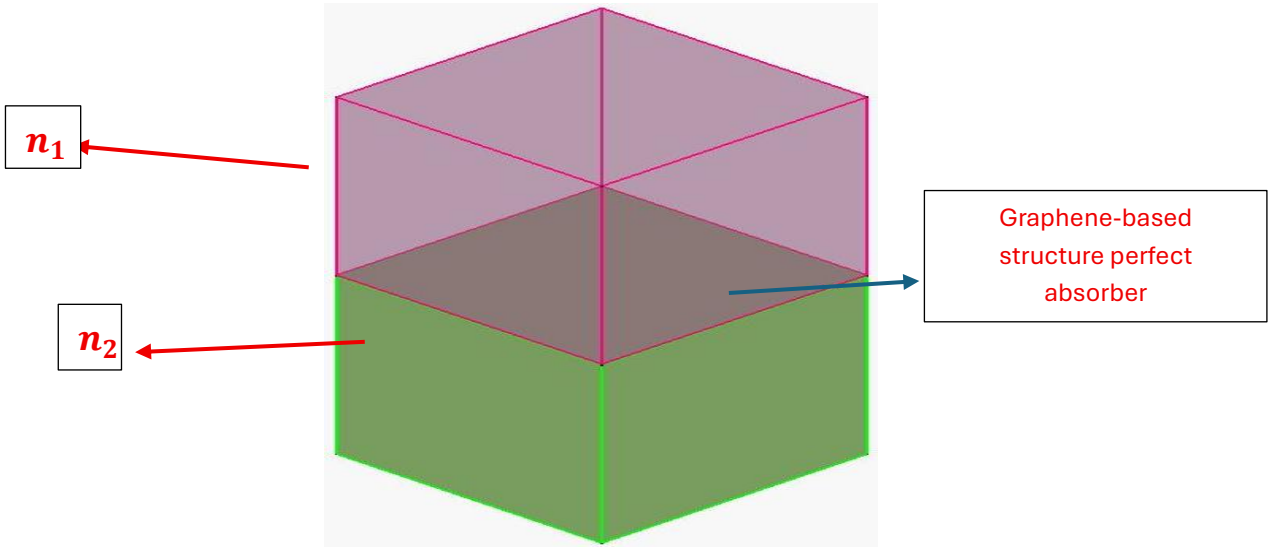

Fig. 6-4. The conductive interface (for example, graphene layer) between two dielectrics is equivalent to a load attached to the junction between two transmission lines.

To prevent any transmission through the structure and enhance the light absorption in the infrared/terahertz frequency range, a perfect electric conductor (PEC) is employed as the back reflector. This configuration effectively blocks transmission and result in near-zero reflection. The absorption rate is determined by the equation A(ω) = 1 − R(ω) − T(ω), where R(ω) and T(ω) represent the reflectance and transmittance, respectively. Due to the complete absence of transmission through the perfect electric conductor layer, the absorption relation is simplified as A(ω) = 1 − R(ω) [39,40].

For the normal incidence the amplitude transmission and reflection coefficients for a wave coming from the first dielectric are [38]:

$$\boldsymbol{r} = \frac{\boldsymbol{n_1 - n_2 - \sigma_s Z_0}}{\boldsymbol{n_1 + n_2 + \sigma_s Z_0}} \quad (6\text{-}35)$$

$$\boldsymbol{t} = \frac{\boldsymbol{2n_1}}{\boldsymbol{n_1 + n_2 + \sigma_s Z_0}} \quad (6\text{-}36)$$

$Z_0 = 120\pi$ Ohm is the free-space impedance. In the case of infinite surface conductivity $\boldsymbol{\sigma_s} = \infty$ the wave will be fully reflected (r = −1). Surface conductivity equal to 0 plays no effect and the formulas become standard Fresnel formulas for the interface between two dielectrics [38].

6.5.1- Effective conductivity of graphene metamaterials:

Along with its linear dispersion, graphene's optical conductivity is the key ingredient in graphene optics and plasmonic, since it contains all the relevant information on the physics governing the electromagnetic interactions between graphene and external stimuli such as electromagnetic radiation or fast electrons. To better characterize the conductivity, it is useful to split this physical quantity into two distinct contributions: one describing intraband transitions (transitions within the conduction (or valence) band where the momentum is not conserved), and another accounting for interband transitions (vertical transitions from the valence to the conduction band, in which case there is momentum conservation), namely

$$\sigma_{gr} = \sigma_{intra}(\omega) + \sigma_{inter}(\omega) \quad (6\text{-}37)$$

It can be derived with the random phase approximation (RPA) theory:

$$\sigma_{intra}(\omega) = \frac{2iK_B T e^2}{\pi\hbar^2(\omega + i\tau^{-1})} Ln(2\cosh(\frac{E_f}{2K_B T}) \quad (6\text{-}38)$$

$$\sigma_{inter}(\omega) = \frac{e^2}{4\hbar}[\frac{1}{2} + \frac{1}{\pi} + \arctan\left(\frac{\hbar\omega - E_f}{2K_B T}\right) - \frac{i}{2\pi} Ln \frac{(\hbar\omega + E_f)^2}{(\hbar\omega - E_f)^2 + (2K_B T)^2} \quad (6\text{-}39)$$

where e is the electron charge, K_B is the Boltzmann's constant, ħ is the reduced Planck's constant, T is the temperature, and ω is the angular frequency of incident light. τ is the relaxation and E_f is the Fermi level [40,41,42,43].

In this study, a graphene-based perfect absorber sensor utilizing surface plasmon resonance was simulated for the detection of β2-microglobulin protein. The simulation was conducted using COMSOL Multiphysics software. Fig. 6-5 illustrates the structure of the proposed sensor along with its geometric dimensions.

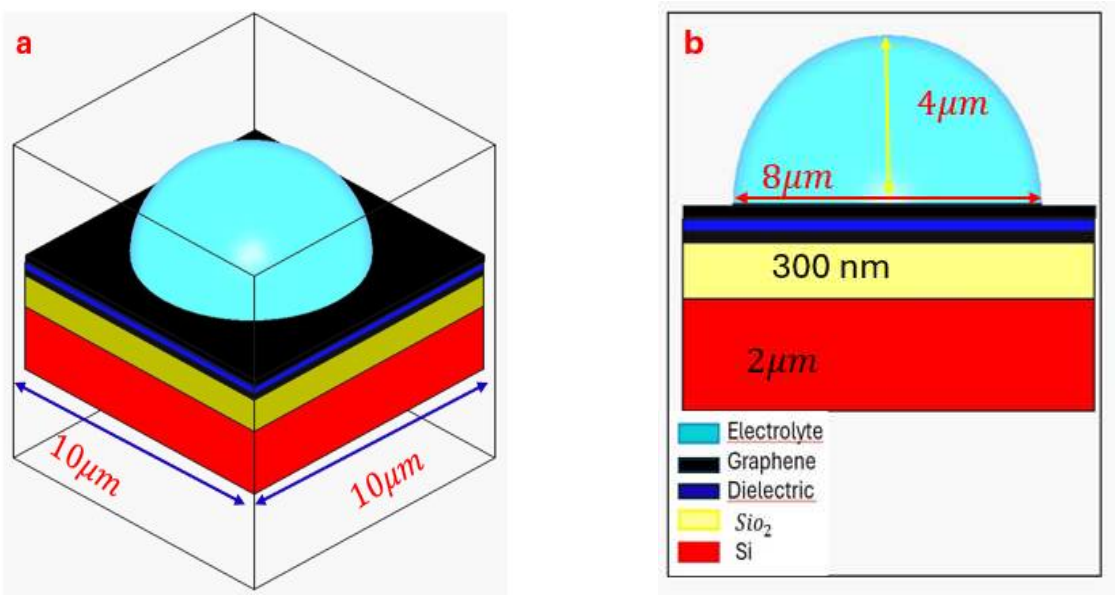

Figure 6–5. Schematic representation of the surface plasmon resonance (SPR) structure, showing (a) a three-dimensional view of the full configuration and (b) a two-dimensional cross-sectional view highlighting the layer arrangement and plasmon excitation at the metal–dielectric interface.

6-6- Theory of electro gating:

Electrostatic gating using electrolytes is a powerful approach for controlling the electronic properties of atomically thin two-dimensional materials such as graphene. The linear dispersion relationship between the energy and momentum of the charge carriers centred around the Dirac point makes graphene a zero-gap semiconductor with a linear dependence of the density of electronic states (DOS)on the Fermi level (E_f) [44]. During nearly two decades of research, it has become apparent that gating using ionic electrolytes, including organic/aqueous solutions, ionic liquids, and solid polymer electrolytes, is among the most efficient ways to induce large densities of charge carriers in graphene [45]. Regardless of the type of gate employed, the mechanism of electrostatic doping remains the same: buildup of the charge upon application of a voltage between graphene and the gate electrode leads to a change in the charge carrier density in graphene and therefore a change in E_f. The operating principle of electrostatic gating involves the creation of a capacitor between graphene and the gate electrode. Application of the gate voltage creates an electrostatic difference between graphene and the gate electrode (φ), which polarizes the graphene/electrolyte interface. This leads to charge accumulation and formation of an electrical double layer (EDL)of ions and counterions at the electrolyte side of the interface. The emergence of EDL induces accumulation of the opposite-sign charge carriers on the graphene side of the interface, which in turn shifts the graphene E_f [46]. The gating process can be described by the following relationship [21]:

$$E_g = \frac{E_f}{e} + \varphi \qquad (6\text{-}40)$$

The Fermi energy in graphene changes as $E_f(n) = \hbar v_f \sqrt{\pi n}$, where $v_f = 1.1 * 10^6 \frac{m}{s}$ is the Fermi velocity and the top gate $\varphi = \frac{ne}{C_{EDL}}$. From equation (40) we get and E_g is fermi energy of graphene after applying electro gating [44].

$$V_g = \frac{\hbar v_f \sqrt{\pi n}}{e} + \frac{ne}{C_{EDL}} \quad (6\text{-}41)$$

By using constant parameters, the final equation which allows us to estimate the doping concentration at each top-gate voltage become as below:

$$V_g = 1.16 * 10^{-7} \sqrt{n} + \frac{ne}{C_{EDL}} \quad (6\text{-}42)$$

The first and simplest model introducing the concept of the formation of a double layer at the electrochemical interface and thus describing the structure of the EDL, was formulated by Helmholtz. Helmholtz envisaged that the total charge on the electrode is balanced by a monolayer of ions of opposite charge located adjacent to the surface, referred to as the Helmholtz layer. so, the Helmholtz layer capacitance computed through below equation [47,48,49, 50,51]:

$$C_H = \frac{\varepsilon_0 \varepsilon_H}{d_H} \quad (6\text{-}43)$$

where ε_0 is the permittivity of free space, ε_H the relative permittivity of the electrolyte inside the Helmholtz layer and d_H size of the solvated ions. In more detail, Helmholtz model, it does not consider three important physical factors, which are the applied potential, the interplay between the randomized thermal motion of the ions and that imposed by the polarity of the electrode as well as the interaction between solvent molecules' dipole moments and the electrode [48].

Gouy and Chapman postulated that even though the charge at the electrode is strictly located at the surface, this might not be the case for the solution side. In dilute electrolytes, one must consider the low density of charge carriers in the solution phase. Under such conditions, the excess charge required to counterbalance that confined to the surface of the electrode will be distributed within a larger region in the solution. This newly introduced layer will have a composition different from the bulk and it will exhibit characteristics of a diffuse layer. The potential within the diffuse layer is expected to drop smoothly from the surface of the electrode to the bulk, with a decreasing gradient across the layer. Adopting this approach for the case of a symmetrical electrolyte, the expression for the Gouy–Chapman differential capacitance per unit area is derived to be [48, 7, 51]:

$$C_{Gc} = \frac{\varepsilon_r \varepsilon_0}{\lambda_D} \cosh\left(\frac{2e\varphi}{2K_B T}\right) \quad (6\text{-}44)$$

Where λ_D is a Debye length which given by $\lambda_D = (\frac{2ce^2}{\varepsilon_r \varepsilon_0 K_B T})^{-\frac{1}{2}}$ for a monovalent electrolyte, where c is the concentration of the electrolyte, e is the electric charge and $K_B T$ is the thermal energy [52] .

The next step towards the establishment of a solid theory for the structure of the EDL, was made by Stern.His suggestion was to combine the approaches of Helmholtz and Gouy Chapman and thus consider the electrochemical interface as consisting of two layers. In the first compact layer, the charge on the solution side is located close to the electrode surface, the Helmholtz layer, and the rest of it is distributed in the solution within the limits defined by the compact layer and the bulk solution, the Gouy–Chapman diffuse layer. Hence, as would be expected for two electrical capacitors connected in series, we can write the reciprocal of the total capacitance of the EDL as [53]:

$$\frac{1}{C_{EDL}} = \frac{1}{C_H} + \frac{1}{C_{Gc}} \qquad (6\text{-}45)$$

While extensive research on graphene has emphasized its exceptional electrical and structural characteristics, an equally important parameter-quantum capacitance-has received comparatively limited attention. In the present study**,** direct measurements of the quantum capacitance of graphene were performed under varying protein concentrations to explore its sensitivity to biomolecular interactions. The results show that the quantum capacitance exhibits a nonzero minimum at the Dirac point**.** These findings align with prior studies, including those by Jilian Xia *et al.*, which suggest that charged impurities in the graphene environment play a significant role in modulating quantum capacitance by altering the local carrier density. Such deviations from ideal theoretical behaviour underscore the impact of disorder and environmental factors on graphene's electronic response [54].

To carry out the theoretical computation, a minimal model was employed in which the impurity concentration serves as the sole adjustable parameter. For ideal, impurity-free graphene, the quantum capacitance can be analytically derived based on the density of states arising from its linear energy–momentum dispersion relation [54]**:**

$$C_Q = \frac{2e^2 K_B T}{\pi(\hbar v_f)^2} Ln[2\left(1 + cosh\frac{eV_{ch}}{K_B T}\right)] \qquad (6\text{-}46)$$

where ħ is the Planck constant, e the electron charge, K_B the Boltzmann constant, $v_f = \frac{C}{300}$ the Fermi velocity of the Dirac electron (The symbol *c* represents the speed of light in a vacuum), and $V_{ch} = \frac{E_f}{e}$ is the potential of graphene. When $eV_{ch} \gg K_B T$ equation number (26) reduced to below equation (54):

$$C_Q = \frac{2e^2}{\hbar v_f \sqrt{\pi}} \sqrt{n} \qquad (6\text{-}47)$$

The total capacitance of a graphene-based system in an electrolyte environment arises from the series combination of two distinct components: the quantum capacitance of graphene and the electric double-layer (EDL) capacitance formed at the graphene–electrolyte interface. Due to this series configuration, the overall capacitance C_t is governed by the reciprocal sum of the individual capacitances, expressed as [53,54]:

$$\frac{1}{C_t} = \frac{1}{C_{EDL}} + \frac{1}{C_Q} \qquad (6\text{-}48)$$

In this research we use electrolyte contain β_2- macroglobulin (β2M) with different concentration as sample to affect charge density of graphene consequently the fermi energy of graphene will be changed. Result of the Molecular Dynamics (MD) which conducted by Professor Georgia Brancolini showed that the EDL near the graphene surface is affected not only by ions but also by large biomolecules like β2M. Because β2M has a distinct size, shape, and surface charge distribution, it influences the local potential differently than small ions. β2M is a protein of 12 kDa in terms of molecular mass and it has a diameter of around 3-nanometers. When β2M is in proximity (e.g., at 50 mM), it will alter the Helmholtz potential in a manner specific to its total charge. In this calculations, β2M at a given ionic strength, such as 50 mM, will generally carry a net negative charge, resulting in a net charge of −2 for the Wild Type protein. During atomistic Molecular Dynamics simulations, they observed that the protein lies horizontally on the graphene surface with a patch that involves C strand (Ile35, Val37, Leu39), C' strand (Glu44, Arg45) and CD loop (Ile46, Lys48). Glu44 is a negatively charged residues, Arg45 and Lys48 are positively charged residues, Ile35, Val37, Leu39 and Ile46 are neutral residues. Since β2M can adsorbs directly, it will generate a stable and distinct signal due to its size and charge. This adsorption alters the graphene's surface potential, detectable by changes in the sensor response [55].

6-7- Result and discussion:

To calculate the electric field and electrostatic potential within the Electric Double Layer (EDL) caused by the presence of a protein near the graphene surface, we begin with the Poisson equation. After designing the computational model, we generated a series of plots and graphs to visualize and compare key parameters. These visualizations allowed for a comprehensive evaluation of how incorporating quantum capacitance influences both the electric field and potential. The electric field distribution and mass transport behaviour were analysed by solving an electrostatic problem governed by the Poisson equation, $\nabla(\varepsilon\varepsilon_0\nabla\varphi) = 0$, was solved in the compact layer. In the diffuse layer, a

coupled Nernst–Planck and electrostatic model was employed to capture the transport phenomena more accurately [58,59]

$$\frac{\partial c_i}{\partial t} = \nabla(D_i \nabla c_i + z_i F D_i c_i \nabla \frac{\varphi}{RT}) \qquad (6\text{-}49)$$

and $\nabla(\varepsilon\varepsilon_0\nabla\varphi) = \rho$, where $\rho = \sum z_i c_i$, is solved in the electrolytic domain outside of the compact layer. HereD_i , z_i, andc_i are respectively the diffusivity, the charge valence and the concentration of the protein species i, t is time, F is the Faraday constant, R is the gas constant, T is the absolute temperature, φ is potential, ε is the dielectric constant, ε_0 is the vacuum permittivity, and ρ is charge density. Fig 6-6(a-b) illustrates the migration of protein, as well as the distribution of electric potential and electric field within the electric double layer (EDL) in stern model of EDL and fig 6-7(a-b) stern model by considering impact of quantum capacitance in computation [47,58].

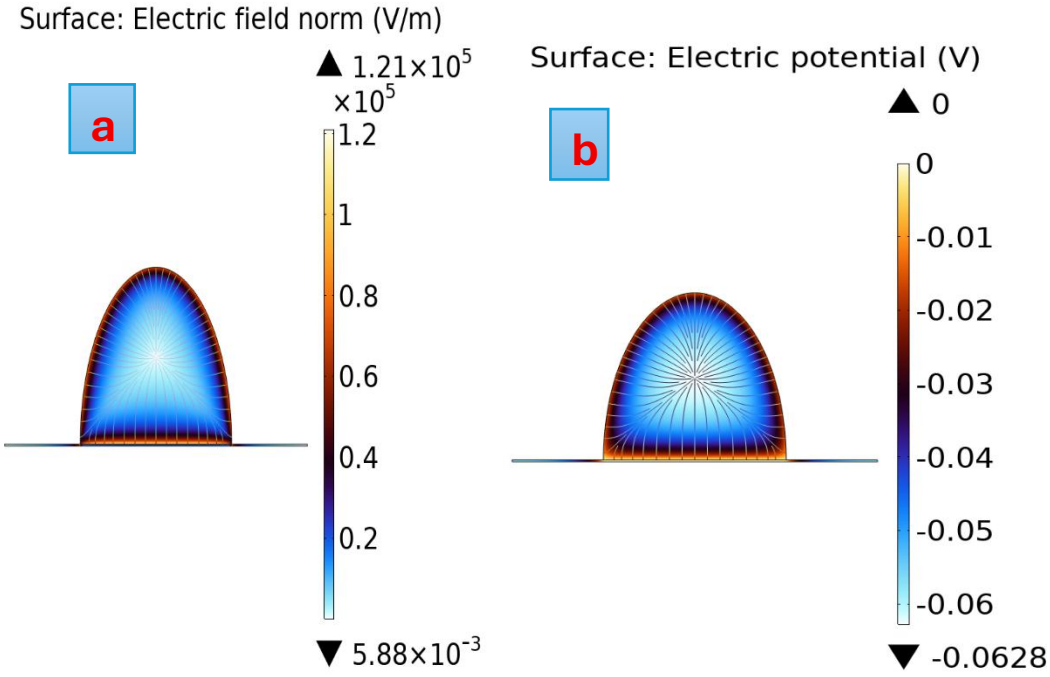

Figure 6-6. (a) Electric field, (b) electric potential in the Stern model of the electrical double layer (EDL); incorporating quantum capacitance

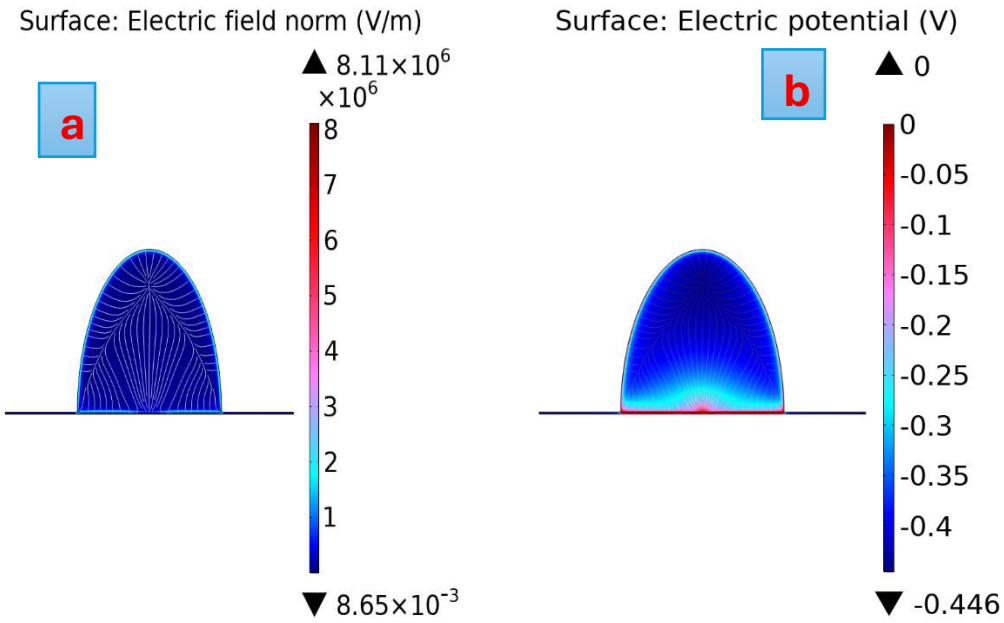

Figure 6-7. (a) Electric field, (b) electric potential in the Stern model of the electrical double layer (EDL); incorporating quantum capacitance.

Next step is a calculation of the potential within the layer at different concentrations of $\beta_2 - microgloblien$ and varying distances from the electrolyte-graphene interface. Due to the pivotal influence of the electrolyte potential within the broader computational model, this parameter was first assessed at two distinct concentrations while systematically altering the separation from the electrode–electrolyte boundary. The outcomes of these simulations are illustrated in Figures 8 and align well with the trends predicted by Equation (6-50) [52].

$$\varphi(x) = \varphi_0(x)\exp\left(\frac{-x}{\lambda_D}\right) \qquad (6\text{-}50)$$

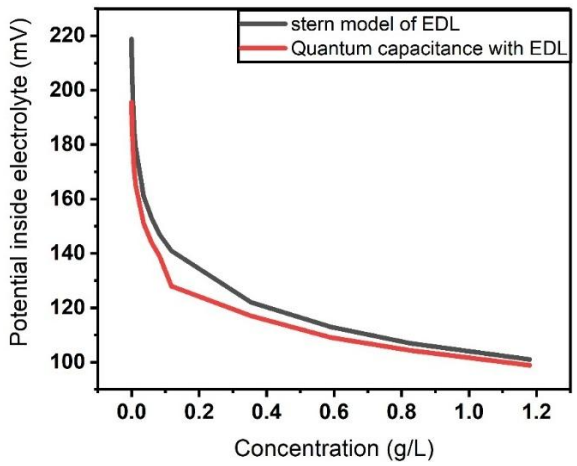

Figure. 6-8. Electrolyte Potential for (a) the Stern Model of the EDL and (b) the Stern Model of the EDL Considering the Effect of Quantum Capacitance

To investigate the broadband absorption properties of the graphene-based structure, a frequency-domain solver utilizing the finite element method (FEM) is adopted. In order to suppress transmission and maximize electromagnetic wave absorption within the infrared to terahertz frequency range, a perfect electric conductor (PEC) is strategically placed as a back reflector. This setup serves to eliminate transmitted waves while simultaneously minimizing reflection, thereby enabling highly efficient light absorption across the targeted spectrum. Figure 9 illustrates the band spectrum of the proposed structure. Since the primary objective of this study is to investigate the influence of electrostatic gating on the absorption and reflection performance-specifically, the effect of varying the Fermi energy of graphene-we evaluate the absorption and reflection characteristics at different Fermi energy levels. After identifying the Fermi energy value at which maximum absorption and minimum reflection occur, that optimal value is selected for further analysis and implementation.

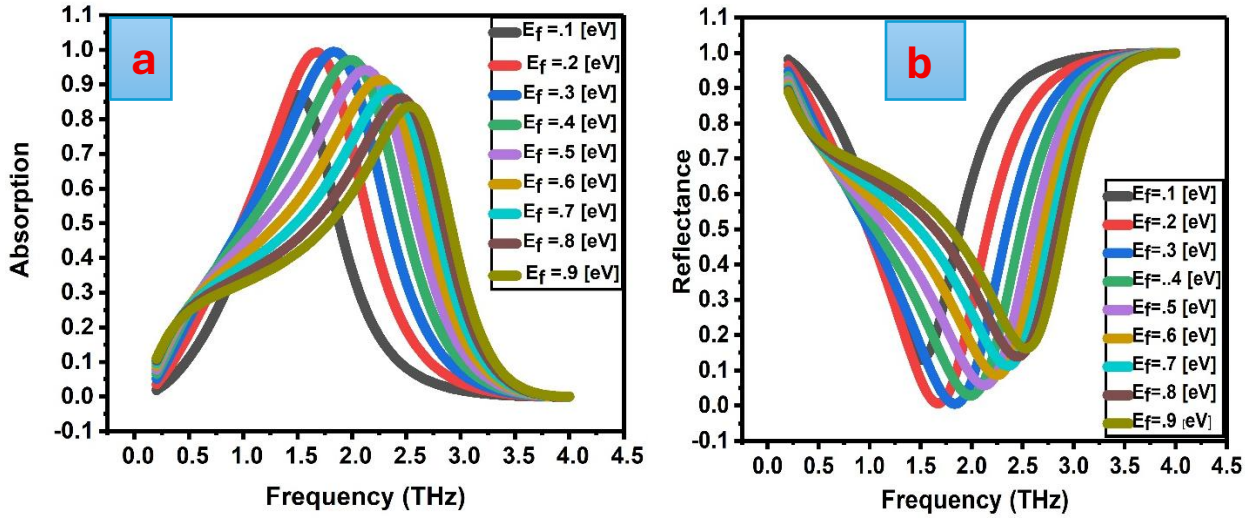

Figure.6-9. Optical response of graphene at different Fermi energy levels. (a) Absorption spectra and (b) reflectance spectra of graphene for Fermi energy values ranging from 0.1 to 0.9 eV (step of 0.1 eV), illustrating the tunability of graphene's optical properties through Fermi level modulation.

The graphene-based structure exhibits its highest absorption performance at a Fermi energy level of 0.3 eV. At this specific value, the absorption reaches approximately 99.211%**,** while the corresponding reflection is minimized to an exceptionally low value of 0.00789. These results indicate that the structure is capable of near-perfect absorption and negligible reflection under the given conditions. Owing to this optimal performance, all subsequent simulations and analyses are carried out using a Fermi energy of 0.3 eV, as it ensures the most efficient interaction between the incident electromagnetic waves and the graphene layer.

In the following section, we investigate the effect of specific concentrations of β2-microglobulin on the variation of the Fermi energy and the quantum capacitance of graphene. As previously discussed,

the presence of this protein in proximity to the graphene surface induces a modification in the local charge carrier density. This alteration occurs due to the interaction between the protein's electric field and the delocalized π-electrons of graphene. Since both the Fermi energy and quantum capacitance are directly dependent on the charge carrier density, any variation in the protein concentration will consequently lead to measurable changes in these parameters.

Fig 6-10 illustrates the quantitative effects of different concentrations of β2-microglobulin on the Fermi energy and quantum capacitance. As the concentration increases, the perturbation to the charge distribution becomes more significant, resulting in a noticeable shift in the Fermi level. This shift, in turn, affects the quantum capacitance, which is sensitive to changes in the electronic density of states near the Dirac point.

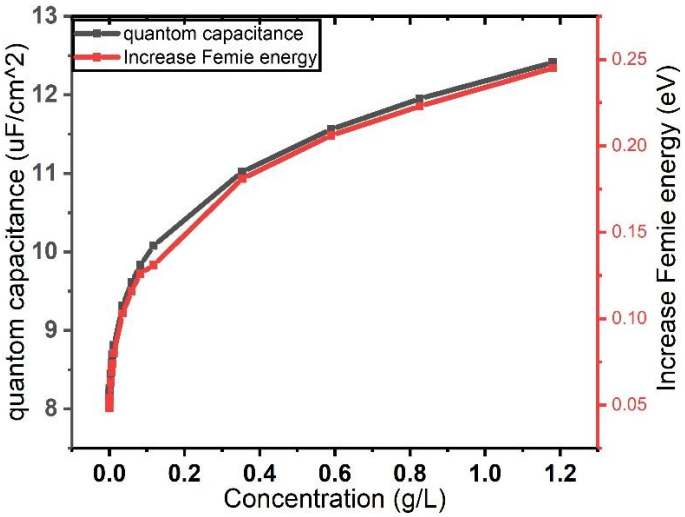

Figure. 6-10. Quantum capacitance and Fermi energy shift at different concentrations of β_2-microglobulin.

In this study, the primary objective is to investigate the effect of protein concentration on the optical properties of graphene-based perfect absorber structure, specifically focusing on the shift in the absorption peak position and the minimum reflectance wavelength. The analysis explores how varying concentrations of β2-microglobulin protein near the graphene surface influence its electronic properties, particularly the Fermi energy level.

As the concentration of β2-microglobulin increases, the extent of Fermi level alteration becomes more pronounced, resulting in a larger shift in the resonance frequency observed in the absorption spectrum. Notably, this shift is directed towards higher frequencies, corresponding to a rightward shift in the spectral position. This rightward shift can be attributed to the interaction between the protein molecules and graphene's surface, which effectively dopes the graphene and increases its

carrier concentration. This doping modifies the plasmonic behaviour of graphene, causing the resonance peaks to move to shorter wavelengths (higher energies).

To accurately model the interaction between charged biomolecules and the graphene surface, the Stern model for the electrical double layer is employed. Figure 11 illustrates this shift clearly, showing the progressive movement of the absorption peak and reflectance minimum to the right as the β2-microglobulin concentration increases. This visualization confirms the direct correlation between protein concentration and the spectral shift of graphene's optical features.

For this research, physiologically relevant concentrations of β2-microglobulin protein are selected: 0.00118 g/L, 0.0118 g/L, 0.118 g/L, and 1.18 g/L. These concentrations correspond to levels commonly found in biological systems and are therefore particularly significant for medical diagnostics and biosensing applications.

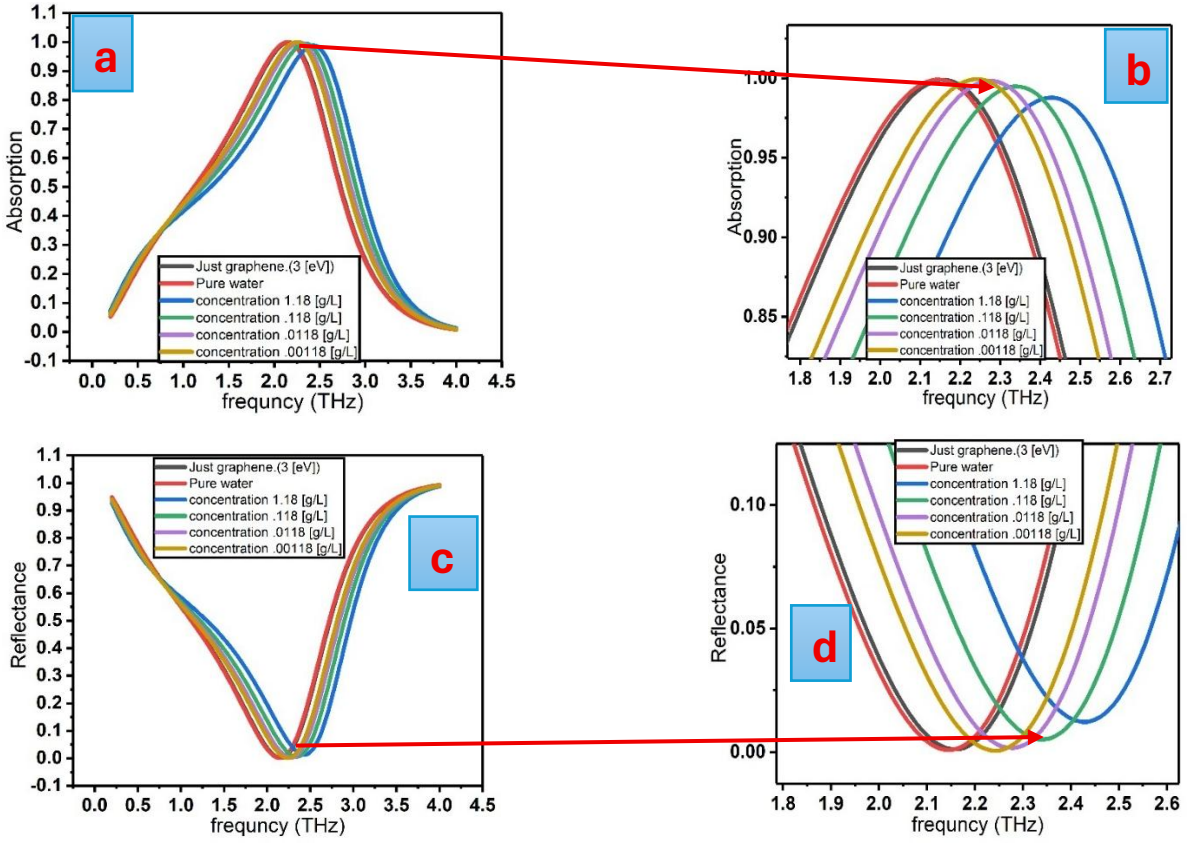

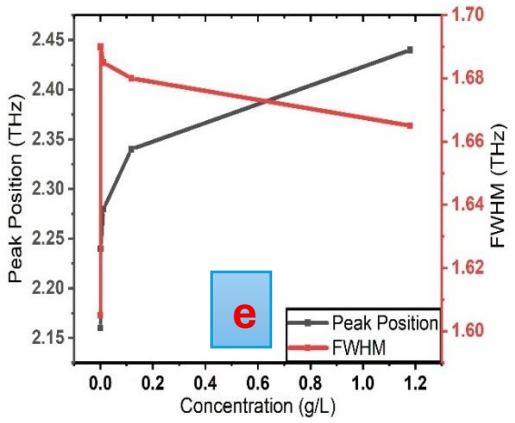

Figure 6-11- . Optical response of graphene in the presence of different concentrations of β2-microglobulin within the Stern model of the electrical double layer (EDL), including the effect of quantum capacitance. (a) Absorption spectra of graphene for varying β2-microglobulin concentrations. (b) Reflectance spectra of graphene for different β2-microglobulin concentrations. (c) Corresponding resonance peak position and full width at half maximum (FWHM) as a function of analyte concentration, illustrating the impact of quantum capacitance on the concentration-dependent optical response. (d) Enlarged view of the absorption spectra highlighting the shift in the resonance peak (region indicated by the red dashed box). (e) Enlarged view of the reflectance spectra showing the corresponding resonance peak shift.

To obtain more accurate results that align closely with experimental observations, it is essential to account for all relevant factors influencing the computational model. Therefore, in Fig. 6-12, the same optical parameters of the graphene-based perfect absorber are calculated while incorporating the impact of quantum capacitance. Considering quantum capacitance allows for a more realistic representation of the charge accumulation behaviour in graphene, particularly under conditions where the density of states near the Dirac point significantly affects the system's electrostatic and optical response.

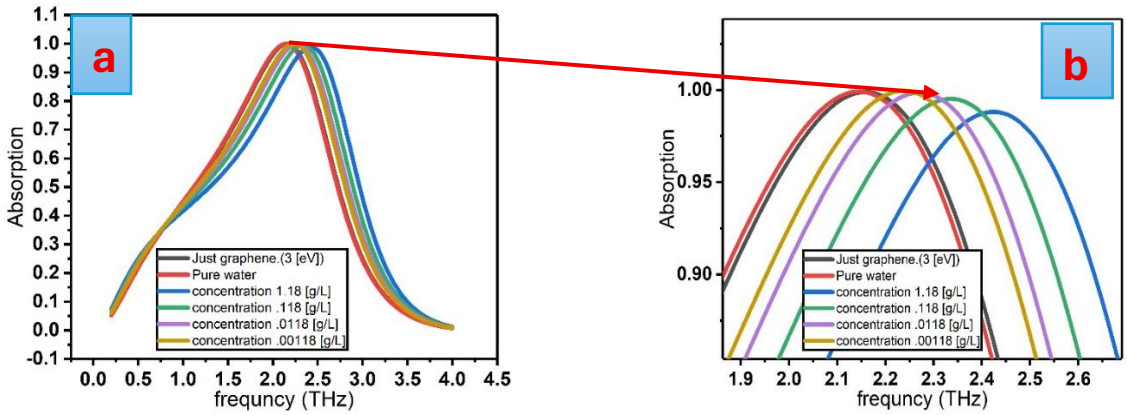

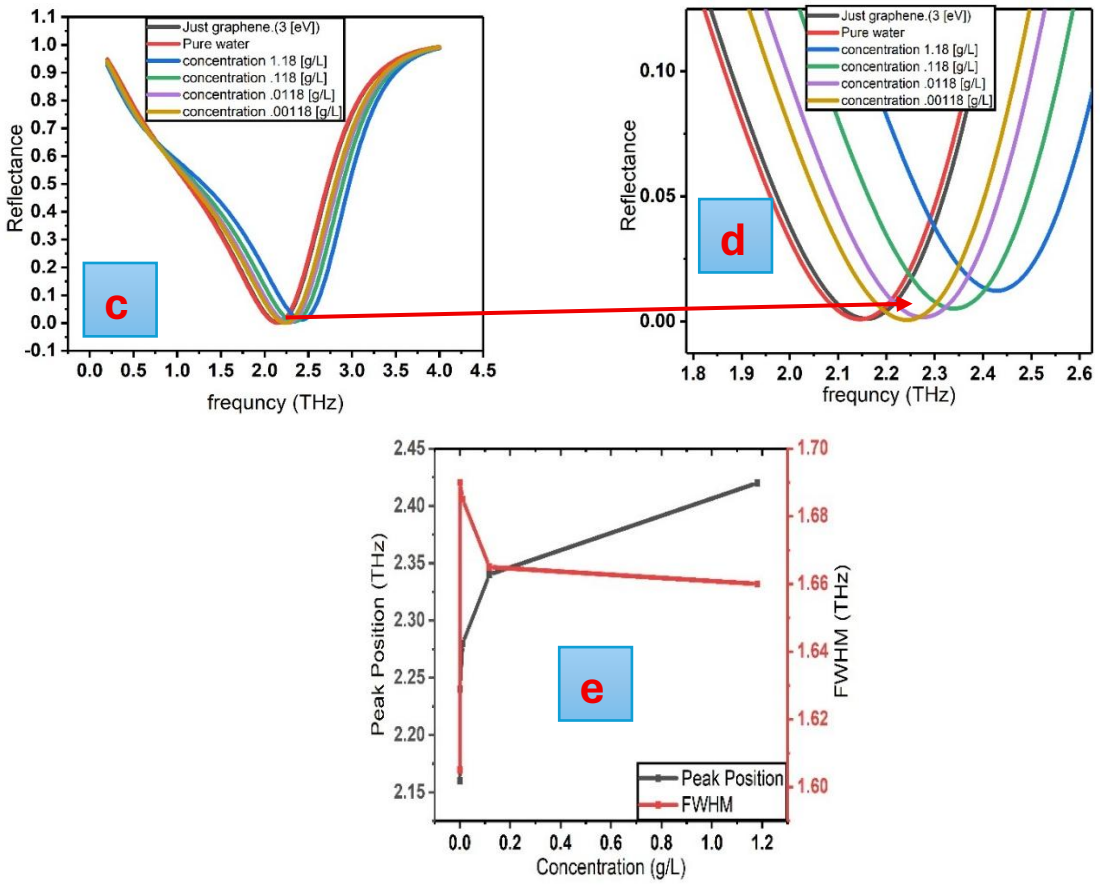

Figure 6- 12- . Optical response of graphene in the presence of different concentrations of β2-microglobulin within the Stern model of the electrical double layer (EDL), including the effect of quantum capacitance. (a) Absorption spectra of graphene for varying β2-microglobulin concentrations. (b) Reflectance spectra of graphene for different β2-microglobulin concentrations. (c) Corresponding resonance peak position and full width at half maximum (FWHM) as a function of analyte concentration, illustrating the impact of quantum capacitance on the concentration-dependent optical response. (d) Enlarged view of the absorption spectra highlighting the shift in the resonance peak (region indicated by the red dashed box). (e) Enlarged view of the reflectance spectra showing the corresponding resonance peak shift

6.7.1-Performance Evaluation Metrics:

Sensor functionality is affected by multiple variables, making it essential to consider these factors when assessing overall performance. The accuracy and reliability of sensor measurements can be impacted by a range of influences. Key performance metrics used to evaluate sensor effectiveness are outlined below [60]:

$$S = \frac{\Delta f}{\Delta C} \tag{6-51}$$

$$FOM = \frac{S}{FWHM} \tag{6-52}$$

$$Q = \frac{f_r}{FWHM} \tag{6-53}$$

$$SNR = \frac{\Delta f}{FWHM} \quad (6\text{-}54)$$

$$DA = \frac{1}{FWHM} \quad (6\text{-}55)$$

In this context, f denotes the frequency, c represents the protein concentration, f_r is the peak position of absorption, S indicates the sensitivity, $FWHM$ refers to the full width at half maximum, Q is the quality factor, FOM stands for the figure of merit, SNR denotes the signal-to-noise ratio, and DA represents detection accuracy. **Table.6-1** illustrates the sensor's performance at two protein concentrations, representing the highest and lowest concentrations used in this study.

Sensor parameters performance	C=1.18 [g/L]		C=.00118 [g/L]	
	EDL in Stern model	EDL + quantom capacitance	EDL in Stern model	EDL + quantom capacitance
S (THz L/g)	.169	.254	33.9	84.74
FOM (L/g)	.097	.141	20.42	51
Q	1.38	1.39	1.35	1.38
SNR	.115	.166	.023	.06
DA (1/THz)	.58	.55	.574	.602

Table. 6-1. Key parameters influencing the performance of the sensor in different models of the electric double layer (EDL) at two concentrations of β_2-macroglobulin.

6.8- Conclusion:

In conclusion, we have presented a novel design for a perfect absorber biosensor operating in the terahertz frequency range. The proposed structure features a layered configuration of graphene/dielectric/graphene, which enables dynamic tunability by adjusting the Fermi energy of the graphene layers. Numerical simulations demonstrate that, by varying the doping level from 0.1 eV to 0.9 eV, the absorber exhibits distinct absorption peaks, with notable resonance observed around 0.3 eV in the terahertz range.

To explore biosensing applications, we introduced an electrolyte containing the protein β2-microglobulin to polarize the graphene surface and modulate its Fermi level. As the concentration of the protein increases, a corresponding shift in the absorption peak is observed, confirming the sensor's responsiveness to biochemical changes. The sensitivity of the biosensor was calculated to be .169 THz*L/g at the maximum concentration (1.18 g/L) and 33.9 THz*L/g at the minimum concentration (0.00118 g/L).

Furthermore, we evaluated the impact of quantum capacitance of graphene on the sensor's performance. The results indicate that accounting for quantum capacitance—beyond the conventional electrical double-layer model—significantly enhances sensitivity. Under the same concentration range, the improved sensitivities were .254 THz*L/g and 84.74 THz*L/g, respectively. This innovative absorber structure demonstrates strong potential for the development of tunable terahertz biosensors based on graphene-dielectric-graphene composites, offering high sensitivity and dynamic control for advanced biochemical detection applications.

Reference:

[1]- Turner, Anthony PF. "Biosensors: sense and sensibility." *Chemical Society Reviews* 42.8 (2013): 3184-3196.

[2]- Thévenot, Daniel R., et al. "Electrochemical biosensors: recommended definitions and classification." *Analytical Letters* 34.5 (2001): 635-659.

[3]- Helmerhorst, Erik, et al. "Real-time and label-free bio-sensing of molecular interactions by surface plasmon resonance: a laboratory medicine perspective." *The Clinical Biochemist Reviews* 33.4 (2012): 161.

[4]- Li, Ying, Xia Liu, and Zhao Lin. "Recent developments and applications of surface plasmon resonance biosensors for the detection of mycotoxins in foodstuffs." *Food Chemistry* 132.3 (2012): 1549-1554.

[5]- Yang, Yuqing, et al. "Surface enhanced Raman spectroscopy: applications in agriculture and food safety." *Photonics*. Vol. 8. No. 12. MDPI, 2021.

[6]- Masson, Jean-Francois. "Surface plasmon resonance clinical biosensors for medical diagnostics." *ACS sensors* 2.1 (2017): 16-30.

[7]- Mariani, Stefano, and Maria Minunni. "Surface plasmon resonance applications in clinical analysis." *Analytical and bioanalytical chemistry* 406.9 (2014): 2303-2323.

[8]- Mahmoudpour, Mansour, et al. "Nanomaterials based surface plasmon resonance signal enhancement for detection of environmental pollutions." *Biosensors and Bioelectronics* 127 (2019): 72-84.

[9]- Mahmood, Aseel I., et al. "Design and simulation of surface plasmon resonance sensors for environmental monitoring." *Journal of Physics: Conference Series*. Vol. 1003. No. 1. IOP Publishing, 2018.

[10]- Dahlin, Andreas, et al. "Localized surface plasmon resonance sensing of lipid-membrane-mediated biorecognition events." *Journal of the American Chemical Society* 127.14 (2005): 5043-5048.

[11]- Mozsolits, Henriette, and Marie-Isabel Aguilar. "Surface plasmon resonance spectroscopy: an emerging tool for the study of peptide–membrane interactions." *Peptide Science: Original Research on Biomolecules* 66.1 (2002): 3-18.

[12]- Pattnaik, Priyabrata. "Surface plasmon resonance: applications in understanding receptor-ligand interaction." *Applied biochemistry and biotechnology* 126.2 (2005): 79-92.

[13]- Fong, Kah Ee, and Lin-Yue Lanry Yung. "Localized surface plasmon resonance: a unique property of plasmonic nanoparticles for nucleic acid detection." *Nanoscale* 5.24 (2013): 12043-12071.

[14]- Ferreira, Jacqueline, et al. "Attomolar protein detection using in-hole surface plasmon resonance." *Journal of the American Chemical Society* 131.2 (2009): 436-437.

[15]- Fägerstam, Lars G., et al. "Detection of antigen—antibody interactions by surface plasmon resonance. Application to Epitope Mapping." *Journal of molecular recognition* 3.5-6 (1990): 208-214.

[16]- Salvi, Jérôme, and Dominique Barchiesi. "Measurement of thicknesses and optical properties of thin films from surface plasmon resonance (SPR)." *Applied Physics A* 115.1 (2014): 245-255.

[17]- Gupta, R., M. J. Dyer, and W. A. Weimer. "Preparation and characterization of surface plasmon resonance tunable gold and silver films." *Journal of Applied Physics* 92.9 (2002): 5264-5271.

[18]- Yesudasu, Vasimalla, Himansu Shekhar Pradhan, and Rahul Jasvanthbhai Pandya. "Recent progress in surface plasmon resonance based sensors: A comprehensive review." *Heliyon* 7.3 (2021)

[19]- Ramoso, John Paolo, Manoochehr Rasekh, and Wamadeva Balachandran. "Graphene-Based Biosensors: Enabling the Next Generation of Diagnostic Technologies—A Review." *Biosensors* 15.9 (2025): 586.

[20]- Wu, Judy, and Maogang Gong. "ZnO/graphene heterostructure nanohybrids for optoelectronics and sensors." *Journal of Applied Physics* 130.7 (2021).

[21]- Jablan, Marinko, Hrvoje Buljan, and Marin Soljačić. "Plasmonics in graphene at infrared frequencies." *Physical Review B—Condensed Matter and Materials Physics* 80.24 (2009): 245435.
[22]- Mak, Kin Fai, et al. "Measurement of the optical conductivity of graphene." *Physical review letters* 101.19 (2008): 196405.
[23]- Sabaeian, Mohammad, and Ghassem Baridi. "Graphene plasmonic-assisted enhancement of linear and nonlinear optical properties of conic-shaped InAs/GaAs quantum dots with wetting layer." *Superlattices and Microstructures* 144 (2020): 106582.
[24]- Koppens, Frank HL, Darrick E. Chang, and F. Javier García de Abajo. "Graphene plasmonics: a platform for strong light–matter interactions." *Nano letters* 11.8 (2011): 3370-3377.
[25]- Grigorenko, Alexander N., Marco Polini, and Kostya S. Novoselov. "Graphene plasmonics." *Nature photonics* 6.11 (2012): 749-758.
[26]- Low, Tony, and Phaedon Avouris. "Graphene plasmonics for terahertz to mid-infrared applications." *ACS nano* 8.2 (2014): 1086-1101.
[27]- Woessner, Achim, et al. "Highly confined low-loss plasmons in graphene–boron nitride heterostructures." *Nature materials* 14.4 (2015): 421-425.
[28]- Ju, Long, et al. "Graphene plasmonic for tunable terahertz metamaterials." *Nature nanotechnology* 6.10 (2011): 630-634.
[29]- Youn, S. J., et al. "Extended Drude model analysis of noble metals." *physica status solidi (b)* 244.4 (2007): 1354-1362.
[30]- Kiwi, Miguel, and Jaime Rössler. "The Drude Model." *Revista Brasileira de Ensino de Física* 46 (2024): e20240199.
[31]- Gonçalves, Paulo André Dias, and Nuno MR Peres. *An introduction to graphene plasmonics*. World Scientific, 2016.
[32]- Dressel, Martin, and Marc Scheffler. "Verifying the Drude response." *Annalen der Physik* 518.7-8 (2006): 535-544.
[33]- Wang, Heng, et al. "Extended Drude model for intraband-transition-induced optical nonlinearity." *Physical Review Applied* 11.6 (2019): 064062.
[34]- Zayats, Anatoly V., Igor I. Smolyaninov, and Alexei A. Maradudin. "Nano-optics of surface plasmon polaritons." *Physics reports* 408.3-4 (2005): 131-314.
[35]- Hacyan, S., and R. Jáuregui. "Electromagnetic waves in uniaxial crystals: General formalism with an application to Bessel beams." *arXiv preprint arXiv:0811.4378* (2008).
[36]- Ghohroodi Ghamsari, Farnood, and Reza Asgari. "Plasmon-phonon-polaritons in encapsulated phosphorene." *Plasmonics* 15.5 (2020): 1289-1304.
[37]- Guo, Chucai, et al. "Graphene-based perfect absorption structures in the visible to terahertz band and their optoelectronics applications." *Nanomaterials* 8.12 (2018): 1033.
[38]- Andryieuski, Andrei, and Andrei V. Lavrinenko. "Graphene metamaterials based tunable terahertz absorber: effective surface conductivity approach." *Optics express* 21.7 (2013): 9144-9155.
[39]- Zanbouri, Zeinab, et al. "Triple-band anisotropic absorber based on the hybrid graphene/black phosphorene disk-plus-shaped structure." *Optical and Quantum Electronics* 57.5 (2025): 302.

[40]- Zanbouri, Zeinab, Yaser Hajati, and Mohammad Sabaeian. "Investigation of anisotropic absorption in the hybrid L-shaped graphene-black phosphorene structure." *Physica E: Low-dimensional Systems and Nanostructures* 146 (2023): 115554.

[41]- Zekavat, Mohammad Amin, Mohammad Sabaeian, and Ghahraman Solookinejad. "Graphene plasmonic coupling with intersubband radiation of truncated pyramidal-shaped InAs/GaAs quantum dots." *Journal of the Optical Society of America B* 38.6 (2021): 1824-1833.

[42]- Baridi, Ghassem, et al. "Hybrid quantum dot-graphene layers with improved optical properties in the terahertz spectrum region." *Physica E: Low-dimensional Systems and Nanostructures* 146 (2023): 115524.

[43]- Sabaeian, Mohammad, and Ghassem Baridi. "Coupling the graphene plasmonic with terahertz emission of truncated conic-shaped InAs/GaAs quantum dots: A passive approach to enhance the intersubband optical properties." *Physica E: Low-dimensional Systems and Nanostructures* 134 (2021): 114834.

[44]- [21]- Abbas, Ghulam, et al. "Electrostatic gating of monolayer graphene by concentrated aqueous electrolytes." *The Journal of Physical Chemistry Letters* 14.18 (2023): 4281-4288.

[45]- Zhao, Jialin, et al. "Lithium-ion-based solid electrolyte tuning of the carrier density in graphene." *Scientific reports* 6.1 (2016): 34816.

[46]- Mišković, Z. L., and Nitin Upadhyaya. "Modeling electrolytically top-gated graphene." *Nanoscale research letters* 5.3 (2010): 505.

[47]- Doblhoff-Dier, Katharina, and Marc TM Koper. "Electric double layer of Pt (111): Known unknowns and unknown knowns." *Current Opinion in Electrochemistry* 39 (2023): 101258.

[48]- Gongadze, E., Petersen, S., Beck, U., & Van Rienen, U. (2009, October). Classical Models of the Interface between an Electrode and an Electrolyte. In *COMSOL conference* (pp. 14-16).

[49]-Ivanov, Vladimir D. "The Helmholtz model." *Journal of Solid State Electrochemistry* 28.8 (2024): 2487-2493.

[50]- Bard, Allen J., Larry R. Faulkner, and Henry S. White. *Electrochemical methods: fundamentals and applications*. John Wiley & Sons, 2022.

[51]- Elliott, Joshua D., et al. "The electrochemical double layer at the graphene/aqueous electrolyte interface: what we can learn from simulations, experiments, and theory." *Journal of Materials Chemistry C* 10.41 (2022): 15225-15262.

[52]- Kesler, Vladimir, Boris Murmann, and H. Tom Soh. "Going beyond the Debye length: overcoming charge screening limitations in next-generation bioelectronic sensors." *Acs Nano* 14.12 (2020): 16194-16201

[53]- Huang, Jun. "Zooming into the inner helmholtz plane of Pt (111)–aqueous solution interfaces: Chemisorbed water and partially charged ions." *JACS Au* 3.2 (2023): 550-564.

[54]- Xia, Jilin, et al. "Measurement of the quantum capacitance of graphene." *Nature nanotechnology* 4.8 (2009): 505-509.

[55]- Clericò, Vito. "Fabrication and characterization of quantum materials: graphene heterostructures and topological insulators." (2020)

[56]- Froehlicher, Guillaume, and Stéphane Berciaud. "Raman spectroscopy of electrochemically gated graphene transistors: Geometrical capacitance, electron-phonon, electron-electron, and electron-defect scattering." *Physical Review B* 91.20 (2015): 205413.

[57]- Male, MARIA CELESTE. "Modeling of an amyloidogenic protein in solution and on surfaces." (2019).

[58]- Zhang, Guigen. "Simulating the electrical double layer capacitance." *Excerpt from Proceedings of the COMSOL Conference. Boston*. 2010.

[59]- Wekalao, Jacob, et al. "Graphene-based THz surface plasmon resonance biosensor for hemoglobin detection applicable in forensic science." *Plasmonics* 19.4 (2024): 2141-215.

Chapter seven

Nonlinear Optical Detection of β2-Microglobulin Using Graphene-Enhanced Third-Harmonic Generation

7.1- Introduction to Nonlinear Optics:

Nonlinear optical effects are central to the operation of many contemporary photonic technologies. They underpin a wide range of applications, including laser frequency control [1], the creation of ultrashort pulses [2], all-optical signal manipulation [3], and rapid optical switching [4]. These effects have also become increasingly important in nanoscale optical platforms [5].

At its core, nonlinear optics examines how materials respond to light when the optical intensity is sufficiently high that the induced polarization no longer scales linearly with the electric field. Under these conditions, conventional linear phenomena-such as reflection, refraction, and scattering, which arise mainly from photon-electron interactions-occur alongside much weaker nonlinear contributions. These nonlinear processes originate from effective photon-photon interactions and typically emerge only under strong electromagnetic fields. However, in suitably engineered materials or structures that boost local field strength, nonlinear responses can be greatly amplified, enabling higher efficiency and stronger functional effects [6].

The field of nonlinear optics is generally considered to have begun with the observation of second-harmonic generation by Franken and colleagues in 1961, shortly after Maiman demonstrated the first functioning laser in 1960. Optical effects are termed *nonlinear* when a material's response to an electromagnetic field no longer scales proportionally with the field's strength. A common example is second-harmonic generation, which arises from components of the atomic polarization that vary with the square of the applied field. As a result, the output at twice the fundamental frequency grows roughly with the square of the incident laser intensity [7].

To clarify what is meant by an optical nonlinearity, consider how the polarization $\tilde{P}(t)$-the dipole moment per unit volume-depends on an applied electric field $\tilde{E}(t)$. In the linear regime, the induced polarization is directly proportional to the field amplitude and can typically be represented by a simple linear relation [8]:

$$\tilde{P}(t) = \epsilon_0 \chi^{(1)} \tilde{E}(t) \qquad (7\text{-}1)$$

where the constant of proportionality $\chi^{(1)}$ is known as the linear susceptibility and ϵ_0 is the permittivity of free space [8].

In nonlinear optics, the optical response can often be described as a generalization of Eq. (7-1) by expressing the polarization $\tilde{P}(t)$ as a power series in the field strength $\tilde{E}(t)$ as:

$$\tilde{P}(t) = \epsilon_0[\chi^{(1)}\tilde{E}(t) + \chi^{(2)}\tilde{E}(t)^2 + [\chi^{(3)}\tilde{E}(t)^3 + \cdots] \quad (7\text{-}2)$$

$$\equiv \tilde{P}^{(1)}(t) + \tilde{P}^{(2)}(t) + \tilde{P}^{(3)}(t) + \ldots$$

The quantities $\chi^{(2)}$ and $\chi^{(3)}$ are known as the second- and third-order nonlinear optical susceptibilities, respectively.

We shall refer to $\tilde{P}^{(2)}(t) = \chi^{(2)}\tilde{E}(t)^2$ as the second-order nonlinear polarization and $\tilde{P}^{(3)}(t) = \chi^{(3)}\tilde{E}(t)^3$ to as the third-order nonlinear polarization, and so on for higher-order terms. In the present section, we present brief qualitative descriptions of second Harmonic Generation and Third Harmonic Generation nonlinear optical processes [8].

7.2- Second-Harmonic Generation:

As a representative example of a nonlinear optical process, we can examine second-harmonic generation, shown schematically in Fig. 1, the electric field of the beam can be expressed as:

$$\tilde{E}(t) = Ee^{-i\omega t} + c.c \quad (7\text{-}3)$$

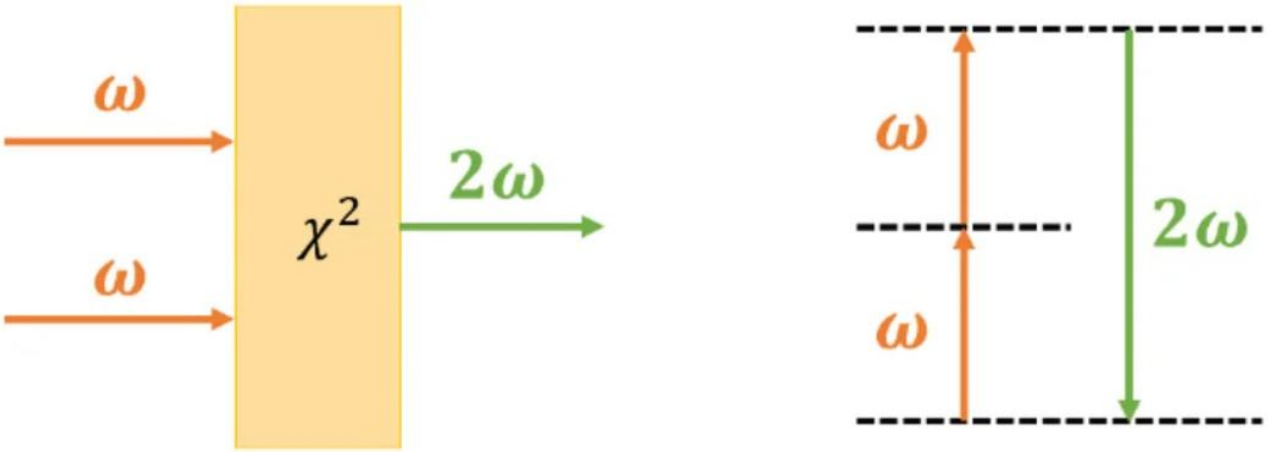

Figure 7.1- (a) Geometry of second-harmonic generation, illustrating the nonlinear optical interaction that produces radiation at twice the fundamental frequency. (b) Corresponding energy-level diagram describing the frequency-doubling process through virtual states and photon coupling

The nonlinear polarization created in such a crystal is given according to Eq. (7-2) by

$$\tilde{P}^{(2)}(t) = \chi^{(2)}\tilde{E}(t)^2 \quad (7\text{-}4)$$

or explicitly by:

$$\tilde{P}^{(2)}(t) = 2\epsilon_0\chi^{(2)}EE^* + (\epsilon_0\chi^{(2)}E^2e^{-i2\omega t} + .c) \quad (7\text{-}5)$$

We see that the second-order polarization consists of a contribution at zero frequency (the first term) and a contribution at frequency 2ω (the second term) [9].

When the experimental conditions are optimized, second-harmonic generation can become highly efficient-so efficient that almost all the incident optical power at frequency ω is transformed into light at the doubled frequency 2ω. This mechanism is widely employed to shift the output of fixed-frequency lasers into other spectral regions. A well-known example is the Nd:YAG laser, which naturally emits in the near-infrared at 1.06 μm. By applying second-harmonic conversion, this wavelength can be halved to approximately 0.53 μm, placing the resulting radiation squarely within the visible range [10].

Second-harmonic generation can also be interpreted by viewing the interaction as a redistribution of photons among the different frequency components of the electromagnetic field. In this photon-based picture-shown in Fig. 7-1(b)-two photons at frequency ω are absorbed, and a single photon at frequency 2ω is produced in the same quantum event. In the diagram, the solid line corresponds to the atomic ground state, while the dashed lines indicate virtual states. These virtual states are not true energy eigenstates of the isolated atom; instead, they represent intermediate energy configurations formed by combining an atomic energy level with the energy carried by one or more photons of the field [8].

7.3- Third-Order Nonlinear Optical Processes:

In next step we consider the third-order contribution to the nonlinear polarization:

$$\tilde{P}^{(3)}(t) = \epsilon_0 \chi^{(3)} \tilde{E}(t)^3 \qquad (7\text{-}6)$$

For the general case in which the field $\tilde{E}(t)$ is made up of several different frequency components, the expression for $\tilde{P}^{(3)}(t)$ is very complicated. For this reason, we first consider the simple case in which the applied field is monochromatic and is given by:

$$\tilde{E}(t) = \varepsilon \, cos\omega t \qquad (7\text{-}7)$$

Then, through use of the identity $cos^3\omega t = \frac{1}{4}\cos 3\omega t + \frac{3}{4}\cos \omega t$, we can express the nonlinear polarization as below [8]:

$$\tilde{P}^{(3)}(t) = \frac{1}{4}\epsilon_0 \chi^{(3)} \varepsilon^3 cos3\omega t + \frac{3}{4}\epsilon_0 \chi^{(3)} \varepsilon^3 cos\omega t \qquad (7\text{-}8)$$

7.4- Third-Harmonic Generation:

The first term in Eq. (7-8) describes a response at frequency 3ω that is created by an applied field at frequency ω. This term leads to the process of third-harmonic generation, which is illustrated in Fig. 7-2. According to the photon description of this process, shown in part (b) of the figure, three photons of frequency ω are destroyed and one photon of frequency 3ω is created in this process [11,12,13,14].

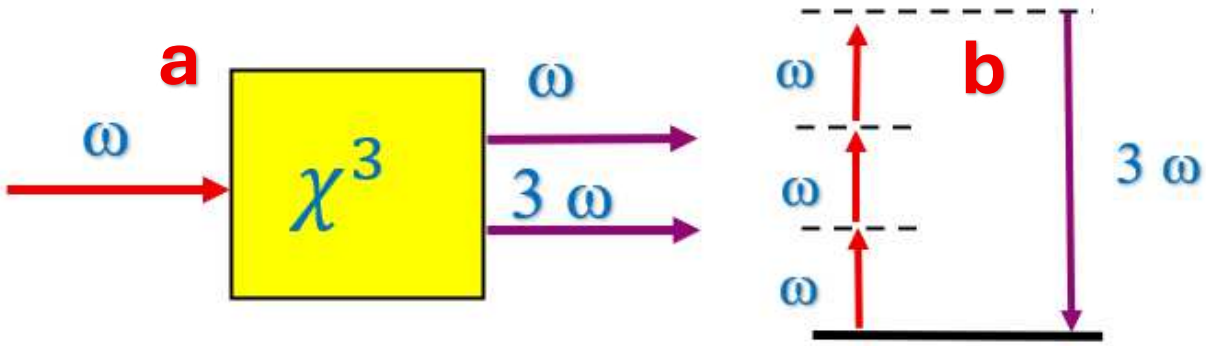

Figure7.2- Third-harmonic generation. (a) Geometry of the nonlinear interaction producing radiation at three times the fundamental frequency. (b) Corresponding energy-level diagram illustrating the frequency-tripling process via virtual states and photon coupling.

7.5- Influence of Inversion Symmetry on the Second-Order Nonlinear Response:

One of the symmetry properties that some but not all crystals possess is centrosymmetry, also known as inversion symmetry. For a material system that is centrosymmetric (i.e., possesses a center of inversion) the $\chi^{(2)}$ nonlinear susceptibility must vanish identically. We assume that the nonlinear polarization is given by $\tilde{P}(t) = \epsilon_0 \chi^{(2)} \tilde{E}^2(t)$, and the applied field is given by

$\tilde{E}(t) = \epsilon cos\omega t$, If we now change the sign of the applied electric field $\tilde{E}(t)$, the sign of the induced polarization $\tilde{P}(t)$ must also change, because we have assumed that the medium possesses inversion symmetry. Hence the polarisation must be replaced by [8]:

$$-\tilde{P}(t) = \epsilon_0 \chi^{(2)} [-\tilde{E}(t)]^2 \qquad (7\text{-}9)$$

Which show that:

$$-\tilde{P}(t) = \epsilon_0 \chi^{(2)} \tilde{E}^2(t) \qquad (7\text{-}10)$$

By comparison of this result, we see that $\tilde{P}(t)$ must equal $-\tilde{P}(t)$, which can occur only if $\tilde{P}(t)$ vanishes identically. This result shows that:

$$\chi^{(2)} = 0 \qquad (7\text{-}11)$$

In other words, in centrosymmetric materials, the second-order nonlinear susceptibility, $\chi^{(2)}$, is zero, in contrast, third-order nonlinear interactions are not subject to this limitation and can occur in all materials, regardless of their symmetry [8].

Among the various nanomaterials studied today, graphene has attracted exceptional attention because it consists of a single atomic layer of carbon arranged in a hexagonal honeycomb lattice. The first theoretical description of its electronic properties was provided by Wallace using the tight-binding

model. His analysis showed that graphene behaves as a zero-band-gap semiconductor: its valence and conduction bands meet at the Dirac points (K and K′) in the first Brillouin zone [15].

The significance of these Dirac points is that, near them, charge carriers in graphene-electrons and holes-behave like massless Dirac particles. They obey a relativistic-type Dirac equation but with an effective "speed of light" reduced to about $c/300$. Consequently, these Dirac fermions exhibit a linear relationship between energy and momentum, $E_p = v_f p$, where $v_f$is the Fermi velocity. This linear dispersion stands in stark contrast to the quadratic energy-momentum relation, $E_p = \pm p^2/(m^*)$, followed by conventional Schrödinger fermions with effective mass m^*[16].

Graphene exhibits remarkably strong nonlinear optical behavior when subjected to an electromagnetic field. Owing to the linear energy dispersion of its Dirac fermions, graphene shows pronounced nonlinear responses, particularly in the terahertz and microwave regimes. Its nonlinear optical characteristics have been extensively explored through techniques such as four-wave mixing, which reveal that graphene possesses a very large third-order optical susceptibility that varies only slightly with wavelength in the infrared range. Moreover, this third-order nonlinearity can be controlled electrically, allowing tunability of the optical response. In general, the nonlinear pattern of an optical medium arises from changes in its optical constants under the influence of intense electromagnetic fields [17].

When oxygen is adsorbed onto graphene, its linear optical characteristics-including the dielectric function, optical absorption, optical conductivity, loss spectrum, reflectivity, and refractive index-undergo notable modifications. Furthermore, both third-harmonic generation (THG) and the intensity-dependent refractive index of graphene can be actively tuned through the application of an external gate voltage, providing a convenient means of controlling its nonlinear optical behavior [18].

7.6- Linear and nonlinear Optical Conductivity of Graphene:

The remarkable optical behavior of graphene originates from its distinctive two-dimensional electronic band structure, which gives rise to interaction mechanisms that differ fundamentally from those in conventional semiconductors. In graphene, optical processes are dominated by two classes of electronic transitions.

The first class consists of intraband transitions, which take place within the same energy band-either the valence band or the conduction band. These processes are typically driven by low-energy excitations and often do not obey strict crystal-momentum conservation, particularly when scattering

mechanisms such as impurities, phonons, or defects assist the transition. Intraband transitions strongly influence graphene's response at terahertz and microwave frequencies and are responsible for its Drude-like free-carrier behavior [19, 20,21].

The second class, interband transitions, involves vertical excitations from the valence band to the conduction band across the Dirac point. Because the momentum of the electrons is largely preserved in these transitions, they play a dominant role at optical and near-infrared frequencies. Interband processes give rise to graphene's nearly constant universal optical absorption (~2.3%), its broadband spectral response, and its capability for ultrafast carrier generation and recombination [19,20,21].

Together, the interplay between intraband and interband transitions shapes graphene's wideband linear optical conductivity, ultrafast carrier dynamics, and its unusually strong interaction with electromagnetic radiation despite being only one atom thick. These features position graphene as a highly versatile material for advanced photonic, optoelectronic, and nonlinear-optical device platforms [19,20,21].

The linear optical conductivity associated with intraband transitions is commonly described by the Drude dispersion model, expressed as [21]:

$$\sigma_L \approx \frac{-iD}{\pi(\omega - \frac{i}{\tau})} \tag{7-12}$$

Were

$$D = \frac{e^2 E_f}{\hbar^2} \tag{7-13}$$

τ is the electron relaxation time that accounts to the optical loss, e is the electron charge, is the ω radial frequency, and ħ is the reduced Planck constant [21].

The linear conductivity of graphene is a function of the wave frequency, electron relaxation time, and the Fermi energy. The electron relaxation time can be affected by many factors, such as temperature, Fermi energy, external field, graphene sample quality, and substrate material. Generally, the electron relaxation time is described by:

$$\tau = \frac{\mu E_f}{e v_f^2} \tag{7-14}$$

Where μ is the DC mobility of the graphene sample and v_f is the Fermi velocity $1 * 10^6 ms^{-1}$. It has been reported that the mobility of graphene can exceed $20\ m^2V^{-1}s^{-1}$ at room temperature and the value of τ is in the picosecond range [13].

Due to its 2D nature, graphene has a sub-nanometre thickness, which can be neglected in numerical modelling and treated as a surface current. The linear component of this surface current is expressed as:

$$j(\omega) = \sigma_{gr}(\omega)E(\omega) \quad (7\text{-}15)$$

Where $E(\omega)$ is the electric field along the x-direction on the surface [13].

Graphene's crystal lattice belongs to the D_{6h} point group, which characterizes it as a centrosymmetric two-dimensional material. Because of this inversion symmetry, all second-order nonlinear optical processes are forbidden in pristine graphene under the electric–dipole approximation. As a result, phenomena such as second-harmonic generation (SHG), second-order susceptibility $\chi^{(2)}$, and related second-order nonlinear conductivities do not occur intrinsically in ideal monolayer graphene [18].

Despite the absence of second-order responses, graphene exhibits exceptionally strong third-order nonlinear optical behavior. In particular, its third-harmonic generation (THG) efficiency is remarkably high compared to many conventional bulk materials, owing to its linear energy dispersion, high carrier mobility, and strong light–matter interaction at atomic thickness. These third-order effects-including THG, Kerr nonlinearity, and four-wave mixing-enable graphene to serve as a powerful platform for nonlinear photonic devices [22].

Because of these characteristics, graphene is widely regarded as a promising 2D material for applications in ultrafast optics, all-optical signal processing, nonlinear modulators, and frequency-conversion technologies. Its ability to combine strong nonlinearity with electrical tunability further enhances its potential in next-generation integrated photonics [23].

The nonlinear optical response of 2D materials, in general, can be described in terms of the nonlinear surface conductivity tensor ($\sigma_s^{(3)}$). It reads as follows [11,13,18]:

$$\sigma_{gr}^{(3)} = \frac{i\sigma_0(\hbar v_f e)^2}{48\pi(\hbar\omega)^4} T\left(\frac{\hbar\omega}{2E_f}\right) \quad (7\text{-}16)$$

$$T(x) = 17G(x) - 64G(2x) + 45(3x) \quad (7\text{-}17)$$

And

$$G(x) = \left|\left(\frac{1+x}{1-x}\right)\right| + i\pi\theta(|x| - 1) \quad (7\text{-}18)$$

With $\theta(z)$ being the Heaviside step function. The real part of the third-order conductivity is negligible, and its primary behavior is governed by the imaginary part. In deriving Eq. 16, the electron-electron and electron phonon scattering as well as thermal effects have been excluded [11,18,18,24].

Third-harmonic generation is the simultaneous creation of a new photon with an angular frequency ω_{TH} and the absorption of three photons with the same fundamental angular frequencies, ω_{FF} . The connection $\omega_{TH} = 3\omega_{FF}$ is the outcome of this procedure, which complies with the energy conservation principle [11,13].

The surface current contributing to the nonlinear third-harmonic generation process is described by [11,13,18]:

$$j(\omega) = N\sigma_{gr}(\omega)E_{TH} + \sigma_{gr}^{(3)}(\omega_{TH}; \omega_{FF}, \omega_{FF}, \omega_{FF})E_{FF}^3 \quad (7\text{-}19)$$

7.7- Theory and Design:

Figure 7-3 depicts the geometry of the proposed nonlinear graphene metasurface. An array of graphene micro-ribbons is placed over a thin dielectric spacer layer that is terminated by a metallic substrate. The spacer layer between graphene micro-ribbons and metal termination is filled with a Kerr nonlinear dielectric material. The linear and nonlinear 2 responses of the metasurface are computed using the electromagnetic solver of COMSOL Multiphysics. Assuming that the length of the graphene micro-ribbons is much larger than their width, the proposed metasurface is uniform along the direction of z-axis and 2D simulations are used to calculate its linear and nonlinear responses. The simulation domain is terminated by periodic boundary conditions normal to the x-axis with an optimized periodicity of a 3.88 = μm.

To minimize reflection and absorption of scattered waves at the boundaries, perfectly matched layers (PMLs) are implemented at both the top and bottom of the structure. The overall schematic of this setup is shown in Figure 7-3. The computational domain is discretized using a highly refined mesh, with the maximum element size set to 0.25 nm.

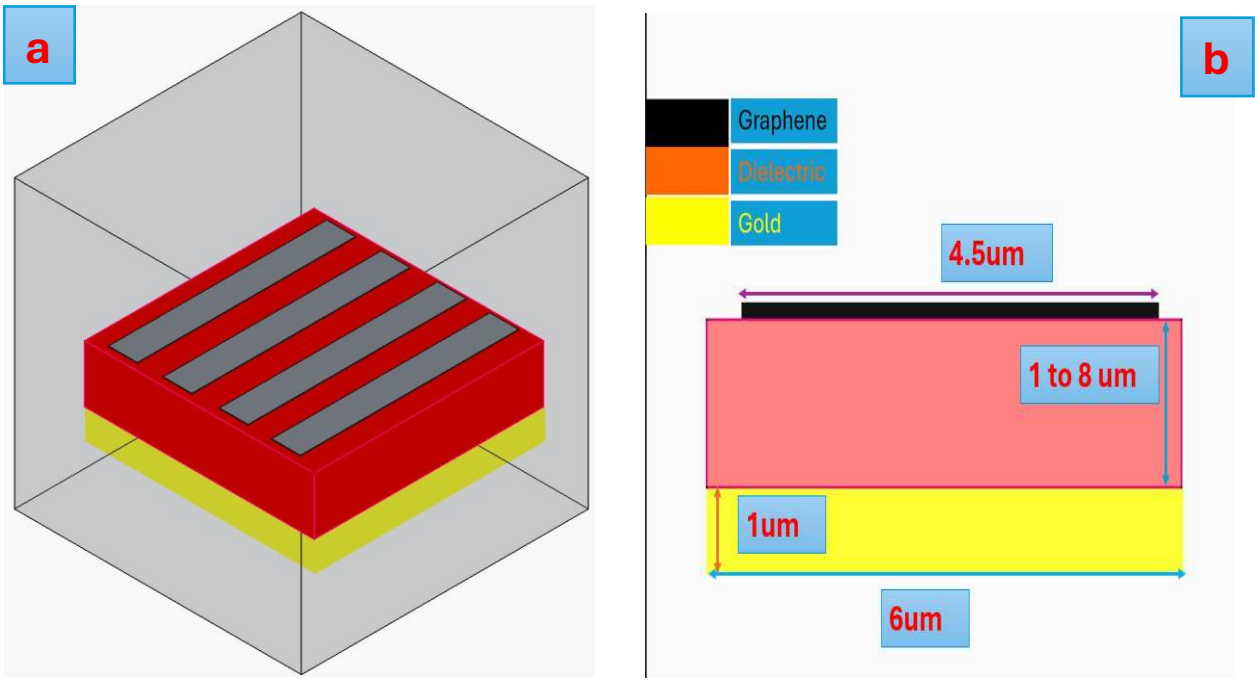

Figure7.3- Schematic representation of the Surface Plasmon Resonance (SPR) structure: (a) 3D view and (b) 2D cross-sectional view.

Third-order nonlinear effects in ultra-thin materials, such as graphene, are inherently weak, which requires high input intensities to generate noticeable nonlinear responses. Despite these high inputs, the resulting nonlinear signals are often small, limiting the overall efficiency of nanoscale optical devices [25]. At the nanoscale, enhancing nonlinear effects relies critically on the strong confinement of the optical field and its spatial overlap with the material. Plasmonic and metasurface structures can provide this confinement by concentrating light into deep subwavelength volumes, thereby boosting light–matter interactions. Consequently, both theoretical and experimental efforts in nonlinear nanophotonics have focused on designing structures that maximize near-field enhancement and mode overlap, enabling more efficient third-order nonlinear processes in ultra-thin materials [26].

Plasmonics is the study and manipulation of light at the nanoscale, focusing on how electromagnetic waves interact with collective electron oscillations in metals, referred to as surface plasmons [27]. In practical optical devices, metallic plasmons are often constrained by ohmic losses and the inherently fixed properties of metals, which lead to energy dissipation as heat and limit the propagation length of plasmonic waves. Furthermore, the shallow penetration of electromagnetic waves into metals means that the optical response of bulk metals is largely dominated by weak light–matter interactions near the metal–dielectric interface. At the nanoscale, however, surface plasmon polaritons (SPPs) can significantly strengthen light–matter interactions, enabling enhanced nonlinear optical phenomena [28].

Graphene plasmonics has attracted considerable attention due to its ability to confine electromagnetic energy at scales below the wavelength of light. A key feature of graphene is its strong near-field confinement enabled by surface plasmon polaritons (SPPs). Unlike metals, graphene's optical response can be actively tuned through gate voltage or chemical doping, making it a highly adaptable material for optoelectronic applications. Its two-dimensional structure allows SPP-induced field enhancement to surpass what is typically achievable in conventional metallic systems. Additionally, graphene exhibits relatively low losses at high carrier densities, further increasing its appeal for photonic and optical devices. These properties make graphene a promising platform for advanced applications such as optical sensing, photonic switching, and communication technologies [29].

Surface plasmons (SPs) are collective oscillations of free electrons in a metal's conduction band that occur at the boundary between a metal and a dielectric. These oscillations can propagate along the interface as electromagnetic waves, producing strongly enhanced optical fields in the vicinity of the surface. The behavior of surface plasmon resonance (SPR) is described by the following dispersion relation:

$$K_{sp} = K_0\sqrt{\frac{\varepsilon_d\varepsilon_m}{\varepsilon_d+\varepsilon_m}} \qquad (7\text{-}20)$$

Where K_0 is the free-space wavevector, ε_d is the permittivity of the dielectric medium, and ε_m is the permittivity of the metal [18].

To achieve our purpose, we apply incident wave with an intensity of $30kWcm^{-2}$ is incident vertically from the top with transverse magnetic (TM) polarization from the first port, while the second port is located at the bottom of the structure. Photons with frequency ω are extinguished, and third-order harmonic (TH) radiation with a frequency of 3ω is generated.

The thickness of the backside metal, assumed to be gold, is chosen to be much larger than its THz skin depth. As a result, the metallic layer functions as a perfect reflecting mirror, achieving zero transmission. The optical constants of gold in the terahertz range are described using the Drude model as follows:

$$\varepsilon_{L,Di} = \varepsilon_\infty - \frac{\omega_p^2}{\omega^2 - i\gamma\omega} \qquad (7\text{-}21)$$

Where $\omega_p = 2\pi * 2069\frac{rad}{s}$ is the plasma frequency, $\gamma = 2\pi * 17.65\frac{rad}{s}$ is the damping frequency, and $\varepsilon_\infty = 1.53$ is the dielectric constant at in finite frequency [30,31].

It should be noted that gold exhibits a third-order nonlinear susceptibility of $\chi_{\mathrm{Au}}^{(3)} = 2.45 \times 10^{-19}\,\mathrm{m^2V^{-2}}$in the near-infrared region. However, its nonlinear behavior at low THz frequencies has not been reported in the literature. At these frequencies, gold possesses extremely high conductivity and can be effectively treated as a perfect electric conductor. Consequently, electromagnetic fields do not penetrate the gold, preventing any interaction with its nonlinear properties. Therefore, the contribution of gold to the nonlinear response of the metasurface at low THz frequencies can be considered negligible.

This design leverages the unique properties of Graphene, such as its strong nonlinear optical response and tunable bandgap, to enhance third harmonic generation (THG) and other nonlinear effects in the far-infrared and THz frequency ranges. By combining localized plasmon-polaritons resonances, and electrical tunability, the proposed metasurface offers significant potential for advanced nonlinear optical applications.

The conversion efficiency (CE) of third-harmonic generation is defined as:

$$CE = \frac{P_{O,TH}}{P_{i,FF}} \tag{7-22}$$

Where $P_{O,TH}$ is the output power at the third-order harmonic frequency, and $P_{i,FF}$ is the input power at the fundamental frequency [32]. The output radiation is calculated via

$$P_{O,TH} = \int (S.n)da \tag{7-23}$$

Where S is the Poynting vector passing through the boundary curve and n is the normal vector to the boundary surface. By normalizing the computed power values, which are given in Watts, this assumption enables us to analyze the results on a consistent and physically reasonable scale [33].

As discussed in earlier chapters, the primary goal of this work is to develop a highly sensitive sensor based on third harmonic generation (THG) in graphene, capable of detecting extremely low concentrations of biomolecules such as β2-microglobulin (wild type). This protein behaves as an ion with a net charge of -2 and a molecular diameter of approximately 14 Å. The presence of such charged biomolecules near the graphene surface significantly affects the local electrostatic environment, which is critical for the sensor's operation. To enhance the sensitivity of graphene to these biomolecules, electrostatic gating using electrolytes is employed. Over the past two decades, electrolyte gating-including aqueous or organic solutions, ionic liquids, and solid polymer electrolytes-has been demonstrated as an effective method to induce high charge carrier densities in graphene [34].

The operating principle of electrolyte gating relies on the formation of a capacitor-like structure between the graphene layer and a gate electrode. When an electrolyte gate is applied, an electrical double layer (EDL) forms at the graphene/electrolyte interface. This layer consists of two capacitance components arranged in series: the Helmholtz layer, which contains ions directly adsorbed on the graphene surface, and the diffuse Gouy-Chapman layer, which extends into the bulk solution. The formation of the EDL leads to an accumulation of opposite-sign charge carriers on the graphene surface, shifting its Fermi level (E_f) and effectively modulating its electronic properties [35].

In addition to the EDL, the intrinsic quantum capacitance of graphene plays an important role in determining the overall charge distribution. Quantum capacitance arises due to the limited density of electronic states near the Dirac point and is especially significant when the Fermi level is close to the charge neutrality point. In our analysis, the quantum capacitance is treated as being in series with the EDL capacitance, resulting in a combined effective capacitance that governs the local electric field and charge accumulation at the graphene surface. This combined effect is crucial for enhancing the local electromagnetic field experienced by nearby biomolecules, which in turn strongly affects the efficiency of third harmonic generation [36,37].

By carefully modelling the contributions of both the EDL and graphene's quantum capacitance, the proposed sensor can detect biomolecules at extremely low concentrations with high sensitivity. The tunable nature of graphene via electrostatic gating, combined with the strong field confinement induced by the EDL, enables precise control over the optical and electronic response of the sensor. This approach not only leverages the unique nonlinear optical properties of graphene but also exploits its high surface-to-volume ratio and adaptable electronic properties, making it a promising platform for advanced biosensing applications such as optical detection of low-abundance proteins, real-time physiological monitoring, and high-sensitivity medical diagnostics.

The model, already introduced in the previous chapter, describes how the adsorption of target molecules modifies the Fermi energy of graphene through the electrostatic potential they generate at its surface. This shift depends on the carrier concentration and the applied top-gate voltage, linking the electronic properties of graphene to molecular doping. To accurately capture this behavior in an electrolyte environment, the electric double layer (EDL) is modeled using the Stern approach, where the total capacitance arises from the series combination of the compact Helmholtz layer and the diffuse Gouy–Chapman layer. The Helmholtz contribution depends on the permittivity and effective thickness of the interfacial layer, while the Gouy–Chapman term accounts for the spatial distribution of ions in the diffuse region and its dependence on temperature and electrolyte concentration. In

addition, the quantum capacitance of graphene is included to reflect its finite density of states, which becomes especially significant at low carrier densities. The overall capacitance of the system is therefore determined by the series combination of the EDL capacitance and the graphene quantum capacitance, enabling a more precise estimation of the carrier concentration and electrostatic response under varying gating conditions.

7-8. Result and discussion:

The proposed structure employs a carefully engineered multilayer configuration optimized to enhance third-order harmonic generation (THG). In this design, the interplay between material dispersion, plasmonic response, and field confinement is tuned to maximize nonlinear interaction within the active region. A comprehensive analysis is conducted to evaluate the absorption and reflection spectra and power outflow characteristics. These optical and electromagnetic responses are examined under varying Fermi energy levels, dielectric layer thicknesses, and carrier relaxation times. The performance of the system is studied across a broad frequency range from 1.5 to 3.5 THz, enabling a detailed assessment of how tunable material parameters influence the nonlinear conversion process. This investigation provides valuable insights into optimizing multilayer photonic platforms for high-efficiency THz harmonic generation.

To further optimize the nonlinear response of the proposed structure, we investigate the influence of key geometric parameters, with particular emphasis on the thickness of the dielectric layer. For this purpose, the previously analysed factors-absorption, reflection and power outflow-are re-evaluated for different dielectric thicknesses. Figure 7-4(a–c) illustrates the corresponding results, highlighting how variations in dielectric thickness modify field confinement and consequently alter the overall nonlinear performance of the device. These observations provide a deeper understanding of the geometric tuning mechanisms that can be employed to enhance third-order harmonic generation in multilayer THz structures.

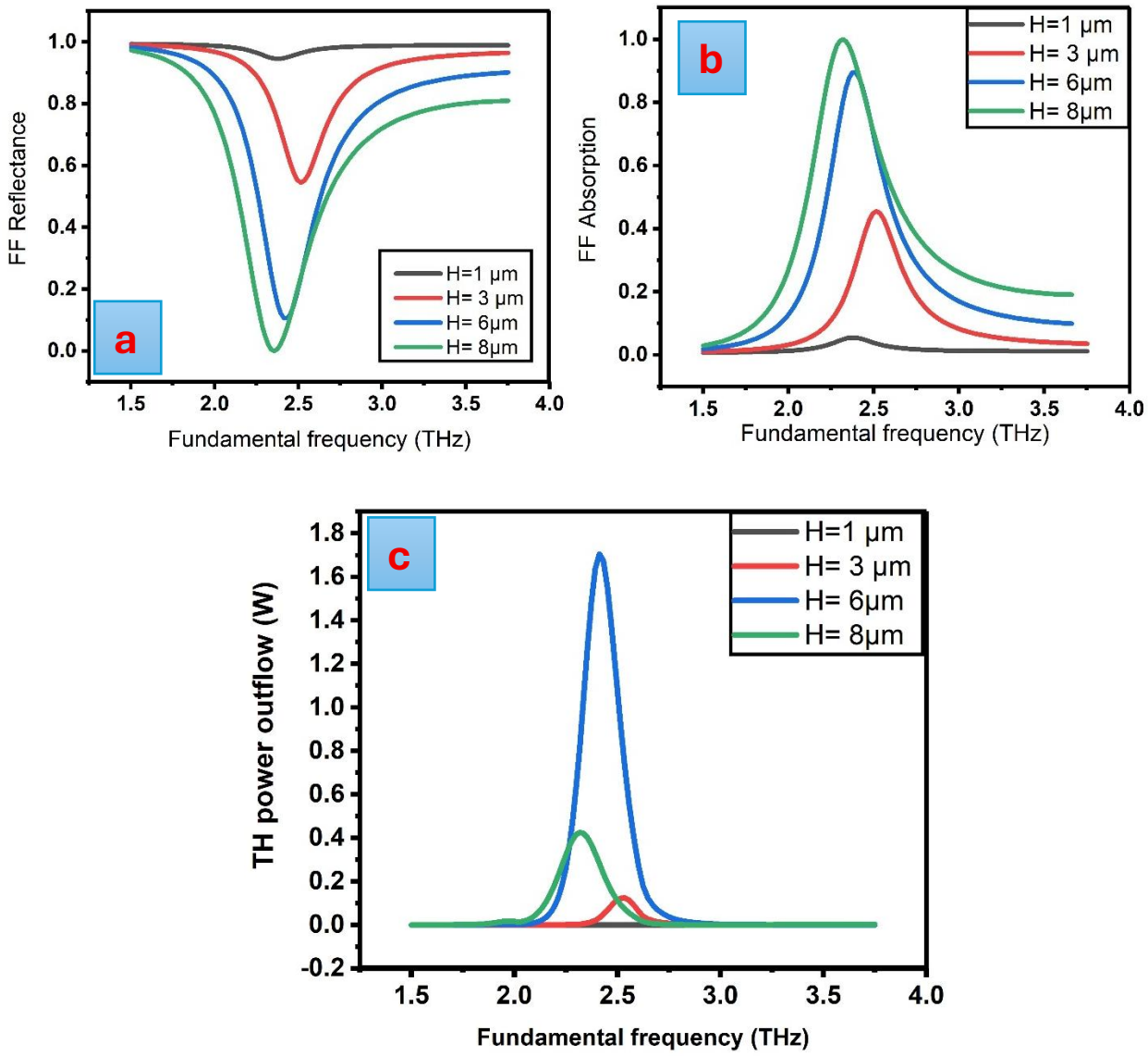

Figure 7-4(a-c). Absorption, reflection, and Third Harmonic Generation (THG) power outflow spectra for different dielectric thicknesses (H) across the frequency range of 1.5–3.5 THz. In all simulations, the graphene relaxation time, Fermi energy of graphene and irritated wave are taken as 0.5 ps, 0.3 eV and 30 $\frac{kW}{cm^2}$ respectively.

As shown in Figure 7-4, increasing the dielectric height shifts the resonance peak toward lower frequencies. This shift indicates a transition of the resonant frequency to lower energy. The behavior can be attributed to the decreased vertical confinement of the plasmonic modes and the redistribution of the local electromagnetic field, which effectively increases the optical mode volume and reduces the resonance energy.

Figure 7-5(a–d) illustrates the normalized spatial distribution of the electric field (V/m) for the fundamental signal at the plasmonic resonance frequency of 1.5 THz for different dielectric layer heights (H). The electric field intensity at the fundamental frequency increases gradually with increasing dielectric thickness. However, this enhancement is relatively weak when compared to the corresponding enhancement observed for third-harmonic generation (THG).

Specifically, increasing the dielectric height from 1 μm to 8 μm results in an enhancement factor of approximately 5.71 for the fundamental frequency. In contrast, as shown in Figure 7-5(a–d), the THG signal exhibits an enhancement exceeding 170 times over the same range of dielectric thickness. This pronounced difference highlights the strong nonlinear sensitivity of third-harmonic generation to the dielectric thickness.

The observed behavior indicates that THG is significantly more responsive to variations in dielectric-induced polarization and local field confinement than the fundamental mode. The increase in dielectric thickness enhances the local electric field localization and polarization effects, which play a critical role in nonlinear optical processes. Consequently, even modest changes in the dielectric geometry led to substantial amplification of the THG response, whereas the fundamental frequency remains comparatively insensitive. This result underscores the effectiveness of dielectric engineering as a powerful approach for optimizing nonlinear plasmonic responses, particularly for high-order harmonic generation.

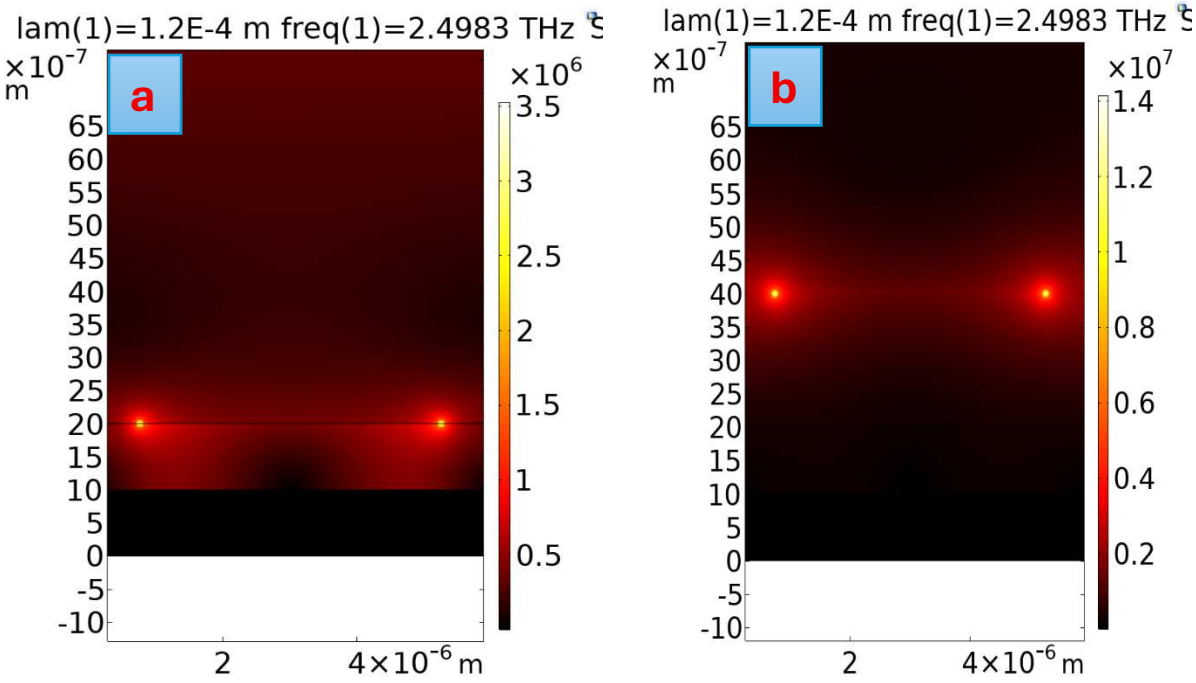

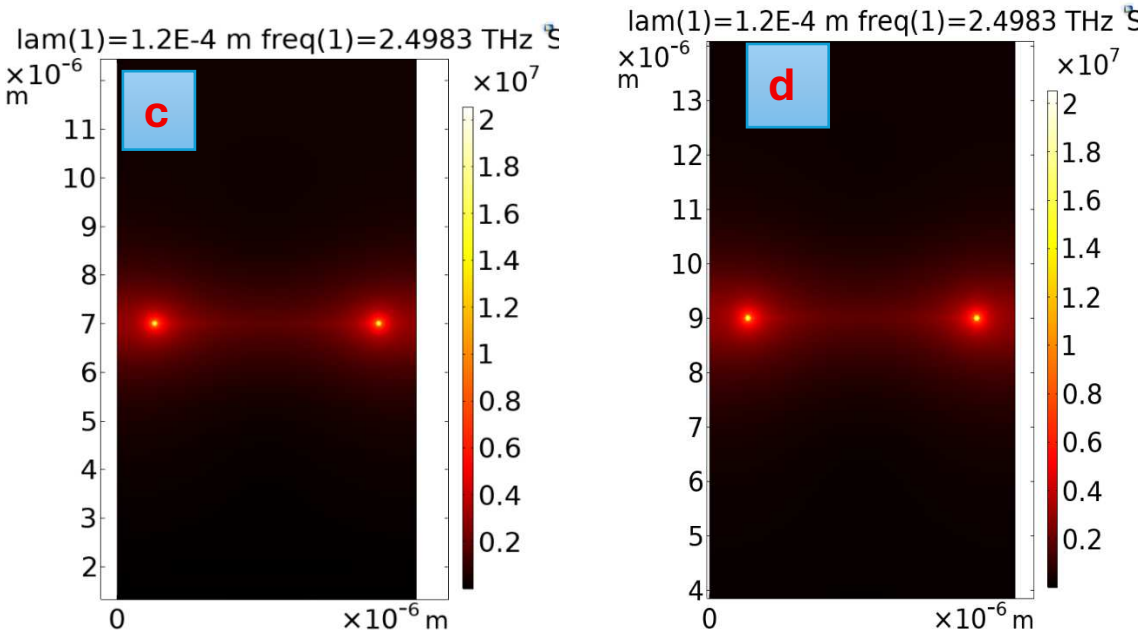

Figure 7-5 (a–d). Normalized spatial distribution of the electric field (V/m) for the fundamental signal wave at the plasmon resonance frequency of 1.5 THz for different dielectric heights $\boldsymbol{H}$: (a) $\boldsymbol{H} = \mathbf{1}\ \boldsymbol{\mu}$m, (b) $\boldsymbol{H} = \mathbf{3}\ \boldsymbol{\mu}$m, (c) $\boldsymbol{H} = \mathbf{6}\ \boldsymbol{\mu}$m, and (d) $\boldsymbol{H} = \mathbf{8}\ \boldsymbol{\mu}$m. In all simulations, the graphene relaxation time and Fermi energy are taken as 0.5 ps and 0.3 eV, respectively.

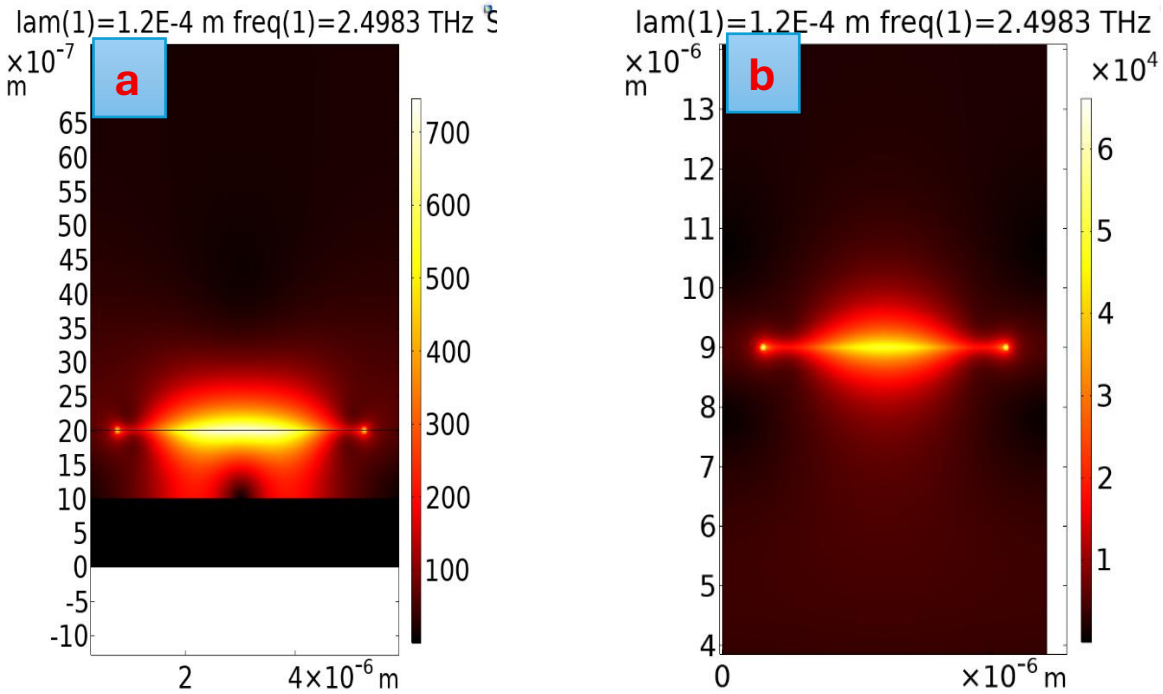

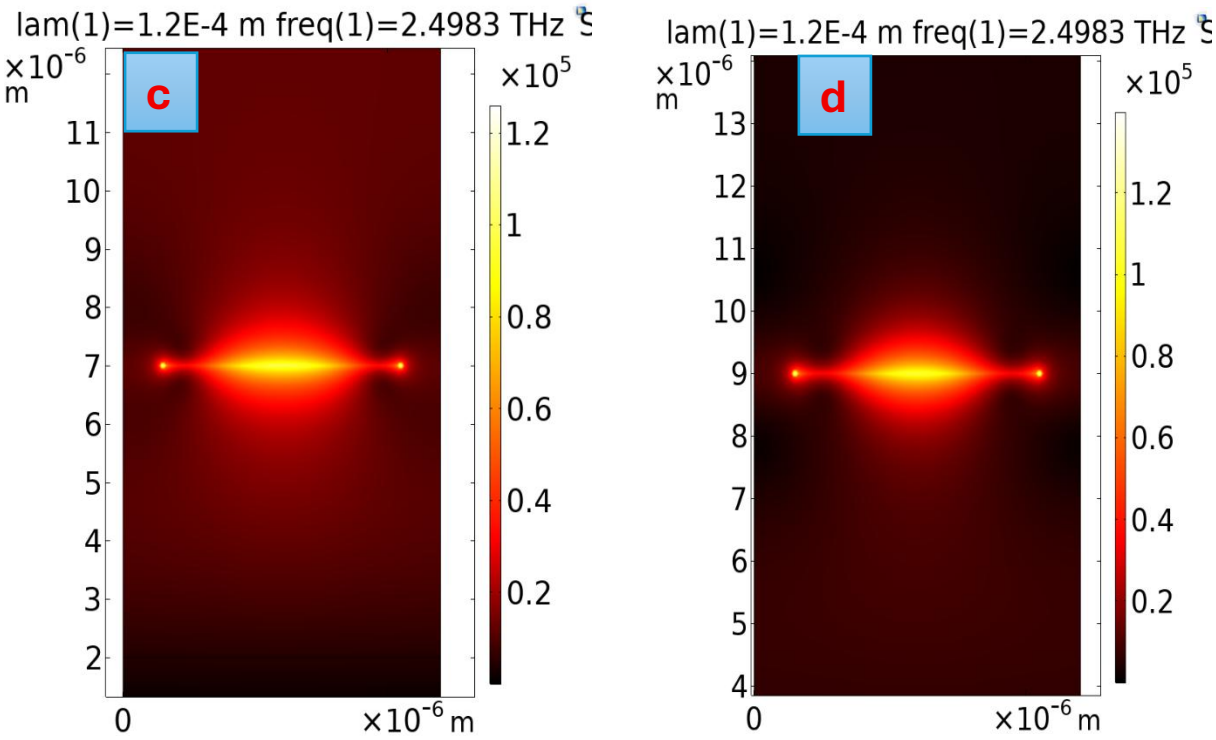

Figure 7-6(a-d)- Normalized spatial distribution of the electric field (V/m) for the Third Harmonic Generation wave at the plasmon resonance frequency of 1.5 THz for different dielectric heights $\boldsymbol{H}$: (a) $\boldsymbol{H = 1\ \mu}$m, (b) $\boldsymbol{H = 3\ \mu}$m, (c) $\boldsymbol{H = 6\ \mu}$m, and (d) $\boldsymbol{H = 8\ \mu}$m. In all simulations, the graphene relaxation time and Fermi energy are taken as 0.5 ps and 0.3 eV, respectively.

The absorption, reflectance, and TH power outflow spectra of the structure are analysed for various Fermi energies-Ef = 0.2, 0.3, 0.4, 0.46, and 0.5 eV across the same frequency range, with the corresponding results presented in Figures 7-7(a-c). It is evident that each Fermi energy level produces a distinct resonance associated with the excitation of surface plasmon polaritons. This pattern demonstrates that graphene absorbs light at specific frequencies, thereby reducing the transmission of the fundamental field. As the Fermi energy increases, the electron population in higher energy states also increases, resulting in a shift of both the resonance frequency and the transmission minimum toward higher values. In these simulations, Fermi energies of 0.2 eV, 0.3 eV, 0.4 eV, and 0.5 eV were used, while the relaxation time was fixed at 0.5 ps and the dielectric thickness at 8 µm. Figures 7-**7(a**-c) illustrate the absorption, reflectance, and TH power outflow of graphene at different Fermi energies, respectively.

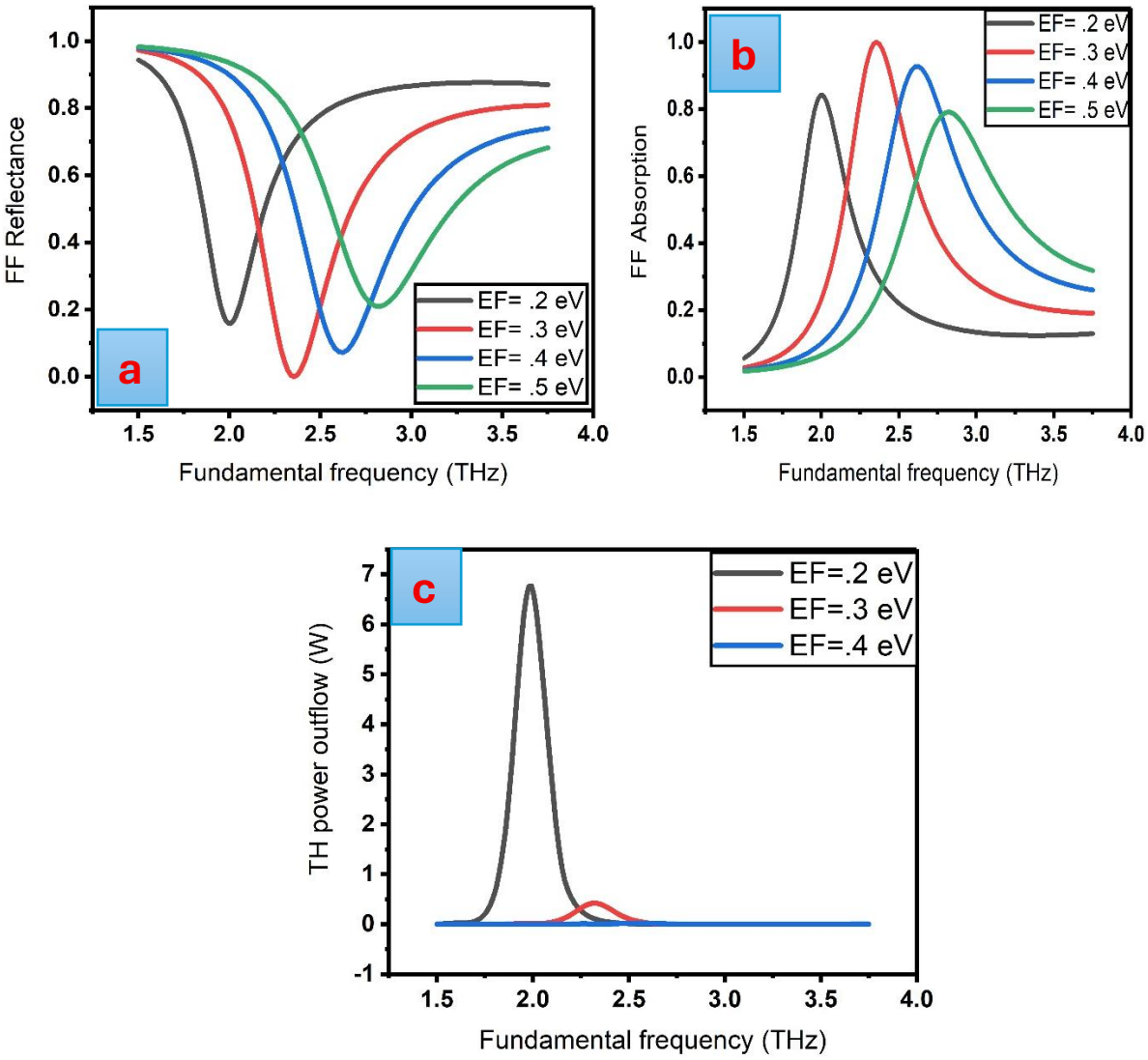

Figure 7-7(a-c). Absorption, reflection, and Third Harmonic Generation (THG) power outflow spectra for different Fermi energy of Graphene (E_f) across the frequency range of 1.5–3.5 THz. In all simulations, the graphene relaxation time, thickness of dielectric and irritated wave are taken as 0.5 ps, 8um and 30 $\frac{kW}{cm^2}$ respectively.

Figures 7-8(a–d) and 8-8(a–d) illustrate the normalized spatial distribution of the electric field (V/m) for the fundamental and Third Harmonic Generation signal at the plasmonic resonance frequency of 1.5 THz under different graphene Fermi energy levels respectively. As the Fermi energy increases, a pronounced enhancement in the peak electric-field intensity at the fundamental frequency is observed, indicating stronger plasmonic confinement and improved light-matter interaction within the graphene-based structure. Notably, the most significant enhancement occurs at a Fermi energy of 0.3 eV, where both the fundamental response and third-harmonic generation (THG) are maximized.

At a Fermi energy of 0.3 eV, the enhancement factor for the fundamental frequency reaches approximately 2.85. This increase is attributed to the tuning of graphene's surface conductivity, which directly modifies the plasmon resonance condition and leads to improved field localization at the

graphene-dielectric interface. Interestingly, this enhancement level is comparable to that observed in the nonlinear response. As shown in Figures 7-9(a–d), the THG signal exhibits an even stronger enhancement, exceeding a factor of 3.4 over the same parameter range. This pattern highlights the strong sensitivity of both linear and nonlinear optical responses of graphene to variations in Fermi energy.

The computational results confirm that a Fermi energy of 0.3 eV represents the optimal operating point for the proposed structure, yielding maximum field enhancement, strongest plasmonic resonance, and highest absorption. Since the primary objective of this chapter is to achieve maximum absorption and enhanced nonlinear performance, this Fermi energy is identified as the most suitable choice for the designed system. These findings demonstrate the effectiveness of Fermi-level tuning as a practical strategy for optimizing terahertz plasmonic and nonlinear optical devices based on graphene.

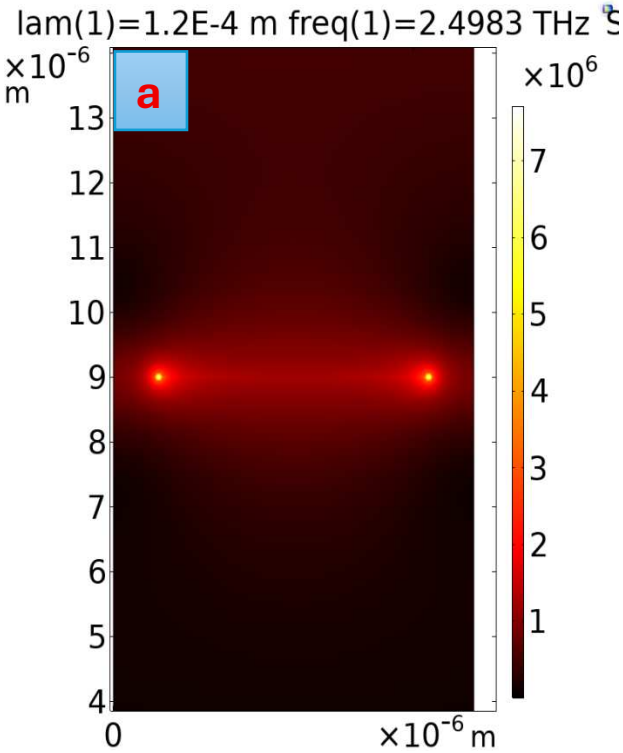

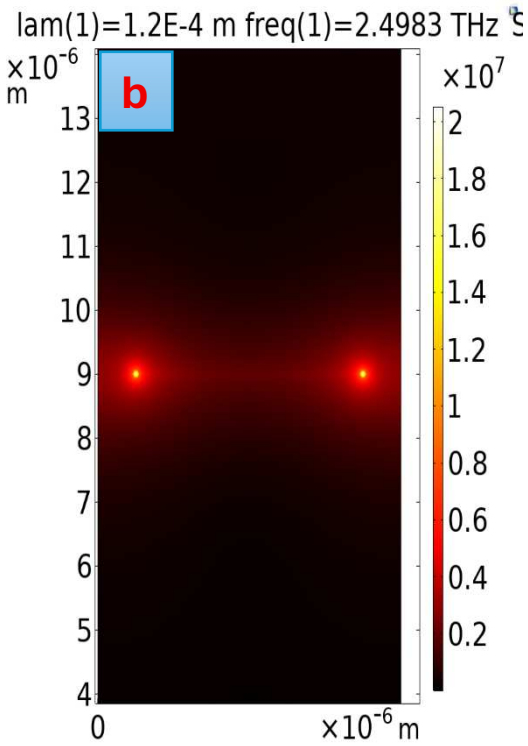

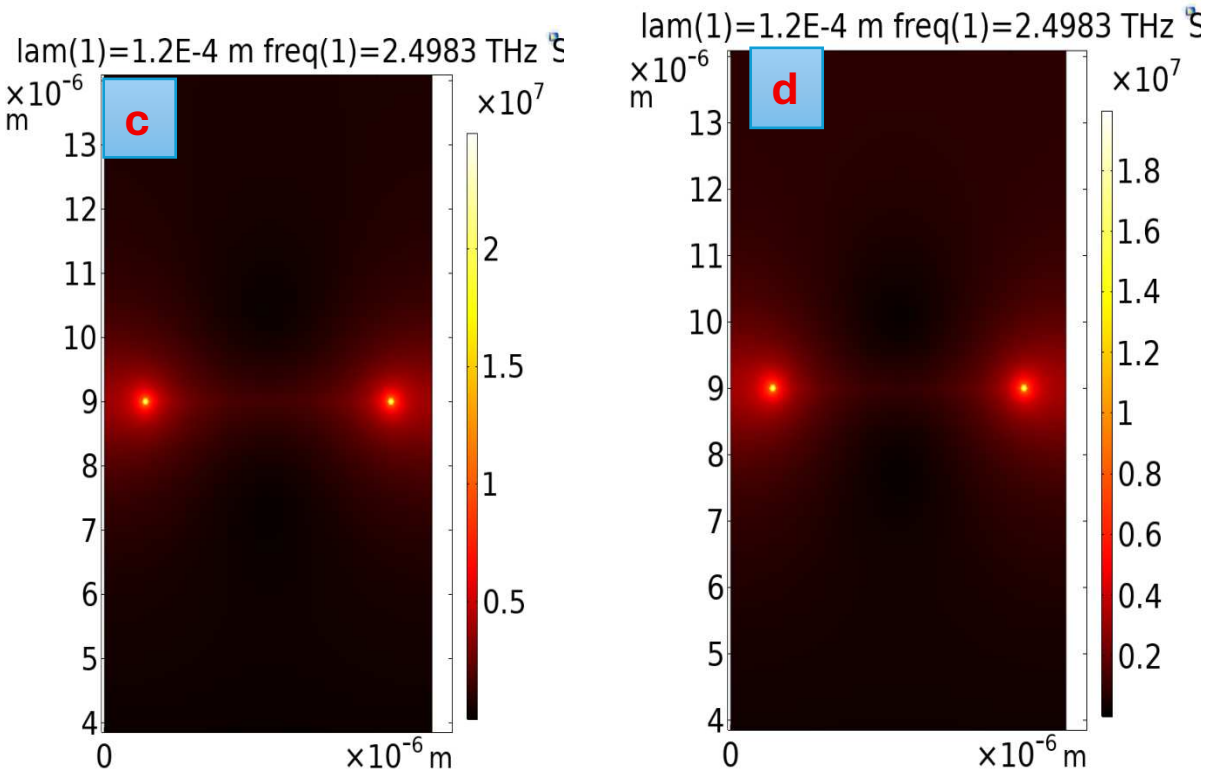

Figure 7-8(a-d)- Normalized spatial distribution of the electric field (V/m) for the fundamental signal wave at the plasmon resonance frequency of 1.5 THz for different Femi energy of Graphene micro ribbon E_f: (a) $E_f = .2\ eV$, (b) $E_f = .3\ eV$, (c) $E_f = .4\ eV$, and (d)- $E_f = .5\ eV$. In all simulations, the graphene relaxation time and dielectric high are taken as 0.5 ps and$8\ \mu$m, respectively.

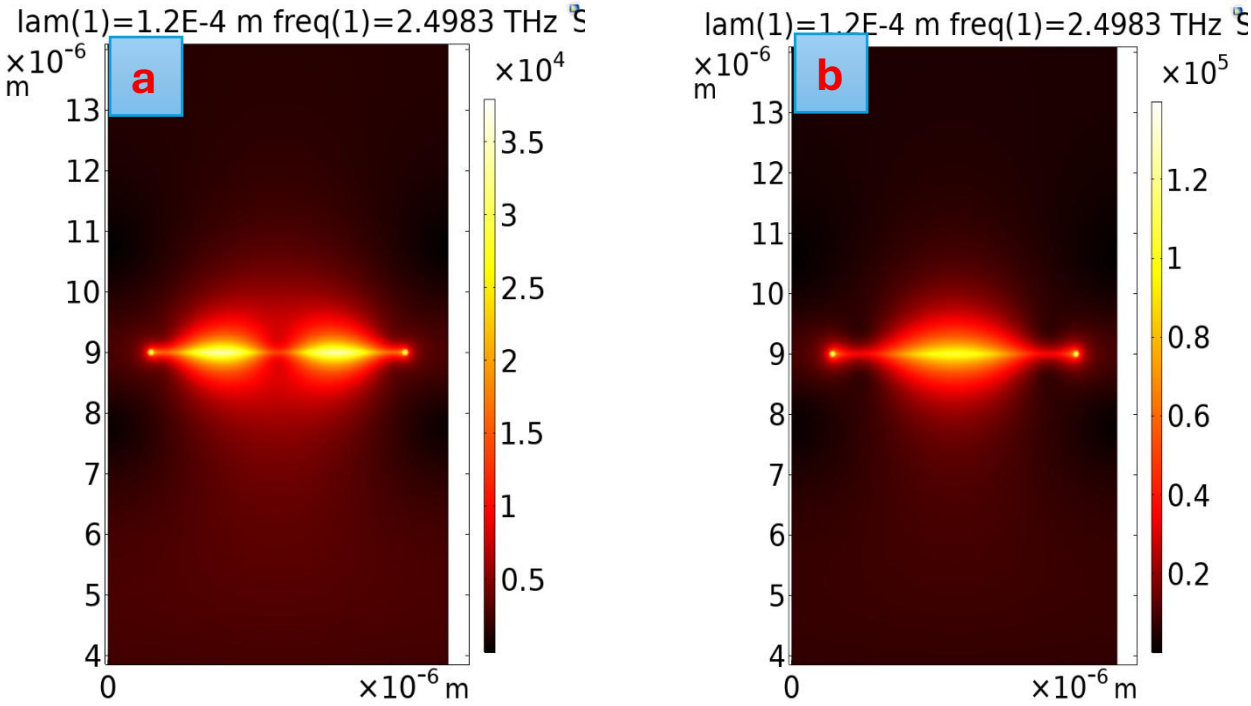

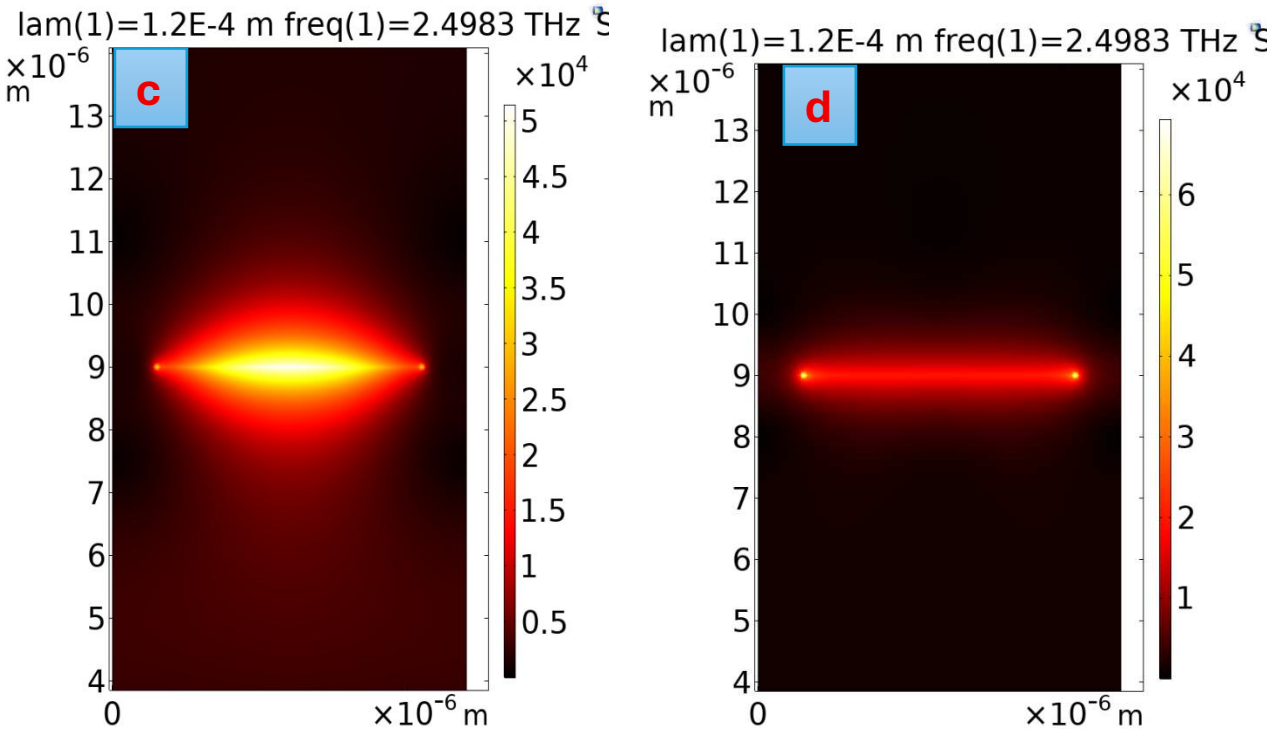

Figure 7-9 (a-d)- Normalized spatial distribution of the electric field (V/m) for the Third harmonic Generation wave at the plasmon resonance frequency of 1.5 THz for different Femi energy of Graphene micro ribbon $\boldsymbol{E_f}$: (a) $\boldsymbol{E_f} = .\mathbf{2}\ \boldsymbol{eV}$, (b) $\boldsymbol{E_f} = .\mathbf{3}\ \boldsymbol{eV}$, (c) $\boldsymbol{E_f} = .\mathbf{4}\ \boldsymbol{eV}$, and (d)- $\boldsymbol{E_f} = .\mathbf{5}\ \boldsymbol{eV}$. In all simulations, the graphene relaxation time and dielectric high are taken as 0.5 ps and$\mathbf{8}\ \boldsymbol{\mu}$m, respectively.

In the next step of our optimization, we investigate the optical performance of the sensor under different carrier mobilities. To achieve this, we use the relationship between the relaxation time and the carrier mobility of graphene, as described by Equation (7-14). This equation indicates a direct correlation between these parameters. Accordingly, in this computation we apply three different relaxation times: 0.3 ps, 0.5 ps, and 0.7 ps. Throughout this analysis, the Fermi energy is fixed at 0.3 eV, and the dielectric thickness is maintained at 8 μm.

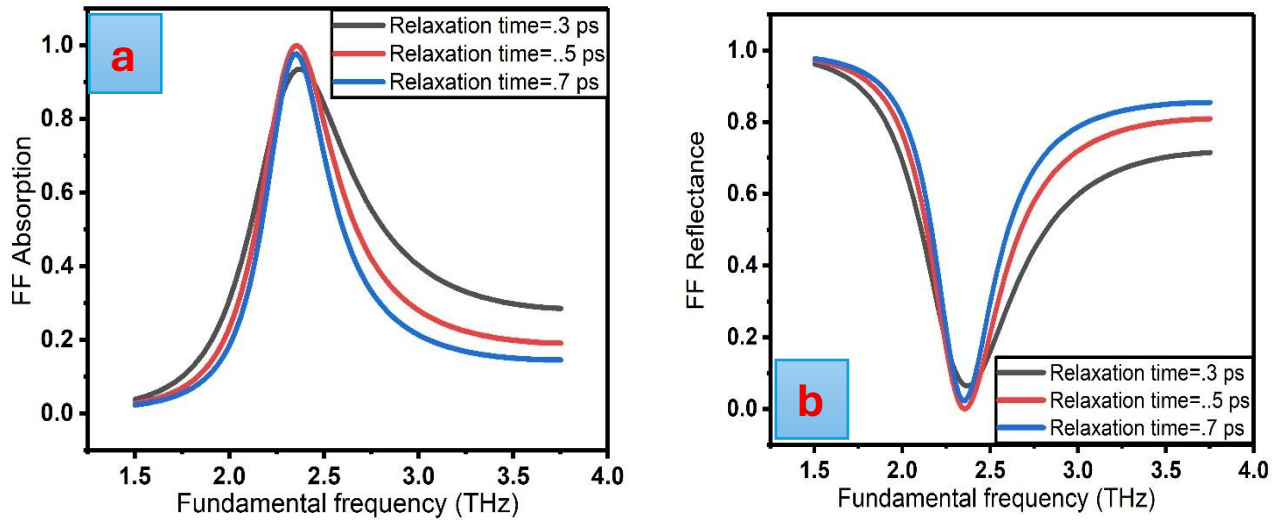

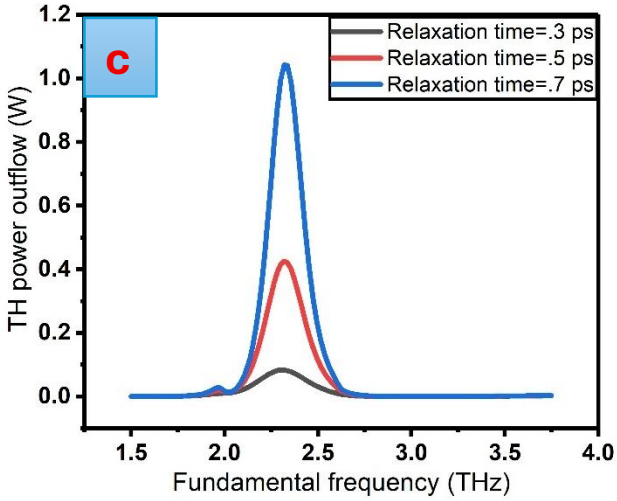

Figure 7-10 (a-c). Absorption, reflection, and Third Harmonic Generation (THG) power outflow spectra for different relaxation time (τ) of Graphene micro ribbon across the frequency range of 1.5–3.5 THz. In all simulations, the thickness of dielectric, Fermi energy of graphene and irritated wave are taken as 8um, 0.3 eV and 30 $\frac{kW}{cm^2}$ respectively.

Figures 7-11(a–c) and 7-12(a–c) illustrate the normalized spatial distribution of the electric field (V/m) for the fundamental signal and third-harmonic generation (THG) at the plasmonic resonance frequency of 1.5 THz for different graphene relaxation times (τ). As the relaxation time increases, a gradual enhancement in the electric-field intensity is observed for both the fundamental and THG signals. This behavior arises from the direct relationship between relaxation time and carrier mobility in graphene, where a longer relaxation time corresponds to reduced carrier scattering and, consequently, higher mobility.

Physically, increasing the relaxation time enhances graphene's surface conductivity by lowering ohmic losses, which leads to improved plasmon propagation and stronger field confinement at the resonance frequency. As a result, both linear (fundamental) and nonlinear (THG) optical responses experience enhanced local electric fields. However, compared to Fermi energy tuning, the effect of relaxation time on field enhancement remains relatively weak. The maximum enhancement factor reaches approximately 1.25 for the fundamental frequency, while the THG signal exhibits a higher enhancement of about 3.

The comparatively stronger enhancement observed in THG is consistent with the nonlinear nature of harmonic generation, which depends on higher powers of the local electric field. Nonetheless, the overall influence of relaxation time is limited, indicating that while carrier mobility plays a role in reducing plasmonic damping, it is not the dominant parameter governing field enhancement and absorption in this structure. These results suggest that relaxation time acts as a secondary optimization

parameter, whereas Fermi energy tuning remains the primary mechanism for achieving strong plasmonic resonance and enhanced nonlinear performance in graphene-based terahertz devices.

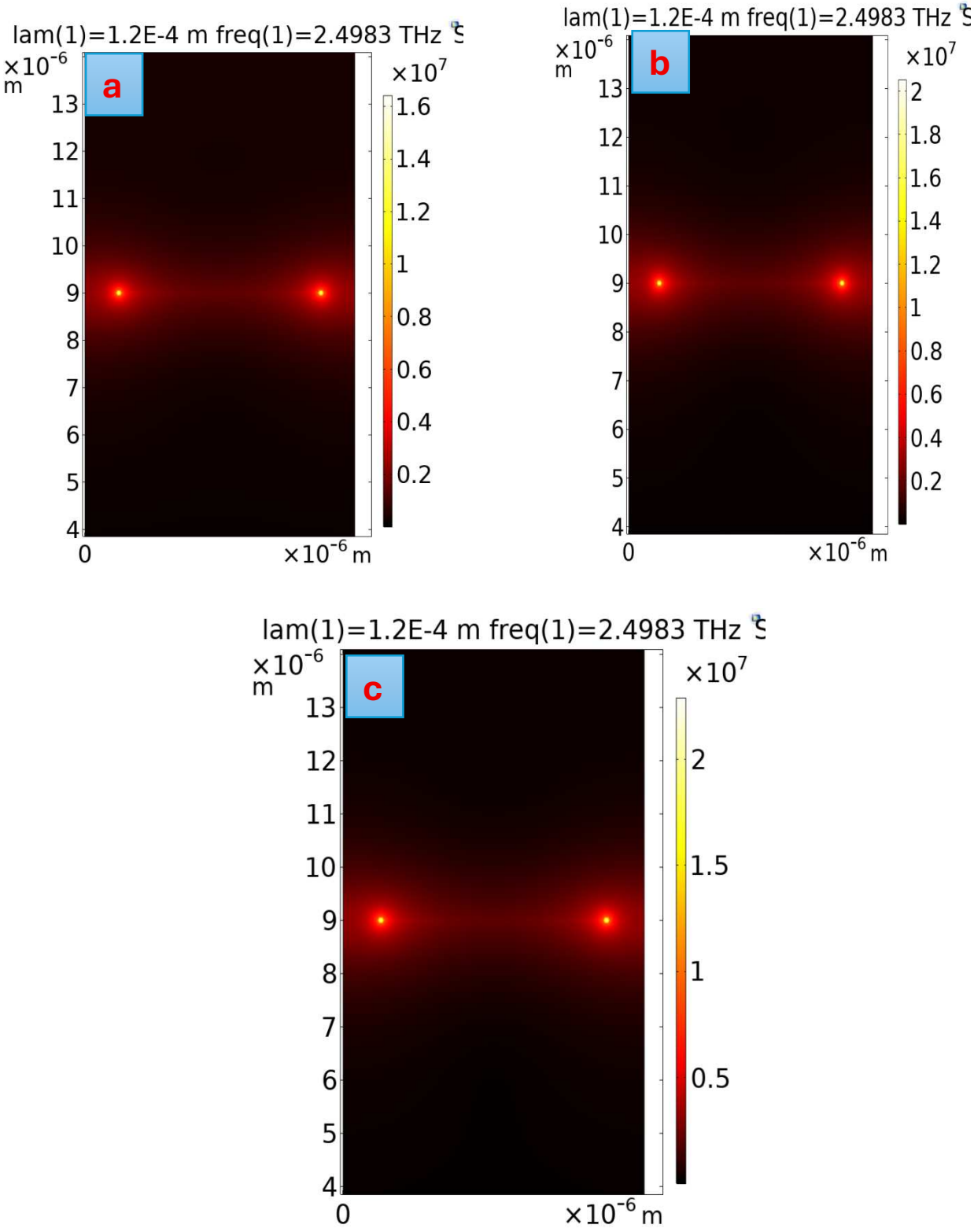

Figure 7-11(a-c)- Normalized spatial distribution of the electric field (V/m) for the fundamental signal wave at the plasmon resonance frequency of 1.5 THz for different relaxation time ($\boldsymbol{\tau}$) in Graphene micro ribbon: (a)$\boldsymbol{\tau} = .\mathbf{3}\ \boldsymbol{ps}$, (b) $\boldsymbol{\tau} = .\mathbf{5}\ \boldsymbol{ps}$ and (c) $\boldsymbol{\tau} = .\mathbf{7}\ \boldsymbol{ps}$. In all simulations, the Fermi energy of graphene and dielectric high are taken as .3 eV and $\mathbf{8}\ \boldsymbol{\mu}$m, respectively.

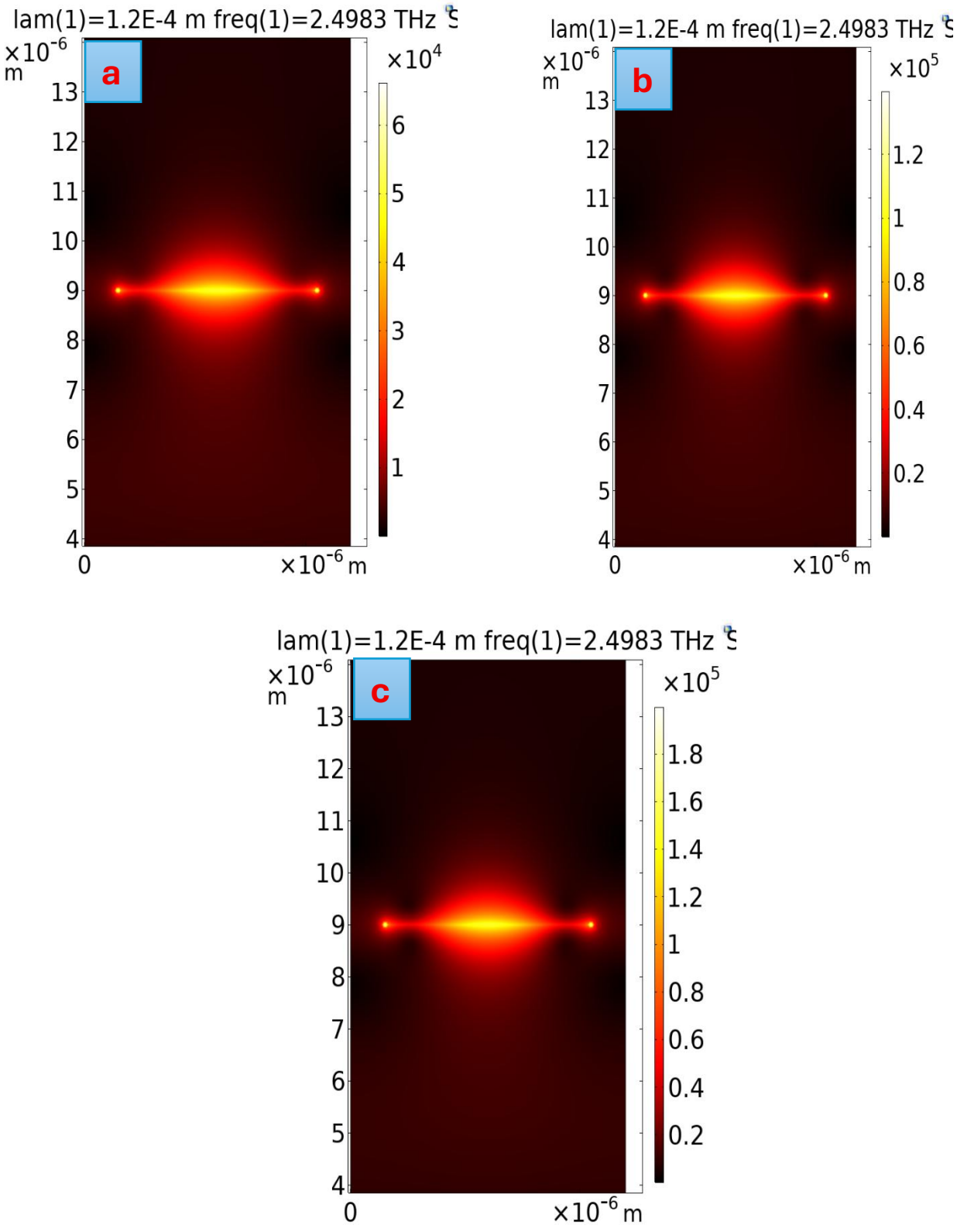

Figure 7-12 (a-c)- Normalized spatial distribution of the electric field (V/m) for the Third Harmonic Generation wave at the plasmon resonance frequency of 1.5 THz for different relaxation time ($\boldsymbol{\tau}$) in Graphene micro ribbon: (a) $\boldsymbol{\tau} = .\mathbf{3}\ \boldsymbol{ps}$, (b) $\boldsymbol{\tau} = .\mathbf{5}\ \boldsymbol{ps}$ and (c) $\boldsymbol{\tau} = .\mathbf{7}\ \boldsymbol{ps}$. In all simulations, the Fermi energy of graphene and dielectric high are taken as .3 eV and $\mathbf{8}\ \boldsymbol{\mu}$m, respectively.

To study the impact of the input field intensity on the generated field power and conversion efficiency, the input intensity was varied from 0.001 to 0.12 MW·cm^{-2} at a fixed frequency of 3 THz, as shown

in Figure 7-13. Higher input intensities increase the number of photons in the structure, thereby enhancing the probability of three photons at frequency ω interacting to generate a photon at frequency 3ω. Interestingly, the THG conversion efficiency can reach relatively high values (−65 dB) even at comparatively low fundamental-field input intensities when exciting the proposed nonlinear graphene metasurface. In these simulations, the parameters used were a Fermi energy of 0.3 eV**,** a relaxation time of 0.5 ps**,** and a dielectric thickness of 8 μm**.**

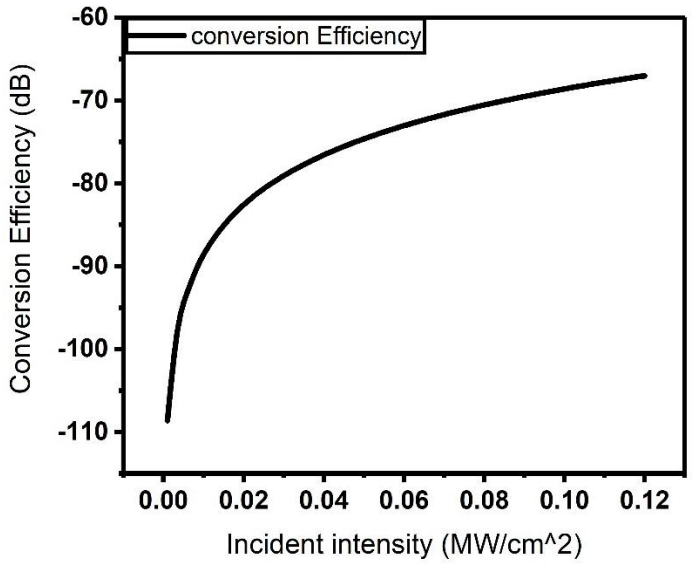

Figure 7-13. Computed THG conversion efficiency as functions of the incident FF wave intensity at fundamental frequency of 3 THz. In all simulations, the graphene relaxation time, Fermi energy of graphene and thickness of dielectric are taken as 0.5 ps, 0.3 eV and 8um respectively.

Figures 7-14(a–d) and 7-15(a–d) illustrates the normalized spatial distribution of the electric field (V/m) for both the fundamental signal and the third-harmonic generation (THG) at the plasmonic resonance frequency of 1.5 THz for different incident wave intensities (I_0) applied to the graphene microribbon structure. As previously discussed, the generation of higher-order harmonics, particularly THG, requires significantly higher incident intensities compared to linear optical phenomena due to the intrinsically nonlinear nature of the process.

As shown in Figures 7-14(a–d), increasing the incident intensity from 0.1 kW/cm² to 100 kW/cm² results in a moderate enhancement of the electric-field intensity at the fundamental frequency, with an enhancement factor of approximately 35. This increase reflects the stronger excitation of graphene surface plasmons and improved field confinement at higher excitation levels. In contrast, As shown in figures 7-15(a–d), the enhancement observed for the THG signal is dramatically larger, reaching a factor of approximately 32,000 over the same intensity range.

This pronounced difference arises from the nonlinear dependence of third-harmonic generation on the incident electric field, where the THG intensity scales with the cube of the fundamental field amplitude. Consequently, even relatively small increases in the fundamental field lead to disproportionately large enhancements in the generated harmonic signal. These results clearly demonstrate the critical role of high incident intensity in enabling strong nonlinear optical responses in graphene-based plasmonic structures.

Overall, the findings confirm that while the fundamental response exhibits a quasi-linear dependence on incident intensity, the nonlinear THG response is highly sensitive to excitation strength. This highlights graphene's exceptional potential for high-efficiency nonlinear terahertz applications, particularly when operated under strong-field excitation conditions.

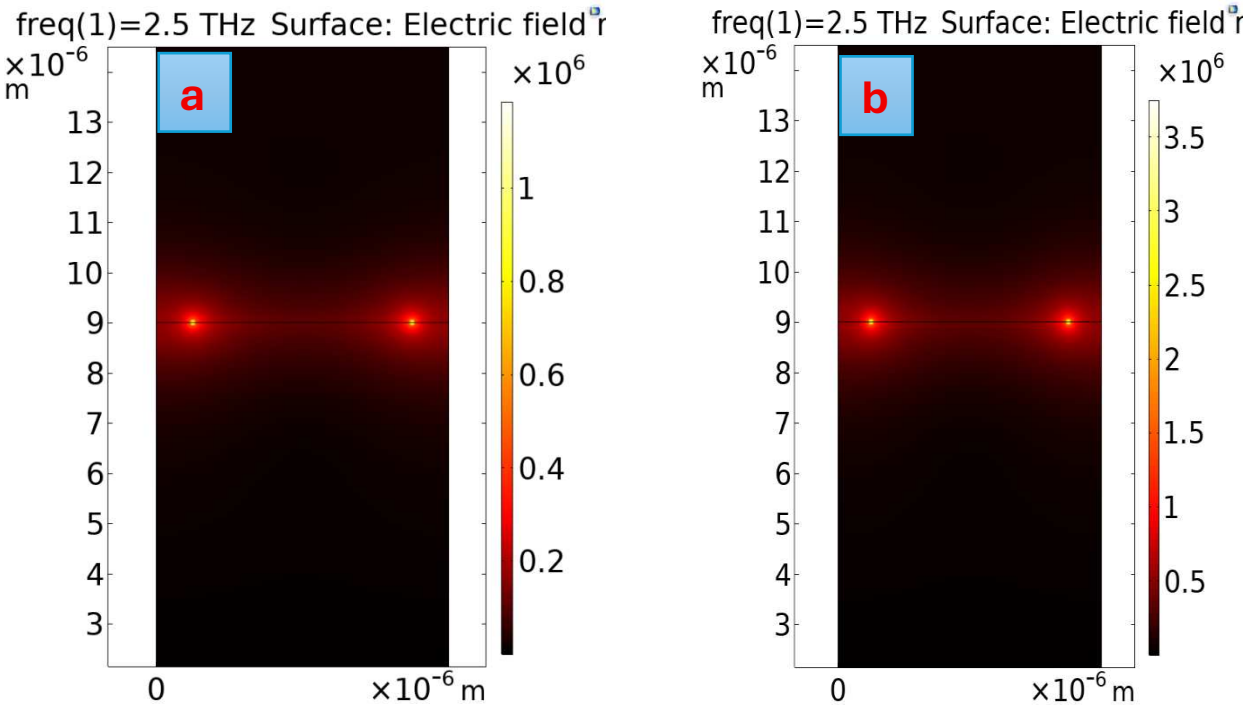

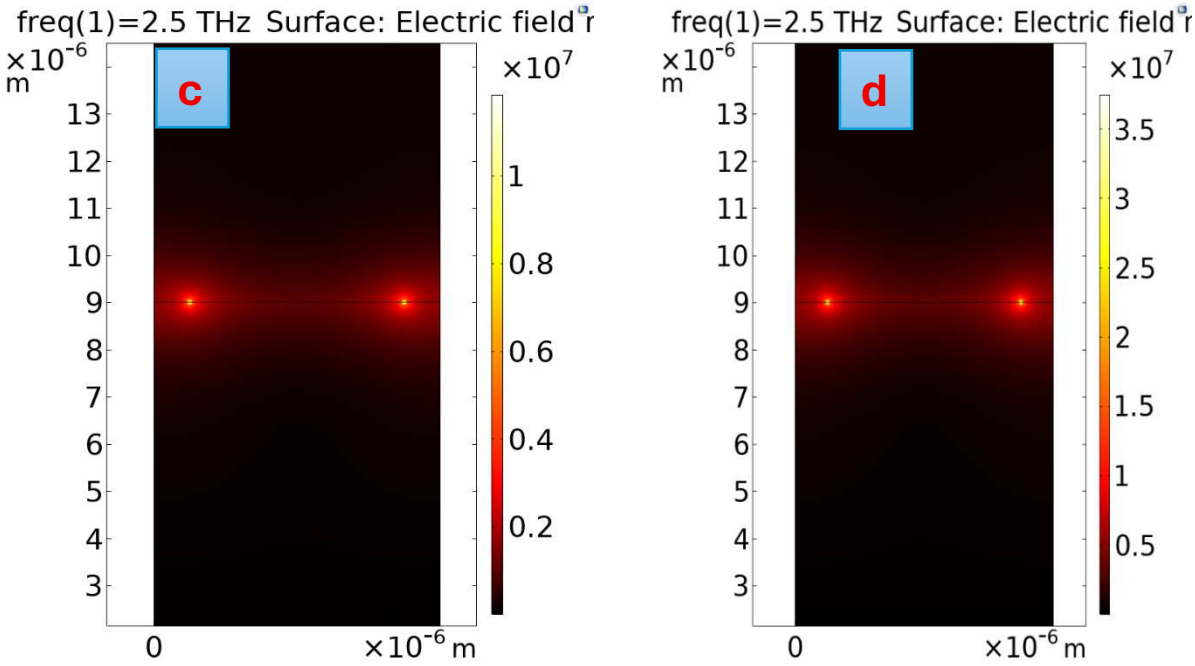

Figure 7-14(a-d)- Normalized spatial distribution of the electric field (V/m) for the fundamental signal wave at the plasmon resonance frequency of 1.5 THz for different intensity of irritated ($\boldsymbol{I_0}$)wave in Graphene micro ribbon: (a) $\boldsymbol{I_0} = .\mathbf{1}\frac{\boldsymbol{kW}}{\boldsymbol{cm^2}}$, (b) $\boldsymbol{I_0} = \mathbf{1}\frac{\boldsymbol{kW}}{\boldsymbol{cm^2}}$, (c)$\boldsymbol{I_0} = \mathbf{10}\frac{\boldsymbol{kW}}{\boldsymbol{cm^2}}$ and (d) $\boldsymbol{I_0} = \mathbf{100}\frac{\boldsymbol{kW}}{\boldsymbol{cm^2}}$. In all simulations, the Fermi energy of graphene, dielectric high and relaxation time are taken as .3 eV, $\mathbf{8}\,\boldsymbol{\mu}$m and .5 ps respectively.

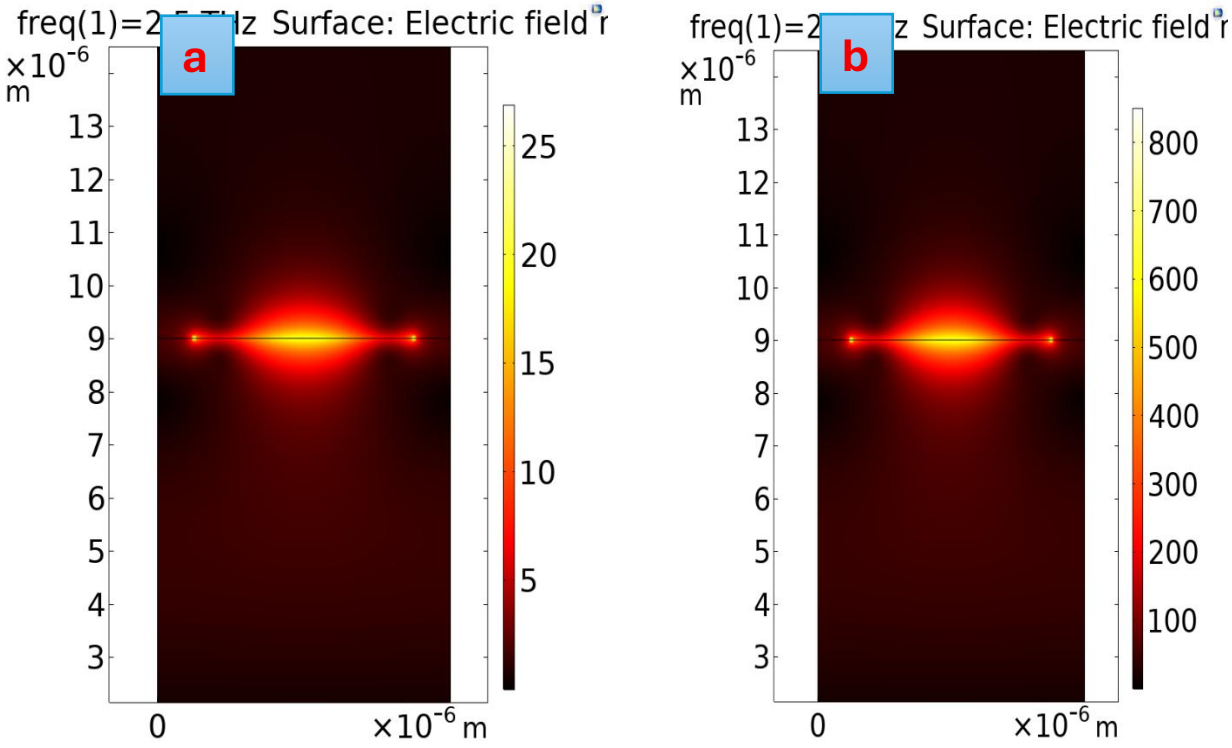

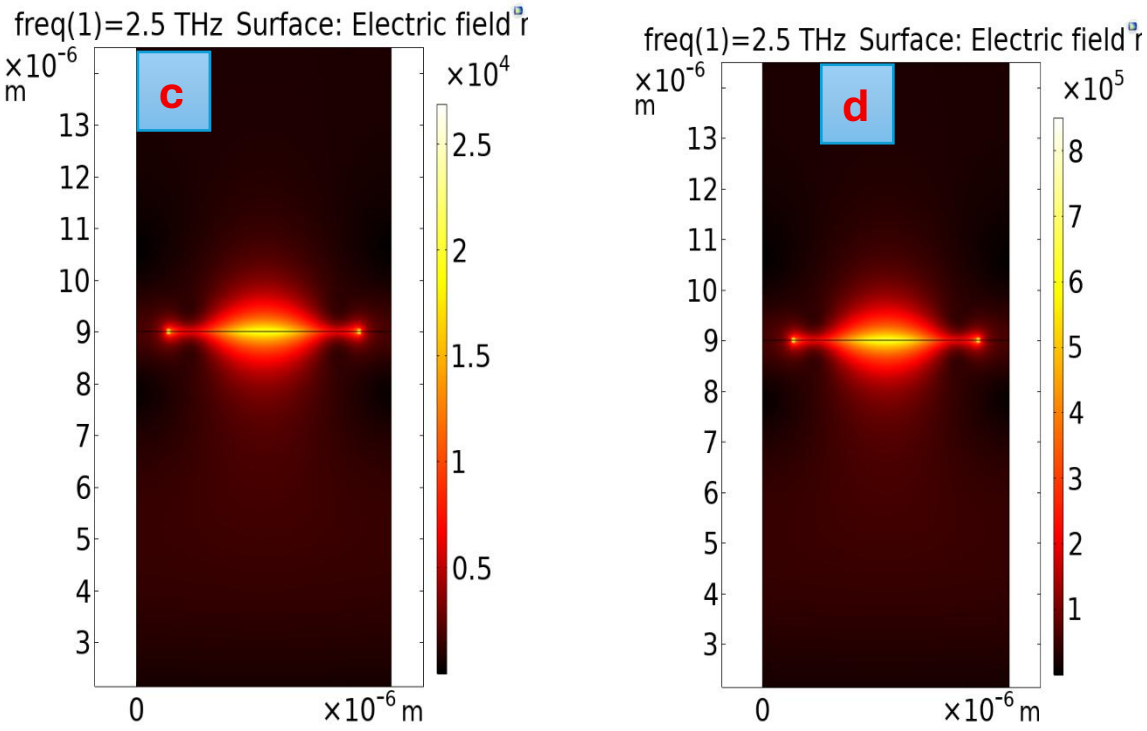

Figure 7-15(a-d)- Normalized spatial distribution of the electric field (V/m) for the Third Harmonic Generation wave at the plasmon resonance frequency of 1.5 THz for different intensity of irritated ($\boldsymbol{I_0}$)wave in Graphene micro ribbon: (a) $\boldsymbol{I_0} =. \mathbf{1}\frac{\boldsymbol{kW}}{\boldsymbol{cm^2}}$, (b) $\boldsymbol{I_0} = \mathbf{1}\frac{\boldsymbol{kW}}{\boldsymbol{cm^2}}$, (c)$\boldsymbol{I_0} = \mathbf{10}\frac{\boldsymbol{kW}}{\boldsymbol{cm^2}}$ and (d) $\boldsymbol{I_0} = \mathbf{100}\frac{\boldsymbol{kW}}{\boldsymbol{cm^2}}$. In all simulations, the Fermi energy of graphene, dielectric high and relaxation time are taken as .3 eV, $\mathbf{8}\,\boldsymbol{\mu}$m and .5 ps respectively.

In this section, we examine how the proximity of a protein molecule alters the electrostatic environment adjacent to a graphene surface. Building on the theoretical framework introduced earlier, the evaluation of the electric field and potential inside the Electric Double Layer (EDL) begins with the Poisson equation. After establishing the computational domain and boundary conditions, a set of numerical simulations was carried out to extract and compare the relevant electrostatic profiles. These graphical outputs enabled a detailed assessment of the modifications introduced when quantum capacitance is incorporated into the model, particularly regarding the spatial variation of potential and field strength.

Within the compact layer, the electrostatic behaviour was determined by solving the Poisson equation, $\nabla(\varepsilon\varepsilon_0\nabla\varphi) = 0$, In contrast, transport in the diffuse region was described using a coupled Nernst–Planck–Poisson formulation to provide a more realistic depiction of ion and protein motion [46, 47]:

$$\frac{\partial c_i}{\partial t} = \nabla(D_i\nabla c_i + z_i F D_i c_i \nabla\frac{\varphi}{RT}) \tag{7-34}$$

together with

$$\nabla(\varepsilon\varepsilon_0\nabla\varphi) = \rho \tag{7-35}$$

Here, D_i, z_i, and $c_i$represent the diffusivity, charge valence, and concentration of species i; $t$is time; $F$is the Faraday constant; $R$is the universal gas constant; $T$is temperature; $\varphi$is the electrostatic potential; $\varepsilon$and $\varepsilon_0$are the medium and vacuum permittivities; and ρdenotes the net charge density.

Figure 7-16(a–c) presents the resulting distributions, highlighting the drift of protein molecules, as well as the corresponding potential and electric-field patterns formed within the EDL.

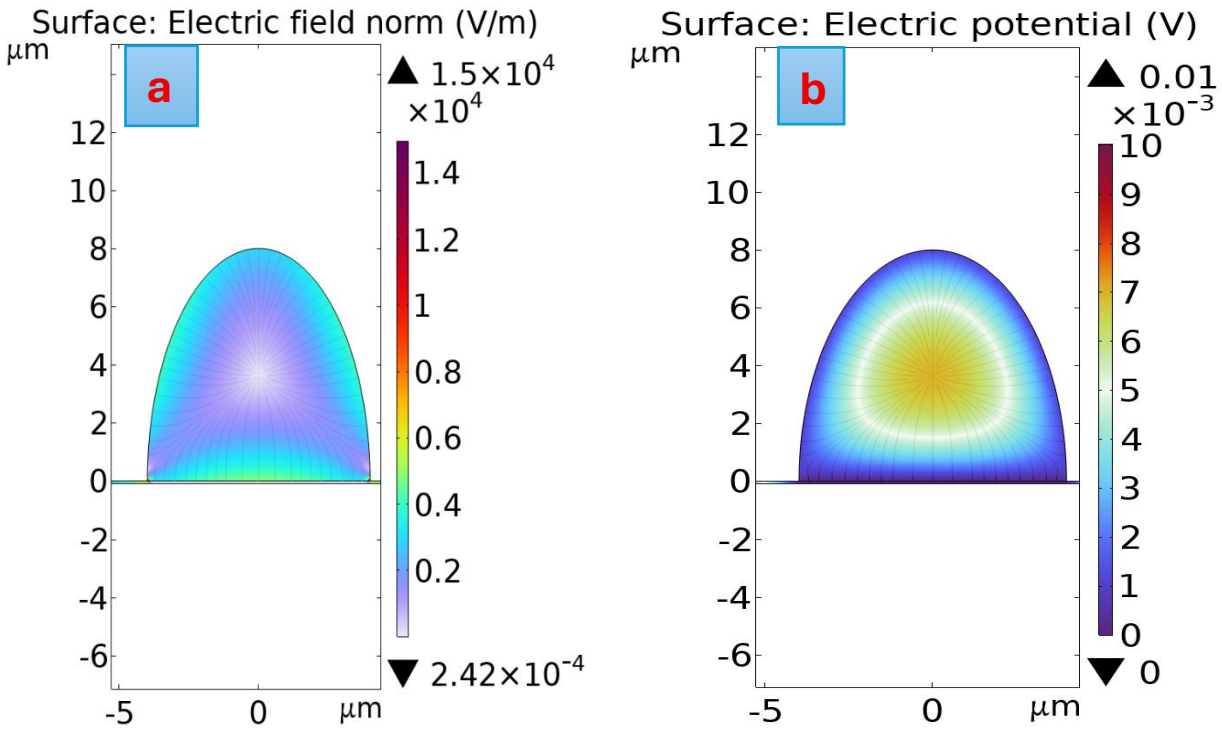

Figure 7-16. Panels a–b shows the electric potential (a), electric field (b) in the electrolyte, including the region near the electric double layer (EDL). The simulation uses the Stern model of EDL integrated with quantum capacitance of Graphene.

In this step, we compute the absorption, reflectance, and third-harmonic power outflow for different concentrations of β2-microglobulin. As discussed in the previous chapter, the presence of this protein in its wild-type form carries a net charge of −2. This negative charge induces electron doping in graphene, leading to an increase in its Fermi energy. As a consequence, the optical response of graphene is modified, resulting in a noticeable shift of the absorption and reflectance peaks toward higher frequencies.

β2-M concentration	Potential near to Graphene surface (mV)	Amount of Fermi energy of graphene (eV)
.0001 [g/L]	194.77	.346
.001 [g/L]	188.56	.35
.01 [g/L]	167	.369
.1 [g/L]	136	.395

Table 7-1. Information on the potential inside the electrolyte near the graphene surface and the corresponding Fermi energy of graphene in the presence of different β2-M concentrations.

Figure 7-17(a-d) illustrates this pattern clearly, where increasing the concentration of β2-microglobulin produces a systematic blue shift in the spectral features. This shift arises from the strong coupling between the charged biomolecules and the graphene surface, which alters the carrier density and thus the nonlinear optical properties of the system. Moreover, the enhancement in Fermi energy significantly influences the third-harmonic generation process, leading to changes in the magnitude of the third-harmonic power outflow. These results highlight the sensitivity of graphene's linear and nonlinear optical responses to biomolecular adsorption, underscoring its potential application as a highly sensitive biosensing platform.

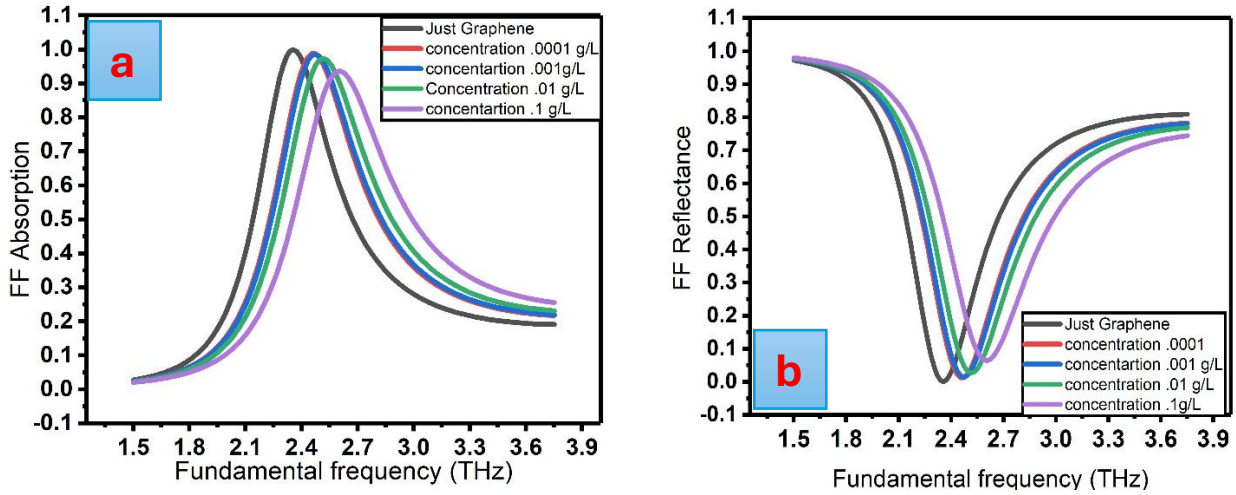

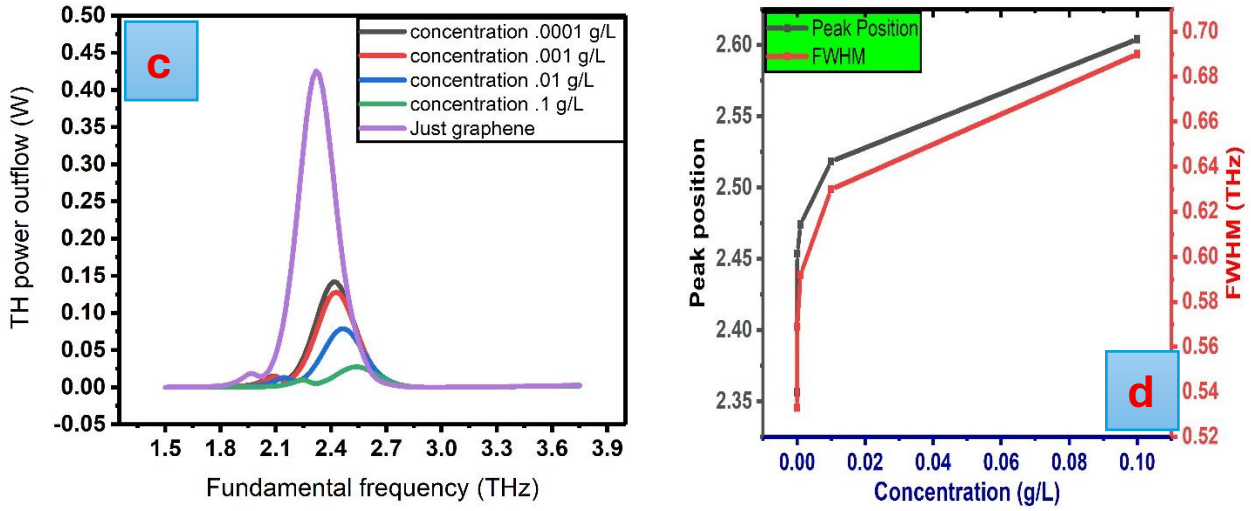

Figure 7-17(a-d)- (a) Absorption, (b) reflection, (c) Third Harmonic Generation (THG) power outflow spectra and (d) FWHM for different protein concentration across the frequency range of 1.5–3.5. In all simulations, the graphene relaxation time, Fermi energy of graphene, irritated wave intensity and thickness of dielectric are taken as 0.5 ps, 0.3 eV, 30 $\frac{kW}{cm^2}$ and 8um respectively.

Figures 7-18(a–d) and 7-19(a–d) illustrate the normalized spatial distribution of the electric field (V/m) for both the fundamental signal and the third-harmonic generation (THG) at the plasmonic resonance frequency of 1.5 THz for different protein concentrations in the vicinity of the graphene microribbon. As discussed previously, the presence of protein molecules near the graphene surface modifies its local electronic environment, leading to a change in the effective Fermi energy due to charge transfer and dielectric screening effects. Consequently, increasing the protein concentration results in an effective increase in the graphene Fermi energy.

In the present simulations, the intrinsic Fermi energy of the graphene microribbon is fixed at 0.3 eV, which has already been identified as the optimal value for achieving maximum field enhancement and absorption for this specific structure. Therefore, any further increase in Fermi energy induced by higher protein concentrations shifts the plasmonic resonance toward higher frequencies. Since the excitation frequency is maintained at 1.5 THz, this resonance detuning leads to a reduction in plasmonic coupling efficiency and weaker field confinement.

As a result, both the fundamental and THG electric-field intensities decrease with increasing protein concentration, as observed in Figures 7-18(a–d) and 7-19(a–d). This behavior confirms the high sensitivity of the graphene plasmonic response to surface-bound biomolecules and highlights the potential of the proposed structure for biosensing applications. The observed decrease in electric-field intensity serves as a measurable optical signature of protein concentration, demonstrating the feasibility of using Fermi-energy modulation in graphene for label-free terahertz biosensing.

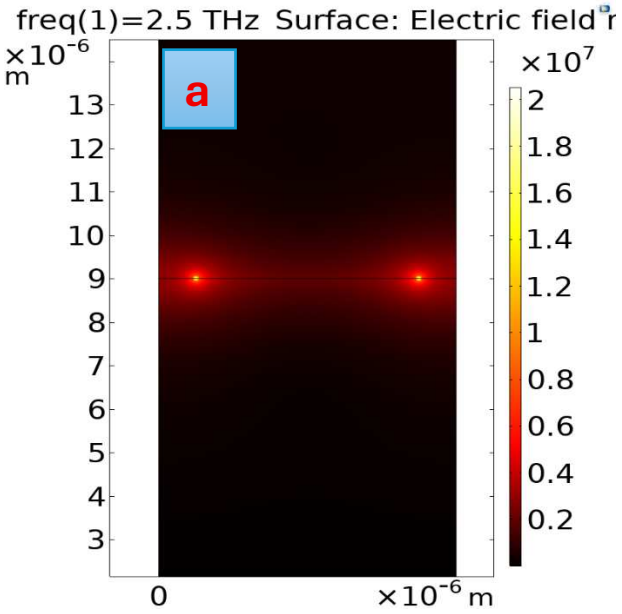
freq(1)=2.5 THz Surface: Electric field r
×10^-6 m
13
12
11
10
9
8
7
6
5
4
3
0
×10^-6 m
a
×10^7
2
1.8
1.6
1.4
1.2
1
0.8
0.6
0.4
0.2

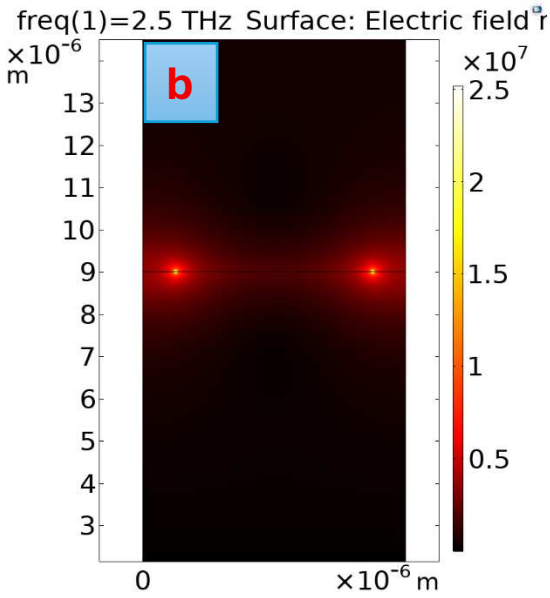
freq(1)=2.5 THz Surface: Electric field r
×10^-6 m
13
12
11
10
9
8
7
6
5
4
3
0
×10^-6 m
b
×10^7
2.5
2
1.5
1
0.5

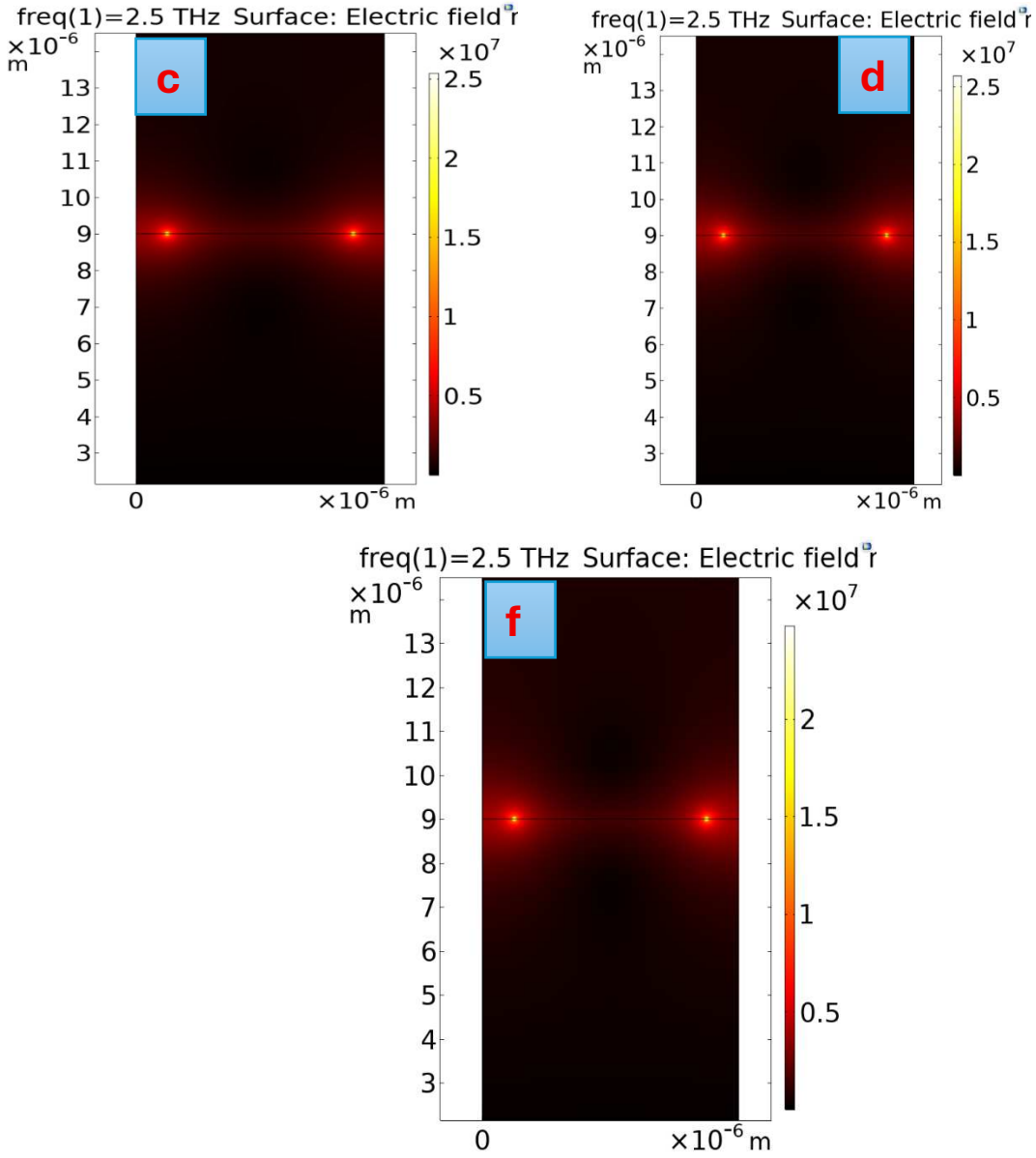

Figure 7-18 (a-f)- Normalized spatial distribution of the electric field (V/m) for the fundamental signal wave at the plasmon resonance frequency of 1.5 THz for different concentration (C)of β2-M on top of surface of Graphene micro ribbon: (a) C=0, (b) C=.0001g/L , (c)C=.001g/L, (d) C=.01g/L and (f) $\mathbf{C = .1g/L}$. In all simulations, the Fermi energy of graphene, dielectric high and relaxation time and intensity of irradiated wave are taken as .3 eV, $\mathbf{8}\ \boldsymbol{\mu}$m, .5 ps and 30 $\frac{\boldsymbol{kW}}{\boldsymbol{cm^2}}$ respectively.

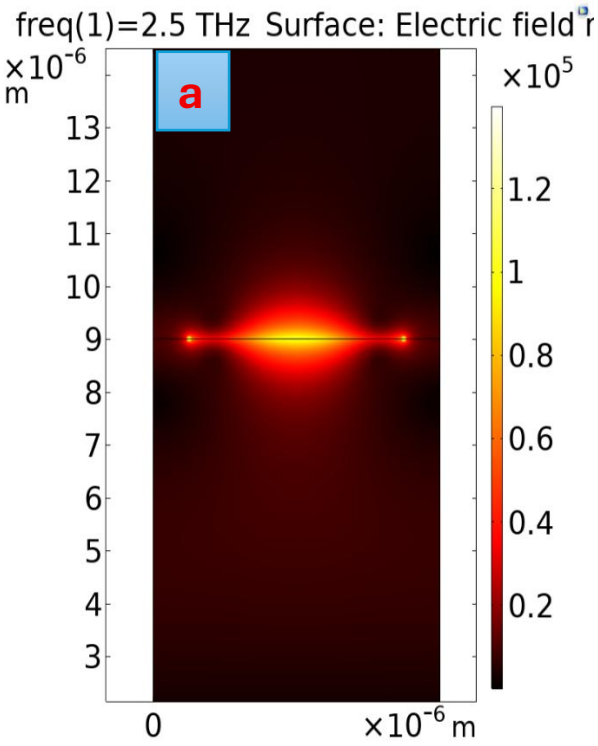
freq(1)=2.5 THz Surface: Electric field r
a
×10^-6 m
×10^5
1.2
1
0.8
0.6
0.4
0.2
13
12
11
10
9
8
7
6
5
4
3
0
×10^-6 m

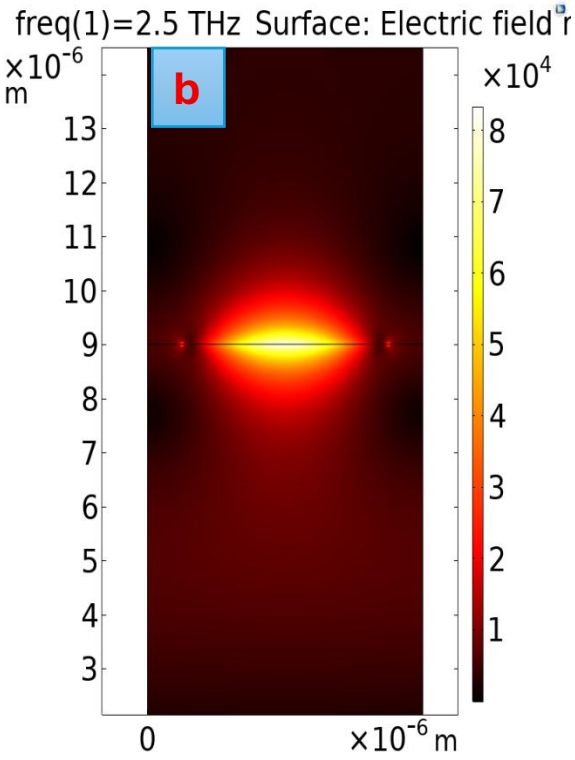
freq(1)=2.5 THz Surface: Electric field r
b
×10^-6 m
×10^4
8
7
6
5
4
3
2
1
13
12
11
10
9
8
7
6
5
4
3
0
×10^-6 m

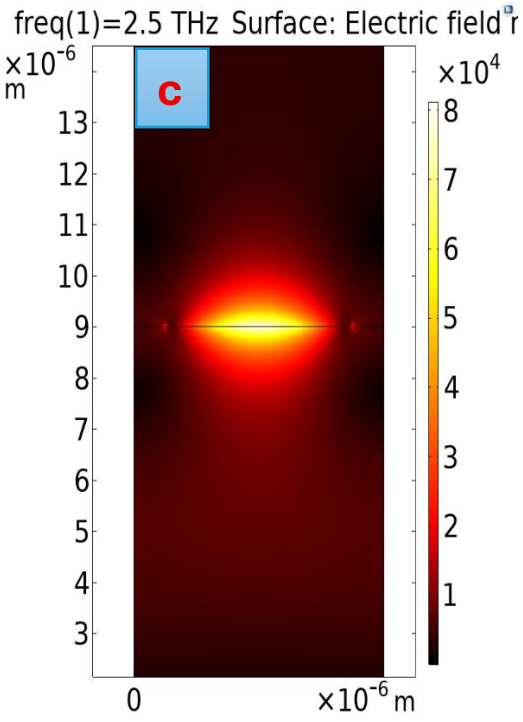
freq(1)=2.5 THz Surface: Electric field r
c
×10^-6 m
×10^4
8
7
6
5
4
3
2
1
13
12
11
10
9
8
7
6
5
4
3
0
×10^-6 m

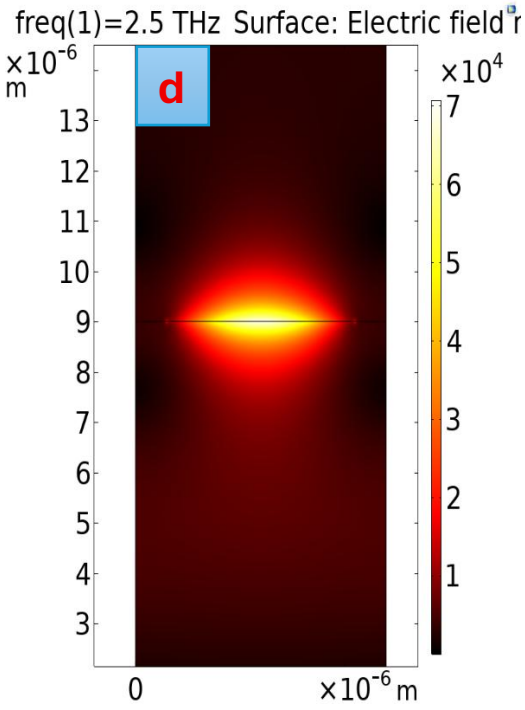
freq(1)=2.5 THz Surface: Electric field r
d
×10^-6 m
×10^4
7
6
5
4
3
2
1
13
12
11
10
9
8
7
6
5
4
3
0
×10^-6 m

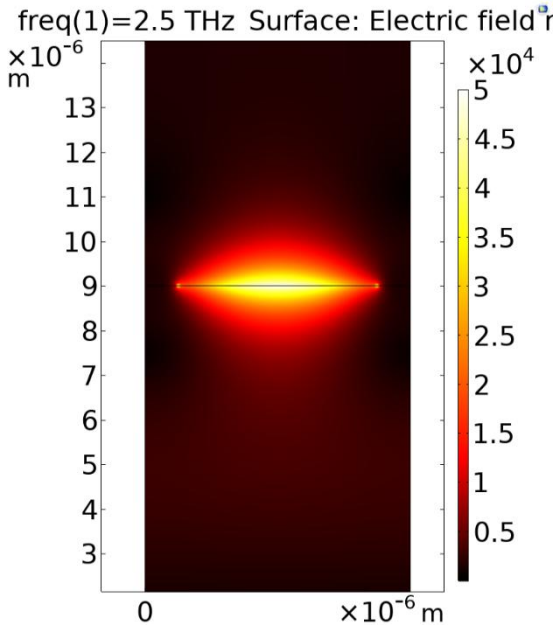

Figure 7-18 (a-f)- Normalized spatial distribution of the electric field (V/m) for the fundamental signal wave at the plasmon resonance frequency of 1.5 THz for different concentration (C)of β2-M on top of surface of Graphene micro ribbon: (a) C=0, (b) C=.0001g/L , (c)C=.001g/L, (d) C=.01g/L and (f) $\mathbf{C = .1g/L}$. In all simulations, the Fermi energy of graphene, dielectric high and relaxation time and intensity of irradiated wave are taken as .3 eV, $\mathbf{8}\ \boldsymbol{\mu}$m, .5 ps and 30 $\frac{\boldsymbol{kW}}{\boldsymbol{cm^2}}$ respectively.

In the final step of our computation, we investigate the conversion efficiency and third-harmonic power outflow as functions of the incident optical intensity. For this purpose, the input intensity is varied from 0.001 MW/cm² to 0.12 MW/cm² for different concentrations of the biomolecule. As shown in the figure below, increasing the incident intensity leads to pronounced variations in both the conversion efficiency and the third-harmonic output.

This behavior is attributed to the nonlinear optical response of graphene, where higher input intensities enhance the nonlinear polarization responsible for third-harmonic generation. These results demonstrate that both incident intensity and molecular concentration are key factors in optimizing third-harmonic generation, reinforcing the potential of this system for tunable nonlinear optical and biosensing applications.

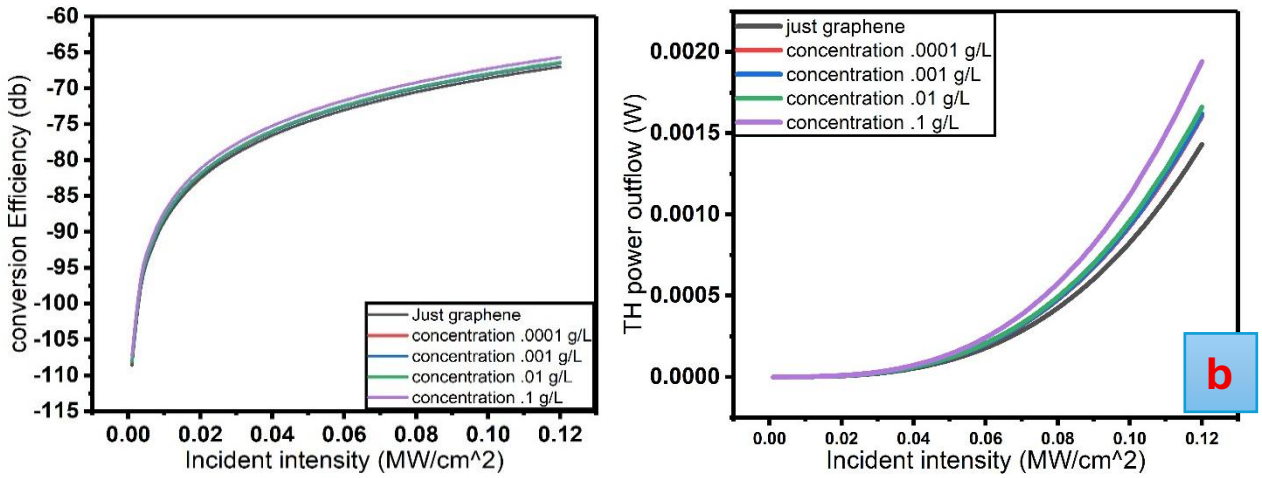

Figure 7-20. Effect of incident intensity on (a) conversion efficiency and (b) third harmonic generation power outflow as functions of the incident wave intensity at fundamental frequency of 3 THz with different concentration of protein. In all simulations, the graphene relaxation time, Fermi energy of graphene and thickness of dielectric are taken as 0.5 ps, 0.3 eV and 8um respectively.

7-9. Conclusion:

Conventional subwavelength structures typically suffer from low nonlinear conversion efficiency, requiring extremely high input intensities to generate detectable third-harmonic signals. To overcome this limitation, this work proposed and investigated a nonlinear ultrathin metasurface based on periodically patterned graphene micro-ribbons for efficient third-harmonic generation (THG) at terahertz (THz) frequencies under low excitation intensities. The proposed design exploits strong electromagnetic field confinement arising from the simultaneous excitation of surface plasmon resonances along the graphene ribbons and Fabry–Pérot resonances within the dielectric substrate. This dual-resonance mechanism leads to a substantial enhancement of the local electric field at the fundamental frequency, which is a key factor in boosting the nonlinear response.

Moreover, graphene exhibits an exceptionally strong third-order nonlinear conductivity in the THz regime compared to most conventional dielectrics and noble metals. As a result, when the incident wave is tuned to the metasurface resonance, the THG conversion efficiency is enhanced by several orders of magnitude. The highest conversion efficiency is achieved under normal incidence of the fundamental wave, highlighting the favorable symmetry and coupling conditions of the proposed structure. Notably, unprecedented conversion efficiencies on the order of -65 dB are obtained at low THz frequencies with relatively low incident intensities (~0.1 $MW \cdot cm^{-2}$). This low-power requirement represents a significant advantage, particularly given the limited availability of high-power THz sources, and greatly improves the practicality of graphene-based THz nonlinear devices.

In addition to high efficiency, the proposed graphene metasurface demonstrates remarkable tunability and reconfigurability. Systematic analysis reveals that key parameters-including the graphene Fermi energy (doping level), dielectric thickness, and relaxation time associated with carrier mobility-can effectively control the resonance frequency, nonlinear conductivity, and optical losses of the metasurface. By dynamically tuning these parameters, the structure can be engineered to emit TH radiation at different frequencies, enabling adaptable and multifunctional operation.

Furthermore, the optical performance of the metasurface was evaluated in the presence of varying concentrations of β2-microglobulin. The results show that increasing protein concentration induces a noticeable shift of the resonance toward higher energies. This behavior is attributed to the net negative charge of the protein (−2), which increases the effective Fermi energy of graphene upon adsorption and consequently shifts the plasmonic resonance frequency. This sensing capability highlights the strong interaction between graphene plasmons and biochemical environments.

Overall, the findings reported in this work pave the way for the development of compact, efficient, and tunable nonlinear THz devices at the chip scale. The proposed graphene metasurface holds strong potential for applications as adaptive THz and infrared sources, frequency mixers, and highly sensitive biosensing platforms. Compared to conventional biosensors, the demonstrated approach offers enhanced sensitivity and tunability, making it promising for the detection and characterization of physiological tissues and biomolecules in future integrated THz photonic systems.

The application of third-harmonic generation (THG) for the detection of physiological tissue demonstrates significantly higher sensitivity compared with conventional linear sensing techniques.

Refernces:

[1]- Ohtsu, Motoichi, et al. "Frequency control of semiconductor lasers." *Journal of applied physics* 73.12 (1993): R1-R17.

[2]- Akhmanov, S., et al. "Nonstationary nonlinear optical effects and ultrashort light pulse formation." *IEEE Journal of Quantum Electronics* 4.10 (1968): 598-605.

[3]- Ma, Ming, and Lawrence R. Chen. "Harnessing mode-selective nonlinear optics for on-chip multi-channel all-optical signal processing." *APL Photonics* 1.8 (2016).

[4]- Castet, Frederic, et al. "Design and characterization of molecular nonlinear optical switches." *Accounts of chemical research* 46.11 (2013): 2656-2665.

[5]- Suresh, Sagadevan, and Dakshanamoorthy Arivuoli. "Nanomaterials for nonlinear optical (NLO) applications: a review." *Rev. Adv. Mater. Sci* 30.3 (2012): 243-253.

[6]- Kauranen, Martti, and Anatoly V. Zayats. "Nonlinear plasmonics." *Nature photonics* 6.11 (2012): 737-748.

[7]- Shen, Yuen-Ron. "Principles of nonlinear optics." (1984).

[8]- Boyd, Robert W., Alexander L. Gaeta, and Enno Giese. "Nonlinear optics." *Springer Handbook of Atomic, Molecular, and Optical Physics* . Cham: Springer International Publishing, 2008. 1097-1110.

[9]- Butet, Jérémy, Pierre-François Brevet, and Olivier JF Martin. "Optical second harmonic generation in plasmonic nanostructures: from fundamental principles to advanced applications." *ACS nano* 9.11 (2015): 10545-10562.

[10]- Sevilla-Sierra, Nuria, et al. "Unveiling second harmonic generation from femtosecond-laser microstructured Nd: YAG crystal." *Optics Express* 32.10 (2024): 16845-16854.

[11]- Yan, Dexian, et al. "Enhanced terahertz third-harmonic generation based on the graphene-assisted meta-grating structure." *Diamond and Related Materials* 142 (2024): 110818.

[12]- Kumar, VIPin. “Linear and Nonlinear Optical Properties of Graphene: A Review.” *Journal of Electronic Materials* 50.7 (2021).

[13]- Jin, Boyuan, Tianjing Guo, and Christos Argyropoulos. "Enhanced third harmonic generation with graphene metasurfaces." *Journal of Optics* 19.9 (2017): 094005.

[14]- Zanbouri, Zeinab, Mohammad Sabaeian, and Ehsan Shakerzadeh. "Tunable third-harmonic generation in black phosphorus nanoribbon in the terahertz frequency." *Optics Express* 33.16 (2025): 33750-33767.

[15]- Castro Neto, Antonio H., et al. "The electronic properties of graphene." *Reviews of modern physics* 81.1 (2009): 109-162.

[16]- Ornigotti, Marco, David N. Carvalho, and Fabio Biancalana. "Nonlinear optics in graphene: theoretical background and recent advances." *La Rivista del Nuovo Cimento* 46.6 (2023): 295-380.

[17]- Cheng, Jin-Luo, Nathalie Vermeulen, and J. E. Sipe. "Third order optical nonlinearity of graphene." *New Journal of Physics* 16.5 (2014): 053014.

[18]- Davoudi, Maryam, Zeinab Zanbouri, and Mohammad Sabaeian. "Enhancing third-order harmonic generation in a graphene-gold grating structure with MgF2 substrate at terahertz frequencies." *Physica Scripta* 100.8 (2025): 085559.

[19]- Sabaeian, Mohammad, and Ghassem Baridi. "Graphene plasmonic-assisted enhancement of linear and nonlinear optical properties of conic-shaped InAs/GaAs quantum dots with wetting layer." *Superlattices and Microstructures* 144 (2020): 106582.

[20]- Sabaeian, Mohammad, and Ghassem Baridi. "Coupling the graphene plasmonic with terahertz emission of truncated conic-shaped InAs/GaAs quantum dots: A passive approach to enhance the intersubband optical properties." *Physica E: Low-dimensional Systems and Nanostructures* 134 (2021): 114834.

[21]- Baridi, Ghassem, et al. "Hybrid quantum dot-graphene layers with improved optical properties in the terahertz spectrum region." *Physica E: Low-dimensional Systems and Nanostructures* 146 (2023): 115524.

[22]- Soavi, Giancarlo, et al. "Broadband, electrically tunable third-harmonic generation in graphene." *Nature nanotechnology* 13.7 (2018): 583-588.

[23]- Rostami, Habib, and Marco Polini. "Theory of third-harmonic generation in graphene: A diagrammatic approach." *Physical Review B* 93.16 (2016): 161411.

[24]- Xu, Mingjun, et al. "Enhanced terahertz dual-band third-harmonic generation in graphene-assisted metamaterial." *Optics and Lasers in Engineering* 181 (2024): 108407.

[25]- Shang, Meng, et al. "Third-order nonlinear optical properties of graphene composites: A review." *Chinese Physics B* 30.8 (2021): 080703.

[26]- Ri, Chol-Song, et al. "Nanoscale magnetization and third-order nonlinearity by the plasmon-induced inverse Faraday effect in graphene-covered semiconductors." *Physical Review B* 100.15 (2019): 155404.

[27]- Gray, Stephen K. "Theory and modeling of plasmonic structures." *The Journal of Physical Chemistry C* 117.5 (2013): 1983-1994.

[28]- Khurgin, Jacob B. "How to deal with the loss in plasmonics and metamaterials." *Nature nanotechnology* 10.1 (2015): 2-6.

[29]- Jablan, Marinko, Hrvoje Buljan, and Marin Soljačić. "Plasmonics in graphene at infrared frequencies." *Physical Review B—Condensed Matter and Materials Physics* 80.24 (2009): 245435.

[30]- Liu, Yulian, et al. "Enhanced third-harmonic generation induced by nonlinear field resonances in plasmonic-graphene metasurfaces." *Optics Express* 28.9 (2020): 13234-13242.

[31]- Yan, Dexian, et al. "Enhanced terahertz third-harmonic generation based on the graphene-assisted meta-grating structure." *Diamond and Related Materials* 142 (2024): 110818.

[32]- Xu, Mingjun, et al. "Enhanced terahertz dual-band third-harmonic generation in graphene-assisted metamaterial." *Optics and Lasers in Engineering* 181 (2024): 108407.

[33]- Nasari, H., and M. S. Abrishamian. "Nonlinear terahertz frequency conversion via graphene microribbon array." *Nanotechnology* 27.30 (2016): 305202.

[34]- Male, MARIA CELESTE. "Modeling of an amyloidogenic protein in solution and on surfaces." (2019).

[35]- Demir, Baris, and Debra J. Searles. "Investigation of the ionic liquid graphene electric double layer in supercapacitors using constant potential simulations." *Nanomaterials* 10.11 (2020): 2181.

[36]- Xu, Huilong, Zhiyong Zhang, and Lian-Mao Peng. "Measurements and microscopic model of quantum capacitance in graphene." *Applied Physics Letters* 98.13 (2011).

[37]- Xia, Jilin, et al. "Measurement of the quantum capacitance of graphene." *Nature nanotechnology* 4.8 (2009): 505-509.

[39]- Abbas, Ghulam, et al. "Electrostatic gating of monolayer graphene by concentrated aqueous electrolytes." *The Journal of Physical Chemistry Letters* 14.18 (2023): 4281-4288.

[40]-Wu, Jianzhong. "Understanding the electric double-layer structure, capacitance, and charging dynamics." *Chemical Reviews* 122.12 (2022): 10821-10859.

[41]- Burt, Ryan, Greg Birkett, and X. S. Zhao. "A review of molecular modelling of electric double layer capacitors." *Physical Chemistry Chemical Physics* 16.14 (2014): 6519-6538.

[42]- Doblhoff-Dier, Katharina, and Marc TM Koper. "Electric double layer of Pt (111): Known unknowns and unknown knowns." *Current Opinion in Electrochemistry* 39 (2023): 101258.
[43]- Gongadze, E., Petersen, S., Beck, U., & Van Rienen, U. (2009, October). Classical Models of the Interface between an Electrode and an Electrolyte. In *COMSOL conference* (pp. 14-16).
[44]- Meric, Inanc, et al. "Current saturation in zero-bandgap, top-gated graphene field-effect transistors." *Nature nanotechnology* 3.11 (2008): 654-659.
[45]- Béraud, Anouk, et al. “Graphene field-effect transistors as bioanalytical sensors: Design, operation and performance.” *Analyst* 146.2 (2021): 403-428.

List of publication:

1- Ghassem Baridi et.al: Graphene-based chemical field effect transistors: impact of electric double layer model and quantum capacitance on $\boldsymbol{Na^+}$ detection capabilities. Micromachine 2026

2- Ghassem Baridi et.al: Computational Simulation of Surface Plasmon Resonance Biosensor for β2-Microglobulin based on Electrolyte-Gated Graphene. Sensor 2026

3- Ghassem Baridi et.al: Nonlinear Optical Detection of β2-Microglobulin Using Graphene-Enhanced Third-Harmonic Generation (under review). Sensor 2026

4- Arsalan Liaquat, Ghassem Baridi et. al. Enhanced Biomarker detection of Albumin using Electrolyte Gated Graphene Field Effect transistor (EGFET). (under review). Biosensor and Bioelectronics 2026.

5- Arsalan Liaquat, Ghassem Baridi et. al. Electrolyte Gated Graphene Field Effect Transistor (EGFET) as PH sensor. (preparing). Predicted Journal (ACS Applied Nano materials).

6- Quantum-Electrostatic Modelling of Graphene FET Biosensors for β2-Microglobulin Detection. (under review). Electronics 2026

Conference and workshop:

1- Ghassem Baridi et.al: simulation of Graphene-based chemical field effect transistors: impact of electric double layer model and quantum capacitance on β2-Microglobulin detection capabilities**.** Conference FISMAT 2025**.**

2- Ghassem Baridi et.al: Potential application: optically detecting the presence and concentration of β-2 microglobuline. Workshop Modena 2025.